AN ABSTRACT OF THE THESIS OF

<u>Kathleen I. Schaffers</u> for the degree of <u>Doctor of Philosophy</u> in

<u>Chemistry</u> presented on <u>September 16, 1992</u> .

Title: <u>A Study of New Optical Materials</u>

   <u>I. Crystal-Chemical Development of New Optical Frequency Converters</u>

   <u>II. New Hosts for Cr^{3+} Luminescence and Lasing</u>

Redacted for Privacy

Abstract approved: _____
                              Douglas A. Keszler

The emphasis of this work has been in two areas of optical materials - the crystal-chemical development of new optical frequency converters and the synthesis and study of new hosts for Cr^{3+} luminescence and lasing.

A simple method has been developed to identify promising frequency-doubling materials containing triangular oxoanions by estimation of nonlinear susceptibilities. Implementation of this method and its results have generated predictive capabilities in determining the relationships among crystal structure, nonlinear properties, and threshold powers. The new noncentrosymmetric borate $SrLiB_9O_{15}$ is discussed; its structure is built from a 3-dimensional condensation of B_3O_7 units with channels alternately filled with Sr and Li atoms. From these

studies, a prescription for new pyroborate frequency converters has been developed. The material $CdCl_2C_3H_7NO_2$, has been synthesized and structurally characterized by single-crystal X-ray diffraction.

Three new alkaline-earth beryllium borates, built from unique 2- and 3-dimensional networks and frameworks, have been identified. The structure of $SrBe_2(BO_3)_2$ consists of layers of composition $[Be_2(BO_3)_2]^{2-}$ interleaved by Sr atoms. $CaBeB_2O_5$ is constructed from a CaO_9 polyhedral network and a beryllium borate network. In $BaBe_2(BO_3)_2$ the structure is composed of a beryllium borate framework intermingled with a Ba-centered dodecahedral framework.

Several materials with potential as hosts for Cr^{3+} lasing have been analyzed. The structural study of the laser host $LiSrAlF_6$ revealed the distortions at the Al site that contribute to the unique optical properties of the Cr^{3+}-doped crystals. The family of solid state oxide $A_6MM'(BO_3)_6$ is one of the largest families of oxide reported to date. Metal site preferences, disorder, solid solubility, and the interrelationship between this structure and the layered structure type of $Ba_3Sc(BO_3)_3$ are detailed. An optimal synthetic procedure has been developed for these materials to provide pure, highly crystalline phases. Also, the structural and optical features of (Cr^{3+}:) $Sr_3In(BO_3)_3$ with A= Sr and M=M'= In have been studied.

The material $Sr_2LiInB_4O_{10}$, was discovered while searching for a suitable lithium borate flux for crystal growth of the compound $Sr_3In(BO_3)_3$.

A Study of New Optical Materials

I. Crystal-Chemical Development of New Optical

Frequency Converters

II. New Hosts for Cr^{3+} Luminescence and Lasing

by

Kathleen I. Schaffers

A THESIS

submitted to

Oregon State Unversity

in partial fulfillment of

the requirements for the

degree of

Doctor of Philosophy

Completed September 16, 1992

Commencement June 1993

APPROVED:

_____

Professor of Chemistry in charge of major

_____

Head of Department of Chemistry

_____

Dean of Graduate School

Date thesis is presented _____ September 16, 1992 _____

Prepared and presented by _____ Kathleen I. Schaffers _____

ACKNOWLEDGMENTS

This work was accomplished with the support and assistance of many people to whom I am immeasurably indebted.

Above all, I am grateful to my major professor Doug Keszler; he has been a tremendous inspiration to me in the past four years and will continue to be in the future. Without his support, guidance, and friendship my graduate career would not have been as successful or gratifying.

I wish to thank my fellow colleagues in the Keszler group: Dr. Tom Reynolds, Ted Alekel III, Jim Cox, Yaobo Yin, Jun Ming Tu, Annapoorna Akella, Chris Orf, George Pon, Dr. Rob Smith, Dr. Hongxing Sun, and Dr. Paul Thompson. They have continually made me laugh and have supported me through the good times and the bad. I have great respect for them and will always treasure their friendship.

I would like to thank my parents, Clem and Lola, and my sister and brothers, Susanne, Paul, Will, and Joe. Their love and encouragement have motivated me to strive for excellence in every aspect of my life.

Finally, I wish to acknowledge the faculty and staff of the Chemistry Department for their kindness and assistance.

TABLE OF CONTENTS

LIST OF FIGURES

LIST OF TABLES

CONTRIBUTION OF AUTHORS

Dr. Thomas A. Reynolds aided in the second-harmonic generation (SHG) experiments and the excitation and luminescence measurements described in Chapters 3 and 8, respectively.

The data presented in Chapter 10 resulted from a collaboration of Theodore Alekel III, James R. Cox, Dr. Paul D. Thompson, Dr. Douglas A. Keszler, and myself. Specifically, Theodore Alekel performed the crystal studies on $Sr_6Y_{1.07}Al_{0.93}(BO_3)_6$ and the powder studies on the $A_6M^{2+}(Zr^{4+}$ or $Ti^{4+})(BO_3)_6$ derivatives. James Cox solved the structure of $Ba_6Gd_{1.28}Sc_{0.72}(BO_3)_6$, aided in the study of the solid solution series $Sr_6La_xSc_{2-x}(BO_3)_6$, and provided all of the data on the $A_6MM'(BO_3)_6$ derivatives where A= Ba. Paul Thompson examined the solid solution series $Sr_6Sc_{2-x}Al_x(BO_3)_6$ and $Sr_6Y_{2-x}Al_x(BO_3)_6$ for $0 \leq x \leq 2$. Dr. Douglas Keszler solved the crystal structure of $Sr_6Er_{1.40}Sc_{0.60}(BO_3)_6$. I performed the structure analysis on $Sr_6Ho_{0.964}Sc_{1.036}(BO_3)_6$ and $Sr_6La_{0.84}Sc_{1.16}(BO_3)_6$, examined the solid solution series $Sr_6Ho_xSc_{2-x}(BO_3)_6$, and worked with James Cox on the $Sr_6La_xSc_{2-x}(BO_3)_6$ solid solution series. All other data (specifically the powder studies summarized in Table 10.3) were accumulated from a combined effort.

A STUDY OF NEW OPTICAL MATERIALS

I. CRYSTAL-CHEMICAL DEVELOPMENT OF NEW OPTICAL FREQUENCY CONVERTERS

II. NEW HOSTS FOR Cr^{3+} LUMINESCENCE AND LASING

CHAPTER 1

INTRODUCTION

Research in the field of optical materials during the past decade has led to the development of a variety of compounds with unique properties. Because of these properties several materials are rapidly being scrutinized and engineered to improve and displace a number of electronically and mechanically dominated techniques in areas such as communication, defense, computing, general research, data collection, medicine, and dentistry. The advent of new laser and wavelength conversion materials that reach into and bridge regions of the electromagnetic spectrum, unavailable until recently, has acted as a catalyst to spur the investigation of optical materials for new applications.

The emphasis of this work involves two areas of optical materials, one being the crystal-chemical development of new optical frequency converters and the other new hosts for Cr^{3+} luminescence and lasing. A methodical approach is applied to the exploration of phase systems to discover new crystalline structure

types. The motivation for the systems selected for investigation derives from a careful accounting and fusion of the chemical, structural, and optical properties of known materials and a desire to better understand their attributes so that they can be applied with greater accuracy and efficiency. The studies described herein were done as a means to expand and clarify the current working base of information available on these materials.

A simple method has been developed to identify promising frequency-doubling materials by estimation of nonlinear susceptibilities from elementary calculations and visual inspection of crystal structures. A detailed description of the implementation of this method and its results are presented in Chapter 2. In Chapters 3 through 8, the structures and characteristics of six new compounds, discovered while searching for potential new frequency converters, are presented and their structures and properties discussed. The second section of the dissertation on solid state laser materials begins with Chapter 9. In this chapter, the structure of the Cr^{3+} laser host $LiSrAlF_6$ is described. A new family of compounds having the representative formula $A_6MM'(BO_3)_6$ has recently been discovered and christened STACK after its founders (1). It is one of the largest families of oxide reported to date encompassing approximately 50% of the elements in the periodic table. A crystal-chemical study defining the structural and chemical (elemental) boundaries along with the behavioral characteristics of many derivatives is given in Chapter 10. In Chapter 11, a set of experiments is outlined to determine the most efficient synthetic route for these compounds, providing the

purest phase and the highest degree of crystallinity. In Chapter 12, the structural and optical features of the STACK derivative $Sr_3In(BO_3)_3$ are described. Finally, the structure of the new oxide $Sr_2InLiB_4O_{10}$ is detailed in Chapter 13.

Section I. Optical Frequency Converters

The optical conversion of light from one frequency to another by crystalline nonlinear optical (NLO) materials (Figure 1.1) has progressed into a rapidly growing field of study. Frequency conversion of laser light was first witnessed in a quartz crystal in 1961 (2) following the discovery of the laser. It is now widely used in many materials to generate coherent light from the IR to the UV thereby extending the range of intense collimated, monochromatic light for application to wavelengths shorter than those available from a single laser oscillator. We are particularly interested in those materials with wide transparency ranges that can be used to generate coherent light at short wavelengths and high powers. Such light is becoming increasingly important in chemical and physical research as well as in communications, photolithography, and controlled photoinitiation of chemical reactions.

Many factors contribute to the production of doubled, high power laser light. The power extracted from a second harmonic generation (SHG) crystal of length L, may be approximated by Eq. 1.1 (3),

$$P_{2\omega} \propto P_{\omega}^2 \cdot L^2 \cdot d_{jm}^2 \exp\{-L(\alpha_{\omega}+\frac{1}{2}\alpha_{2\omega})\}\,[\frac{\sin^2 L \cdot \Delta K/2}{(L \cdot \Delta K/2)^2}] \qquad [Eq.\ 1.1]$$
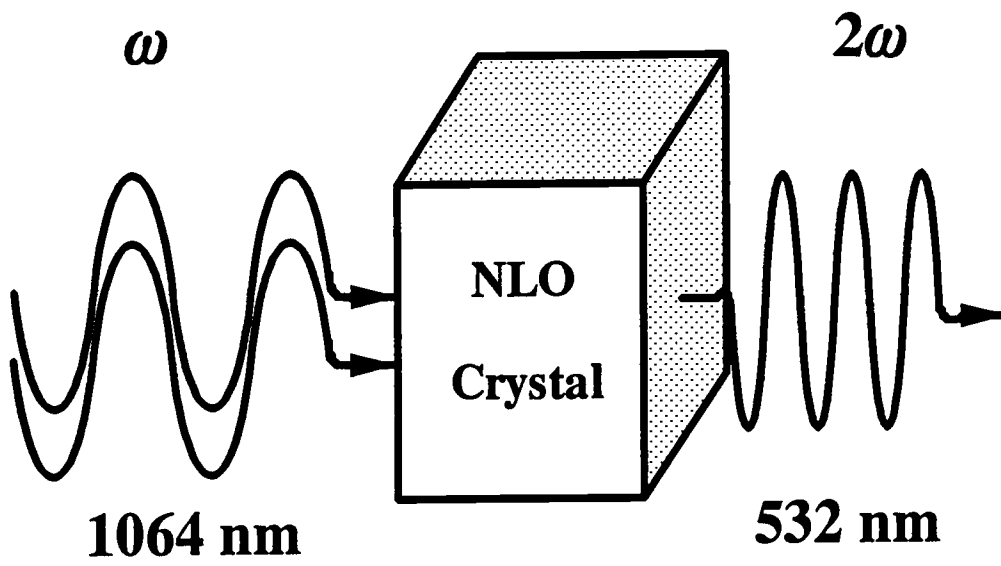
Fig. 1.1. Frequency conversion of light via a crystalline medium.

where P_ω is the power of the incident beam, d_{jm} is the relevant SHG coefficient, α_ω is the absorption coefficient of the crystal at the fundamental wavelength, $\alpha_{2\omega}$ is the absorption coefficient of the crystal at the second harmonic wavelength, and ΔK is the wave vector mismatch between the fundamental and second harmonic waves. Here, the exponential term approximates the absorption characteristics of the NLO crystal and the *sin* term describes the ability to phase match the incoming and doubled waves. From Equation 1.1, it is noted that to achieve high powers for the second harmonic wave with a high power incident beam, a large second harmonic coefficient may be desirable. The absorption of light by the crystal can decrease the output power exponentially if the fundamental or second harmonic overlap an absorption band of the crystal. The second-harmonic power will also be critically affected by the phase mismatch between the fundamental and second harmonic waves. Each of these characteristics must be considered and optimized when searching for an efficient, high-power second harmonic generator.

The second harmonic coefficient is defined as

$$d_{jm} \Rightarrow \chi^{(2)}_{IJK}(\omega,\omega) - \frac{1}{V}\sum_{ijk} R_{Ii} R_{Jj} R_{Kk}\, \beta_{ijk}(\omega,\omega) \qquad [Eq.\ 1.2]$$

where V is the volume of the unit cell, the R direction cosines relate molecular coordinates to crystal coordinates, and the coefficients $\beta_{ijk}(\omega,\omega)$ are the microscopic hyperpolarizability tensor components for the relevant anionic groups.

$$\beta_{ijk}(\omega,\omega) - \frac{1}{4}\hbar^2 \sum_P \sum_{e,e'} \frac{<g|\bar{\mu}_i|e><e|\bar{\mu}_j|e'><e'|\bar{\mu}_k|g>}{(\omega_e - \omega_g - 2\omega)(\omega' - \omega_g - \omega)} \qquad [Eq.\ 1.3]$$

In Eq. 1.3, $|g>$ represents a ground electronic state, and $|e>$ and $|e'>$ represent excited electronic states.

A pictorial explanation of Equation 1.3 may be gained by considering the ijk subscripts for β; here, ijk can be 1, 2, or 3 ($\equiv x, y,$ or z). The subscript i indicates the direction of polarization induced by the incoming photons and the subscripts j and k signify the directions of electric polarization for the incoming photons. For example, β_{333} describes the magnitude of polarization induced in the z direction when two photons also polarized along z impinge on a molecule, Figure 1.2. By permuting over all possible ijk values, every possible interaction is described.

From examination of Equations 1.2 and 1.3 one can set further specifications on the design of a good SHG material. To maintain a large second harmonic coefficient the hyperpolarizability tensors must sum constructively. The SHG crystal must be noncentrosymmetric, for in a centrosymmetric crystal each positive β_{ijk} will have a negative partner $-\beta_{ijk}$ that will lead to Equation 1.2 summing to zero. The integrals specified in the numerator of Equation 1.3 represent the transition moments associated with the ground and excited states in the three-photon process. The denominator represents the differences in energies between the energy gaps and the fundamental and second harmonics. To enhance second-harmonic conversion characteristics from crystals, it has become common to
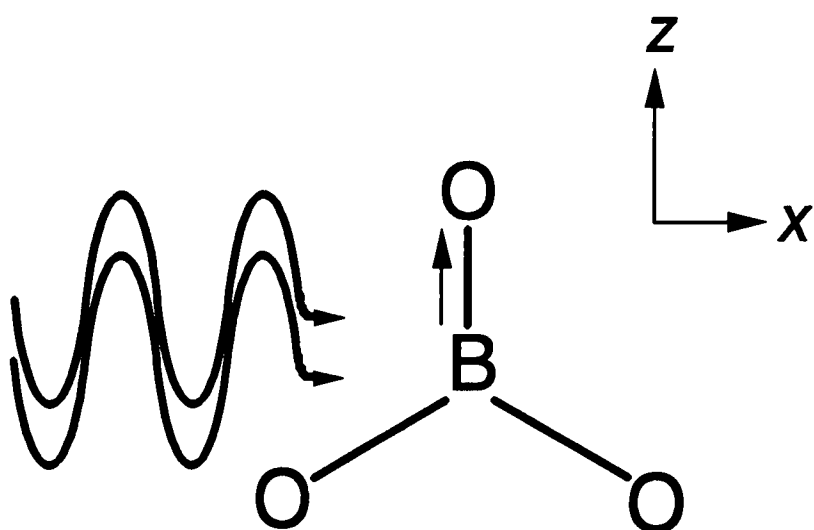
Figure 1.2. Pictoral view illustrating the denotation of β_{333}.

manipulate molecular characteristics to enhance transition moments and to select crystals with absorption edges near the second-harmonic wavelength.

The aforementioned characteristics are only a few of the necessary chemical and mechanical characteristics for a useful frequency-doubler. A more complete listing of the desired properties for a crystal with high power and short wavelength capabilities is given below.

- Melting point (1000-1300°C)
- Congruent melting
- Chemical stability
- Noncentrosymmetric lattice
- High damage threshold
- Excellent optical quality crystals
- Wide transparency range
- Transparent at short wavelengths
- Large birefringence
- Easy phase-matching capabilities
- High refractive index
- Large nonlinear coefficients

The first three characteristics aide in the synthesis, growth, and engineering of the material to obtain large, transparent and easily grown crystals. Also, the damage threshold may be substantially increased by the optical quality of the crystals, making them useful for high power operation. A wide transparency range extending to short wavelengths enables the conversion of light from the IR into the far UV. As discussed in Chapter 2, the refractive indices and

birefringence of a crystal are interdependent in determining phase matching characteristics and the ultimate conversion efficiency. Some relevant properties for some common NLO materials are listed in Table 1.1.

Materials containing a borate framework have been shown to exhibit favorable nonlinear optical properties at high powers and short wavelengths; examples include the frequency converters LiB_3O_5 and BaB_2O_4. The low-temperature form of barium borate (β-BaB_2O_4 or BBO) functions as a frequency converter in the UV region (4). Large nonlinear coefficients, 3 to 6 times that of the well-known converter KDP (5), make BBO an attractive material for efficient frequency conversion (6). It also has high optical transparency down to 200 nm (7) which makes it possible for phase-matchable conversion to the fifth harmonic (204.8 nm) of Nd^{3+}:YAG laser light (6).

Because of its low threshold power and capabilities as an efficient frequency converter at high powers, the borate LiB_3O_5 (LBO) has recently received considerable attention. Crystals of this material are relatively free of inclusions which greatly increases the optical damage threshold, giving LBO the highest damage threshold of any solid-state frequency converter. Also, it has been shown to exhibit a threshold power for 50% conversion efficiency that is two orders of magnitude lower than that of KDP; it is optically transparent in the range 160 nm to 2.6 μm, making it useful for applications in the UV region (7).

The 3-dimensional borate framework of LBO is constructed from a condensation of B_3O_7 rings, Figure 1.3. As a strategy for making new materials

Table 1.1. Common Nonlinear Optical Materials

	Transmission Range (μm)	Damage Threshold (GW/cm^2)	Nonlinear Coefficient*	Threshold Power (MW)
KDP	0.20-1.5	6	d_{36}= 0.76	75
KTP	0.35-4.5	3	d_{31}= 13.5	0.1
			d_{32}= 10.4	
			d_{33}= 28.4	
YAl$_3$(BO$_3$)$_4$	0.16-4.5	-	d_{11}= 5.7	-
BBO	0.19-3.5	13.5	d_{11}= 4.1	90
LBO	0.16-2.6	25	d_{31}= 0.15	0.1
			d_{32}= 2.97	
			d_{33}= 2.75	

*d_{mn} x 10^9 esu cm^{-3}
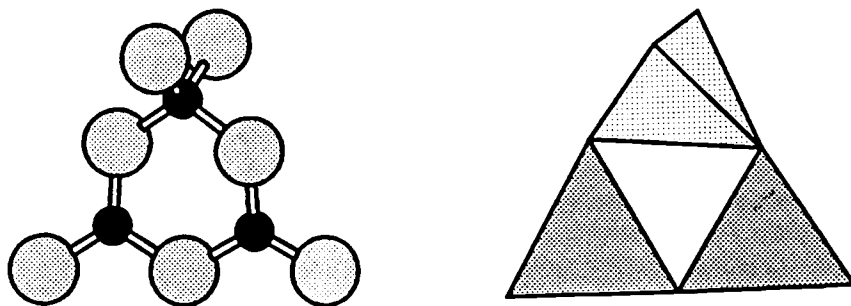
Figure 1.3. Sketch of the B_3O_7 ring in LiB_3O_5.

and maintaining the dimensionality of the lattice, systems with the potential of yielding new alkali or alkaline earth beryllium borates were studied. The primary purpose of this work was to replace the 4-coordinate boron atom in the B_3O_7 ring with a dipositive beryllium atom to retain a framework structure having favorable NLO properties. The results of these investigations are presented in Chapters 5 through 8.

An additional method undertaken for synthesizing new frequency-doubling materials was to guarantee the production of a noncentrosymmetric lattice by making new, crystalline complexes from metal halides and chiral amino acids where the principal chromophore is a carboxyl group. The new, noncentrosymmetric compound $CdCl_2C_3H_7NO_2$ was discovered as a part of this effort, and its structure is discussed in Chapter 4.

Section II. Hosts for Cr^{3+} Luminescence and Lasing

Several materials now function as efficient solid-state lasers when doped with the transition-metal ion Cr^{3+}; examples include alexandrite, Cr^{3+}:BeAlO$_4$ (8); LiCAF, Cr^{3+}:LiCaAlF$_6$ (9); LiSAF, Cr^{3+}:LiSrAlF$_6$ (10); and emerald, Cr^{3+}:Be$_3$Al$_2$(SiO$_3$)$_6$ (11-12). These materials are new sources of laser light and "are now emerging from the laboratory into the real world of laser applications" (13). They are being applied in various applications including scientific studies, remote sensing, and medical procedures.

As noted above and seen in Table 1.2, fluorides have already proven to be efficient hosts for Cr^{3+} lasing. The recently discovered laser materials LiCAF and

Table 1.2. Measured efficiencies of Cr^{3+} lasers.

Host Material	Name	Peak lasing wavelength (nm)	Slope efficiency
$Be_3Al_2(SiO_3)_6$	Emerald	768	64
$LiCaAlF_6$	LiCAF	780	54
$BeAl_2O_4$	Alexandrite	752	51
$LiSrAlF_6$	LiSAF	825	36
$ScBeAlO_4$	Scalexandrite	792	30
$ScBO_3$	Borate	843	29
$Gd_3Sc_2Ga_3O_{12}$	GSGG	785	28
$Na_3Ga_2Li_3F_{12}$	GFG	791	23

LiSAF have sparked a great interest in the laser community as efficient Cr^{3+} lasers (14, 10). The optical properties of these two materials have been studied and compared (15). Even though the luminescent ion occupies a similar site in each host, markedly dissimilar optical properties are seen. LiCAF has been shown to lase at a peak lasing wavelength of 780 nm with a radiative lifetime of 205 μs and a slope efficiency of 54% (9) which is slightly more efficient than the well-known alexandrite laser; LiSAF lases at a peak wavelength of 825 nm with a radiative lifetime of 67 μs and a 36% slope efficiency. To explain these differences, the environment of the Cr^{3+} ion on the Al site in $LiSrAlF_6$ has been studied and compared to that of $LiCaAlF_6$; results are presented in Chapter 9.

Borates have also been shown to have potential for being efficient hosts for Cr^{3+} lasing. The borate $Cr^{3+}:ScBO_3$ ranks sixth in efficiency among all Cr^{3+} lasers and functions as a room temperature, near IR laser (14,16) with a tuning range of 787-892 nm. In the $ScBO_3$ host, the Cr^{3+} ion experiences a weak crystal field as evidenced by a broad-band emission spectrum and an absence of sharp ^2E emission lines. The weak crystal field promotes excited state absorption (ESA), causing a detrimental effect on the lasing efficiency because of the reabsorption of another photon to boost the excited electron into a higher nonradiative state.

To alter the crystal field experienced by the luminescent ion, lessen ESA, and achieve higher lasing efficiencies, electropositive atoms have been incorporated into the $ScBO_3$ lattice. The electropositive nature of the cations forces the crystal field to higher energies where the effects of ESA should be reduced. It is this reasoning that led to the search for new materials in the alkaline earth scandium

borate phase systems (17). Several new compounds resulted from the study of these systems - $Sr_3Sc(BO_3)_3$ (18), $Sr_2Sc_2B_4O_{11}$ and $Ba_2Sc_2B_4O_{11}$ (19), and $Sr_2ScLiB_4O_{10}$ (20). Additional development of the structure of $Sr_3Sc(BO_3)_3$ revealed a new family of isostructural borates with promising properties as discussed in Chapters 10 through 12. One additional material $Sr_2InLiB_4O_{10}$ was discovered during attempts to crystallize the phase $Sr_3In(BO_3)_3$ with a flux containing Li atoms.

Synthesis and Characterization

Discovering materials with promising properties includes the investigation of existing phases and synthesis of new compounds. Much of my work has involved the crystal-chemical development of known structural types and the discovery of completely new types of atomic arrangements. The procedures used in these investigations are briefly outlined here.

Solid-state synthesis and solution reactions have proven to be efficient methods for the synthesis of new materials. New phases were identified by powder X-ray diffraction by using an automated Philips powder diffractometer. Upon discovery of a new material small single crystals were grown by simply melting the compound or by adding a flux, depending on whether the material melted congruently or incongruently. The structure of the compound was then determined by using data from an automated single crystal X-ray diffractometer. If the material exhibited suitable structural and melting characteristics its optical properties were investigated. For noncentrosymmetric structures, a powder second harmonic

experiment was performed to determine its approximate efficiency as a frequency converter. The observed conversion efficiency for each material was then compared with a calculated susceptibility obtained from a set of computer programs written in the Keszler laboratory. The computations provided a means for comparison and allowed for a better understanding of the origin of the observed nonlinear effects.

Absorption, excitation, and emission spectra are recorded on suitably doped samples.

References

1. K. I. Schaffers, T. Alekel III, P. D. Thompson, J. R. Cox, and D. A. Keszler, *J. Am. Chem. Soc.* **112**, 7068 (1990).

2. P. Franken, A. Hill, C. Peters, and G. Weinreich, *Phys. Rev. Lett.* **7**, 118 (1961).

3. M. J. Weber, *CRC Handbook of Laser Science and Technology*, "Section 1: Nonlinear Optical Materials", Boca Raton, Fla.: CRC Press, 1986.

4. C. Chen, B. Wu, A. Jiang, and G. You, *Sci. Sin., Ser B* **28**, 235 (1985).

5. R. C. Eckardt, H. Masuda, Y. X. Fan, and R. L. Byer, *IEEE J. Quantum Electron.* **26(5)**, 922 (1990).

6. D. Eimerl, L. Davis, S. Velsko, E. K. Graham, and A. Zalkin, *J. Appl. Phys.* **62**, 1968 (1987).

7. S. Velsko, Lawrence Livermore National Laboratory, private communication.

8. J. C. Walling, O. G. Peterson, H. P. Jenssen, R. C. Morris, and E. W. O'Dell, *IEEE J. Quantum Electron.* **16**, 1302 (1980).

9. S. A. Payne, L. L. Chase, H. W. Newkirk, L. K. Smith, and W. F. Krupke, *IEEE J. Quantum Electron.* **24**, 2243 (1988).

10. S. A. Payne, L. L. Chase, L. K. Smith, W. L. Kway, and H. W. Newkirk, *J. Appl. Phys.* **66(3)**, 1051 (1989).

11. M. L. Shand and S. T. Lai, *IEEE J. Quantum Electron.* **QE-20**, 105 (1984).

12. S. T. Lai, "Highly efficient emerald laser," presented at the Int. Laser Sci. Conf., Oct. 21-24, 1986, Seattle, WA, paper THH2.

13. P. F. Moulton, *Laser Focus/Electro-Optics*, 56 (August 1987).

14. S. A. Payne, L. L. Chase, and G. D. Wilke, *Phys. Rev. B* **37**, 998 (1988).

15. S. A. Payne, L. L. Chase, and G. D. Wilke, *J. Luminescence* **44**, 167 (1989).

16. J. A. Caird, S. A. Payne, P. R. Staver, A. J. Ramponi, L. L. Chase, and W. F. Krupke, *IEEE J. Quantum Electron.* **24**, 1077 (1988).

17. P. D. Thompson, Doctoral thesis (1991).

18. P. D. Thompson and D. A. Keszler, *Chem. Mat.* **1**, 292 (1989).

19. P. D. Thompson, J. Huang, R. W. Smith, and D. A. Keszler, *J. Solid State Chem.* **95**, 126 (1991).

20. P. D. Thompson and D. A. Keszler, *Solid State Ionics* **32/33**, 521 (1989).

.

CHAPTER 2

OPTICAL SECOND-HARMONIC GENERATION FROM

TRIANGULAR OXOANIONS

Kathleen I. Schaffers and Douglas A. Keszler

Abstract

The orientational dependencies of the hyperpolarizability coefficients β of trigonal oxoanions have been derived to provide a simple model for an initial assessment of borates, nitrates, and carbonates as second-order optical frequency converters. Predictive capabilities are examined and relationships between structure and threshold powers are considered.

Introduction

Solid-state synthetic chemists tend to rely on rather simple models to anticipate the properties of compounds and structures. For example, in the field of electronic materials a solid-state chemist might consider the details of a crystal structure, count valence electrons, and weigh the relative contributions of orbital overlap and energy mismatch to predict whether a new compound is likely to be a metal, semiconductor, or insulator. In the field of optical materials, one can consider the crystal and electronic structures of a particular host to anticipate some of the gross luminescence features of an ion doped into it. A similar model, however, has not been effectively presented for second-harmonic generation from inorganic crystals. We describe in this contribution a simple model for the approximate determination of the second-order optical susceptibility coefficients of noncentrosymmetric orthoborates, carbonates, and nitrates or any material containing independent triangular groups. A semiquantitative predictive capability of nonlinearities is achieved from consideration of a crystal structure only.

We have selected compounds containing triangular groups for study, in part, because of our interests in preparing new types of borate optical frequency converters. Borates, such as BaB_2O_4 (BBO) (1,2) and LiB_3O_5 (LBO) (3), are particularly useful for frequency conversion of high-power pulsed lasers to short wavelengths. They have been useful for frequency conversion of Nd:YAG (2-4), Ti:Al_2O_3 (5), and Cr:LiSrAlF$_6$ laser light into the UV, and they also function as efficient optical parametric oscillators in this wavelength region (6-8). In

synthesizing new simple orthoborates we would like to be able to anticipate the limits of their nonlinearities and potential conversion efficiencies. To address the potential efficiency of these materials we will consider the linear optical properties in terms of the structural arrangement of the oxoanions. This is particularly important, considering the recent finding that the compound $K_2La(NO_3)_5 \cdot 2H_2O$ containing the triangular nitrate oxoanion exhibits the lowest power threshold of any frequency converter for the wavelength range 900-950 nm (9).

A light wave of sufficient intensity impressed on a noncentrosymmetric crystal can induce a nonlinear response in polarization in the crystal that will lead to generation of a second or higher-order harmonic signal. The central feature to be addressed in considering the conversion capacity of a given crystal is the amount of output power than can be obtained from a given input power. We are interested in conversion efficiency, and the minimum input power to convert, for example, 50% of the incoming light to the second harmonic.

What governs these processes for a specific crystal? The second-harmonic power $P_{2\omega}$ generated from a laser beam of power P_ω may be partially described with relationship (1) (10)

$$P_{2\omega} \propto L_{coh}^2 \, d_{jm}^2 \, P_\omega^2 \exp\left[-L\left(\alpha_\omega + \frac{\alpha_{2\omega}}{2}\right)\right] \qquad (1)$$

where L_{coh} represents the thickness and dispersion of the crystal (the linear optical properties), d_{jm} is the relevant SHG coefficient (susceptibility), and the exponential term represents absorption at the fundamental and second harmonic wavelengths.

To achieve a high conversion efficiency there should be little absorption at the fundamental and second-harmonic wavelengths, and a large value of d_{jm} may be desirable. Also inherent in relationship (1) is the condition that the polarization waves having frequencies ω and 2ω be phase matchable, i.e., $n(\omega) = n(2\omega)$. It is generally a small phase mismatch ($n(\omega) \neq n(2\omega)$) that prevents the conversion efficiency of many materials from approaching or exceeding 50%. In general, the most desirable phase-matching conditions for conversion from IR to visible wavelengths are met with crystals having a small birefringence, but phase matching at these wavelengths can also be achieved with a highly birefringent material. Because the refractive indices of the crystals to be considered here increase rapidly at shorter wavelengths (the absorption edge is being approached), it is necessary to have a significant birefringence to be able to achieve phase matching and frequency conversion from the visible into the ultraviolet (the birefringence must be equal to or exceed the normal dispersion of the refractive indices). In addressing the characteristics of a crystalline frequency converter, it will be necessary to consider at some level both the linear and nonlinear optical properties.

Frequency Conversion and The Model

We begin with a simplified description of optical second harmonic generation. In this process, an oscillating electric field (a light wave) interacts with a polar substance to rearrange its electron density and induce a polarization. Two responses of a polar unit B-O which may be considered to be a polar molecule such as HCl or a boron-oxygen bond are depicted in Figure 2.1. At the top of this
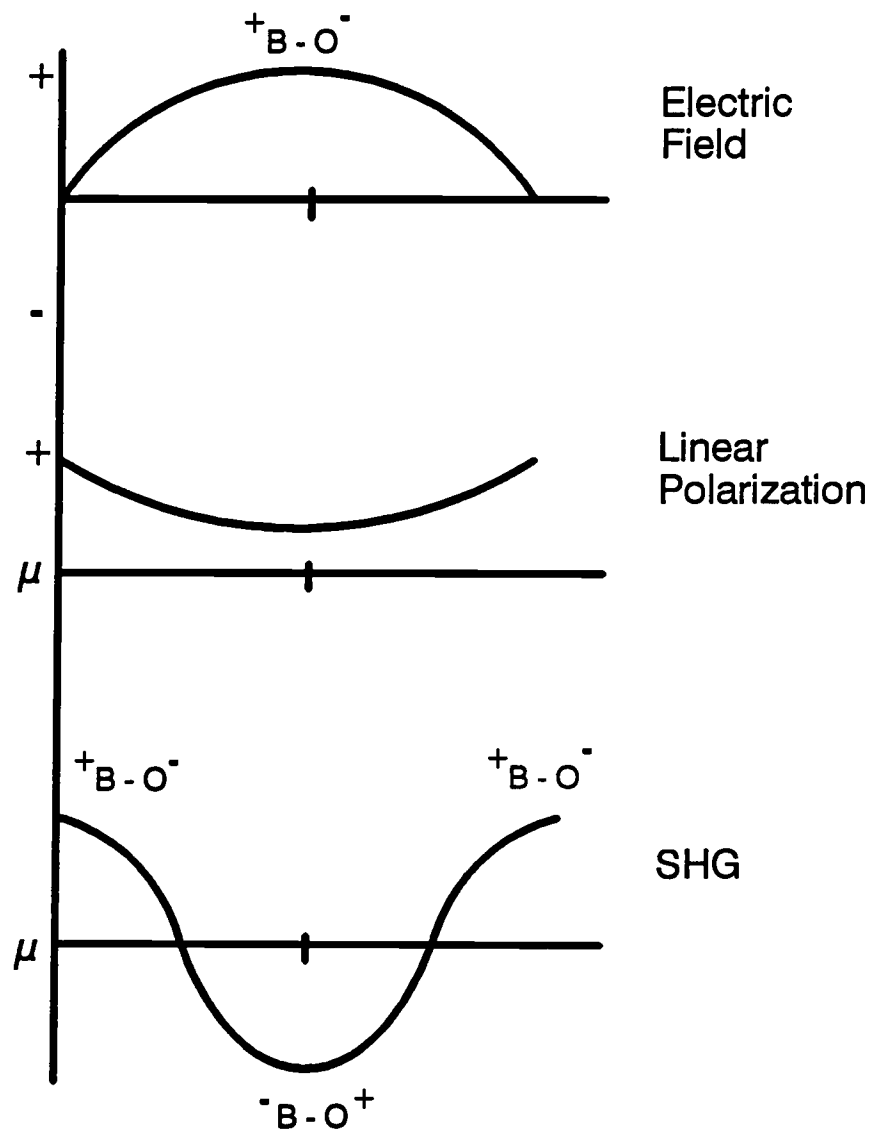
Figure 2.1. Pictorial description of optical second harmonic generation using light waves.

figure is a representation of the electric field associated with a half wavelength of light. As indicated in the middle portion, the typical response of B-O upon interaction with this field is a charge displacement and development of an oscillating dipole that follows the frequency of the incoming light. Such an oscillating dipole produces a linear response and is responsible for a variety of effects, including the scattering of light from a fluorescent lamp off the walls and objects in our work environments.

In the second-order response, we assume two photons interact simultaneously with the B-O unit. In doing so, the unit experiences a much larger electric field. As seen at the bottom of Figure 2.1, at a sufficient field strength the dipole of the B-O unit can be reversed at the apex of the oscillating field. Over one *half-wavelength* oscillation of the two incoming photons the magnitude of the dipole passes through zero twice, completing a *full wavelength*. The two fundamental photons have been fused into a single photon of twice the frequency. This simple illustration is consistent with the anharmonic model of second-harmonic generation, since its application to a nonpolar unit will not produce a second-order polarization.

This notion of dipole reversal, while overly simplified, does emphasize the state mixing that must occur. To alter the dipoles on a molecule in this way, electron density must flow from filled ground states to empty excited states. The probability that a certain state of polarization can be achieved in production of a second-order process is given by the second-order polarizability, β (11).

$$\beta \approx \sum_{g} \sum_{e,e'} \frac{\langle g | r | e \rangle \langle e | r | e' \rangle \langle e' | r | g \rangle}{(\omega_e - \omega_g - \omega)(\omega_{e'} - \omega_g - 2\omega)}$$

In the three photon process, we consider transitions among a ground level and two excited levels, Figure 2.2. The transition moments appear in the numerator, and they are appropriately weighted in the denominator by the energy differences between the transition energies (ω_e - ω_g and $\omega_{e'}$ - ω_g) and the fundamental (ω) and second-harmonic (2ω) wavelengths. In this way, the actual electronic transition associated with the transition-moment integral is characterized as a virtual transition. By summing these interactions over all ground and electronic states, we can visualize the displacement of electric charge on application of the oscillating electric field (the light wave).

This microscopic model of second-order processes for single molecules can now be extended to a macroscopic crystal. In the model we employ here, we assume the bulk characteristics are simply a sum of the microscopic results. The second-order process is a localized effect of the incident light on the electrons of individual molecules or anionic groups, and it is assumed that there is no delocalization of charge beyond these groups. In our application, these anions are NO_3^-, CO_3^{2-}, and BO_3^{3-}. The macroscopic equivalent of β, the second-order susceptibility $\chi^{(2)}$, may then be calculated from expression (2) (12).

$$\chi^{(2)}_{IJK}(\omega, \omega) = \frac{1}{V} \sum_{p=1}^{N} \sum_{ijk} R_{I_i} R_{J_j} R_{K_k} \beta_{ijk}(\omega, \omega) \qquad (2)$$
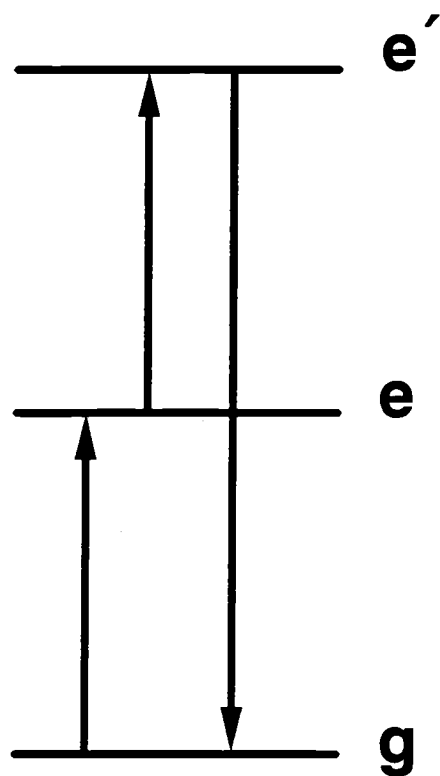
Figure 2.2. Sketch of the three photon process for SHG.

where V is the volume of the unit cell; N is the number of anionic groups in the cell; the coefficients R are the direction cosines between the macroscopic coordinate axes of the crystal and the microscopic coordinate axes of the pth anionic group; and β_{ijk} is the microscopic second-order susceptibility of an individual group. So, from knowledge of the arrangement of the groups in a crystal structure and their microscopic coefficients β_{ijk}, approximate macroscopic values χ_{IJK} may be calculated (this is an *oriented gas model* - local field corrections are not included).

Chen (13) and Zyss and Oudar (12) have successfully applied this theory to a variety of materials and Chen and coworkers have achieved, in cases where the model is applicable, reasonable agreement between the computations and experiments. With this model, the bulk susceptibility coefficients $\chi^{(2)}$ may be calculated from the localized molecular orbital wave functions of the group. In our application of the model we assume that the triangular oxoanions in each structure have D_{3h} symmetry. With this assumption, it is not necessary to specifically compute β values. These values may simply be summed symbolically with (2), since the unique coefficients are related by symmetry, $-\beta_{333} = \beta_{311} = \beta_{131} = \beta_{113}$ (10). Although bond polarizabilities and microscopic nonlinearities are sensitive to distortions from this symmetry, the distortions are small and likely not to be as significant as the large differences that result from the relative orientations of the groups. In our application of the anionic group theory, we will focus on the magnitude of the susceptibility as it relates to a specific structural

arrangement. The approach here provides a more interpretive structural method for estimating nonlinearities.

Before proceeding it is useful to review the meaning of the subscripts ijk associated with β. The numerical counterparts to the ijk subscripts are 1, 2, or 3 corresponding to the $x, y,$ or z cartesian coordinate axes of the chromophore. The i subscript describes the direction of polarization induced by the incoming photons, and the j and k subscripts specify the directions of electric polarization for the incoming photons. Consequently, β_{333} indicates the magnitude of polarization in the z direction from two photons also polarized along z. Likewise, for β_{131}, the magnitude of polarization in the x direction is described, and the directions of polarization for the incident photons are along z and x, Figure 2.3. Because the induced polarization must occur in the plane containing the bond axes, a triangular oxoanion lying in the xz plane cannot be polarized along the y direction; this explains the lack of a 2 (y) component among the unique β coefficients under D_{3h} symmetry.

Susceptibilities

Results from application of (2) to analyses of all noncentrosymmetric structures containing triangular oxoanions are listed in Table 2.1. In this table, values in the column - % of optimum - are a percentage of the maximum susceptibility that could be achieved at the number density of groups for the compound; these values were obtained from the quotient of the highest χ value and number density for each compound. They provide a direct measure of the
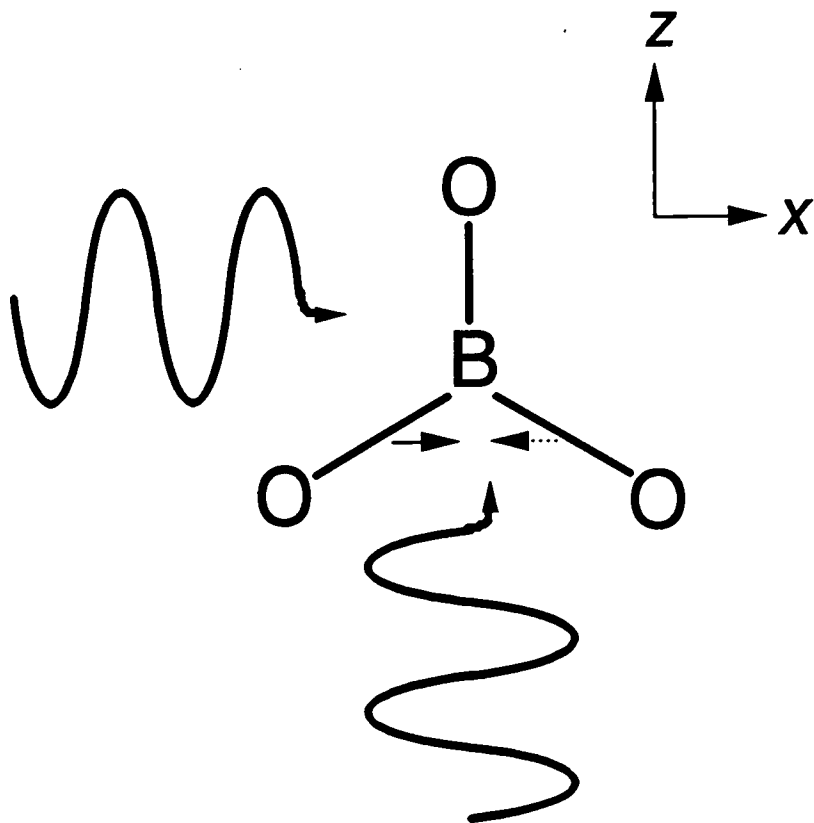
Figure 2.3. Polarization directions of the two incident photons depicted

by β_{131}.

Table 2.1. Calculated nonlinearities for triangular oxoanions:
(a) BO_3, (b) NO_3, and (c) CO_3.

(a) Borates:

Material	Space Group	% of Optimum	Normalized $\chi_{ijk}^{(2)}$	
$La_2Sr_3(BO_3)_4$	$Pc2_1n$	6	$\chi_{113} = \chi_{311} =$	-0.017
			$\chi_{223} = \chi_{322} =$	-0.043
			$\chi_{333} =$	0.060
$Sr_5(BO_3)_3Cl$	$C222_1$	27	$\chi_{123} = \chi_{213} = \chi_{312} =$	-0.21
$Sr_5(BO_3)_3Br$	$C222_1$	29	$\chi_{123} = \chi_{213} = \chi_{312} =$	-0.34
$LiCdBO_3$	$P\bar{6}$	94	$\chi_{111} = -\chi_{122} = -\chi_{212} =$	0.15
			$\chi_{112} = \chi_{211} = -\chi_{222} =$	1.00
$NdSc_3(BO_3)_4$	$R32$	49	$-\chi_{111} = \chi_{122} = \chi_{212} =$	0.62
$YAl_3(BO_3)_4$	$R32$	49	$\chi_{111} = -\chi_{122} = -\chi_{212} =$	0.75
$NdAl_3(BO_3)_4$	$R32$	49	$\chi_{111} = -\chi_{122} = -\chi_{212} =$	0.73
Ag_3BO_3	$R32$	100	$-\chi_{111} = \chi_{122} = \chi_{212} =$	0.73
$BaZn_2(BO_3)_2$	$P2_12_12_1$	4	$\chi_{123} = \chi_{213} = \chi_{312} =$	-0.040
$KBe_2(BO_3)F_2$	$C2$	100	$\chi_{112} = \chi_{211} = -\chi_{222} =$	0.65
			$\chi_{123} = \chi_{213} = \chi_{312} =$	0.007

Table 2.1(a) continued...

Material	Space Group	% of Optimum	Normalized $\chi_{ijk}^{(2)}$	
$Ba_3Sc(BO_3)_3$	$P6_3cm$	0.2	$\chi_{113}= \chi_{223}= \chi_{311}= \chi_{322}=$	-0.0001
			$\chi_{333}=$	0.002
$LaSc_3(BO_3)_4$	Cc	6	$\chi_{111}=$	-0.096
			$\chi_{122}= \chi_{212}=$	0.15
			$\chi_{133}= \chi_{313}=$	-0.051
			$\chi_{113}= \chi_{311}=$	-0.069
			$\chi_{223}= \chi_{322}=$	0.11
			$\chi_{333}=$	-0.039
$Mg_5(BO_3)_3F$	$Pna2_1$	5	$\chi_{113}= \chi_{311}=$	0.006
			$\chi_{223}= \chi_{322}=$	-0.055
			$\chi_{333}=$	0.049
$Ca_5(BO_3)_3F$	Cm	27	$\chi_{111}=$	0.16
			$\chi_{122}= \chi_{212}=$	-0.25
			$\chi_{133}= \chi_{313}=$	0.092
			$\chi_{113}= \chi_{311}=$	0.17
			$\chi_{112}= \chi_{211}=$	0.006
			$\chi_{222}=$	0.007
			$\chi_{223}= \chi_{322}=$	0.18
			$\chi_{333}=$	0.010

Table 2.1(b) Nitrates:

Material	Space Group	% of Optimum	Normalized $\chi_{ijk}^{(2)}$	
$Cd(NO_3)_2$	$Pca2_1$	19	$\chi_{113} = \chi_{311} =$	0.33
			$\chi_{223} = \chi_{322} =$	-0.31
			$\chi_{333} =$	-0.20
$Pr(OH)_2NO_3$	$P2_1$	79	$\chi_{112} = \chi_{211} =$	0.29
			$\chi_{312} = \chi_{123} = \chi_{213} =$	0.031
			$\chi_{233} = \chi_{323} =$	-0.78
			$\chi_{222} =$	0.49
$Ba(NO_3)_2$	$P2_13$	0.4	$\chi_{123} = \chi_{213} = \chi_{312} =$	0.006
$K_2La(NO_3)_5 \cdot 2H_2O$	$Fdd2$	36	$\chi_{113} = \chi_{311} =$	0.46
			$\chi_{223} = \chi_{322} =$	-0.42
			$\chi_{333} =$	-0.036
$Rb_2Na(NO_3)_3$	$Pmc2_1$	82	$\chi_{123} = \chi_{213} = \chi_{312} =$	0.034
			$\chi_{113} = \chi_{311} =$	1.00
			$\chi_{223} = \chi_{322} =$	-0.24
Ag_3INO_3	$P2_12_12_1$	12	$\chi_{123} = \chi_{213} = \chi_{312} =$	-0.12
Ag_2INO_3	$P2_12_12_1$	10	$\chi_{123} = \chi_{213} = \chi_{312} =$	0.073
$AgNO_3$	$P2_12_12_1$	4	$\chi_{123} = \chi_{213} = \chi_{312} =$	0.057

Table 2.1(b) continued...

Material	Space Group	% of Optimum	Normalized $\chi_{ijk}^{(2)}$	
$HNO_3 \cdot 3H_2O$	$P2_12_12_1$	18	$\chi_{111} =$	-0.081
			$\chi_{122} = \chi_{212} =$	0.036
			$\chi_{133} = \chi_{313} =$	0.045
			$\chi_{123} = \chi_{213} = \chi_{312} =$	0.15
			$\chi_{113} = \chi_{311} =$	-0.048
			$\chi_{112} = \chi_{211} =$	0.069
			$\chi_{222} =$	0.008
			$\chi_{233} = \chi_{323} =$	-0.077
			$\chi_{223} = \chi_{322} =$	0.072
			$\chi_{333} =$	-0.025

Table 2.1(c) Carbonates:

Material	Space Group	% of Optimum	Normalized $\chi_{ijk}^{(2)}$	
$Pb_2OCO_3 \cdot 2H_2O$	R3m	100	$-\chi_{112} = -\chi_{211} = \chi_{222} =$	0.51
$CaMg_3(CO_3)_4$	R32	50	$\chi_{111} = -\chi_{122} = -\chi_{212} =$	0.94
$CeFCO_3$	$P\bar{6}2c$	25	$-\chi_{111} = \chi_{122} = \chi_{212} =$	0.33
$BaMg(CO_3)_2$	R32	61	$\chi_{111} = -\chi_{122} = -\chi_{212} =$	0.96
$BaCa(CO_3)_2$	P321	33	$\chi_{111} =$	0.48
			$\chi_{122} = \chi_{212} =$	-0.47
			$\chi_{133} = \chi_{313} =$	-0.003
			$\chi_{123} = \chi_{213} = \chi_{312} =$	0.010
			$\chi_{113} = \chi_{311} =$	0.017
			$\chi_{112} = \chi_{211} =$	0.001
			$\chi_{222} =$	0.004
			$\chi_{233} = \chi_{323} =$	-0.005
			$\chi_{223} = \chi_{322} =$	-0.017
$Ca_2Na_2(CO_3)_3$	Amm2	43	$\chi_{123} = \chi_{213} = \chi_{312} =$	-0.007
			$\chi_{113} = \chi_{311} =$	0.53
			$\chi_{223} = \chi_{322} =$	0.12
			$\chi_{333} =$	-0.65
$Na_2CO_3 \cdot 1\frac{1}{2}D_2O_2$	Aba2	1	$\chi_{113} = \chi_{311} =$	0.008
			$\chi_{223} = \chi_{322} =$	-0.008
			$\chi_{333} =$	-0.0002

Table 2.1(c). continued...

Material	Space Group	% of Optimum	Normalized $\chi_{ijk}^{(2)}$	
$CaNa_2(CO_3)_2 \cdot 2H_2O$	Fdd2	28	$\chi_{111}=$	-0.0002
			$\chi_{122}= \chi_{212}=$	0.0002
			$\chi_{133}= \chi_{313}=$	0.00006
			$\chi_{113}= \chi_{311}=$	-0.30
			$\chi_{112}= \chi_{211}=$	-0.002
			$\chi_{222}=$	0.001
			$\chi_{223}= \chi_{322}=$	0.32
$K_2Cu(CO_3)_2$	Fdd2	26	$\chi_{122}= \chi_{212}=$	0.001
			$\chi_{133}= \chi_{313}=$	-0.001
			$\chi_{123}= \chi_{213}= \chi_{312}=$	0.0008
			$\chi_{113}= \chi_{311}=$	0.042
			$\chi_{112}= \chi_{211}=$	-0.0003
			$\chi_{222}=$	-0.026
			$\chi_{233}= \chi_{323}=$	0.003
			$\chi_{223}= \chi_{322}=$	0.29
			$\chi_{333}=$	-0.33
$BaCa(CO_3)_2$	$P2_1$	46	$\chi_{123}= \chi_{213}= \chi_{312}=$	0.50
			$\chi_{112}= \chi_{211}=$	-0.65
			$\chi_{222}=$	1.00
			$\chi_{233}= \chi_{323}=$	-0.35
$YOHCO_3$	$P2_12_12_1$	14	$\chi_{123}= \chi_{213}= \chi_{312}=$	-0.19

Table 2.1(c). continued...

Material	Space Group	% of Optimum	Normalized $\chi_{ijk}^{(2)}$	
$Na_2CO_3 \cdot H_2O$	$P2_1ab$	75	$\chi_{113} = \chi_{311} =$	0.79
			$\chi_{223} = \chi_{322} =$	0.003
			$\chi_{333} =$	-0.79

structural contribution to the nonlinearity. In the final column $\chi^{(2)}$ values are normalized to the largest value calculated for each type of group. Few individual susceptibility coefficients have been experimentally determined for borates, nitrates, and carbonates. The magnitudes of the calculated nonlinearities, however, have been found to scale with nonlinearities obtained from Kurtz-Perry second-harmonic tests of microcrystalline samples (14) (cf. Tables 2.1 and 2.2).

Interpretation of these values is best appreciated by first considering a few model examples. In Figure 2.4, two BO_3 groups are drawn with all B-O vectors aligned in a unit cell of volume V. (This local coordinate system is retained throughout the paper.) Considering the coefficients β_{333} (polarization of the groups along z from two incident photons having their electric fields directed along z) for each group, we find from (2) that a simple constructive summation affords $\chi_{333} = 1/V \times 2 \times \beta_{333}$. By translating the contents in the cell of Figure 2.4 in the xz plane, layers of BO_3 groups similar to those in the compounds $KBe_2BO_3F_2$ (15) and $LiCdBO_3$ (16) (Figure 2.5) are formed. The difference in the magnitude of the calculated χ_{222} values (Table 2.1) for these crystals is largely determined by the volume of the unit cells and the resulting number density of BO_3 groups. In the compound $KBe_2BO_3F_2$, the BO_3 number density is $0.858 \times 10^{22}/cm^3$, while in $LiCdBO_3$ it is $1.532 \times 10^{22}/cm^3$. The ratio of these densities, 0.56, is similar, but smaller than the ratio of the calculated χ_{222} values, 0.69, so there must be an additional structural effect associated with the smaller susceptibility of the Cd compound. There is only one crystallographic type of BO_3 group in the structure

Table 2.2. Calculated and experimental nonlinearities for selected orthoborates.

Compound	χ^2_{ijk}[a]		I/I_o(quartz)
LiCdBO$_3$	$\chi_{111}=-\chi_{122}=-\chi_{212}=$	0.15	12
	$\chi_{112}=\chi_{211}=-\chi_{222}=$	1.0	
YAl$_3$(BO$_3$)$_4$	$-\chi_{111}=\chi_{122}=\chi_{212}=$	0.65	10[c]
NdSc$_3$(BO$_3$)$_4$	$-\chi_{111}=\chi_{122}=\chi_{212}=$	0.49	09[c]
LaSc$_3$(BO$_3$)$_4$[b]	$\chi_{122}=\chi_{212}=$	0.15	<0.1[c]
KBe$_2$BO$_3$F$_2$	$\chi_{112}=\chi_{211}=-\chi_{222}=$	0.65	
BaZn$_2$(BO$_3$)$_2$[b]	$\chi_{123}=\chi_{213}=\chi_{312}=$	-0.04	0.1[c]
Sr$_5$(BO$_3$)$_3$Cl[b]	$\chi_{123}=\chi_{213}=\chi_{312}=$	-0.21	
Ba$_3$Sc(BO$_3$)$_3$[b]	χ_{333}	0.002	<0.1[c]
	$\chi_{113}=\chi_{223}=\chi_{311}=\chi_{322}=$	-0.0001	

[a]normalized values

[b]material discovered in this lab

[c]value measured in this lab
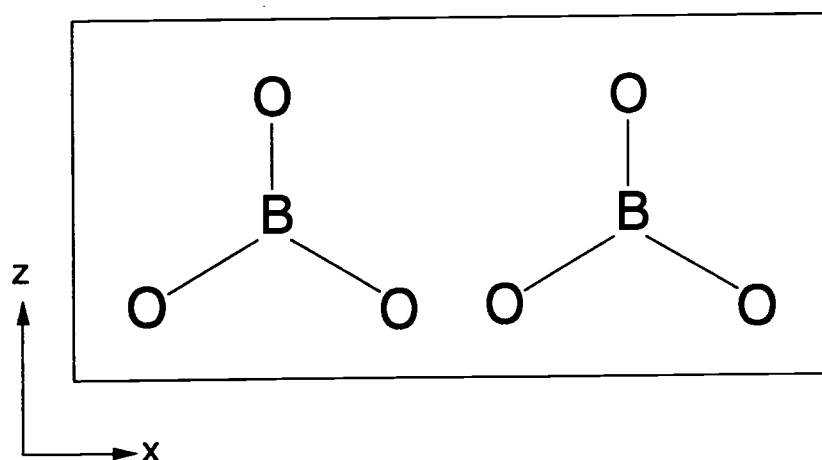
Figure 2.4. Sketch of the alignment of BO_3 groups where all of the B-O

vectors are aligned in the unit cell.
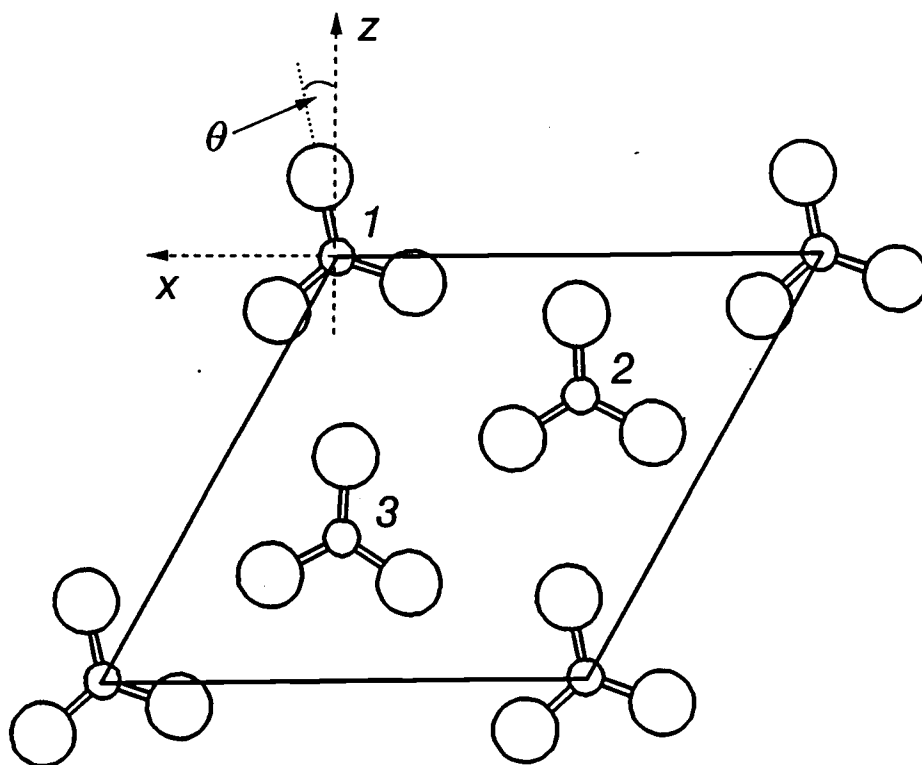
Figure 2.5. Projection of the BO_3 groups of $LiCdBO_3$ onto the ab plane (space group = $P\bar{6}$). The coordinate system for the BO_3 groups is defined.

of the compound $KBe_2BO_3F_2$ (space group C2); under translational symmetry all of the B-O vectors are perfectly aligned. As seen from Figure 2.5, the B-O vectors for the three crystallographically independent BO_3 groups in $LiCdBO_3$ are not exactly aligned. They are each slightly rotated about the 3-fold axis orthogonal to the principal plane, and it is these rotations that lead to the smaller magnitude of χ_{333} (for this example, $|\chi_{333}| = |\chi_{222}|$ of Table 2.1).

How sensitive is the value of χ_{333} to this type of rotation? We modeled this by considering the pairwise summation of groups where the angle of rotation θ for the second group, Figure 2.6, was incrementy varied from 0 - 30°. For $\theta = 30°$, it should be clear that $\chi_{333} = 0$ since translation of each group to a common B-atom point produces a centrosymmetric arrangement and the summation of the $+\beta_{ijk}$ values from one group with $-\beta_{ijk}$ values from the other. Because the relative magnitude of β_{333} will oscillate with a period of $\theta = 2\pi/3$ for this rotation, we find a cos 3θ functional dependence. Of course, the actual functional form will involve a summation of terms constituting the products of a trigonometric function and one of the allowed second-order coefficients $\beta_{333}, \beta_{311}, \beta_{131}$, or β_{113}. Because these β values are related by symmetry, the summation can be reduced to a single trigonometrically equivalent form.

An approximate χ_{333} coefficient for $LiCdBO_3$ may now be calculated from (2) or by using a protractor to measure θ for each of the groups depicted in Figure 2.5, followed by application of the cos 3θ dependence and multiplication by the reciprocal of the unit cell volume. The procedure is the following: $\chi_{333} = 1/V$ $[(\beta_{333})_{group1} + (\beta_{333})_{group2} + (\beta_{333})_{group3}] = 1/V [\beta_{333} \cos (3(10°)) + \beta_{333} \cos (3(8°))$
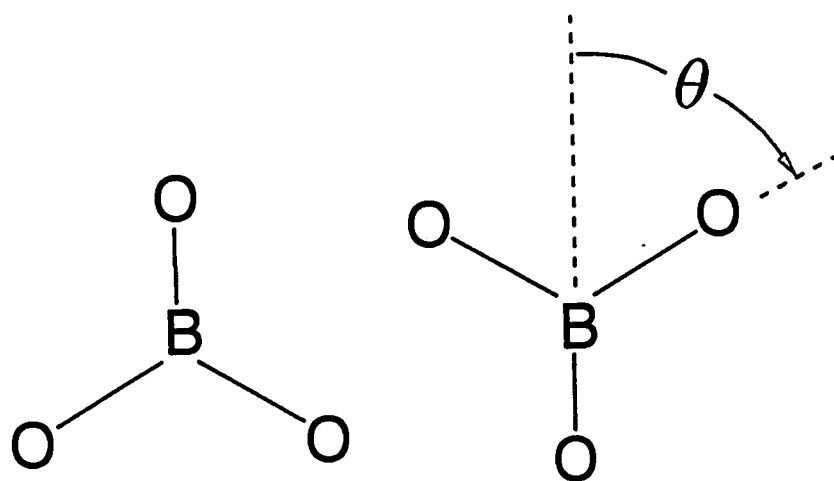
Figure 2.6. Rotation about the C_3 axis.

$+ \beta_{333} \cos (3(-5^{\circ}))] = 1/V [2.7 \cdot \beta_{333}]$. An optimal arrangement of BO_3 groups at this number density would produce a value of $\chi_{333} = 1/V [3 \cdot \beta_{333}]$, so the arrangement in $LiCdBO_3$ is ~90% of optimum. Among the known orthoborates this material should have the highest nonlinearity; the Kurtz-Perry tests support this finding (Table 2.2).

We have extended these analyses to determination of the functional dependencies of the other β values by considering rotations about the cartesian axes, Figure 2.7. One rotation is about a B-O vector and the other at 90° (30° to the nearest B-O vector) in the principal plane of the group. The resulting functional dependencies for rotations about these axes are summarized in Table 2.3. These functions may be used directly to compute approximate susceptibilities. But simply knowing their forms allows us to qualitatively predict the magnitude of a coefficient from a cursory visual inspection of the arrangement of BO_3 groups in a structure.

There are two crystallographically inequivalent borate groups in the material $YAl_3(BO_3)_4$ (space group R32) (17) that lie in planes orthogonal to the c axis. From Figure 2.8a, the $B1O_3$ groups are seen to align with B-O vectors directed along $-a$, opposite from the alignment of the $B2O_3$ groups with B-O vectors directed only slightly off $+a$; three B1-centered planes and nine B2-centered planes occupy each cell. From a cursory examination of the structure, we expect the nonlinearity to be 50% of optimum. The three B1-centered planes may be considered to be centrosymmetrically related to three of the B2-centered planes.
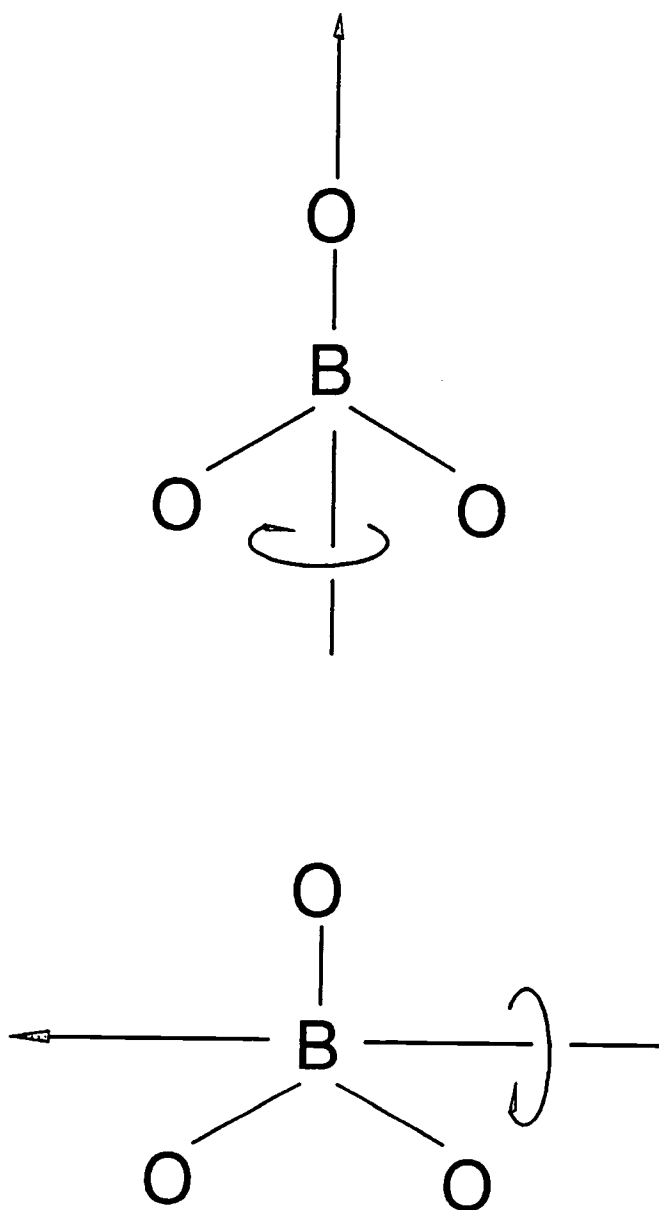
Figure 2.7. Rotation about a B-O vector (top) and at 90° (30° to the nearest B-O vector) in the principal plane (bottom).

Table 2.3. Functional dependencies of the hyperpolarizability coefficients.

Rotation orthogonal to plane (C$_3$ axis)		Rotation about B-O vector (C$_2$ axis)		Rotation in plane at 90° to the C$_2$ axis	
$-\beta_{111}= \beta_{133}= \beta_{313}$	$\Rightarrow \sin3\theta$	$\beta_{113}= \beta_{311}$	$\Rightarrow \cos^2\theta$	$\beta_{113}= \beta_{311}$	$\Rightarrow -\cos\theta$
$-\beta_{113}=-\beta_{311}= \beta_{333}$	$\Rightarrow \cos3\theta$	$\beta_{223}= \beta_{322}$	$\Rightarrow \sin^2\theta$	$\beta_{112}= \beta_{211}$	$\Rightarrow -\sin\theta$
		$\beta_{123}= \beta_{213}= \beta_{312}$	$\Rightarrow \tfrac{1}{2}\sin2\theta$	β_{222}	$\Rightarrow \sin^3\theta$
		β_{333}	$\Rightarrow 1$	β_{333}	$\Rightarrow \cos^3\theta$
				$\beta_{223}= \beta_{322}$	$\Rightarrow \cos\theta\sin^2\theta$
				$\beta_{233}= \beta_{323}$	$\Rightarrow \sin\theta\cos^2\theta$

Figure 2.8a. Sketch of the rotation of the BO_3 groups for $YAl_3(BO_3)_4$ about the C_3 axis.

The β values of these groups cancel, leaving a simple construction summation of the β values of six $B2O_3$ groups among the total of 12 BO_3 groups to determine χ. By applying the functional dependencies, the value of $\chi_{333} = -\chi_{113} = -\chi_{311}$ is easily calculated for the B1-centered group as $1/V\,[\beta_{333}\cos(3(180°))]\cdot 3$ groups $= 1/V\,[-3\cdot\beta_{333}]$. In referring to Table 2.1, the local z axis is projected onto the a axis of the crystal system, so χ_{333} in this example corresponds to χ_{111} in Table 2.1. Alignment of the second group requires rotations of approximately -8° about the axis at 90° to the C_2 axis (Figure 2.8b) and 7° about the B-O vector. Therefore, χ values are obtained by multiplication of the functions (cf. Table 2.3) for the corresponding rotations; ie., $\chi_{333} = 1/V\,[\beta_{333}\cdot\cos^3(-8°)\cdot 1.000]\cdot 9$ groups $= 1/V\,[8.74\cdot\beta_{333}]$ and $\chi_{113} = \chi_{311} = 1/V\,[\beta_{333}\cdot -\cos(-8°)\cdot\cos^2(7°)]\cdot 9$ groups $= 1/V\,[-8.78\cdot\beta_{333}]$. Now the overall coefficients can be determined by adding the sums determined for each type of borate group so that $\chi_{333} = 1/V\,[(-3 + 8.74)\beta_{333}] = 1/V\,[5.74\cdot\beta_{333}]$ and $\chi_{113} = \chi_{311} = 1/V\,[(3 + (-8.78))\beta_{333}] = 1/V\,[-5.78\cdot\beta_{333}]$ comparing to values calculated from (2) of $\chi_{333} = 1/V\,[5.85\cdot\beta_{333}]$ and $\chi_{113} = \chi_{311} = 1/V\,[-5.85\cdot\beta_{333}]$. Overall, the arrangement of BO_3 groups is ~48% (5.78/12) of optimum, as expected.

As an additional example, we present the material $Sr_5(BO_3)_3Cl$ (space group $C222_1$) (18). This structure also contains two types of BO_3 groups; however, only the B1-centered planes need to be considered in the calculation. As seen from Figure 2.9a, pairs of B2-centered planes are related by the C_2 axis along b. Translation of these groups to a common B-atom origin generates a center of symmetry that leads to a complete cancellation of their β values. Consequently,
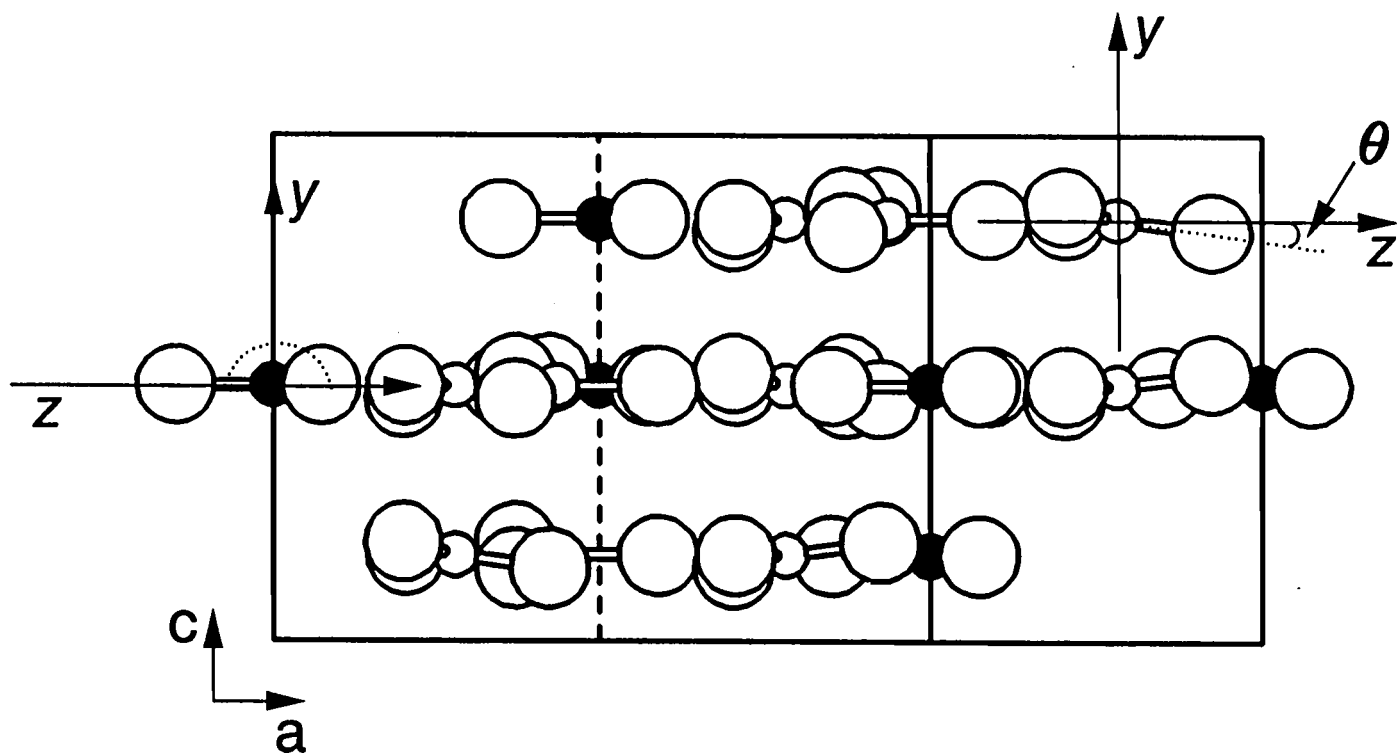
Figure 2.8b. Sketch of the rotation for $YAl_3(BO_3)_4$ at $90°$ to the C_2 axis in the principal plane.
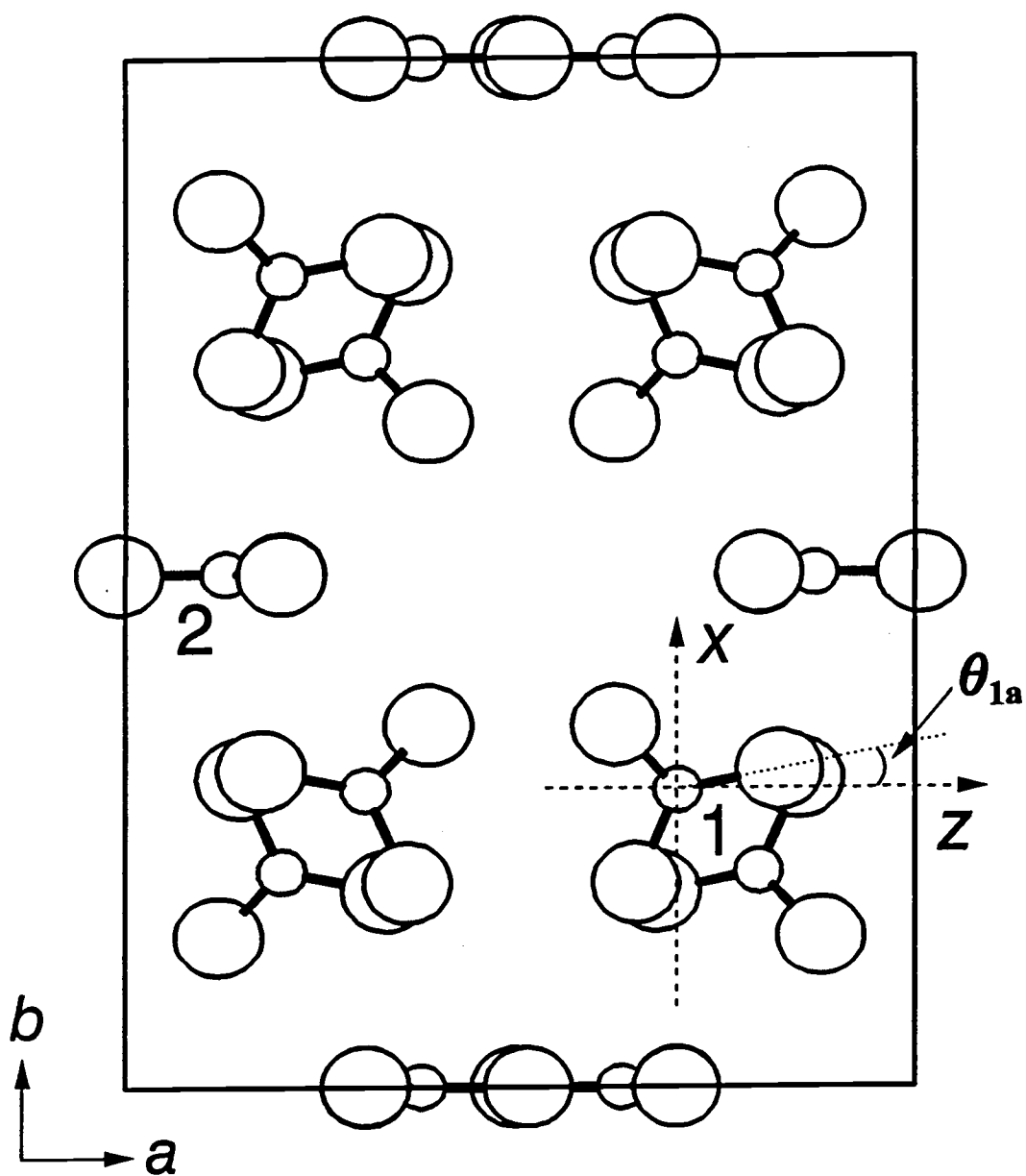
Figure 2.9a. Orientations of the borate groups in $Sr_5(BO_3)_3Cl$ are defined

for rotation about the plane orthogonal to the C_3 axis.

we need only consider the B1O_3 groups where the relevant angles are $10°$ (θ_{1a}) about the C_3 axis (Figure 2.9a) followed by $-28°$ (θ_{1b}) about a B-O vector (Figure 2.9b). Again the local coordinate system chosen for the functions does not match the crystal coordinate system; the transformation from the local coordinate system $\Rightarrow$ crystal coordinate system is $x \Rightarrow b, y \Rightarrow c, z \Rightarrow a$.

From symmetry constraints, the only allowed susceptibility coefficients in this crystal system are $\chi_{123}, \chi_{213},$ and χ_{312} (10). By considering the relationships among the coordinate systems and β values, we find $\chi_{123} = \chi_{213} = \chi_{312} = \beta_{333}$ ½sin (2(-$28°$)) = $-0.415 \cdot \beta_{333}$ where the subscripts on χ refer to the crystal system and the subscripts on β refer to the local system. Addition of the coefficients for the eight B(1)O_3 groups results in $\chi_{123} = \chi_{213} = \chi_{312} = 1/V$ [8 $\cdot$ -0.415 $\cdot \beta_{333}$] = $1/V$ [-3.316 $\cdot \beta_{333}$] comparing to $1/V$ [-3.177 $\cdot \beta_{333}$] calculated from (2). From these calculations we predict that $Sr_5(BO_3)_3Cl$ is approximately 21% (3.316/16) of optimum.

The susceptibilities of the remaining borates may be determined in a similar manner. In those compounds having maximum χ values less than 10% of optimum, an approximate center of symmetry can be associated with the distribution of borate groups. The compound $BaZn_2(BO_3)_2$ (19) contains the two crystallographically equivalent sets of BO_3 groups shown in Figure 2.10. Upon translating two A triangles, one from each set, such that B atoms coincide, we find the groups to be related by an approximate center of symmetry. The same behavior is seen for pairs of A' groups, one from each set. This near centric distribution, of course, leads to the pairwise cancellation of β values and the small
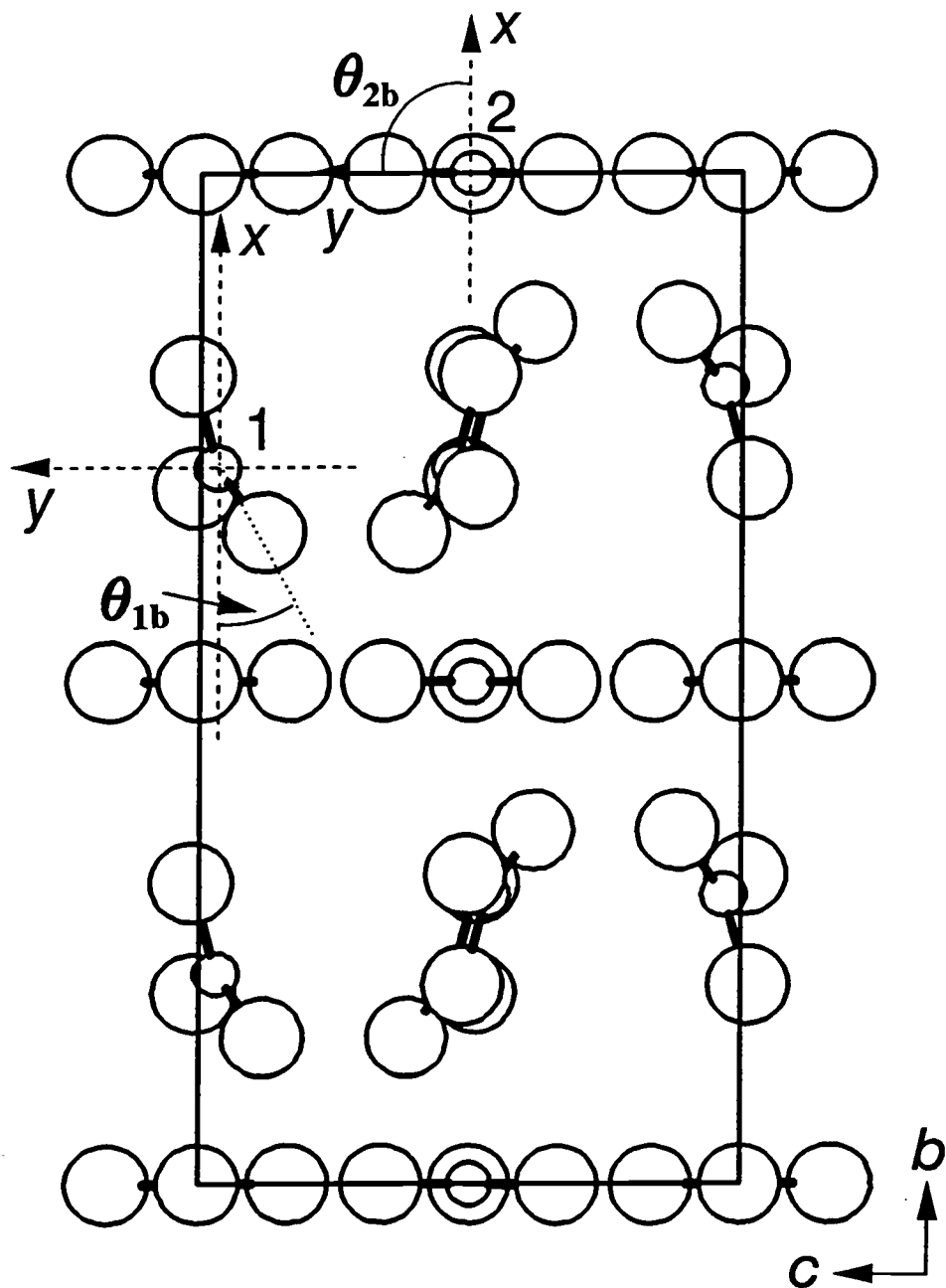
Figure 2.9b. Orientations of the borate groups in $Sr_5(BO_3)_3Cl$ are defined

for rotation about the C_2 axis.
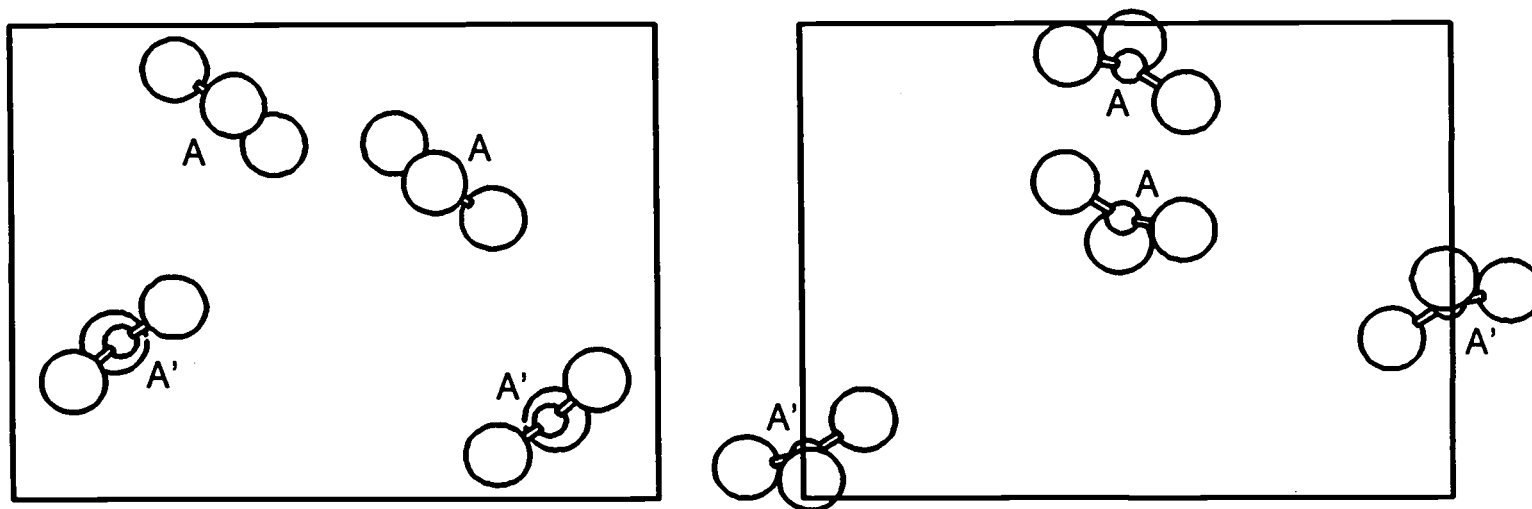
Figure 2.10. Orientation of the BO_3 groups in $BaZn_2(BO_3)_2$.

magnitude of χ. In the compound $Ba_3Sc(BO_3)_3$, a centrosymmetric character is indicated by the small χ values, and examination of its structure indicates the acentricity is primarily dictated by the distribution of the Ba atoms (20). In considering the nonlinearity of the material Ag_3BO_3 due consideration should be given to the electronic properties of the ion Ag^I and its β values. The probable photochemistry and synthesis conditions should also be reviewed in assessing the material as a frequency converter.

In addition to these orthoborates, the method may be extended to condensed borate units. The much used frequency conversion material β-BaB_2O_4 contains B_3O_6 benzene-like rings having D_{3h} symmetry. This compound crystallizes in a noncentrosymmetric structure (space group R3c) containing layers of these rings (Figure 2.11) (21). A segment of the structure about an individual Ba atom, Figure 2.12, reveals the three orientations of the B_3O_6 groups in the structure. To align these groups along the local z axis requires rotations of $11°$, $18°$, and $29°$ about optic axis (C_3 axis). Calculation of χ_{333} by using the functional relations results in $[2 \cdot \cos 3(0°) + 2 \cdot \cos 3(11°) + \cos 3(18°) + \cos 3(29°)] \cdot \beta_{333} = 4.3 \cdot \beta_{333}$; therefore, the B_3O_6 arrangement is approximately 72% (4.3/6) of optimum.

Conversion Efficiency

The susceptibility of a crystal is but one factor in determining its quality as a useful frequency converter. If several crystals satisfy selected power and wavelength criteria of a particular application, one method for comparing their
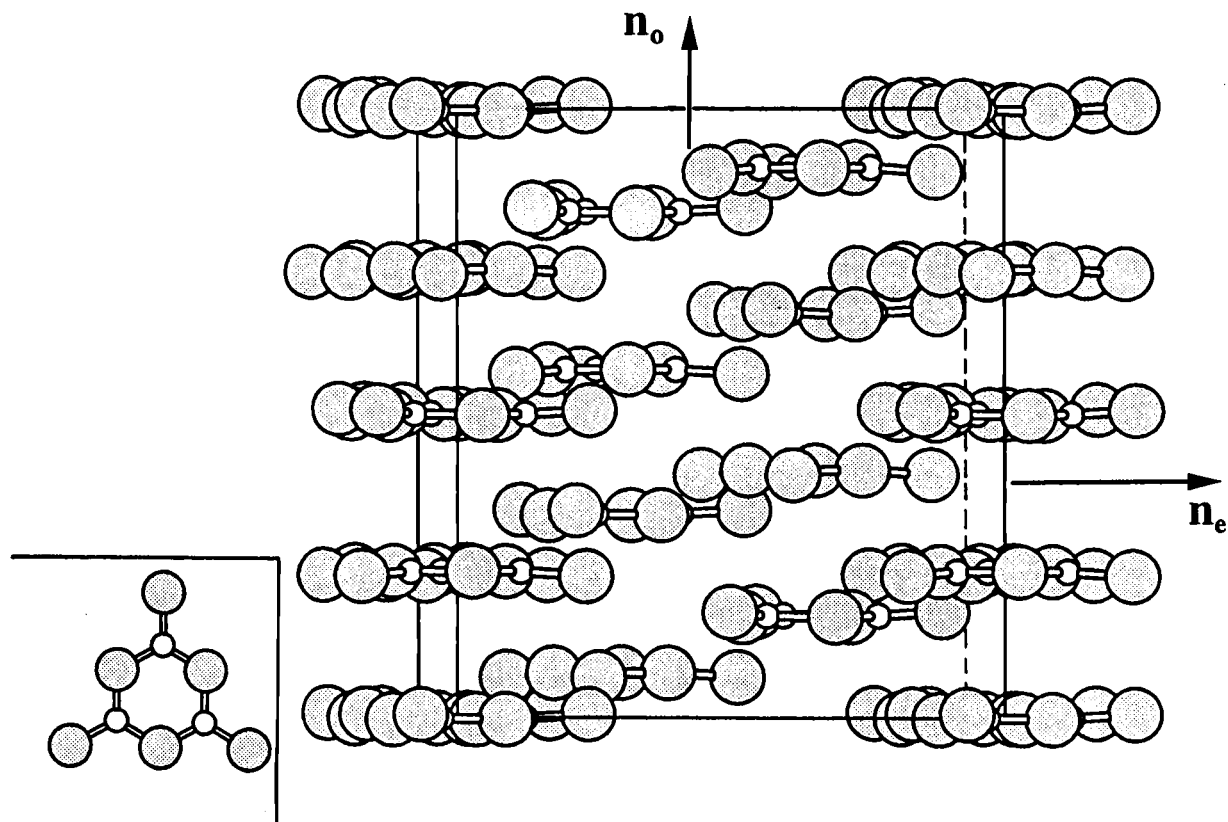
Figure 2.11. B_3O_6 layers in the material β-BaB_2O_4.
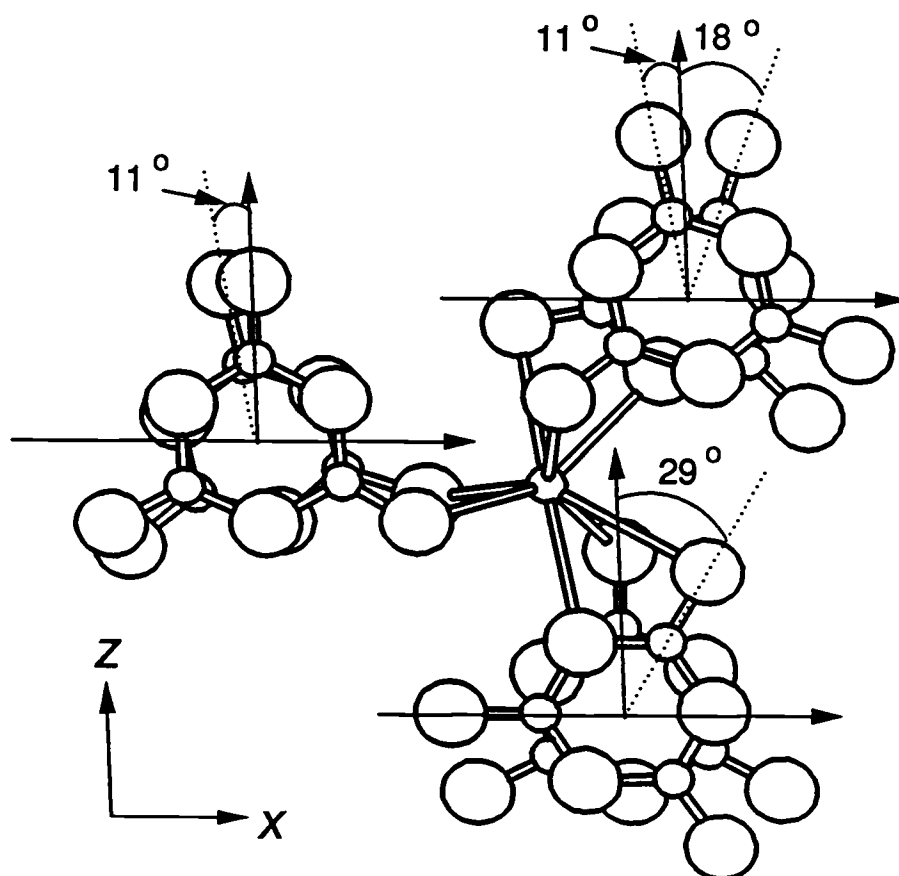
Figure 2.12. Borate environment about a Ba atom in BBO.

performance characteristics is on the basis of their "threshold powers" (22) $P_{th} = (1/F)(\lambda_1\beta_\theta/C)^2$ where $F = \omega_1/\omega_2$, $C \propto d_{eff} / \lambda_1(n_1n_2n_3)^{1/2}$, and β_θ represents the angular sensitivity to phase matching. (The details of phase matching are discussed below.) A nonlinear crystal will convert efficiently if P_{th} is smaller than the peak power of the laser as modified by a beam-quality factor, and, in general, a material having a lower threshold power will be more efficient. Velsko, Webb, Davis, and Huang have computed the optimized threshold powers listed in Table 2.4 (3). Obviously, low threshold powers and high conversion efficiencies will be achieved with materials having large nonlinear susceptibilities (d_{eff}) and small β_θ. The importance of β_θ is seen from a comparison of the characteristics of KD*P (3) with BBO and LBO. The susceptibility of BBO is six-fold greater than that of KD*P but its large angular sensitivity affords a P_{th} that is only 25% less. For LBO, a susceptibility that is nine-fold greater and a β_θ that is almost four-fold less sensitive contribute to a P_{th} that is two orders of magnitude smaller than KD*P. To relate conversion efficiencies to β_θ requires the establishment of quantitative relationships between structure and linear optical properties. While we have yet to fully implement these relationships, we can identify important features from the properties of known compounds.

To realize a significant coherence length and energy generation in a second-harmonic wave the fundamental and second-harmonic waves must be phase matched, i.e., $n(\omega) = n(2\omega)$. The most popular method of phase matching relies on the variation of the refractive index with both the polarization and the

Table 2.4. Parameters for Frequency Doubling 1.064-μm light with Type I phase matching.

	d_{eff} (pm/V)	β_θ (cm$\cdot$ rad)$^{-1}$	P_{th} (MW)	Conversion[b] Efficiency
KD*P[a]	0.34	2390	67	36%
CD*A	0.47	295	0.6	91%
BBO	2.04	10000	49	42%
KTP	3.18	650	0.1	96%
LBO	3.18	650	0.1	76%

[a]Type II phase matching for KD*P

[b]Calculated values assuming a pulsed laser operating at 100 mJ/20 ns pulse with a fluence of 10 J cm^{-2}.

wavelength of a light wave in an anisotropic crystal. BBO is an example of such an anisotropic crystal. The anisotropy derives from the interactions of the electric-field polarizations of the light waves and the layers of B_3O_6 groups. For light propagating in any direction within the planes, the phase velocity of waves polarized in the planes will be less than the velocity of light polarized orthogonal to the planes. The slower velocity derives from the stronger interactions with the B_3O_6 groups. These waves are impeded as they induce a polarization in the groups by shifting electron density through the π system of the groups. For the orthogonal polarization such a strong interaction cannot exist, and the phase velocity of this wave is less affected by the crystal. Such anisotropic crystals where the velocity of light is not always the same and varies with propagation direction are called birefringent. The velocity of light is indicated by its reciprocal, the refractive index. In BBO, the direction orthogonal to polarization within the planes corresponds to the higher index n_o (cf. Figure 2.11) (also the optic axis), and the orthogonal polarization corresponds to the smaller index n_e. The subscript o refers to the ordinary ray and the subscript e refers to the extraordinary ray. When a light ray travels through BBO at some arbitrary angle to the B_3O_6 planes, e.g. 30° to n_o, the ray separates into two components of orthogonal polarization, the ordinary and the extraordinary waves. The velocity of the ordinary wave is dictated by the amplitude of n_o and the velocity of the extraordinary wave is governed by a value of n that is between n_o and n_e. The two rays separate in space (or *walk-off*) by an angle that is determined by the magnitude of the

birefringence. For BBO this value $\Delta n = n_o\text{-}n_e \approx 0.11$. This large birefringence may be compared to the values of 0.009 for quartz (23), 0.012 for MgF_2 (24), and 0.008 for sapphire (24).

Because the interaction between the electric field of the light wave changes with energy and frequency of the light wave, the refractive indices will exhibit dispersion. The dispersion curves for BBO are plotted in Figure 2.13 from published Sellmeier coefficients (25). Now, the phase matching condition is $n(\omega)=n(2\omega)$. To satisfy this condition for a 1064-nm fundamental in the Type I mode, two ordinary waves may be combined to form a second-harmonic extraordinary wave. Because the angle between n_o and n_e is $90°$, the propagation angle relative to the n_o optic axis that is necessary to achieve phase matching may be deduced from Figure 2.13 to be approximately $20°$; the experimentally determined value is $22.7°$.

The high angular sensitivity of BBO at this phase-matching angle derives from the variation of the refractive index with propagation direction, the high birefringence, and anisotropic structure of the material. The variation of n between n_o and n_e will follow expression (3)

$$\frac{1}{n^2} = \frac{\cos^2\theta}{n_o^2} + \frac{\sin^2\theta}{n_e^2} \qquad (3)$$

where θ is the direction of propagation relative to the optic axis. In considering a graph of this function or its derivative, the variations in n with θ values near 0 or $90°$ are found to be small. For intermediate values n will vary widely with
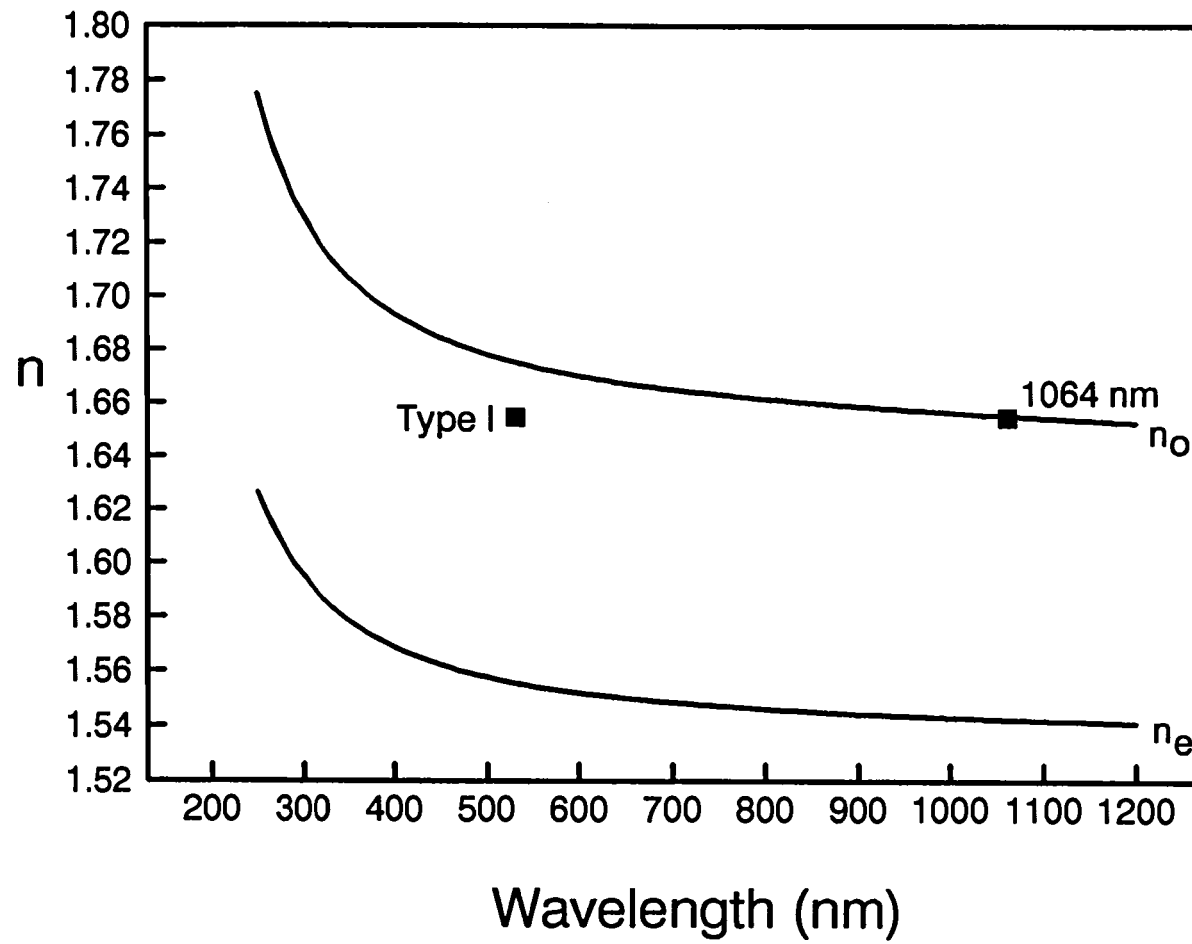
Figure 2.13. Dispersion curves for BBO.

changes in θ. The variations in n will be amplified by the magnitude of the birefringence. In BBO, a highly birefringent material, a slightly divergent or multimode laser will sample a variety of angles θ and refractive indices n. The phase matching condition will not always be strictly satisfied. A high angular sensitivity is anticipated, and a decreased conversion efficiency is observed.

While the high birefringence of BBO may limit the conversion efficiency, it does allow direct conversion processes to short wavelengths. For instance, a 532-nm fundamental may be phase matched to a 266-nm second harmonic (cf. Figure 2.13). Borate anions have absorption edges that fall in the range 160-190 nm. As the energy of incident light approaches the energy of the absorption edge a rapid increase in refractive indices occurs. If the birefringence is not large enough to compensate for this dispersion, it will not be possible to generate light in a second-harmonic process. Such is the case for LBO where an appropriate index $n(2\omega)$ is not available for phase-matching a 532-nm fundamental, Figure 2.14 (3).

An additional example of these considerations is given by the compound $K_2La(NO_3)_5 \cdot 2H_2O$ (KLN) (9). This material has been shown to have the lowest threshold power of any converter in the range 0.9 - 0.95 μm. Its threshold power is also superior to both KTP ($KTiOPO_4$) and LBO for doubling 1.06 μm light. Because the structure of KLN was available prior to any detailed optical measurements, we predicted the relative magnitudes and *signs* of the d coefficients (Table 2.5). The agreement subsequently found with the experiments is reasonable considering the simplicity of the model and the presence of heavy atoms in the material that likely contribute to the susceptibility.
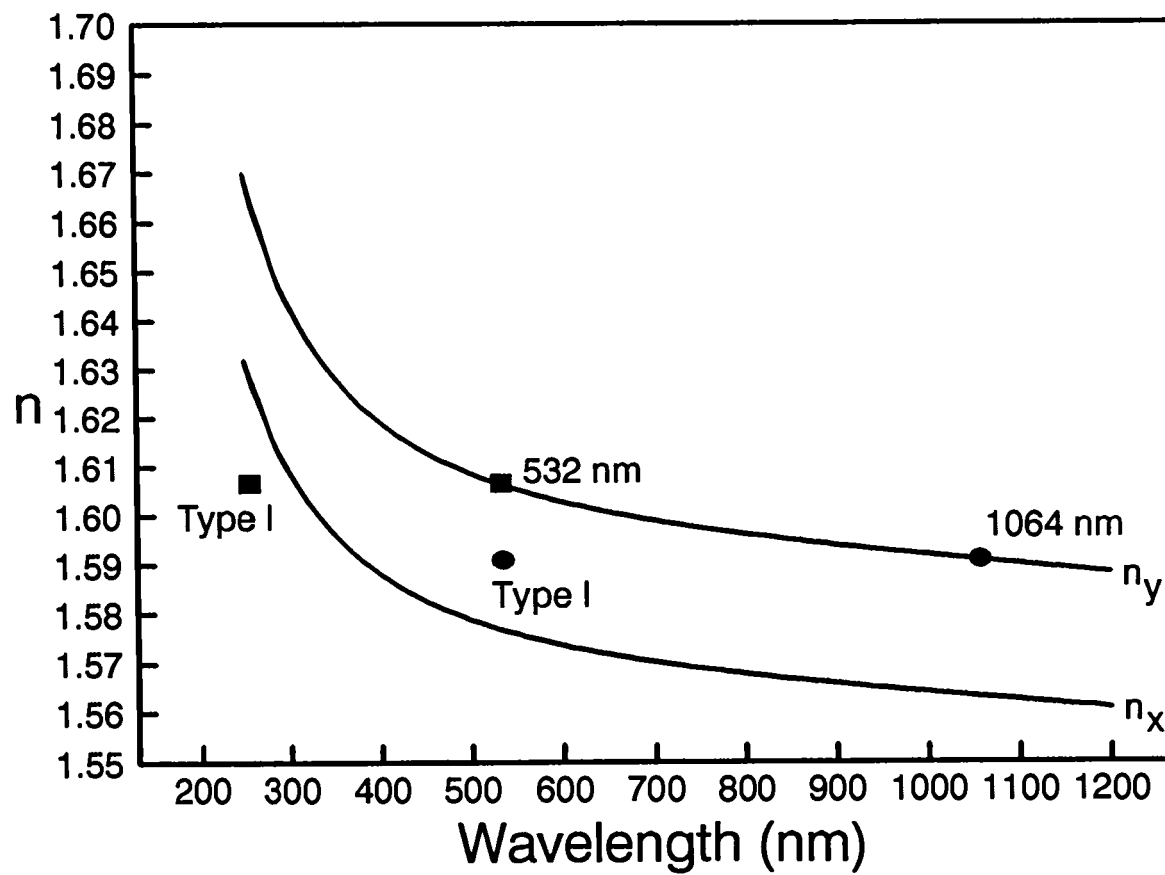
Figure 2.14. Dispersion curves for LBO.

Table 2.5. Experimental and Computed Nonlinearities for $K_2La(NO_3)_5 \cdot 2H_2O$ (9).

Experiment	Computation[*]
$\chi_{311} = +0.90 \pm 0.1$ pm/V	± 0.98
$\chi_{322} = -1.14 \pm 0.15$ pm/V	-1.06
$\chi_{333} = \pm 0.20 \pm 0.10$ pm/V	$+0.08$

[*]β_{333} $(NO_3) = 5.26 \times 10^{-31}$ esu cm^{-3}

Because the nitrate groups do not adopt a coplanar arrangement in the structure, the relevant birefringence of KLN $\Delta n = n_\gamma - n_\beta \approx 0.02$ represents a small value for a crystal composed of triangular oxoanions. For the Type I conversion of 1.06-μm light, the value $\beta_\theta = 50$ (cm $\cdot$ rad)$^{-1}$ has been determined. This small angular sensitivity derives from the magnitude of the birefringence and the dispersion of the refractive indices. The absorption edge of the material, 335 nm, occurs at a considerably lower energy in comparison with a borate. As a result, the rapid rise in the refractive indices begins to occur at longer wavelengths. As seen from Figure 2.15, this combination of effects places the phase matching index $n(2\omega)$ very close to n_β and $\theta=90°$ (noncritical phase matching). From expression (3) the angular sensitivity β_θ is seen to vanish at $\theta=90°$. From phase matching experiments, the deviation from noncritical phase matching has been determined to be less than $1°$, affording small values for β_θ and P_{th}.

We are predicting that the new material $Rb_2Na(NO_3)_2$ (space group $Pmc2_1$) (25) will have the highest nonlinearity among the known nitrates [$d_{15}(Rb_2Na(NO_3)_3$ ≈ 2 x d_{32} ($K_2La(NO_3)_5 \cdot 2H_2O$)]. The three types of groups in the unit cell are sketched in Figure 2.16. Approximate susceptibilities may be readily obtained from the functions for rotation about the axis illustrated at the right of Figure 2.7; here, the designated coordinates coincide with the crystal coordinates and no transformation is required. The results are summarized in Table 2.6 where est. values are derived from the functions following determination of θ, and calc. values are determined from (2). The total value $\chi_{113} = 1.58$ means that the
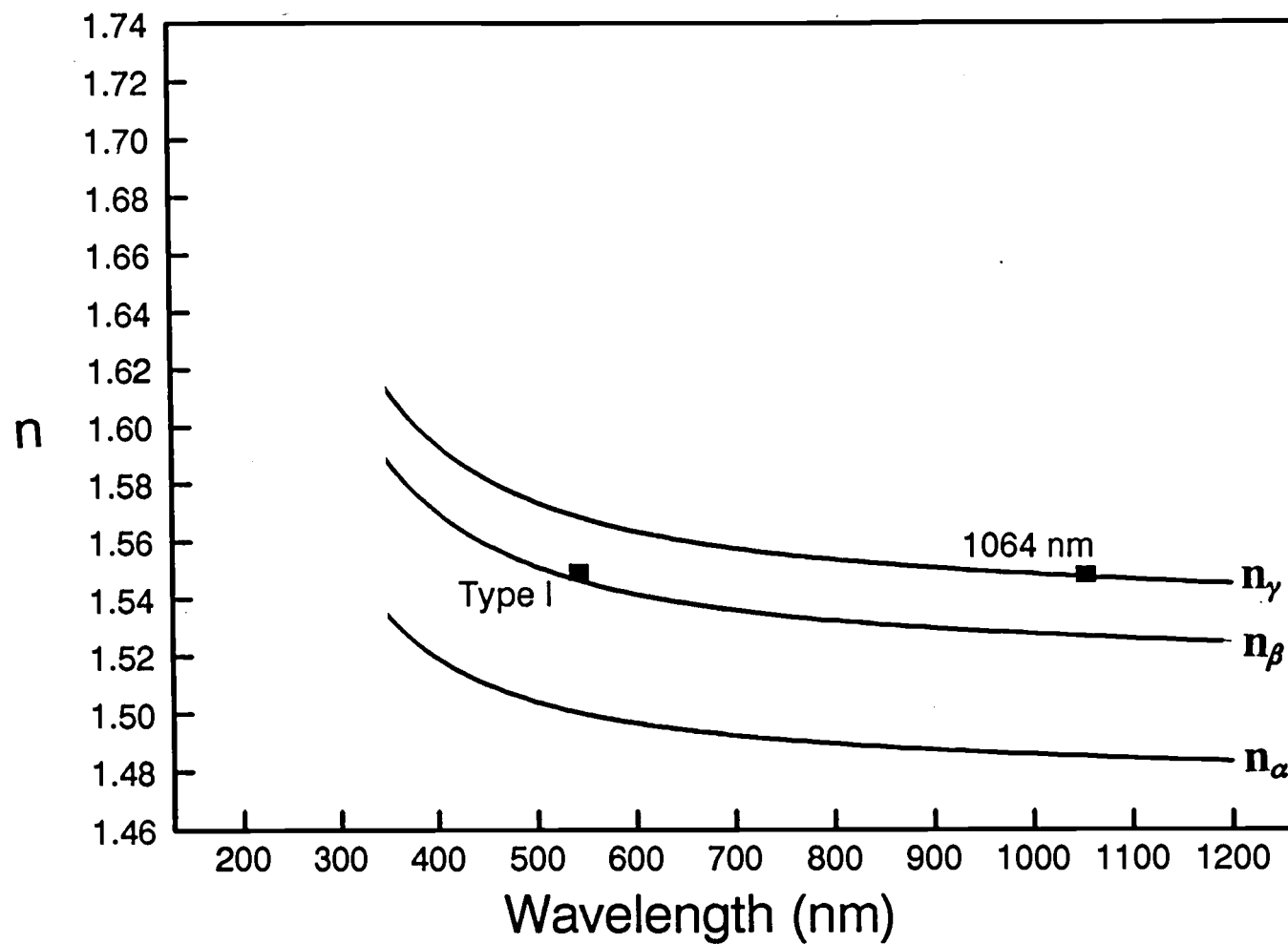
Figure 2.15. Dispersion curves for KLN.
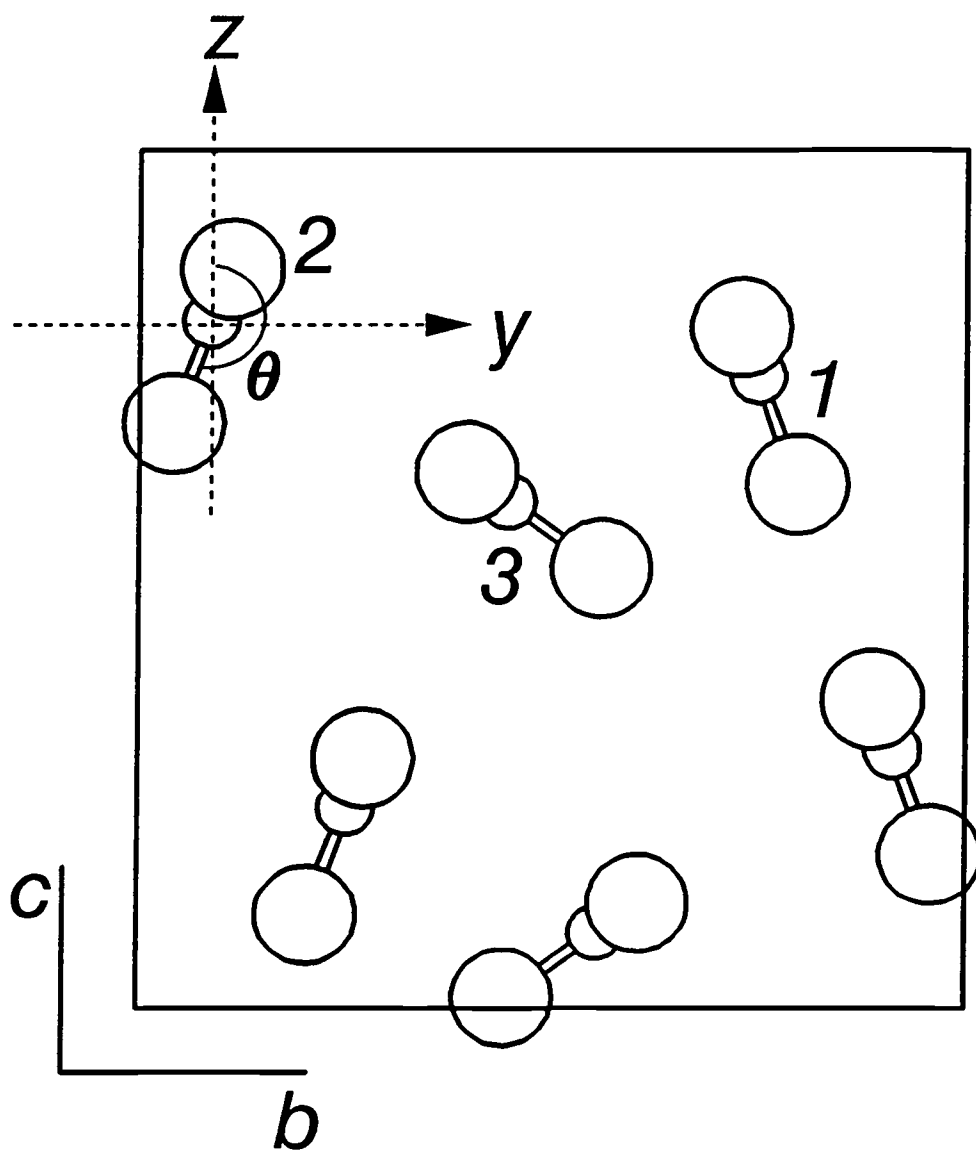
Figure 2.16. Nitrate groups in the unit cell of $Rb_2Na(NO_3)_3$.

Table 2.6. Calculated nonlinearities for $Rb_2Na(NO_3)_3$.

	$N(1)O_3$ $\theta\approx160°$		$N(2)O_3$ $\theta\approx200°$		$N(3)O_3$ $\theta\approx125°$		Total	
	$\chi_{est.}^{\bullet}$	$\chi_{calc.}^{\bullet}$	$\chi_{est.}^{\bullet}$	$\chi_{calc.}^{\bullet}$	$\chi_{est.}^{\bullet}$	$\chi_{calc.}^{\bullet}$	$\chi_{est.}^{\bullet}$	$\chi_{calc.}^{\bullet}$
$\chi_{113}=\chi_{311}=$ $-\cos\theta$	0.60	0.60	0.60	0.61	0.37	0.37	1.57	1.58
$\chi_{112}=\chi_{211}=$ $-\sin\theta$	-0.22	-0.23	0.22	0.21	-0.53	-0.51	-0.53	-0.53
$\chi_{222}=$ $\sin^3\theta$	0.03	0.03	-0.03	-0.02	0.35	0.34	0.35	0.35
$\chi_{333}=$ $\cos^3\theta$	-0.53	-0.52	-0.53	-0.54	-0.12	-0.13	-1.18	-1.19
$\chi_{223}=\chi_{322}=$ $\cos\theta\sin^2\theta$	-0.07	-0.08	-0.07	-0.06	-0.25	-0.24	-0.39	-0.38
$\chi_{233}=\chi_{323}=$ $\sin\theta\cos^2\theta$	0.19	0.20	-0.19	-0.19	0.17	0.18	0.17	0.19

$^{\bullet}\chi$ x 10^{-31} esu

nonlinearity of this material is likely to be ~50% (1.58/3) of the maximum response that could be achieved at this number density of nitrate groups. The lack of coplanarity in the assemblage of the groups (cf. Figure 2.16) should relax the birefringence of the material. Therefore, we anticipate that a small angular sensitivity could combine with a significant nonlinearity to produce a material having a low threshold power. Continued study of this material certainly appears warranted.

These results and considerations can now be used to provide guidelines and further impetus for the synthesis of new borates. We concentrate on borates because of their high damage thresholds (4,26) and their accessibility in crystalline form. To optimize the nonlinearity of an orthoborate, new compounds should have *at least one* B-O bond from each group aligned as in $LiCdBO_3$ and $K_2BeBO_3F_2$. In these known materials, the BO_3 groups form well-defined planes, and a high birefringence is observed. This birefringence will likely increase the angular sensitivities of the materials and their threshold powers. Lower birefringence could be produced *without* a decrease in the nonlinearity from a collection of BO_3 groups as illustrated in Figure 2.17. The nonlinearity is maintained by the invariance of the coefficient β_{333} upon rotation about a B-O vector (Table 2.3). Considering the reported susceptibilities: BBO, $\chi_{111} = 1.6$ pm/V (25) (67% of optimal BO_3 arrangement - calculated from expression (2)); LBO, $\chi_{322} = 0.85$ pm/V [$d_{eff} = 0.82$ pm/V] (3); $YAl_3(BO_3)_4$, $\chi_{111} = 1.5$ pm/V (50% of optimal BO_3 arrangement) [$d_{eff} = 1.23$ pm/V] (27), we anticipate that a simple
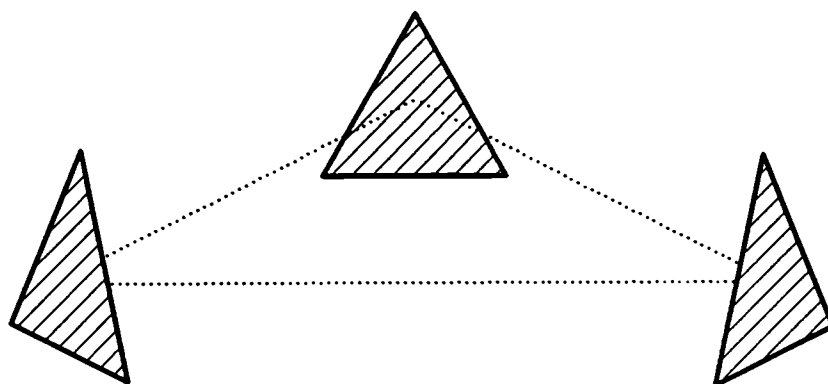
Figure 2.17. Potential arrangement of BO_3 groups for obtaining high

nonlinearity and low birefringence.

orthoborate having a dense, noncentrosymmetric distribution similar to Figure 2.17 may well have properties similar to or exceeding those of LBO. This view is supported by the results obtained from KLN (9) where near noncritical phase matching is achieved.

Summary

In this contribution, we have attempted to give a simple, coherent account of some of the relationships between crystal structures and the properties of second-harmonic generators. In addition to nonlinear susceptibility and angular sensitivity, other properties such as the behavior of d_{eff} with phase-matching angle, temperature sensitivity, thermal conductivity, and optical damage must be examined in appraising a material for a selected application. Considering the multitude of frequency conversion processes and the continuing development of coherent sources, particularly at shorter wavelengths, it is likely that the demand for new materials for conversion into the visible and UV will increase. To this end, the models developed here should contribute to the selection, development, and understanding of new materials.

Acknowledgments

References

1. C. Chen, B. Wu, A. Jiang, and G. You, *Sci. Sin. Ser.* **B28**, 235 (1985).

2. K. Kato, *IEEE J. Quant. Electron.* **QE-22**, 1013 (1986).

3. S. P. Velsko, M. Webb, L. Davis, and C. Huang, *IEEE J. Quant. Electron.* **27(9)**, 2128 (1991).

4. C. Chen, Y. Wu, A. Jiang, B. Wu, G. You, R. Li, and S. Lin, *J. Opt. Soc. Am.* **B6**, 616 (1989).

5. A. Nebel and R. Beigang, *Technical Digest, Advanced Solid-State Lasers*, 8 (1992); D. Chen, M. S. Hopkins, and J. T. Lin, *ibid.*, 11 (1992).

6. M. Ebrahimzadeh, A. J. Henderson, and M. H. Dunn, *IEEE J. Quant. Electron.* **26(7)**, 1241 (1990).

7. W. S. Bosenberg, W. S. Pelouch, and C. L. Tang, *Appl. Phys. Lett.* **55**, 1952 (1989).

8. A. Fix, T. Schroder, and R. Wallenstein, *Laser Optoelektron.* **23**, 106 (1991).

9. C. A. Ebbers, L. Davis, M. Webb, S. P. Velsko, and D. A. Keszler, *IEEE J. Quant. Electron.*, in press.

10. *CRC Handbook of Laser Science and Technology*, M. J. Weber, Ed., CRC Press: Boca Raton, 1986, Vol. 3.

11. S. J. Lalama and A. F. Garito, *Phys. Rev. A* **20(3)**, 1179 (1979).

12. J. Zyss and J. L. Oudar, *Phys. Rev. A* **26(4)**, 2028 (1982).

13. C. T. Chen, *Sci Sinica* **22**, 756 (1979); C. T. Chen and G. Z. Liu, *Ann. Rev. Mater. Sci.* **16**, 203 (1986); C. Chen, Y. Wu, and R. Li, *J. Cryst. Growth* **99**, 790 (1990).

14. S. K. Kurtz and T. T. Perry, *J. Appl. Phys.* **39**, 3798 (1968).

15. L. P. Solov'eva and V. V. Bakakin, *Soviet Physics - Crystallogr.* **15**, 802 (1971).

16. E. V. Sokolova, M. A. Simonov, and N. V. Belov, *Kristallogr.* **25**, 1285 (1980); W. Lin, H. Qingzhen, Z. Zicong, Y. Xiangde, D. Guiqin, and L. Jinhkui, *J. Solid State Chem.*, **89**, 16 (1990).

17. A. A. Ballman, *Amer. Mineral.* **47**, 1380 (1962).

18. T. Alekel III and D. A. Keszler, *Acta Cryst.* **C48**, in press (1992).

19. R. W. Smith and D. A. Keszler, *Chem. Mat.*, in press (1992).

20. J. R. Cox and D. A. Keszler, *Chem. Mat.*, in press (1992).

21. R. Fröhlich, *Z. Kristallogr.* **168**, 109 (1984).

22. D. Eimerl, *IEEE J. Quant. Electron.* **QE-23**, 575 (1987); D. Wimerl, *Ferroelectrics* **72**, 95 (1987); D. Eimerl, S. Velsko, L. Davis, and F. Wang, *Prog. Crystal Growth Charact.*, **20**, 59 (1990).

23. J. D. Dana, *Manual of Mineralogy*, (Eds. C. Klein and C. S. Hurlbut, Jr., John Wiley & Sons, Inc., 1977).

24. R. D. Guenther, *Modern Optics*, (John Wiley & Sons, Inc., 1990).

25. D. Eimerl, L. Davis, S. Velsko, E. K. Graham, and A. Zalkin, *J. Appl. Phys.* **62(5)**, 1 (1987).

26. C. Ebbers and S. Velsko, to be submitted.

27. Y. X. Fon, R. Schlecht, M. W. Qin, D. Luo, A. D. Jiang, and Y. C. Huang, *Technical Digest, Advanced Solid-State Lasers*, 311 (1992).

CHAPTER 3

$SrLiB_9O_{15}$ - NONCENTROSYMMETRIC

CONDENSATION OF B_3O_7 RINGS

Kathleen I. Schaffers and Douglas A. Keszler[*]

Abstract

A new acentric borate containing the B_3O_7 ring has been discovered and characterized. It has the formula $SrLiB_9O_{15}$ and crystallizes in space group R3c(h) with cell constants $a=$ 10.610(1), $c=$ 17.538(2) Å, and V= 1709.9(4) Å^3 and Z= 6. The structure is built from a condensation of BO_3 and BO_4 groups into vertex-sharing B_3O_7 units. The 3-dimensional borate framework contains channels extending along the c axis; sites in these channels are alternately filled with Sr and Li atoms. The magnitude of the optical second-harmonic signal in a Kurtz-Perry test has been found to be equivalent to 85% of that of LBO. Structural and optical results are compared to the similar materials LiB_3O_5 and CsB_3O_5.

Introduction

The compound LiB_3O_5 (LBO) is a relatively new optical frequency converter that has been shown to have a low power threshold, high conversion efficiency, and high damage threshold (1-2). Although the low birefringence of the material prevents direct conversion beyond the third harmonic of Nd:YAG, its wide transmission range makes possible parametric oscillation in the UV (2). The structure of LBO is characterized by the condensation of the B_3O_7 structural unit, Figure 3.1. The favorable optical features of the material derive from the specific electronic structure of this unit and their relative orientations in the noncentrosymmetric crystal.

In this report we describe the structure and optical properties of the new material $SrLiB_9O_{15}$ which also exhibits a noncentrosymmetric structure formed from the condensation of B_3O_7 rings. Examination of the borate framework readily provides a qualitative assessment of the second-order nonlinearity. We compare this new structure to those of LBO and the type CsB_3O_5 (3) to identify important characteristics that contribute to the desirable optical features.
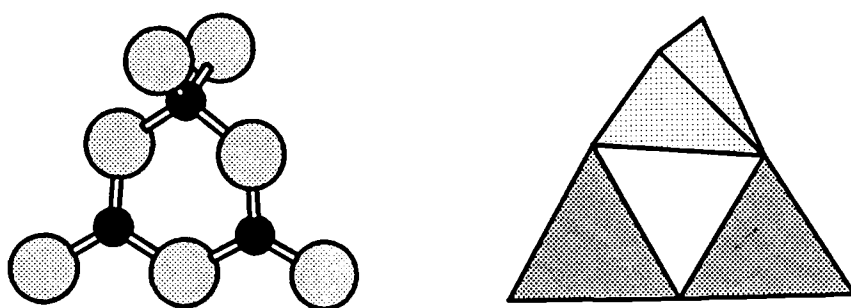
Figure 3.1. Sketch of a B_3O_7 unit.

Experimental

A powder sample of $SrLiB_9O_{15}$ was prepared by grinding together a stoichiometric ratio of $Sr(NO_3)_2$ (AESAR, ACS grade), $LiNO_3$ (Mallinckrodt, analytical grade), and B_2O_3 (ALFA, 99.98%). The nitrates were decomposed at 923 K for ½ h followed by regrinding and heating at 1023 K for 12 h. The resulting powder was confirmed to be single phase by comparing its diffraction pattern to one calculated with the program LAZY-PULVERIX.

Crystals were grown for X-ray structure analysis by melting the sample in a Pt crucible at 1223 K and slowly cooling at 6 K/h to room temperature. A colorless, transparent block of dimensions 0.15(2) x 0.15(2) x 0.20(2) mm was selected and mounted on a glass fiber with epoxy for structure determination. All measurements were made on a single-crystal, rotating-anode Rigaku AFC6R diffractometer with graphite-monochromated Mo Kα radiation. Cell constants and an orientation matrix for data collection were obtained from a least-squares refinement with 19 automatically-centered reflections in the range $30 \leq 2\theta \leq 36°$. The cell constants correspond to a rhombohedral cell (hexagonal axes); Laue symmetry $\overline{3}$m1 was determined on the diffractometer. Intensity data were collected over the range of indices $0 \leq h \leq 14$, $-14 \leq k \leq 14$, $-24 \leq 1 \leq 24$ by using the ω scan technique to a maximum 2θ value of $60°$. Of the 3471 reflections collected, 640 data were unique, and 433 had $F_o^2 \geq 3\sigma(F_o^2)$. The intensities of three representative reflections measured after every block of 200 data varied by an average of 5.4% during the collection.

The structure was solved by utilizing programs from the *TEXSAN* crystallographic software package (4). On the basis of the systematic conditions, hkil, -h+k+l=3n, and hh0l, l=2n, the statistical analysis of the intensity distribution, and the successful refinement of the structure, the crystal was found to form in the noncentrosymmetric space group R3c(h). The position of the Sr atom was derived from the direct methods program SHELXS (5). Each of the remaining atoms was subsequently located from difference electron density maps. After a full-matrix isotropic refinement of the model, an absorption correction was applied (transmission factors: 0.84-1.19) by using the program *DIFABS* (6). The data were averaged (R_{int}=0.093) and then refined with anisotropic thermal displacement coefficients on every atom. Final least-squares refinement on F_o with those reflections having $F_o^2 \geq 3\sigma(F_o^2)$ resulted in the residuals R=0.051 and wR=0.067. The maximum and minimum peaks in the final difference electron density map correspond to 0.6 and 0.4% of the Sr atom, respectively. Important crystal data are outlined in Table 3.1 and atomic positional and isotropic thermal parameters are listed in Table 3.2.

Unit-cell parameters were also determined by least-squares refinement with 2θ values obtained by using a Philips X-ray diffractometer. A set of 15 reflections were collected in the range $22 \leq 2\theta \leq 46°$ with Si (NIST Standard Reference Material 640b) as the internal reference. The refined cell parameters $a=$ 10.617(2) and $c=$ 17.52(1) Å compare to those from single-crystal data, indicating that the crystal chosen for structure analysis was representative of the bulk sample.

Table 3.1. Crystallographic Data for $SrLiB_9O_{15}$.

Formula Weight, amu	431.84
Crystal System	Rhombohedral
Space Group	R3c(h) [#161]
a, Å	10.610(1)
c, Å	17.538(2)
V, Å^3	1709.9(4)
Z	6
D_{calc} g cm^{-3}	2.516
F(000)	1236
Diffractometer	Rigaku AFC6R
Radiation	Mo Kα (λ=0.71069) graphite-monochromated
Data Collection	h, ±k, ±l
No. Observations ($F_o^2 \geq 3\sigma(F_o^2)$)	433
R	0.051
R_w	0.067
Maximum Shift in Final Cycle	0.01

Table 3.2. Positional and Thermal Parameters (B_{eq}) for $SrLiB_9O_{15}$.

	x	y	z	B_{eq}*
Sr	0	0	0.4061	1.31(3)
Li	0	0	0.675(2)	0.7(6)
B1	0.792(1)	0.730(1)	0.1938(7)	0.9(3)
B2	0.731(1)	0.795(1)	0.0727(7)	1.2(4)
B3	0.563(1)	0.559(1)	0.1335(8)	1.1(3)
O1	0.5956(8)	0.678(1)	0.0799(5)	1.2(3)
O2	0.461(1)	0.8899(9)	0.1744(5)	0.9(2)
O3	0.8268(8)	0.8275(7)	0.1327(5)	1.3(2)
O4	0.547(1)	0.437(1)	0.0879(4)	1.4(3)
O5	0.5804(9)	0.9256(8)	0.0198(5)	1.2(3)

$$*B_{eq} = (\frac{8\pi^2}{3})\sum_i \sum_j U_{ij} a_i^* a_j^* a_i \cdot a_j$$

Thermal analysis was performed on a Harrop model DT-726 differential thermal analyzer interfaced to a personal computer through a Metrabyte DAS-8 A/D converter and a Series M1000 signal conditioner. All software for the system was written in this laboratory. Gold was used to calibrate the DTA before analysis of the samples. The sample was heated in a Pt cup with Al_2O_3 as the reference, and data were collected over the temperature range 1073-1273 K with a heating rate of 15 K/min.

The powder and single-crystal (edge lengths = 0.1 mm) SHG signals were measured relative to those of the known frequency converters LiB_3O_5 (LBO) and $KH_2PO_4 \cdot 2H_2O$ (KDP). The experimental method of Kurtz and Perry (7) and a Q-switched Molectron MY-34 Nd:YAG laser operating at 1064 nm were employed for the measurement. A powder sample of LBO was prepared by grinding together a stoichiometric ratio of $LiNO_3$ (Mallinckrodt, analytical grade) and B_2O_3 (ALFA, 99.98%), heating at 923 K for ½ h to decompose the nitrate, regrinding, and heating at 1023 K for 12 h. Formation of the product was confirmed by powder X-ray diffraction as previously described. Single crystals of LBO were obtained from Dr. R. F. Feigelson at Stanford University (Stanford, CA). The measurements were done by using an experimental apparatus engineered in this laboratory (8).

Results and Discussion

Structure

The structure of $SrLiB_9O_{15}$ embodies a 3-dimensional borate framework that encircles the Sr and Li atoms. As seen in Figure 3.2, the framework is built from a condensation of B_3O_7 units, Figure 3.1, that contains channels extending along the c axis. Sites in these channels are alternately filled with Sr and Li atoms that bind to 9 and 6 nearest neighbor O atoms, respectively.

The connectivity within the structure is best appreciated by referring to Figure 3.2 and considering the environments about the high-symmetry Li and Sr sites; the symmetry about each atom is C_3. Each distorted Li-centered trigonal prism shares three of its symmetry-related edges with $B1O_3$ triangles, three vertices in one trigonal plane with $B2O_3$ triangles, and three vertices in the opposite plane with BO_4 groups. Radiating from the LiO_6 polyhedra in the (001) plane, the borate groups act as bridges to the neighboring Sr-centered polyhedra by sharing edges of the BO_4 tetrahedra and vertices of the BO_3 triangles. Without a common O atom between them, the Li- and Sr-centered polyhedra are linked alternately along the c axis by $B2O_3$ triangles and BO_4 tetrahedra (Figure 3.3). By extending these connections within the translational symmetry of the lattice, the entire structure of $SrLiB_9O_{15}$ may be generated.

The Sr atom is bound by nine O atoms in a distorted tricapped trigonal prismatic environment (Figure 3.4). Atoms O2 and O5 define the trigonal faces of the prism and three O1 atoms cap the resulting quadrilateral faces.
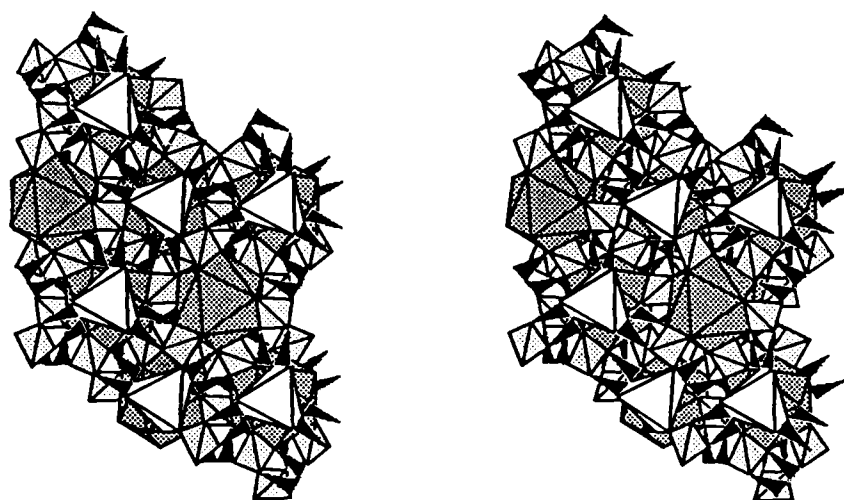
Figure 3.2. Sketch of the dense, three-dimensional structure of $SrLiB_9O_{15}$

presented in stereo where the shaded 9-coordinate sites are SrO_9

polyhedra, the unshaded distorted trigonal prisms are LiO_6 polyhedra,

the tetrahedra are BO_4 groups, and the triangles are BO_3 groups.
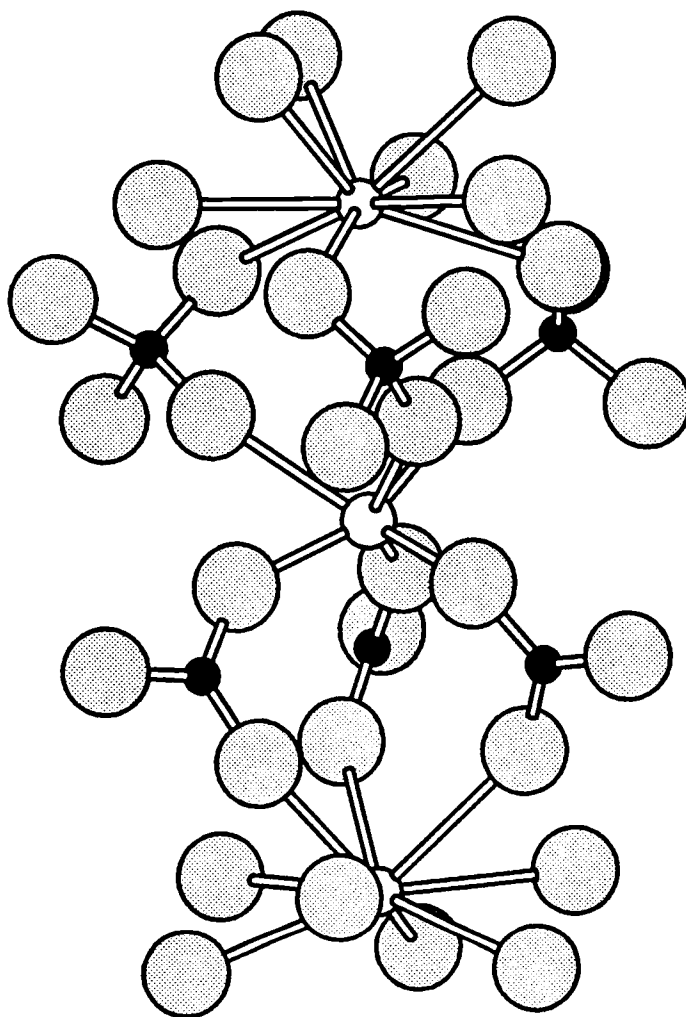
Figure 3.3. Chain of Li- and Sr-centered polyhedra linked alternately

along the c axis by $B2O_3$ groups and BO_4 tetrahedra.
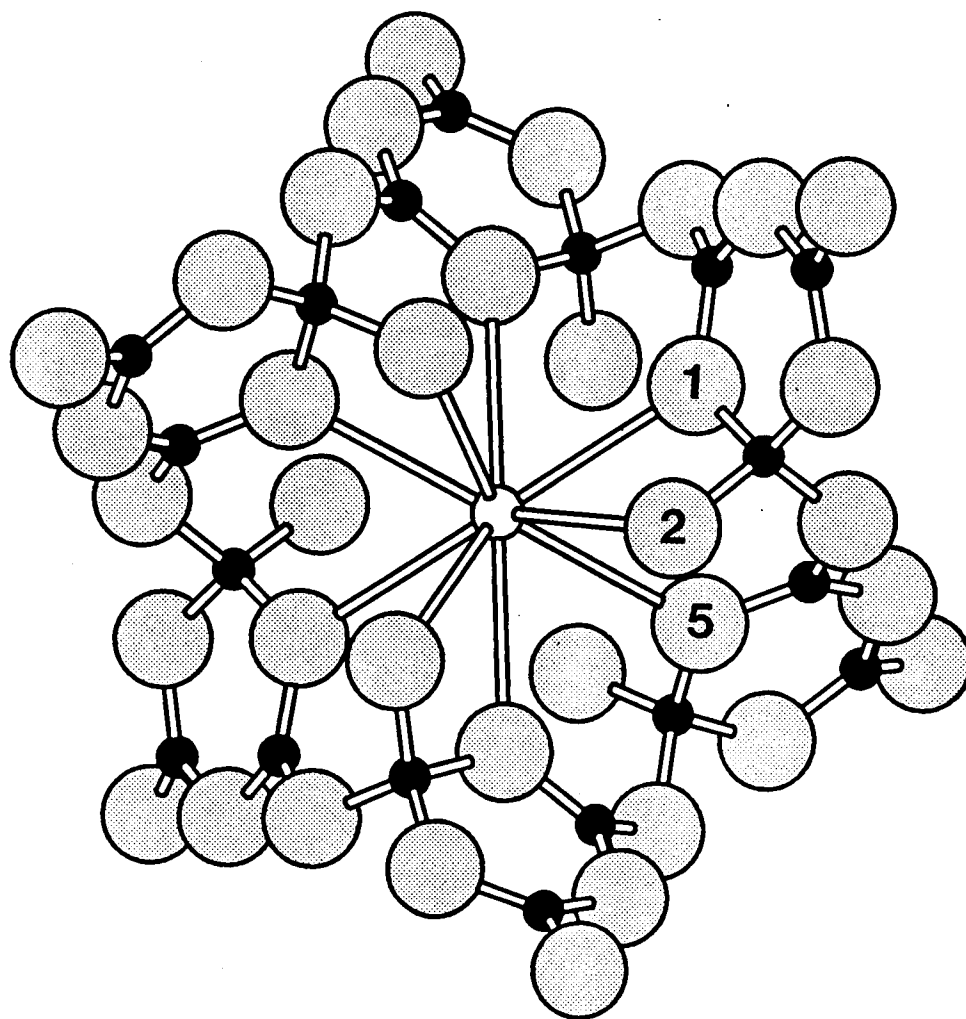
Figure 3.4. Approximate- S_6 symmetry element associated with the borate framework of $SrLiB_9O_{15}$.

Considerable distortion is observed in the prism as the O2 trigonal face is rotated by approximately 22.5° relative to the O5 face (Figure 3.4). Selected interatomic distances and angles are listed in Table 3.3. The Sr -O1, -O2, and -O5 distances of 2.726(7), 2.723(8), and 2.843(8) Å, respectively, affords an average length of 2.76(7) Å which compares favorably to average lengths in other 9-coordinate sites - 2.72(6) Å in $SrBe_2(BO_3)_2$ (9) and 2.69(13) Å in $Sr_3Sc(BO_3)_3$ (10).

The Li atom occupies a highly distorted trigonal prismatic site. It is displaced from the trigonal plane of O3 atoms by 0.74 Å and the plane of O4 atoms by 1.43 Å to give an Li-O3 distance of 1.98(1) Å and an Li-O4 distance of 2.48(2) Å. From a bond-valence calculation (11) the Li-O3 interactions are found to account for approximately 74% of the bonding with the Li⋯O4 interactions making up the remainder. Therefore, the Li environment is best described as 3+3, a distorted 3-coordinate site with three longer bonds to the neighboring O4 atoms. As far as we know the only examples of both triangular and trigonal prismatic Li-O environments are found in the material $Li_{14}Be_5B(BO_3)_9$ (12). For comparison, the Li-O bond lengths are 2.229(1) Å for the 6-coordinate Li and 1.916(1) Å for the 3-coordinate Li. These values may also be compared with the length of 2.18 Å calculated for a 6-coordinate Li atom by using crystal radii (13). An additional distortion of the prism arises from the relative rotation of the two opposite trigonal O faces. The twist angle is approximately 27.5° (cf. Figure 3.2), placing the distorted LiO_6 geometry intermediate to a trigonal prism and an octahedron.

Interatomic distances and angles in the borate framework are normal. Atoms

Table 3.3. Selected Bond Distance (Å) and Angles (°) for SrLiB$_9$O$_{15}$.

Sr -O1 (x 3)	2.726(7)	O1-Sr-O1	119.79(3)
-O2 (x 3)	2.723(8)	O1-Sr-O2	83.0(3)
-O5 (x 3)	2.843(8)		50.7(3)
			131.7(3)
		O1-Sr-O5	62.9(3)
			62.7(3)
		O2-Sr-O2	81.8(3)
		O2-Sr-O5	63.6(3)
			107.6(3)
		O5-Sr-O5	109.9(2)
Li -O3 (x 3)	1.98(1)	O3-Li-O3	106.6(9)
-O4 (x 3)	2.48(2)	O3-Li-O4	149.4(7)
			62.1(4)
			103.9(5)
		O4-Li-O4	91.8(8)
B1 -O3	1.40(1)	O3-B1-O4	117.1(9)
-O4	1.34(1)	O3-B1-O5	119.2(9)
-O5	1.35(1)	O4-B1-O5	123(1)
B2 -O1	1.35(2)	O1-B2-O2	122(1)
-O2	1.35(1)	O1-B2-O3	118.1(9)
-O3	1.38(1)	O2-B2-O3	120(1)

Table 3.3. continued...

B3 -O1	1.47(1)	O1-B3-O2	103.1(9)
-O2	1.51(1)	O1-B3-O4	107(1)
-O4	1.46(2)	O1-B3-O5	113.5(7)
-O5	1.44(1)	O2-B3-O4	116.7(7)
		O2-B3-O5	111(1)
		O4-B3-O5	106(1)
		B1-O3-B2	122.0(9)
		B1-O5-B3	120.2(6)
		B2-O1-B3	120.8(8)

B1 and B2 occupy distorted triangular planar sites and share atom O3 to form a B_2O_5 unit. The B1- and B2- O3 distances are the longer interactions in the BO_3 planes (cf. Table 3.3). The terminal $B1O_2$ and $B2O_2$ planes rotate about the B1-O3 and B2-O3 vectors, respectively, to give an interplanar angle of 22.5° that is common when compared to similar features in other known pyroborate groups (14). The 4-coordinate B3 atom exhibits an average B-O length of 1.47(3) Å that compares to 1.48(7) Å for SrB_4O_7 (15), 1.46(3) Å for ZnB_4O_7 (16), and 1.50(1) Å for $CaBeB_2O_5$ (17).

Frequency conversion

We have determined the magnitude of the second-harmonic signal of $SrLiB_9O_{15}$ relative to LBO by the Kurtz-Perry method (7). The signal produced from a 1064-nm fundamental corresponds to 85% of LBO. The lower value for the Sr compound is related to the number density and orientation of chromophores in the structure. The number density of B atoms in $SrLiB_9O_{15}$ (3.15 x 10^{22} cm^{-3}) is 84% of that observed for LBO (3.75 x 10^{22} cm^{-3}). Only a slight diminution of nonlinearity is expected from this density. A more significant contributor is the disposition of the borate groups in the structure. As seen from Figure 3.3, by neglecting the Sr and Li atoms an approximate S_6 symmetry element positioned near 0, 0, 0.05 may be associated with the borate framework. This element, if actually present, would contain a center of symmetry that would lead to a cancellation of the hyperpolarizability coefficients associated with the borate

repeat units. The presence of this approximate center of symmetry affords the smaller conversion efficiency that is observed.

Condensation of B_3O_7 rings

The only other structures found to form from the condensation of B_3O_7 units are LBO, CsB_3O_5 (3), and TlB_3O_5 (18); the structure of TlB_3O_5 is similar to that of CsB_3O_5. Each of these materials forms a three-dimensional framework with tunnels filled by metal atoms (Figure 3.5). The frameworks exhibit considerable flexibility in adapting to the sizes and coordination demands of the associated cations. This flexibility derives from the various ways by which the B_3O_7 units may condense. These condensation modes may be described by considering the interplanar angles between the B_2O_5 groups that share a common BO_4 tetrahedron (Table 3.4). Comparison of these angles and visual inspection of the fragments for each material (Figure 3.6) reveals the considerable variability attained in connecting the B_3O_7 units to construct the frameworks. The angular freedom is only constrained by the steric hindrance imposed by the neighboring B_2O_5 segments, the chemical and bonding demands of the O atoms and associated metal atoms, and the need to preserve translational symmetry.

A significant difference among these materials is the number density of B_3O_7 rings. The LBO lattice is the densest with a number density of 1.25×10^{22} cm^{-3}, and the CsB_3O_5 and $SrLiB_9O_{15}$ lattices are 33 and 84% of this value, respectively. This observation is consistent with the sizes of the metal atoms in each phase and the associated metal to boron ratio. In LBO the crystal radius of Li (0.73 Å) is
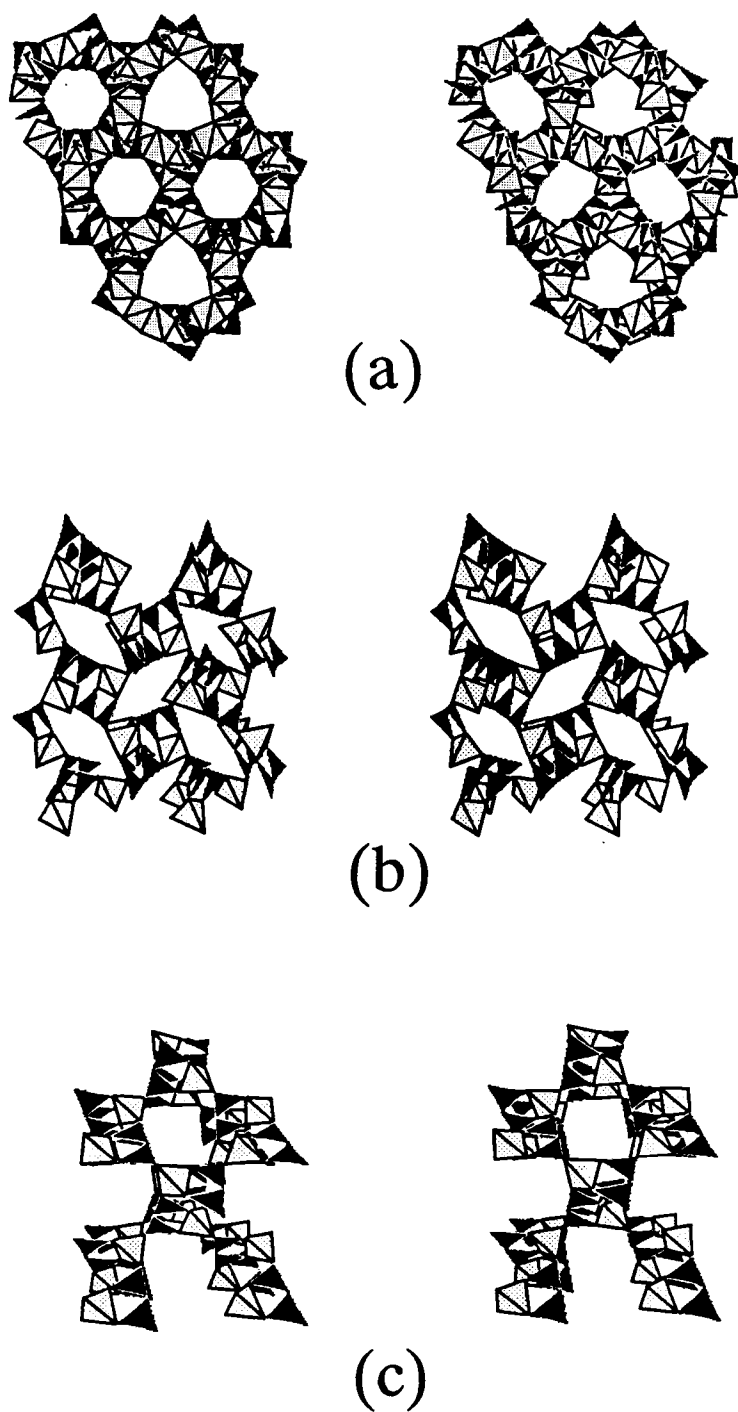
Figure 3.5. Stereoviews of the B_3O_7 arrangements in (a) $SrLiB_9O_{15}$, (b) LBO, and
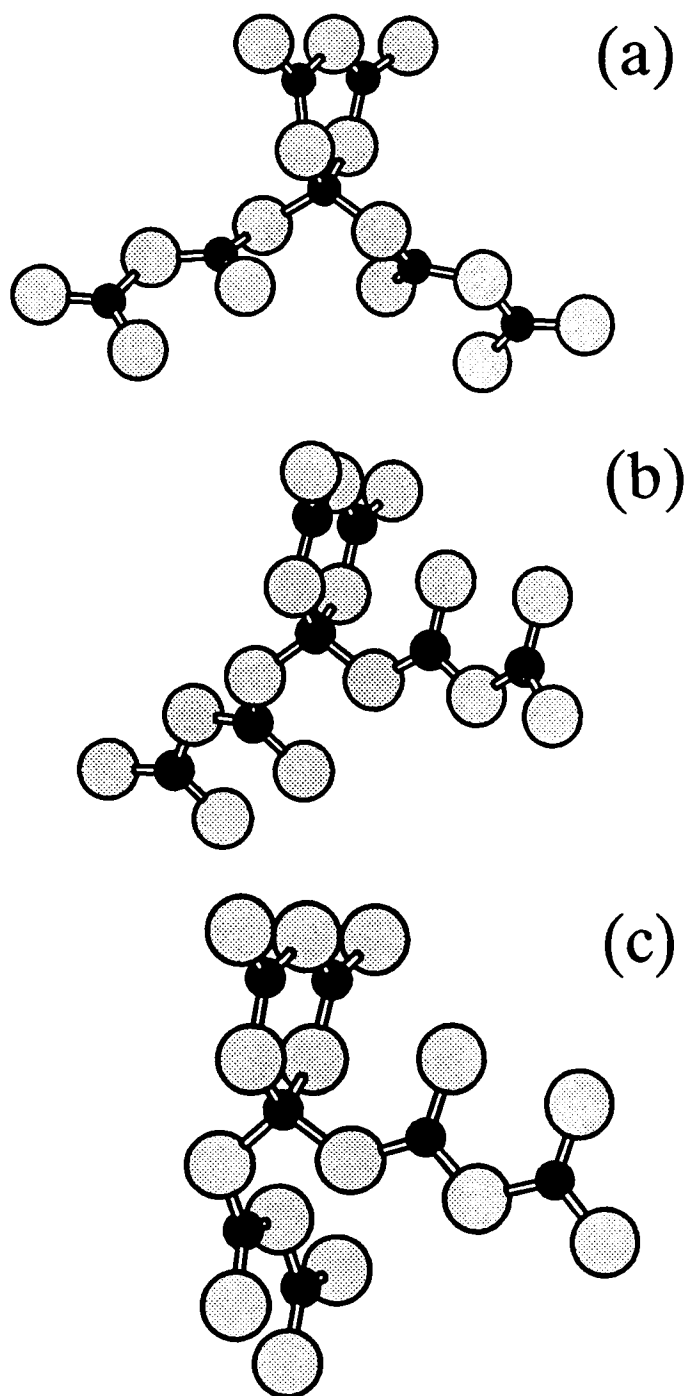
(c) CsB_3O_5.

Figure 3.6. Sketch of the hinging about the pyroborate units in the

[$(B_2O_5)(B_3O_7)(B_2O_5)$] fragments in (a) $SrLiB_9O_{15}$, (b) LBO, and

(c) CsB_3O_5.

Table 3.4. Interplanar angles between the pyroborate units in the $[(B_2O_5)(B_3O_7)(B_2O_5)]$ fragments shown in Figure 3.5.

	A (°)	B (°)
(a) $SrLiB_9O_{15}$	72.1	88.0
(b) LiB_3O_5	83.6	23.0
(c) CsB_3O_5	12.3	45.0

drastically smaller than Cs (1.81 Å) in CsB_3O_5 while the ratio of metal to boron remains the same. For $SrLiB_9O_{15}$, the average crystal radius of the Sr and Li atoms (1.18 Å) is between that of Li and Cs, but the metal to boron ratio is much lower so that the density of B_3O_7 groups is comparable to LBO. These comparisons are useful when seeking an SHG material because higher density of chromophores will provide a larger susceptibility.

An important common feature for each of these materials is their formation in noncentrosymmetric space groups. This acentricity derives from the chirality of the BO_4 group in each B_3O_7 ring. Considering the generic B_3O_7 unit depicted in Figure 3.7a, the simplest condition for achirality would be the presence of an improper rotation axis $\overline{2} \equiv$ mirror plane. Accordingly, with this symmetry, the terminal O_a atoms on the BO_4 group must rest on a mirror plane in a crystal. Also the terminal O_b atoms on the two BO_3 groups must experience identical environments; similar behavior must occur for the two bridging O_c atoms between the tetrahedron and the two triangular planar groups. The likelihood of meeting all of these requirements in the condensation of B_3O_7 rings is remote, considering each example crystallizes in a noncentrosymmetric arrangement. The connectivity of the B_3O_7 groups for $SrLiB_9O_{15}$, LBO, and CsB_3O_5 is represented by the illustrations in Figure 3.7b, c, and d, respectively. One can easily see that none of the groups exhibits C_s symmetry, consequently chirality and a noncentrosymmetric structure ensue. The acentricity of the lattice is predicated on the condensation of the B_3O_7 units into a 3-dimensional framework. The likelihood of observing a
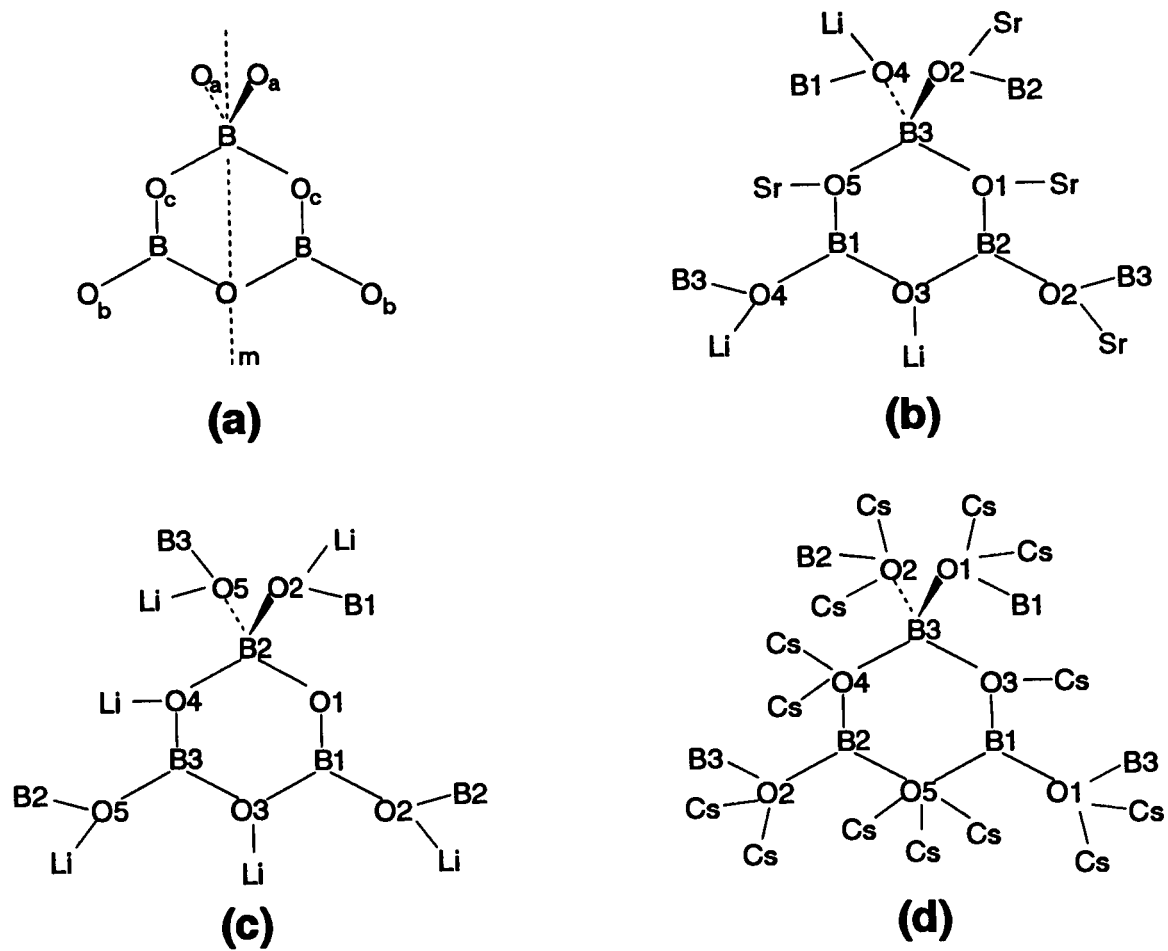
Figure 3.7. Sketch of the bonding interactions about the B_3O_7 rings for (a) an achiral ring, (b) $SrLiB_9O_{15}$, (c) LBO, and (d) CsB_3O_5.

noncentrosymmetric structure containing isolated rings, at least through high temperature synthetic methods, is much lower, making the borate framework an important characteristic for the realization of a new frequency doubler.

It is well-known that a crystal must be noncentrosymmetric to convert to the second harmonic of a fundamental (19). Continued synthetic efforts directed to the preparation of borates with a B:O ratio of 3:5 are likely to produce additional noncentrosymmetric materials from condensation of B_3O_7 rings. The alignment of these rings is very important in determining the magnitude of the nonlinearity for a crystal. One way to achieve the maximum nonlinearity is to have all of the rings aligned parallel to one another. Unfortunately, after considering several models we have determined that a three-dimensional lattice cannot be constructed with such an alignment of B_3O_7 rings. We, therefore, anticipate that all materials formed from condensation of B_3O_7 rings will exhibit skewed interplanar angles among the B_2O_5 groups (cf. Table 3.4). These angles should afford rather small magnitudes of birefringence. This feature is likely to limit the direct conversion to short wavelengths, but will afford the potential to observe small power thresholds and high conversion efficiencies.

A two-dimensional network having an alignment of borate groups for an optimal nonlinearity can be constructed if the tetrahedral BO_4 group is flattened to a square-planar geometry. An example of this network is present in the material $BaCuB_2O_5$ (20), described in the following article, where the B-centered tetrahedra are replaced by tetrahedrally distorted, square-planar CuO_4 polyhedra.

Here, layers of composition $[CuB_2O_5]_{2\infty}$ are bridged by 10-coordinate Ba atoms. Within each layer all of the B_2O_5 groups coincide with each other.

We end by noting that DTA studies reveal a single melting event at 1143 ± 5 K for $SrLiB_9O_{15}$. Upon rapid cooling the material becomes a glass, but it will recrystallize if the temperature is lowered at approximately 60 K/h. Small single crystals have also been pulled directly from a stoichiometric melt by the Czochralski method. Each of these results indicates that the material melts congruently.

Acknowledgments

References

1. C. Chen, Y. Wu, A. Jiang, B. Wu, G. You, R. Li, and S. Lin, *J. Opt. Soc. Am. B* **6(4)**, 616 (1989).

2. S. P. Velsko, M. Webb, L. Davis, and C. Huang, *IEEE J. Quant. Electron.* **27(9)**, 2182 (1991).

3. J. Krogh-Moe, *Acta Cryst.* **B30**, 1178 (1974).

4. Molecular Structure Corporation, *TEXSAN*, Structure Analysis Package, MSC (3200A Research Forest Drive, The Woodlands, TX 77381).

5. G. M. Sheldrick, in "Crystallographic Computing 3" (G. M. Sheldrick, C. Krüger, and R. Goddard, Eds.) pp. 175-189, Oxford Univ. Press, Oxford, (1985).

6. N. Walker and D. Stuart, *Acta Cryst.* **A24**, 214 (1968).

7. S. W. Kurtz and T. T. Perry, *J. Appl. Phys.* **39**, 3798 (1968).

8. T. A. Reynolds and D. A. Keszler, *Chem. Mat.* (1992), submitted.

9. K. I. Schaffers and D. A. Keszler, *J. Solid State Chem.* **85**, 270 (1990).

10. P. D. Thompson and D. A. Keszler, *Chem. Mat.* **1**, 292 (1989).

11. I. D. Brown, *Structure and Bonding in Crystals, Vol. III*, Academic Press, Inc. 1, (1981).

12. J. L. Luce, K. I. Schaffers, and D. A. Keszler, *Inorg. Chem.* (1992), in preparation.

13. R. D. Shannon, *Acta Cryst.* **A32**, 751 (1976).

14. P. D. Thompson, J. Huang, R. W. Smith, and D. A. Keszler, *J. Solid State Chem.* **95**, 126 (1991).

15. A. Perloff and S. Block, *Acta Cryst.* **20**, 274 (1966).

16. M. Martinez-Ripoll, S. Martinez-Carrera, S. Garcia-Blanco, *Acta Cryst.* **B27**, 672 (1971).

17. K. I. Schaffers and D. A. Keszler, *Acta Cryst. C* (1992), in press.

18. C. Chen, Y. Wu, A. Jiang, B. Wu, G. You, R. Li, and S. Lin, *J. Opt. Soc. Am. B* **6(4)**, 616 (1989).

19. C. Chen and G. Liu, *Ann. Rev. Mater. Sci.* **16**, 203 (1986).

20. R. W. Smith and D. A. Keszler, *Chem. Mat.* (1992), submitted.

CHAPTER 4

A PRESCRIPTION FOR NEW BORATE FREQUENCY CONVERTERS

Kathleen I. Schaffers and Douglas A. Keszler

Comment

In the preceding chapters of this dissertation, the desirable characteristics of frequency converters have been discussed. A simple approach was devised for the estimation of second-order nonlinearities, and in Chapter 2 it was applied to materials containing triangular oxoanions. Optimal arrangements for achieving high nonlinearities or conversion to short wavelengths, or both, were identified. Complex borate frameworks built from a condensation of B_3O_7 units were compared in Chapter 3. These materials exhibit favorable nonlinear optical (NLO) properties; however, as discussed in Chapter 3, an optimal arrangement of the principle chromophores, yielding the highest nonlinearity, cannot be produced from condensation of B_3O_7 units alone. Given the intrinsic limits of the hyperpolarizability of the BO_3 group and the structural confines of condensed B_3O_7 frameworks, other types of borates should be examined to realize improved NLO properties. In this chapter, new noncentrosymmetric pyroborates are identified as a likely source of these improved characteristics.

New pyroborates should provide high densities of chromophores having large nonlinearities. Also, the variety of geometries adopted by the B_2O_5 group will affect the linear optical properties, conversion efficiency, and ability to convert to short wavelengths. The number density of B_2O_5 groups in a pyroborate is generally 60% of the density of BO_3 groups in a corresponding simple orthoborate (e.g., number density of BO_3 in $Sr_3(BO_3)_2$ = 13.70 x 10^{21} cm^{-3} and number density

of B_2O_5 in $Sr_2B_2O_5$ = 8.19 x 10^{21} cm^{-3}). For the pyroborate group to be more effective in second-harmonic generation, its maximum hyperpolarizability coefficient should be approximately 1.7 times that of the orthoborate group. Although these coefficients have yet to be calculated or determined experimentally, we expect the magnitude of the maximum coefficient to be similar to β_{333} (= -2.9308 x 10^{-31} esu) of the B_3O_7 ring (1). This coefficient corresponds to in-plane polarization of the B_2O_5 section of the ring; the BO_4 segment of the B_3O_7 ring should have little effect on the magnitude of this coefficient. The magnitude of the coefficient is much larger than the value β_{333} = .641 x 10^{-31} esu for a simple orthoborate group and should exceed any losses from the decreased number density to produce higher nonlinearities for pyroborates.

Thompson, Smith, Huang, and Keszler have recently detailed the considerable structural flexibility of the pyroborate group (2). B-O-B angles through the bridging O atom cover the range 112.1-180°. Rotations about τ_1 (Figure 4.1) afford interplanar angles between the terminal BO_2 groups that range from 0-74°. Very recently, Alekel and Keszler have identified a pyroborate group with nearly orthogonal BO_2 planes (3) (Figure 4.2). This structural variability should produce materials of differing nonlinearities and birefringence. Crystals containing nearly planar pyroborate groups (small τ_1) generally exhibit layered-type structures that can give rise to high birefringence. Such crystals would be of most interest for the generation of short wavelength light. Intermediate angles will cause deviations from planarity, limiting the layered stacking of the groups and producing lower
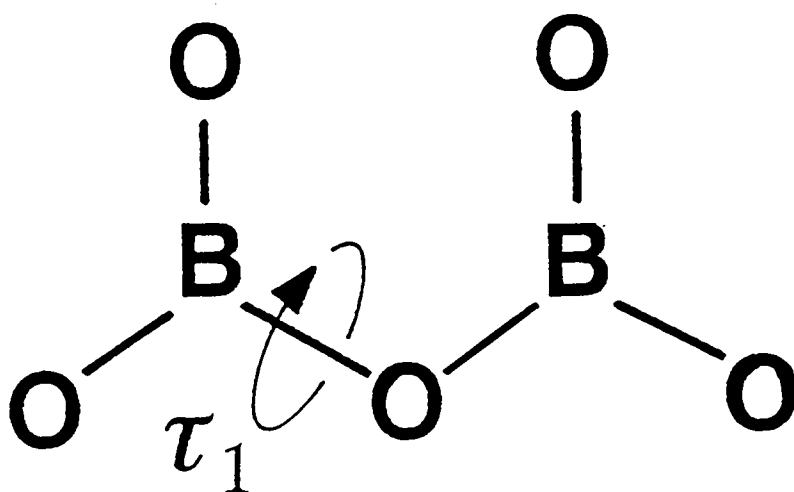
Figure 4.1. Sketch depicting the rotation τ_1 about the hinging O atom of a

pyroborate group.
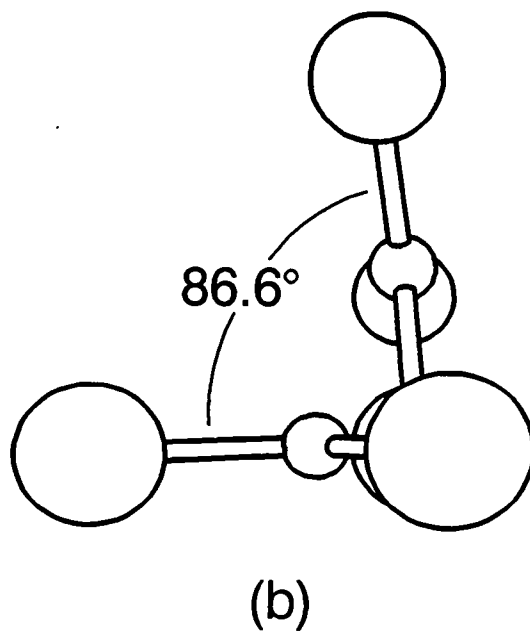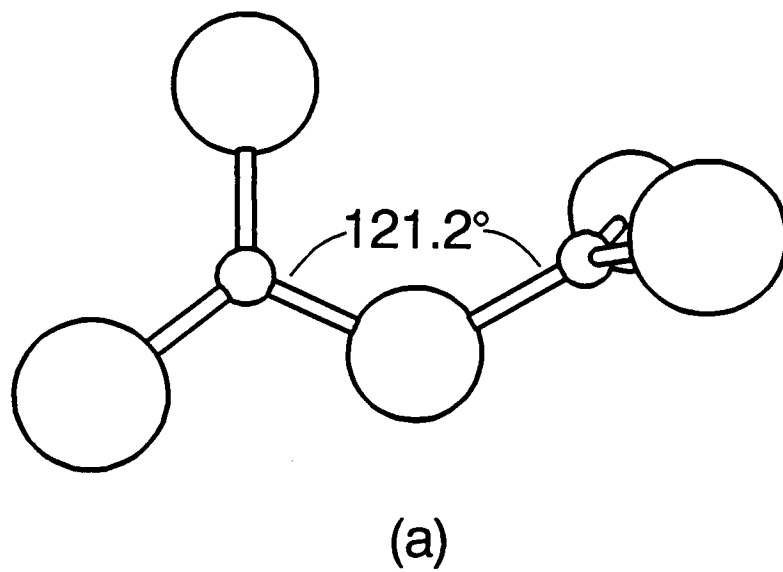
Figure 4.2. The pyroborate group in $Ba_5(B_2O_5)_2F_2$; (a) B-O-B angle and (b) interplanar angle.

birefringence. Such materials in general should produce high conversion efficiencies. If a material is produced with a birefringence near $\Delta n = 0.07$, both high conversion efficiency and the generation of short wavelength light may be achieved. Considerable opportunities exist here to realize materials with variation of physical properties and to correlate them with the microscopic atomic arrangements.

Also, a very pragmatic consideration is the synthetic accessibility of new pyroborates. It is the simplest form of condensation of BO_3 groups and might be expected to form in a variety of phase systems. Indeed, it has been a common component of the phase diagrams investigated in this lab.

To produce a large nonlinearity from a collection of nearly planar B_2O_5 they should be assembled as shown in Figure 4.3. In this arrangement the hyperpolarizability coefficients simply sum constructively. Figure 4.3 is a portion of the noncentrosymmetric structure of $BaCuB_2O_5$ (4). Although the orientations of the B_2O_5 groups are favorable for harmonic generation, the absorption bands associated with the Cu^{2+} ion may obviate the use of this material in the visible portion of the spectrum.

An additional material that has not been studied is the oxide pyroborate $RbNbOB_2O_5$ (5) (Figure 4.4). This compound contains inequivalent pyroborate groups having interplanar angles of 11 and $15°$ between the terminal BO_2 groups. We estimate that the alignment of these groups will produce a susceptibility of nearly 85% of optimum at this number density. This value may be compared to
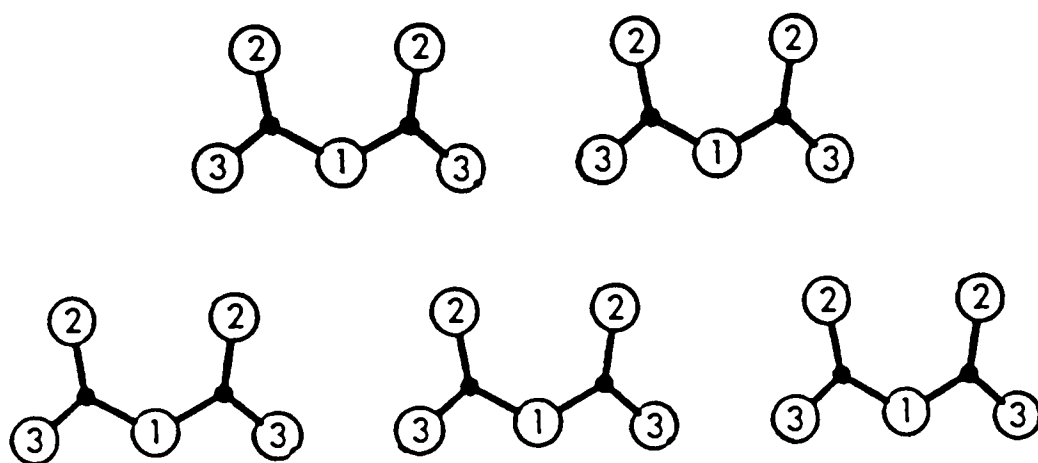
Figure 4.3. Arrangement of B_2O_5 groups in the layered structure of $BaCuB_2O_5$.
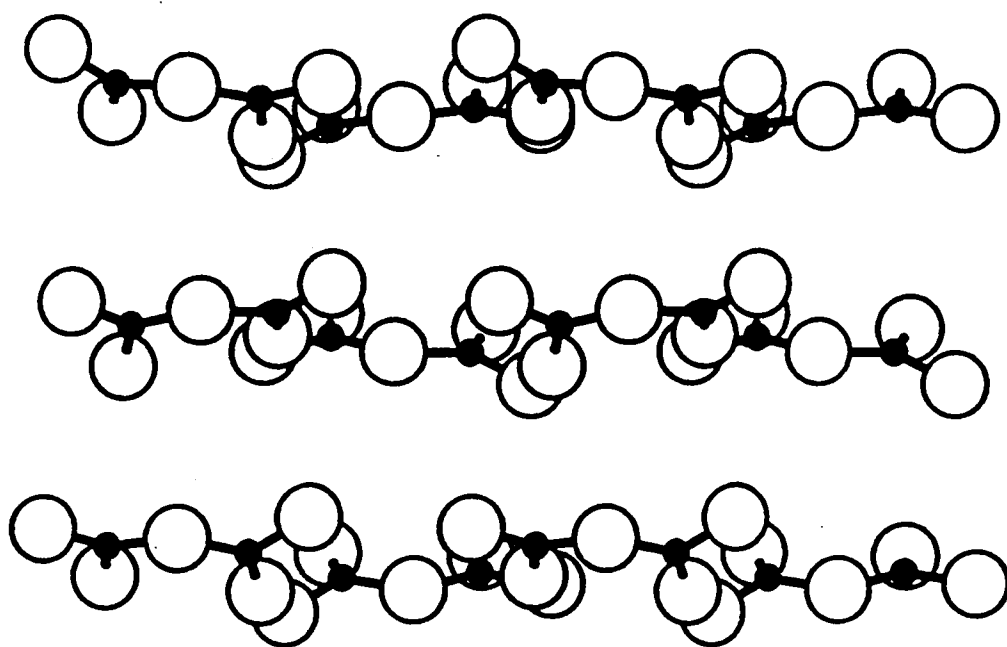
Figure 4.4. Layers of B_2O_5 groups in $RbNbOB_2O_5$.

LBO where we estimate the alignment of the B_2O_5 groups (containing the primary hyperpolarizability coefficient) to be only 40% of optimum. This analysis, however, is clouded because of the extended $\cdots$O-Nb-O-Nb-O$\cdots$ chains present in the structure that could make a considerable contribution to the nonlinearity; the influence of these chains is observed in the linear properties, i.e., the large refractive indices (n $\approx$ 1.8) and the small birefringence $\Delta n = 0.033$ ($\lambda = $ 800 nm). How these chains might affect the nonlinearity cannot be predicted with certainty, but NLO experiments on this material are certainly warranted. To realize a higher birefringence and to investigate the intrinsic characteristics of the B_2O_5 alignment the derivative $RbZrFB_2O_5$ should be synthesized.

The synthesis of new pyroborate structures provides a practical means for developing NLO properties. Desirable structures should be accessible in alkali- and alkaline earth-borate systems containing an additional ion having a preference for octahedral coordination. Also, substitution of one atom for another in known materials, such as Be or Al, for the tetrahedrally coordinated B atom in the B_3O_7 unit of LiB_3O_5 (LBO), could produce materials containing pyroborate anions. Thus, we conclude that investigation of such systems provides a worthwhile strategy for synthesizing new frequency converters with preferred NLO characteristics.

References

1. C. T. Chen, *Sci Sinica* **22,** 756 (1979); C. T. Chen and G. Z. Liu, *Ann. Rev. Mater. Sci.* **16,** 203 (1986); C. Chen, Y. Wu, and R. Li, *J. Cryst. Growth* **99,** 790 (1990).

2. P. D. Thompson, J. Huang, R. W. Smith, and D. A. Keszler, *J. Solid State Chem.* **95,** 126 (1991).

3. T. Alekel III and D. A. Keszler, *J. Solid State Chem.* (1992), to be submitted.

4. R. W. Smith and D. A. Keszler, *Chem. Mat.* (1992), to be submitted.

5. P. A. Baucher and M. G. B. Cervelle, *Acta Cryst.* **B32,** 2211 (1976).

CHAPTER 5

STRUCTURE OF $CdCl_2C_3H_7NO_2$

Kathleen I. Schaffers and Douglas A. Keszler[*]

Abstract

catena-poly[cadmium-di-μ-chloro-μ-L-alanine-O:O'], $CdCl_2C_3H_7NO_2$, has been synthesized and structurally characterized. The Cd atom occupies a distorted octahedral environment of four Cl atoms and two O atoms. These octahedra are linked through Cl···Cl edges and bridged by carboxyl groups of the alanine molecules to form one-dimensional rods that extend along [010].

Comment

We have recently crystallized several new complexes incorporating the amino acid L-alanine; this work is part of an effort in examining and modelling the optical second-order nonlinearities of compounds containing a carboxyl group as the principal chromophore. In this contribution we describe the structure of the adduct formed between this acid and cadmium chloride.

Crystals were grown by dissolving a 1:1 molar ratio of $CdCl_2 \cdot 2\frac{1}{2}H_2O$ (Aldrich, 98%) and L-alanine (Aldrich, 99%) in warm distilled water. The solution was set aside at room temperature, and crystals formed upon slow evaporation of the solvent. Structure solution data are provided in the table titled Experimental Details (Table 5.1). Positional parameters and equivalent isotropic displacement coefficients are listed in Table 5.2.

As seen in Figure 5.1, the Cd atoms bind to four Cl atoms and two O atoms in a distorted octahedral environment. The octahedra are spanned by the carboxyl group of the alanine molecule and fuse directly by sharing Cl1⋯Cl2 edges to form one-dimensional chains that extend along the b axis. If the carboxyl group is regarded as a single atom, the condensation of octahedra may be considered to result from a sharing of triangular faces as occurs in the chains of the compound $CsNiCl_3$ (1) and related derivatives. We derive this description, in part, from the lack of coplanarity between adjacent $CdCl_4$ planes. The angle between these flats

Table 5.1. Experimental details for the structure solution of $CdCl_2C_3H_7NO_2$.

Compound *[e.g. (1), (2) etc.]*	Cadmium Chloride Alanine	
CRYSTAL DATA		
Chemical formula $CdCl_2C_3H_7NO_2$	Crystal System Monoclinic	
M_r 272.4	Space Group C2	
a (Å) 16.240(2)	α (°)	
b (Å) 7.272(1)	β (°) 116.44(1)	
c (Å) 7.987(2)	γ (°)	
Z 4	D_m (Mg m^{-3})	
V (Å^3) 844.7(2)	D_x (Mg m^{-3}) 2.142	
Radiation Mo Kα	No. of reflections for lattice parameters 20	
Wavelength (Å) 0.71069	θ range for lattice parameters (°) $30 \leq 2\theta \leq 36$	
Absorption coefficient (mm^{-1}) 3.155	Temperature (K) 296	
Crystal source Grown from a H_2O solution fo $CdCl_2 \cdot 2\frac{1}{2}H_2O$ and L-$C_3H_7NO_2$		
Crystal colour Colorless	Crystal description Plate	
Crystal size (mm) 0.20(2) x 0.08(2) x 0.35(2)		
DATA COLLECTION		
Diffractometer type Rigaku AFC6R	Collection method ω-2θ	
Absorption correction type (circle appropriate description) DIFABS analytical integration empirical refdelf sphere cylinder none	Absorption correction (T_{min}, T_{max}) 0.63 - 1.44	
No. of reflections measured 2120	R_{int} 0.046	
No. of independent reflections 2008	θ_{max}(°) 37.5	
No. of observed reflections 1900	No. of standard reflections (and interval) 3 standards: {6,4,1; 8,4,0; & 2,6,1} (every 200 data)	
Criterion for observed $F_o^2 \geq 3\sigma(F_o^2)$	Variation of standards ~3.5% in intensity	
h_{min} -27	h_{max} 27	
k_{min} 0	k_{max} 12	
l_{min} 0	l_{max} 13	

Table 5.1. continued.

EXPERIMENTAL DETAILS *(continued)*	
REFINEMENT	
Treatment of hydrogen atoms (circle appropriate entry, or describe in box below) refall refxyz refU noref	F, F² or I **F**

R
      0.063
	No. of parameters refined
	      81

wR
      0.088
	No. of reflections used in refinement
	      1900

S 1.95	Weighting scheme $\Sigma w(\,\lvert F_o \rvert - \lvert F_c \rvert\,)^2$ $w = \quad 1/\sigma(F_o)$

$(\Delta/\sigma)_{max}$
      0.02
	$(\Delta\rho)_{min}$ (e Å⁻³)
	      2.072

Extinction correction method (if applied)	$(\Delta\rho)_{max}$ (e Å⁻³) 10.420
Primary- and secondary-extinction values	Source of atomic scattering factors International Tables for X-ray Crystallography

Table 5.2. Positional parameters and B_{eq} for $CdCl_2C_3H_7NO_2$.

	x	y	z	B_{eq}^{*}
Cd	0.24399(4)	0.2755	0.48899(7)	1.83(2)
Cl1	0.3733(1)	0.0347(5)	0.5409(3)	2.17(5)
Cl2	0.1283(2)	0.0117(4)	0.3200(3)	2.60(6)
O1	0.2177(5)	0.3773(9)	0.1974(9)	2.3(2)
O2	0.2392(6)	0.176(1)	0.7653(9)	2.5(2)
N	0.3836(6)	-0.096(1)	1.165(1)	2.2(2)
C1	0.2804(5)	0.036(1)	0.861(1)	1.8(2)
C2	0.3350(6)	0.073(1)	1.075(1)	2.0(2)
C3	0.4028(8)	0.234(1)	1.113(2)	3.2(3)

$$^{*}B_{eq} = (\frac{8\pi^2}{3}) \sum_{i} \sum_{j} U_{ij} a_i^{*} a_j^{*} a_i \cdot a_j$$
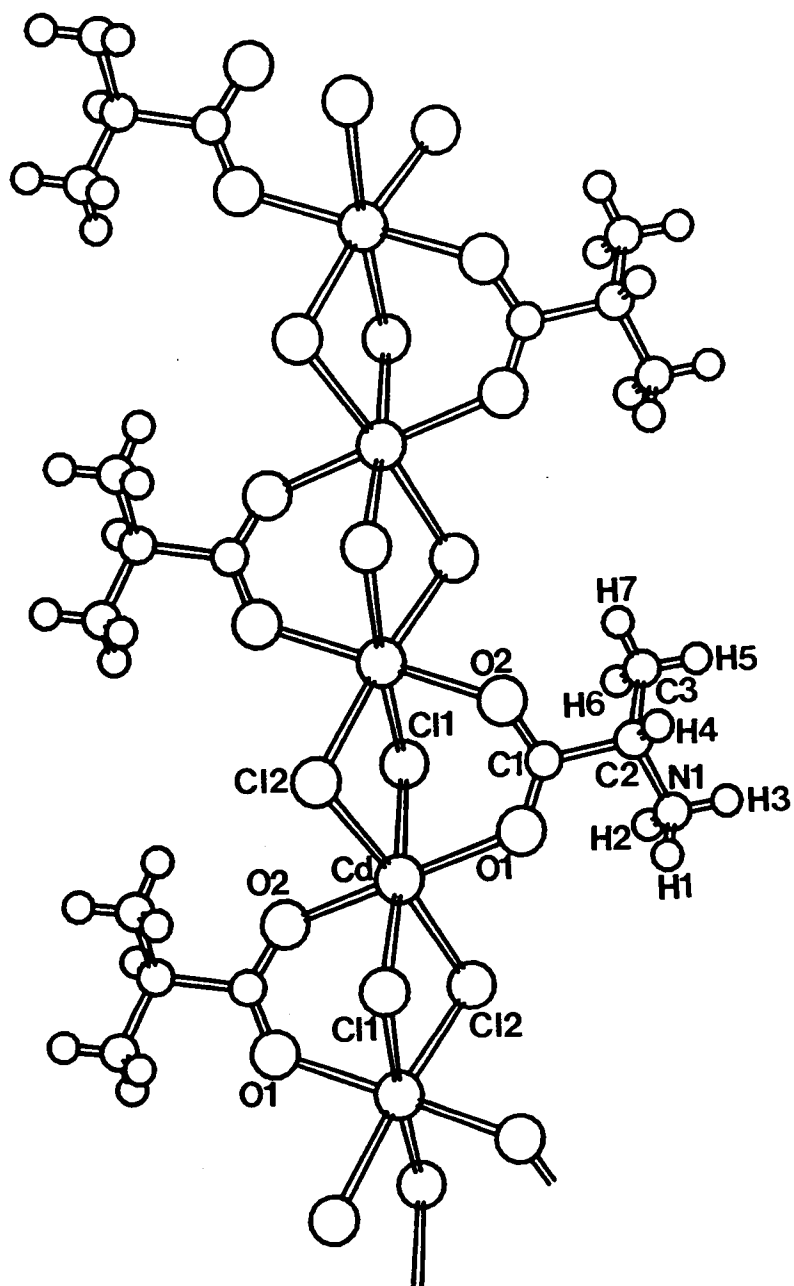
Figure. 5.1. Labeled sketch of the one-dimensional chain of edge-sharing $CdCl_2$ units bridged by $C_3H_7NO_2$ molecules.

is 145.7° which compares with the angle 114° for similar planes in the structure of CsNiCl$_3$.

The angle in the present chain structure is actually intermediate to those found in the face-sharing chain and the more common Cl-bridged strings depicted in Figure 5.2. In these chains the Cd atoms are bridged through Cl···Cl edges, and monodentate X ligands occupy *trans* vertices in the distorted octahedron about each Cd atom. Such structures have been reported for X = pyridine (2), urea (3), H$_2$O (4), cyandiamide (5), and imidazole (6).

A packing diagram is depicted in Figure 5.3, where adjacent chains are seen to be crystallographically related by the C$_2$ rotation axis. The interchain distances N···Cl1 = 3.224 Å and N···O2 = 2.83(1) Å as well as the intrachain distance N···O1 = 2.63(1) Å indicate the presence of hydrogen bonding.

Selected interatomic distances and angles are listed in Table 5.3. The average Cd-Cl distance, 2.61(1) Å, compares to similar distances of 2.60(1) Å and 2.65 Å in the compounds CdCl$_2$·4H$_2$O (4) and CdCl$_2$·2(pyridine) (2), respectively, and contrasts to the longer distances of 2.706(2) and 2.731(2) Å reported for CdCl$_2$·2(imidazole) (6). The average Cd-O distance, 2.33(4) Å, compares to the value 2.33 Å calculated from crystal radii (7) for a 6-coordinate Cd atom. Considerable deviations from the orthogonal angles of an octahedron are evident from consideration of Table 5.3; the largest excursion is represented by the angle of 82.9(2)° for Cl1-Cd-O1. The O1-Cd-O2 angle is distorted to 168.7° by

opposing rotations of the neighboring carboxyl groups approximately along the c

axis as seen in the packing diagram, Figure 5.2.
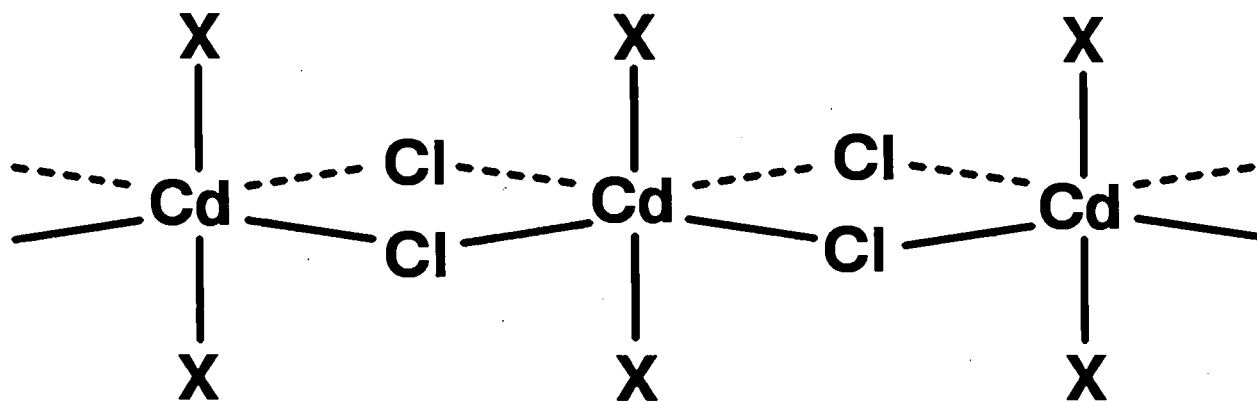
Figure 5.2. Typical face-sharing $[CdCl_2X]_n$ chain.

Table 5.3. Selected Interatomic Distances (Å) and Angles (°) for $CdCl_2C_3H_7NO_2$.

Cd -Cl1	2.621(3)	Cl1-Cd-Cl2	86.1(1)
-Cl1	2.614(3)		88.57(7)
-Cl2	2.603(3)		98.96(7)
-Cl2	2.600(3)		86.3(1)
-O1	2.295(6)	Cl1-Cd-O1	98.6(2)
-O2	2.357(7)		82.9(2)
		Cl1-Cd-O2	90.3(2)
			88.9(2)
		Cl2-Cd-O1	97.0(2)
			86.9(2)
		Cl2-Cd-O2	86.7(2)
			90.2(2)
		O1-Cd-O2	168.7(3)
C1 -O1	1.25(1)	O1-C1-O2	127.6(7)
-O2	1.27(1)	O1-C1-C2	118.2(7)
-C2	1.56(1)	O2-C1-C2	114.2(7)
C2 -N1	1.47(1)	C1-C2-C3	110.9(7)
-C3	1.54(1)	N1-C2-C1	108.0(7)
		N1-C2-C3	111.0(8)
O1 -O2	2.26(1)		
Cl1-Cl2	3.566(3)	Cd-Cl1-Cd	88.15(6)
Cl1-Cl2	3.646(3)	Cd-Cl2-Cd	88.83(7)
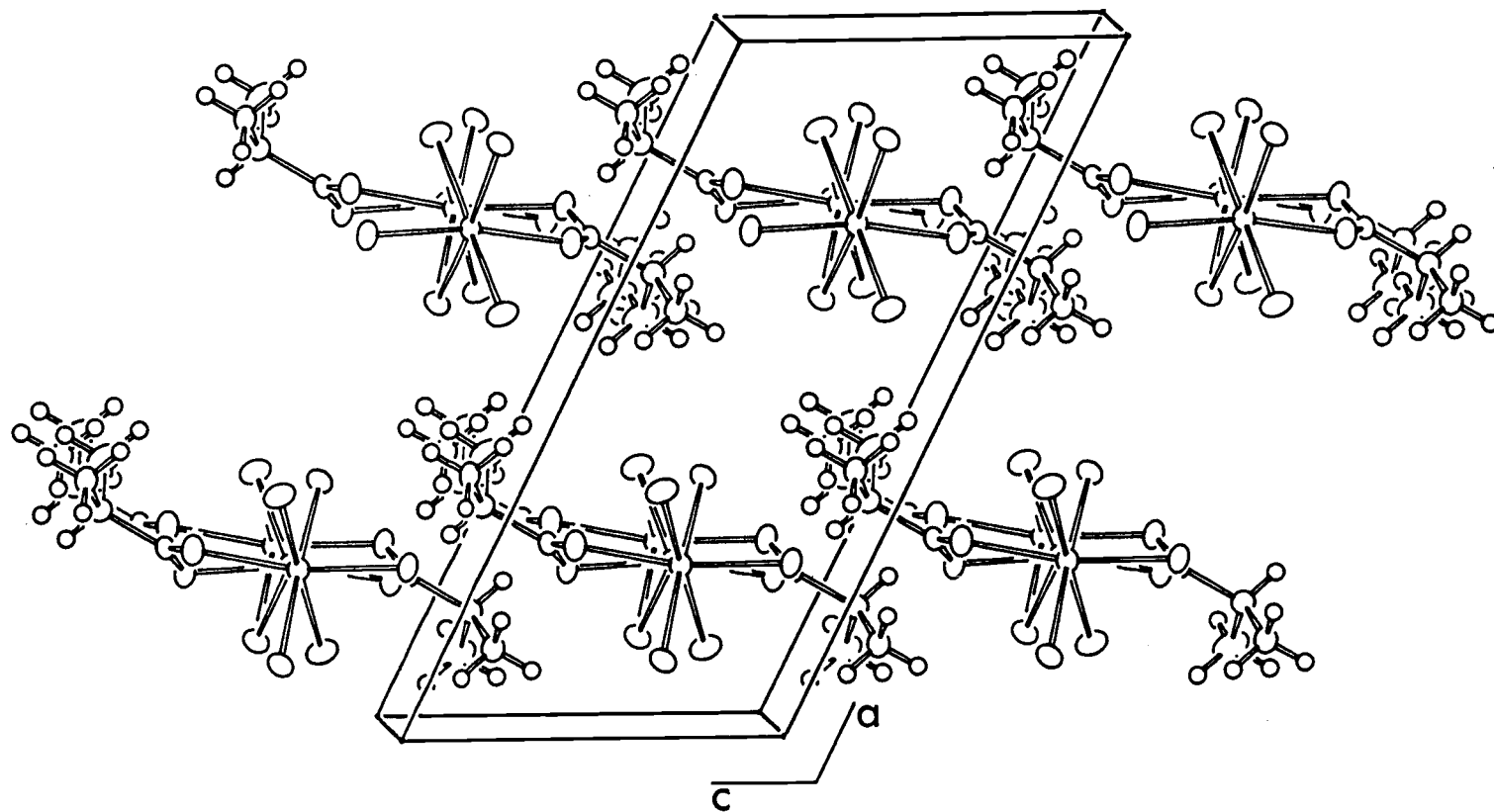
Figure 5.3. Packing diagram of $CdCl_2C_3H_7NO_2$ viewed along the [010] direction; the unit cell is outlined.

The distances and angles in the alanine ligand compare favorably to those of the crystallized molecule. Bridging of the Cd atoms by the carboxyl group affords an O1-C1-O2 angle of 127.6(7)$^\circ$ that is slightly wider than the 125.6° angle for O1-C1-O2 in an L-alanine molecule (8). As noted above, pairs of carboxyl groups in adjacent chains are related by a C_2 rotation. Because the plane normals of the groups are canted with respect to the rotation axis (*b*), an interplanar angle of 27.6° is observed.

Acknowledgments

References

1. G. N. Tiščenko, *Trudy Inst. Krist. Akad. Nauk* **11**, 93 (1955).

2. V. H. Paulus, *Z. Anorg. Allg. Chem.* **369**, 38 (1969).

3. M. Nardelli, L. Cavalca, and G. Fava, *Gazz. Chim. Ital.* **87**, 1232 (1957).

4. H. Leligny and J. C. Monier, *Acta Cryst.* *B***35**, 569 (1979).

5. A. C. Villa, L. Coghi, A. Mangio, M. Nardelli, and G. Pelizzi, *J. Cryst. Mol. Struct.* **1**, 291 (1971).

6. R. J. Flook, H. C. Freeman, F. Hug, and J. M. Rosalky, *Acta Cryst.* *B* **29**, 903 (1973).

7. R. D. Shannon, *Acta Cryst.* *A* **32**, 751 (1976).

8. H. J. Simpson, Jr. and R. E. Marsh, *Acta Cryst.* **20**, 550 (1966).

CHAPTER 6

THE LAYERED BORATE $SrBe_2(BO_3)_2$

Kathleen I. Schaffers and Douglas A. Keszler

Abstract

The compound $SrBe_2(BO_3)_2$ crystallizes in the monoclinic space group

$P2_1/n$ in a cell of dimensions $a = 9.247(1)$ Å, $b = 4.492(2)$ Å, $c = 11.561(1)$ Å, and

$\beta = 112.17(1)°$ with $Z = 4$. Least squares refinement affords the final residuals

$R = 0.034$ and $R_w = 0.045$. The structure consists of layers of composition

$[Be_2(BO_3)_2]^{2-}$ that are interleaved by Sr atoms. Each layer contains two

crystallographically inequivalent Be and B atoms; the Be atoms occupy distorted

O tetrahedra while the B atoms occupy distorted triangular planar environments.

Two Be atoms of one type share two O atoms to form a dimer of edge-shared

tetrahedra. The Sr atom occupies a distorted monocapped 8-coordinate site.

Introduction

As part of our continuing studies of structural and optical characteristics of new borates (1-3) we have been involved in the synthesis of compounds having the formula $XY_2(BO_3)_2$ where X and Y are cations of disparate sizes with formal dipositive charges (4, 5). We have been particularly interested in new compounds with X or Y = Be since such materials are likely to exhibit structures and properties similar to those observed for polyborates containing an admixture of 3- and 4-coordinate B atoms.

Little information on anhydrous beryllium borates has been reported; only the borate fluorides Be_2BO_3F (6) and $KBe_2BO_3F_2$ (7) have been described. In each of these compounds the larger size of the Be atom relative to that of the B atom renders a selective occupation of tetrahedral sites by Be atoms and triangular sites by B atoms even though triangular coordination of Be atoms is known to occur (8). We observe a similar distribution of the Be and B atoms in the new compound $SrBe_2(BO_3)_2$ which we describe here.

Experimental

Single crystals of the compound $SrBe_2(BO_3)_2$ were grown from a melt of composition 33 mol% SrO, 33 mol% BeO, and 33 mol% B_2O_3 that was cooled in a Pt crucible from $1100°C$ to $900°C$ at $8°C/hr$. Clear, colorless crystals were physically separated from the solidified melt.

A crystal of approximate dimensions 0.2 x 0.2 x 0.1 mm was selected and mounted on a glass fiber with epoxy for X-ray structure determination. Diffraction data were collected with a Rigaku AFC6R diffractometer equipped with Mo $K\alpha$ radiation. Unit-cell parameters were determined by automatic centering and least-squares refinement of 20 reflections in the range $30 < 2\theta < 36°$. Intensity data were collected with ω-2θ scans and a scanning speed of $16°$/min. in ω. Three standard reflections, monitored every 200 reflections, exhibited no significant fluctuations throughout the collection. A total of 1651 reflections were measured over the range $2 \le 2\theta \le 62°$, affording 1285 unique reflections with $F_o2 \ge 3\sigma(F_o^2)$. The systematic extinctions, h0l, h + l = 2n + 1 and 0k0, k = 2n + 1, are consistent with the space group $P2_1/n$ (#14). Computer programs from the TEXSAN crystallographic software package (9) were used to determine the structure. The position of the Sr atom was located by application of the direct methods program SHELXS (10). The positions of the remaining atoms were determined by examining subsequent difference electron density maps. Following refinement of the model with isotropic thermal parameters, the data were

corrected for absorption with the program DIFABS (11). Final least-squares refinement on F with those 1222 reflections having $F_o^2 \geq 3\sigma(F_o^2)$ and anisotropic thermal displacement coefficients on each atom affords the final residuals R = 0.034 and R_w = 0.045. Analysis of the final difference electron density map reveals a maximum peak of density 1.5 e/Å^3 which corresponds to 0.79% of a Sr atom. Crystallographic data and final atomic parameters are listed in Tables 6.1 and 6.2, respectively.

Table 6.1. Crystallographic Data for $SrBe_2(BO_3)_2$.

Formula Weight, amu	223.26
Crystal System	Monoclinic
Space Group	$P2_1/n$ (#14)
a, Å	9.247(1)
b, Å	4.492(2)
c, Å	11.561(1)
β, deg.	112.17(1)
V, Å^3	444.7(2)
Z	4
D_{calc}, g cm^{-3}	3.33
F(000)	416
Diffractometer	Rigaku AFC6R
Radiation	Mo Kα (λ = 0.71069) Graphite-monochromated
Data Collection	$\pm$h, k, l
No. Observations ($F_o^2 > 3\sigma(F_o^2)$)	1222
R	0.034
R_w	0.045
Maximum Shift in Final Cycle	0.01

Table 6.2. Atomic Coordinates and Thermal Displacement

Coefficients for $SrBe_2(BO_3)_2$.

	x	y	z	$B_{eq}(\text{Å}^2)$[a]
Sr	0.42743(4)	0.02664(8)	0.65652(3)	0.39(1)
Be(1)	0.6266(6)	-0.099(1)	0.0490(5)	0.5(2)
Be(2)	0.2164(6)	-0.062(1)	0.3077(5)	0.4(1)
B(1)	0.4501(5)	-0.437(1)	0.8549(4)	0.3(1)
B(2)	0.2948(5)	0.409(1)	0.4246(4)	0.4(1)
O(1)	0.2848(3)	-0.4868(6)	0.5315(3)	0.48(9)
O(2)	0.3442(3)	0.1210(7)	0.4217(3)	0.40(9)
O(3)	0.5401(3)	-0.5118(7)	0.7886(3)	0.6(1)
O(4)	0.4728(3)	-0.1635(7)	0.9127(3)	0.6(1)
O(5)	0.1635(3)	-0.1286(7)	0.6418(3)	0.7(1)
O(6)	0.7576(3)	-0.0814(7)	0.8177(3)	0.42(9)

$$^{a}B_{eq} = (\frac{8\pi^2}{3}) \sum_i \sum_j U_{ij} a_i^* a_j^* a_i \cdot a_j$$

Results and Discussion

A labeled sketch of the contents of the unit cell is provided in Figure 6.1. The nature of the structure is best appreciated by inspection of the perspective view along the b axis given in Figure 6.2. Layers of composition $[Be_2(BO_3)_2]^{2-}$ separated by planes of Sr atoms may be identified. A drawing of a single beryllium borate layer as viewed orthogonal to the b axis is given in Figure 6.3. Each layer contains two crystallographically inequivalent Be atoms and two inequivalent B atoms. The Be atoms occupy distorted tetrahedral sites and the B atoms occupy triangular sites. The BeO_4 and BO_3 groups are connected one to the other by sharing O vertices. The tetrahedra occupied by atom Be(2) share vertices to form chains that extend along the *b* axis. This contrasts to the tetrahedra occupied by atom Be(1) that are present as isolated pairs sharing an edge.

Selected interatomic distances and angles are listed in Table 6.3. The mean Be-O distance, 1.63(4) Å, compares to that, 1.61 Å, computed for a 4-coordinate Be atom from crystal radii (12) and the mean B-O distance, 1.37(1) Å, is also similar to that, 1.36 Å, computed for a 3-coordinate B atom, suggesting there is little disorder among the Be and B sites. The sensitivity of the intensity data to the distribution of the Be and B atoms was examined in two ways. The refinement was repeated with the Be atoms on B sites and B atoms on Be sites. This procedure afforded larger residuals and equivalent temperature factors for the Be atoms that were not positive-definite and increased by a factor of three for the B
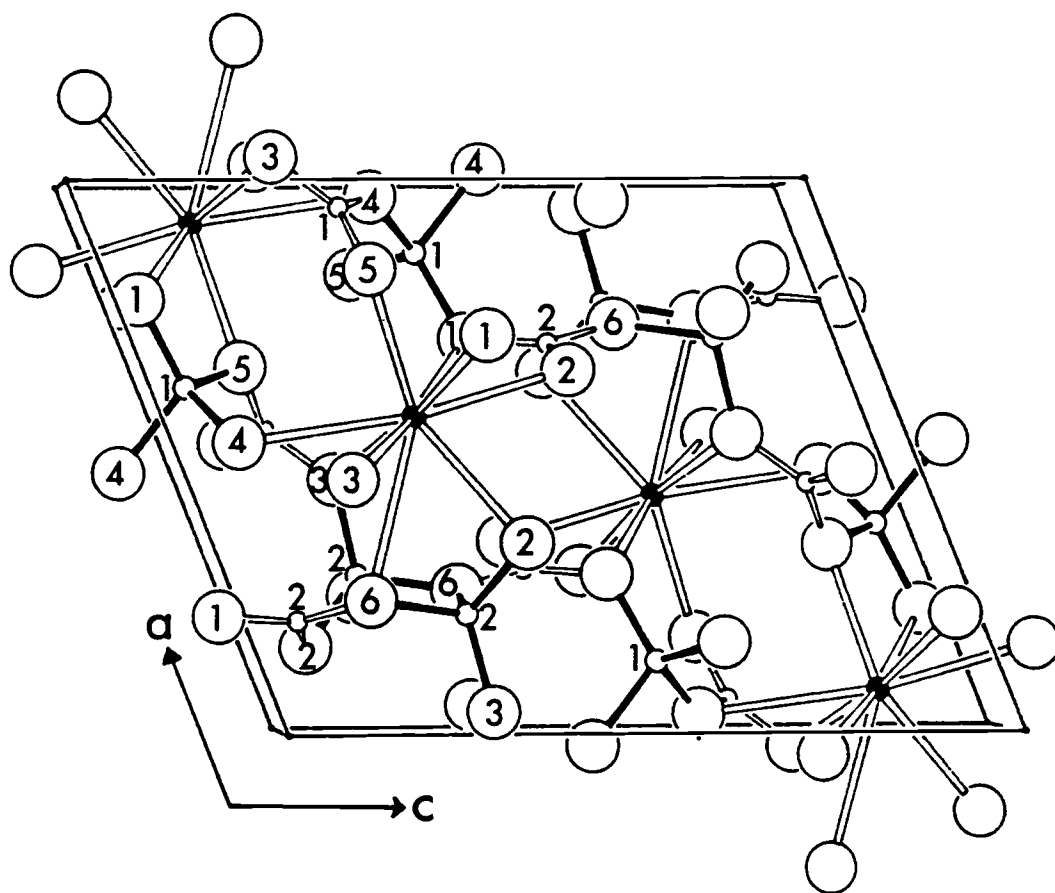
Figure 6.1. Sketch of a labeled unit cell of the compound $SrBe_2(BO_3)_2$ viewed

along the *b* axis. Large open circles represent O atoms, small

filled circles represent Sr atoms, the open circles with open

bonds represent B atoms, open circles with filled bonds represent

Be atoms, here, and in ensuing figures.
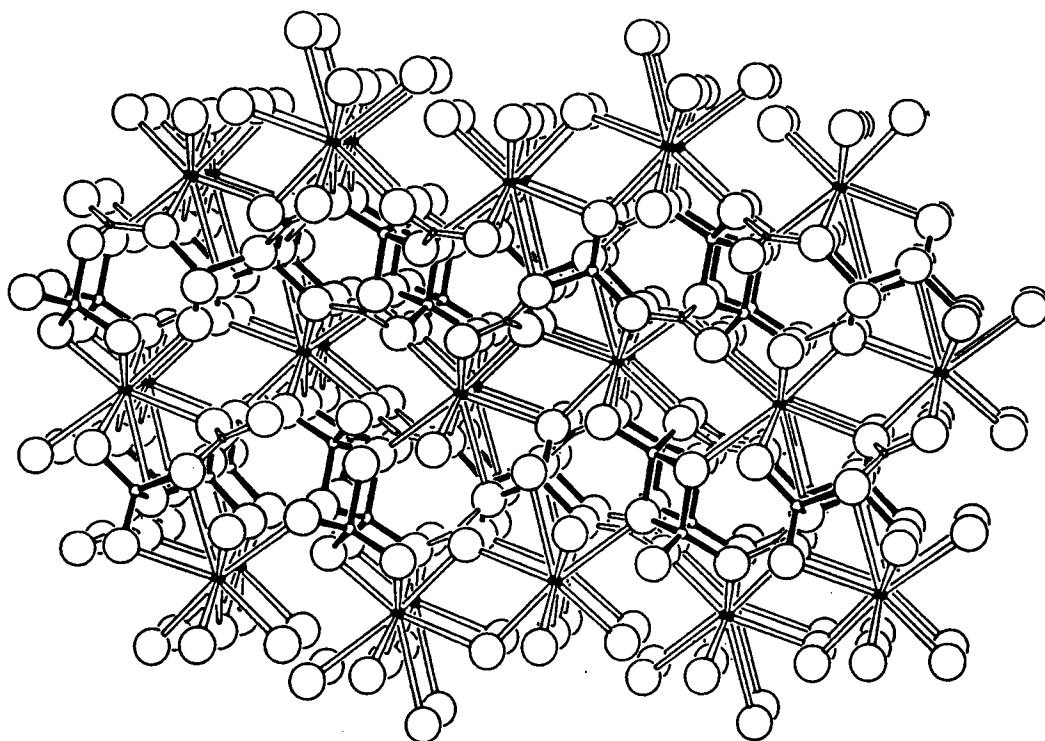
Figure 6.2. Perspective view of the structure of $SrBe_2(BO_3)_2$ along the b axis.
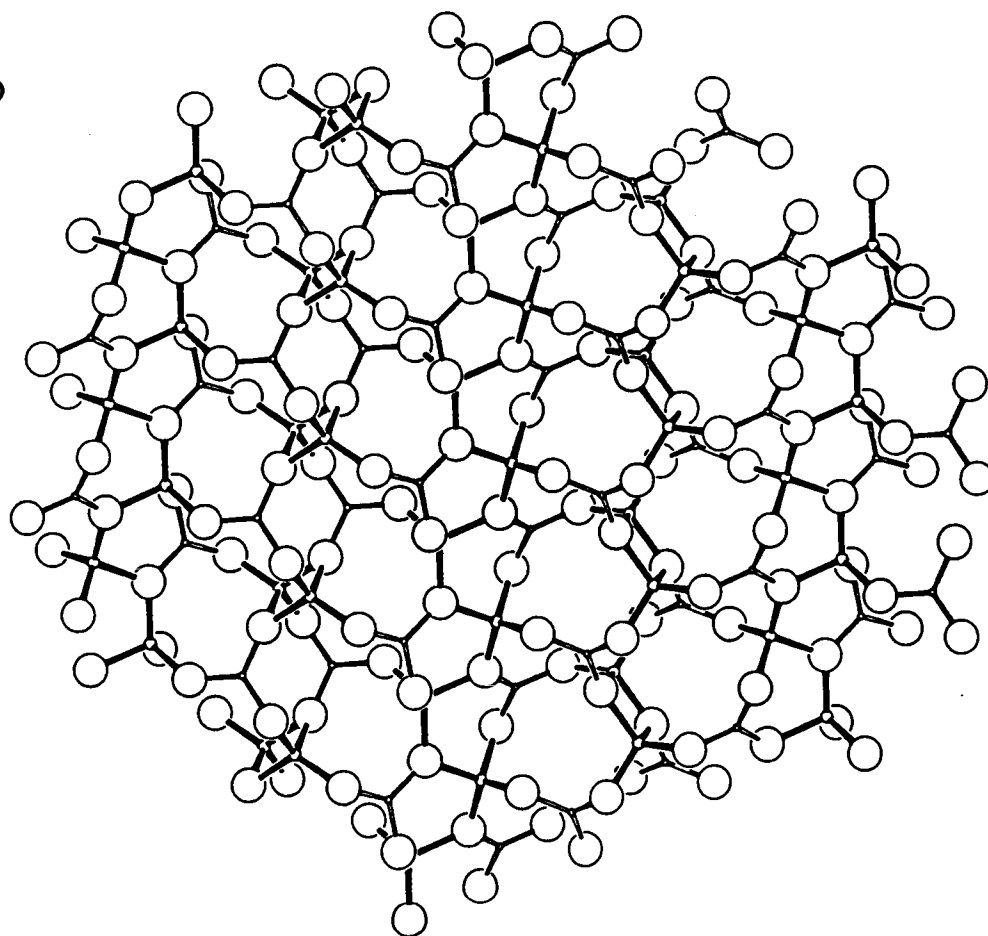
Figure 6.3. Sketch of a single compositional layer $[Be_2(BO_3)_2]^{2-}$ viewed orthogonal to the b axis.

Table 6.3. Selected Interatomic Distances (Å) and Angles (°) for $SrBe_2(BO_3)_2$.

Sr -O(1)	2.677(3)	O(1)-Sr-O(1)	110.9(1)
Sr -O(1)	2.776(3)	O(1)-Sr-O(2)	84.19(9)
Sr -O(2)	2.562(3)	O(1)-Sr-O(4)	98.13(9)
Sr -O(2)	2.676(3)	O(1)-Sr-O(5)	85.5(1)
Sr -O(3)	2.840(3)	O(2)-Sr-O(3)	78.12(9)
Sr -O(3)	2.552(3)	O(2)-Sr-O(4)	115.81(9)
Sr -O(4)	2.957(3)	O(2)-Sr-O(5)	94.6(1)
Sr -O(5)	2.482(3)	O(3)-Sr-O(4)	76.34(9)
Sr -O(6)	2.955(3)	O(3)-Sr-O(6)	70.42(9)
		O(4)-Sr-O(5)	75.61(9)
		O(4)-Sr-O(6)	66.35(8)
Be(1)-O(1)	1.597(6)	O(1)-Be(1)-O(4)	114.2(3)
Be(1)-O(4)	1.653(6)	O(1)-Be(1)-O(5)	107.4(4)
Be(1)-O(4)	1.702(6)	O(4)-Be(1)-O(4)	90.3(3)
Be(1)-O(5)	1.580(7)	O(4)-Be(1)-O(5)	111.7(3)
		O(4)-Be(1)-O(5)	112.8(4)
Be(2)-O(2)	1.623(6)	O(2)-Be(2)-O(3)	113.6(3)
Be(2)-O(3)	1.595(6)	O(2)-Be(2)-O(6)	111.0(3)
Be(2)-O(6)	1.683(6)	O(3)-Be(2)-O(6)	114.2(4)
Be(2)-O(6)	1.641(6)	O(3)-Be(2)-O(6)	105.8(3)
		O(6)-Be(2)-O(6)	109.2(3)

B(1)-O(3)	1.369(5)	O(3)-B(1)-O(4)	118.5(4)
B(1)-O(4)	1.378(5)	O(3)-B(1)-O(5)	119.8(4)
B(1)-O(5)	1.369(5)	O(4)-B(1)-O(5)	121.6(4)
B(2)-O(1)	1.359(5)	O(1)-B(2)-O(2)	119.0(4)
B(2)-O(2)	1.374(5)	O(1)-B(2)-O(6)	122.5(4)
B(2)-O(6)	1.388(5)	O(2)-B(2)-O(6)	118.5(4)

atoms. A partial disorder was imposed by altering the occupancy factors for the B and Be atoms to correspond to a 20% occupancy of B sites by Be atoms and Be sites by B atoms. The occupancy factor of each atom was then refined. All factors refined to within 5% of unity and their magnitudes were contraposed to values expected for any model of disorder among the Be and B sites.

The Be(1) atoms related by a center of symmetry across the shared edge O(4)···O(4) of the tetrahedra are separated by 2.35(1) Å, Figure 6.4. The angle between the plane of atoms Be(1), O(4), and O(4) and the plane of atoms Be(1), O(1), and O(5) is 87.7°. The 4-membered ring Be(1)-O(4)- Be(1)-O(4) exhibits minimal deviations from a square as shown by consideration of the angles O(4)-Be(1)-O(4), 90.9(3)°, and Be(1)-O(4)- Be(1), 89.1(3)°. A dimer of tetrahedra formed by sharing an edge is relatively rare in oxides, although more common in chalcogenides and halides; a similar unit Be_2O_6 has been identified in the mineral epididymite, $Na_2Be_2Si_6O_{15}·H_2O$ (13). The metrical data above may be compared to the 4-membered Si-O-Si-O ring in the compound tetramesityl-cyclodisoloxane (14). The Si-O bond lengths are 1.66 and 1.72 Å and
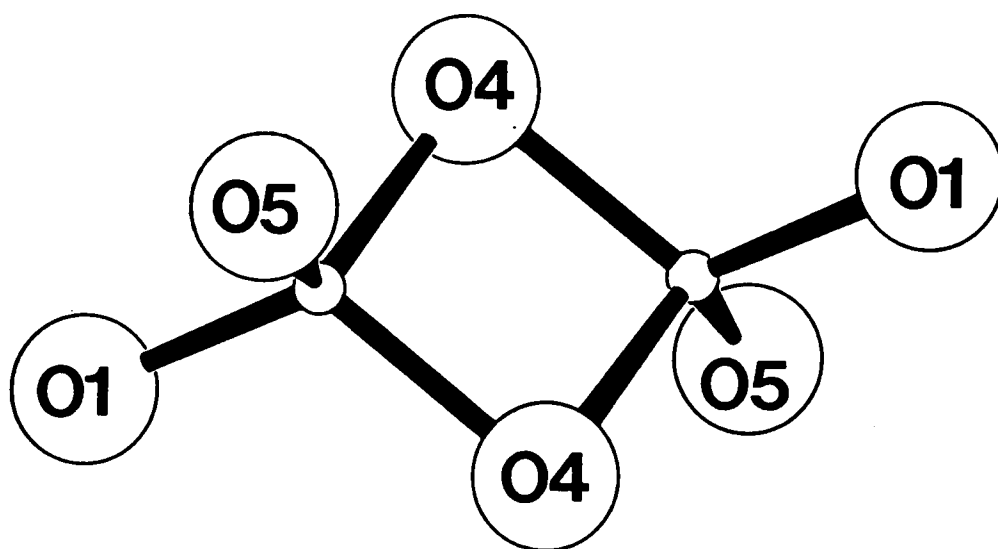
Figure 6.4. Sketch of the Be_2O_6 dimer.

the Si···Si separation is 2.31 Å; evidence for greater deviation from a square is provided by the O-Si-O angle of 94°. The tetrahedron about atom Be(2) is only slightly distorted (cf. Table 6.3).

The Sr atom occupies a distorted monocapped 8-coordinate environment, Figure 6.5, between layers. The Sr-O distances range from 2.552(3) to 2.957(3) Å with a mean of 2.72(6) Å. These distances compare to those observed for the 9-coordinate Sr atom in the compounds $Sr_3Sc(BO_3)_3$, 2.500(2) - 2.857(2)Å (1), and $SrNaBO_3$, 2.539(7) - 2.93(2)Å (15).

Despite the existence of an extensive structural chemistry of simple anhydrous borates as well as polyborates exhibiting an admixture of 3- and 4-coordinate B atoms, only a limited number of chains, layers, and networks formed from combinations of tetrahedra and triangles selectively centered by atoms of different types are known. Examples include the aluminum orthoborates $Sr_2Al_2B_2O_8$ (16), $Li_6Al(BO_3)_3$ (17), $CaAlBO_4$ (18), and $CaAl_2B_2O_7$ (19); the zinc borates $Zn_3(BO_3)_2$ (20), $LiZnBO_3$ (21), $KZn_4(BO_3)_3$ (22), and $BaZn_2(BO_3)_2$ (23); and the beryllium borates mentioned here. Given the expectation and observation that Be atoms prefer in oxides tetrahedral sites in the presence of B atoms because of their larger size and greater electropositive nature, it is likely that many additional tetrahedral-triangular networks containing these atoms will be synthesized in the future.
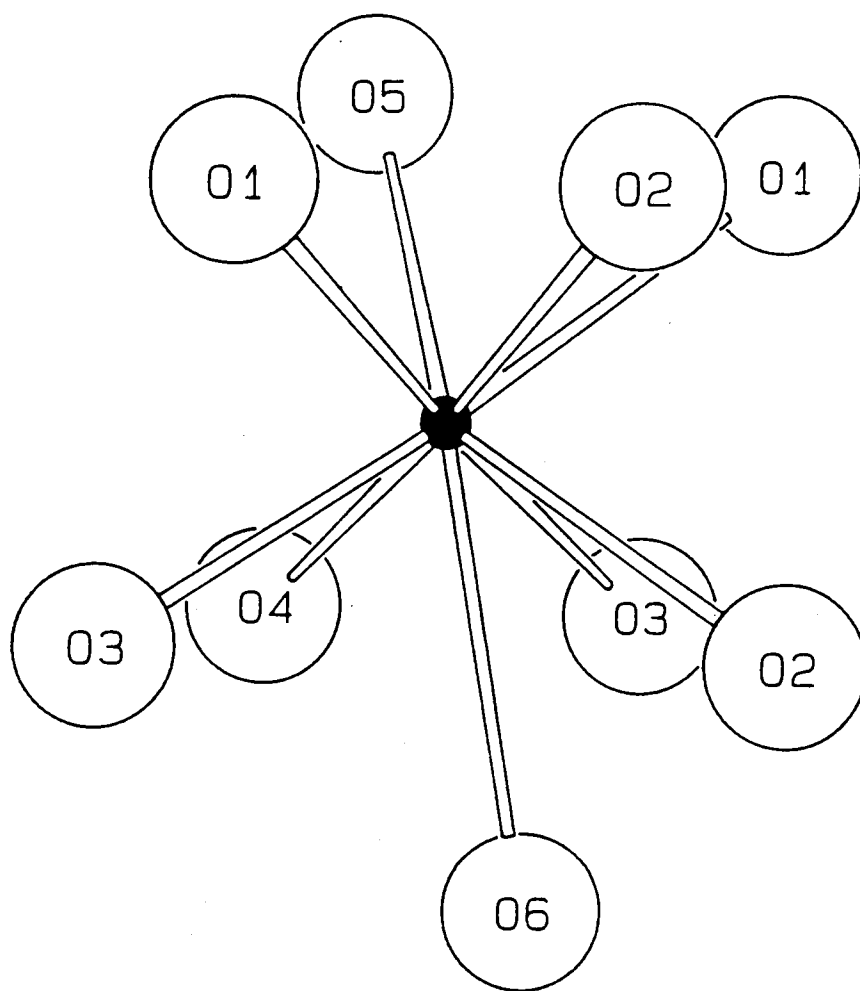
Figure 6.5. Sketch of the Sr atom that occupies a distorted 9-coordinate site.

Acknowledgments

References

1. P. D. Thompson and D. A. Keszler, *Chemistry of Materials* **1**, 292 (1989).

2. H. Sun, Ph.D. Dissertation, Oregon State University (1989).

3. R. W. Smith, Ph.D. Dissertation, Oregon State University (1989).

4. R. W. Smith and D. A. Keszler, *J. Solid State Chem.* **81**, 305 (1989).

5. R. W. Smith and D. A. Keszler, *Acta Crystallogr., Sect. C*, in press.

6. I. A. Bajdina, V. V. Bakakin, N. V. Podberizskaja, B. I. Alekseev, L. R. Bacanova, and V. S. Pavlijucenko, *Z. Strukt. Khim.* **19**, 125 (1978).

7. L. P. Solov'eva and V. V. Bakakin, *Kristallografija* **15**, 922 (1970).

8. L. A. Harris and H. L. Yakel, *Acta Crystallogr.* **22**, 354 (1967).

9. Molecular Structure Corporation, TEXSAN, Structure Analysis Package, MSC (3200A Research Forest Drive, The Woodlands, TX 77381, USA).

10. G. M. Sheldrick, "Crystallographic Computing 3," Eds. G. M. Sheldrick, C. Krüger, and R. Goddard, pp. 175-189, Oxford University Press, Oxford (1985).

11. N. Walker and D. Stuart, *Acta Crystallogr., Sect. A* **24**, 214 (1968).

12. R. D. Shannon and C. T. Prewitt, *Acta Crystallogr., Sect. B* **25**, 925 (1969).

13. J. H. Fang, P. D. Robinson, and Y. Ohya, *Amer. Miner.* **57**, 1345 (1972).

14. M. J. Fink, K. J. Haller, R. West, and J. Michel, *J. Am. Chem. Soc.* **106**, 822 (1984); Also, see M. O'Keeffe and G. V. Gibbs, *J. Phys. Chem.* **89**, 4574 (1985).

15. H. Sun and D. A. Keszler, unpublished results.

16. T. Nagai and M. Ihara, *Yogyo-Kyokai-Shi* **80**[11], 432 (1972).

17. G. K. Abdullaev and K. S. Mamedov, *Sov. Phys. Crystallogr.* **19**, 98 (1974).

18. W. Schuckmann, *Neues Jb. Miner. Mh.* **80** (1968).

19. U. L. Shäfer and H.-J. Kuzel, *Neues Jb. Miner. Mh.* **4 & 5**, 131 (1967).

20. W. H. Baur and E. Tillmanns, *Z. Kristallogr.* **131**, 213 (1970).

21. O. S. Bondareva, M. A. Simonov, Yu. K. Egorov-Tismenko, and N. V. Belov, *Sov. Phys. Crystallogr.* **23**, 269 (1978).

22. R. W. Smith, J. L. Luce, and D. A. Keszler, unpublished results.

23. R. W. Smith and D. A. Keszler, unpublished results.

CHAPTER 7

THE ALKALINE EARTH BERYLLIUM BORATE CaBeB$_2$O$_5$

Kathleen I. Schaffers and Douglas A. Keszler[*]

Abstract

Calcium Beryllium Diborate, $CaBeB_2O_5$, M_r= 150.71, monoclinic, $P2_1/n$, $a=$ 5.167(2), $b=$ 3.756(2), $c=$ 17.160(2) Å, $\beta=$ 98.12(2)°, V= 329.7(2) Å^3, Z= 4, $D_x=$ 3.036 g cm^{-3}, Mo Kα, $\lambda=$ 0.71069 Å, $\mu=$ 17.38 cm^{-1}, F(000)= 296, T= 298 K, R= 0.039 for 508 reflections having $F_o^2 \geq 3\sigma(F_o^2)$. The structure is constructed from two intermingled networks - a CaO_9 polyhedral system and a beryllium-borate complex constructed from four-coordinate Be and three- and four-coordinate B atoms. The extended beryllium-borate complex results from the unique condensation of six-membered rings containing the triangular and distorted tetrahedral beryllate and borate groups.

Introduction

The simple pyroborate group B_2O_5 - two triangular planar BO_3 units sharing an O atom - has been found to exist in the alkaline-earth materials $AE_2B_2O_5$ where AE= Mg, Ca, or Sr (1-3) and in the mixed phase $CaMgB_2O_5$ (4). No data are available in the literature on a simple pyroborate with AE= Be.

In this contribution we describe the structure of the mixed alkaline-earth compound $CaBeB_2O_5$. Although the formula indicates the structure could contain a pyroborate group, we have found instead an admixture of three- and four-coordinate B atoms in a complex beryllium borate network. So, a unique atomic arrangement is provided for addition to the small muster of known anhydrous beryllium borates - $SrBe_2(BO_3)_2$ (5), $BaBe_2(BO_3)_2$ (6), Be_2BO_3F (7), and $KBe_2BO_3F_2$ (8).

Experimental

Crystals of $CaBeB_2O_5$ were grown in a Pt crucible from a melt consisting of 26.6 mol% CaB_2O_4 prepared from $Ca(NO_3)_2 \cdot 4H_2O$ (ALFA, reagent grade) and B_2O_3 (ALFA, 99.98%), 43.2 mol% BeO made by heating BeF_2 (CERAC, 99.5%) in air, and 30.2 mol% $LiBO_2$ (AESAR, 99.9%). The melt was cooled from 1198 K to 698 K at 6 K/h. The crystals were washed in hot distilled water to remove excess flux. A clear, block-shaped crystal of approximate dimensions 0.25(2) x 0.22(2) x 0.20(2) mm was mounted on a glass fiber with epoxy for X-ray structure analysis. Data were collected by using a Rigaku AFC6R single-crystal diffractometer and Mo Kα radiation (λ = 0.71069 Å). Sixteen automatically-centered peaks in the range $30 \leq 2\theta \leq 36°$ were used for refinement of unit cell parameters. The ω scan technique was used to collect a total of 762 data to sin θ/λ = 1.08 Å^{-1} with a scan speed of 16.0°/min in ω and a scan width of (4.50 + 0.30 tan θ)°; $0 \leq h \leq 6$, $0 \leq k \leq 4$, and $-20 \leq l \leq 20$. From the 683 unique reflections measured, 508 reflections had $F_o^2 \geq 3\sigma(F_o^2)$. Three standard reflections were monitored throughout the data collection and an average fluctuation of 2.0% in intensity was detected.

The *TEXSAN* crystallographic software package (9) was used to solve the crystal structure. The position of the Ca atom was determined by using the direct methods program *SHELXS* (10) and the atomic positions of the remaining atoms were deduced by subsequent examination of difference electron density maps. After isotropic refinement, the data were averaged (R_{int} = 0.053) and corrected

for absorption (transmission coefficients = 0.88-1.09) with the computer program

DIFABS (11). Final least-squares refinement on F_o for those 507 reflections

having $F_o{}^2 \geq 3\sigma(F_o{}^2)$ and anisotropic displacement coefficients on each atom,

resulting in 82 variables, afforded the final residuals R= 0.039 and *w*R= 0.063

where the function $\Sigma w(|F_o|-|F_c|)^2$ is minimized with weights derived from

$w=1/\sigma^2(F_o)$. Atomic scattering factors are from *International Tables for X-ray*

Crystallography (12). S= 1.69, Δ/σ= 0.01, and the maximum and minimum peaks

in the final difference electron density map correspond to 0.92% and 0.82% of a

Ca atom, respectively. Atomic coordinates and isotropic thermal parameters are

listed in Table 7.1.

Table 7.1. Atomic Coordinates and Isotropic Thermal Parameters for $CaBeB_2O_5$.

	x	y	z	B_{eq}
Ca	0.7915(1)	0.6212(2)	0.07348(5)	1.87(5)
Be	0.604(1)	0.238(2)	0.2122(3)	1.5(2)
B1	0.300(1)	0.974(1)	0.0963(3)	1.6(2)
B2	1.1122(9)	0.252(1)	0.2119(3)	1.7(2)
O1	0.3561(5)	0.479(1)	0.2236(2)	1.7(1)
O2	1.0854(5)	0.0934(8)	0.1302(2)	1.8(1)
O3	0.8679(5)	0.457(1)	0.2178(2)	1.8(1)
O4	0.5484(6)	0.0793(8)	0.1265(2)	1.8(1)
O5	0.2560(6)	0.763(1)	0.0321(2)	2.4(1)

$$B_{eq} - (\frac{8\pi^2}{3})\sum_i \sum_j U_{ij} a_i^* a_j^* a_i \cdot a_j$$

Discussion

A drawing of the unit cell of $CaBeB_2O_5$ is given in Figure 7.1. Inspection of the diagram reveals that the Ca atom is bound by nine, the Be atom by four, the B1 atom by three, and the B2 atom by four O atoms. A perspective view indicating the nature of the structure is presented in Figure 7.2. Two commingled polyhedral networks extend in the a,b plane. One of these is a Ca double layer formed from the vertex-, edge-, and face-sharing of the CaO_9 polyhedra. The other is represented by a double layer of vertex-sharing BO_4 and BeO_4 tetrahedra that is capped on opposite surfaces by triangular BO_3 groups.

By considering the numbering scheme in Figure 7.2 the CaO_9 polyhedral connections can be established. The polyhedra share faces comprised of atoms O2, O4, and O5a to give extension along the b axis and vertices O5b to give extension along the a axis. The double layer is formed by edge sharing through atoms O5a and O5b.

The characteristics of the extended beryllium borate complex are best appreciated by considering Figure 7.2 and the representation in Figure 7.3. The Be-centered distorted tetrahedra share vertices to form chains extending along the b axis. In like manner, the B2-centered tetrahedra form similar chains that also extend along the same axis. These chains are alternately conjoined along the a axis by sharing vertices O1 and O3. Apices of neighboring Be and B-centered tetrahedra are also bridged along this axis by the triangular $B(1)O_3$ group. With
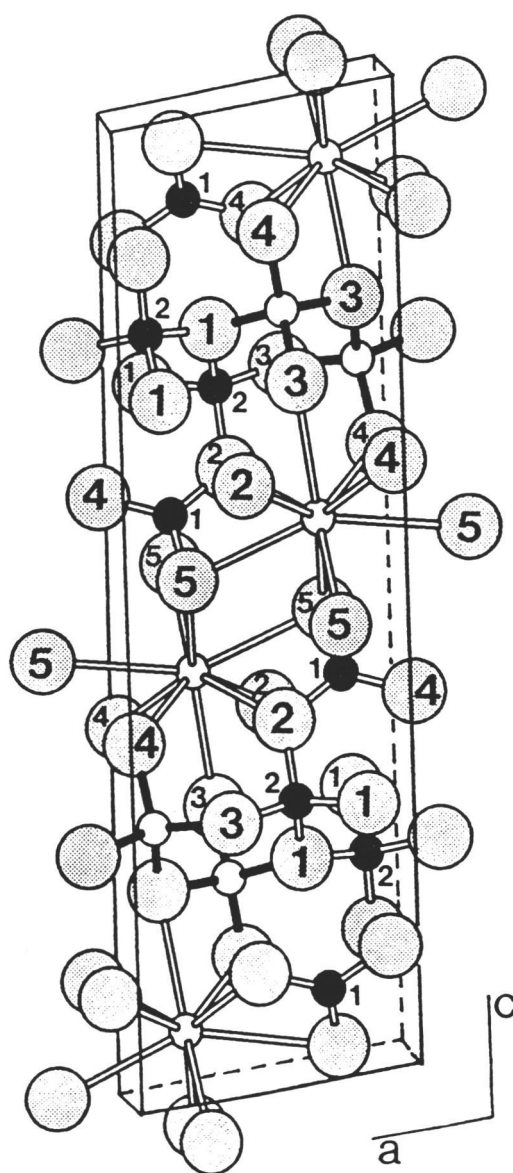
Figure 7.1. Sketch of the unit cell of $CaBeB_2O_5$ viewed down the b axis where the small open circles with open bonds represent Ca atoms, the small open circles with shaded bonds Be atoms, the small shaded circles with open bonds B atoms, and the large shaded circles O atoms, here, and in Figures 7.2 & 7.3.
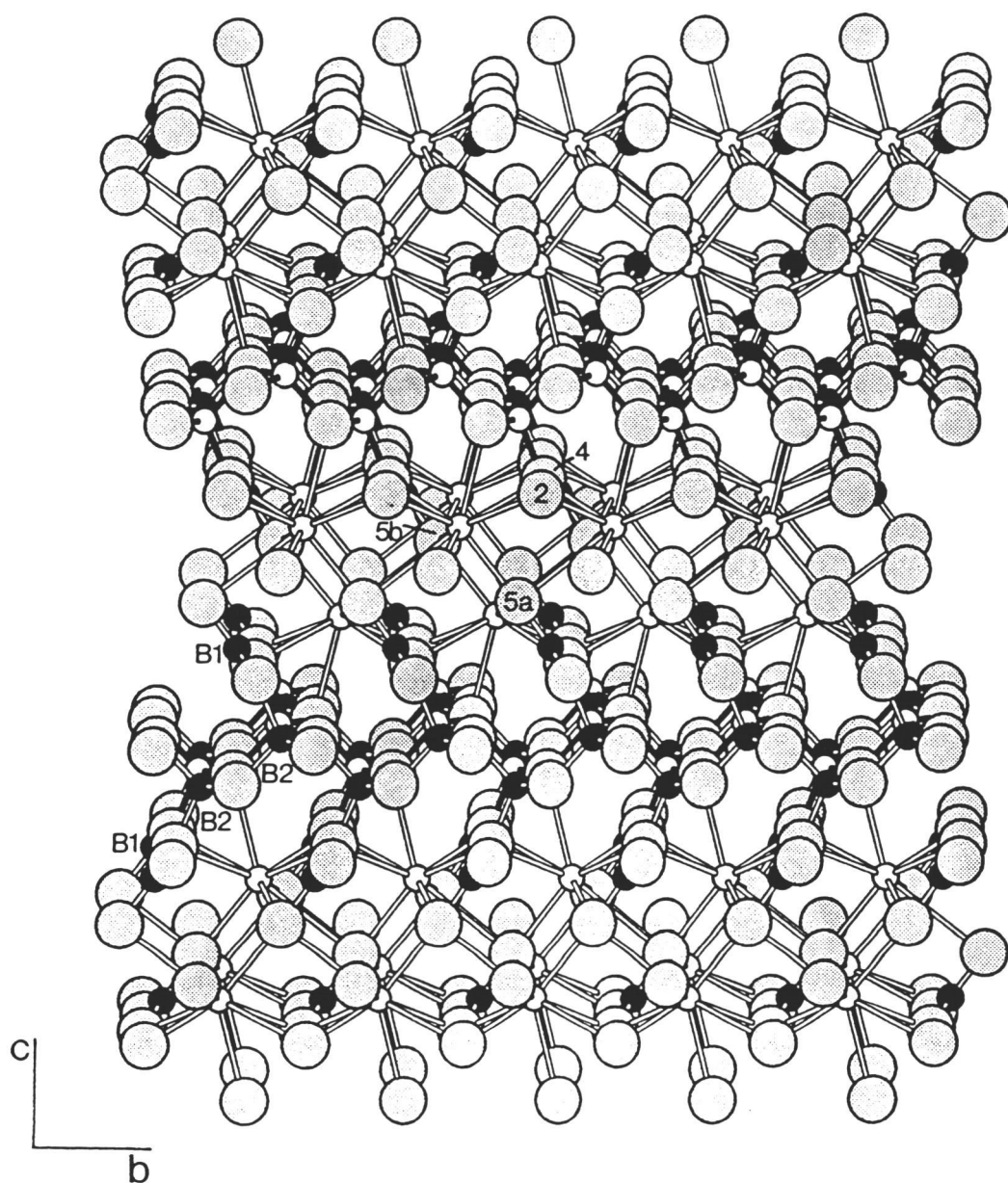
Figure 7.2. Perspective view down the *a* axis of the interpenetrating CaO_9
polyhedral framework and beryllium-borate framework of $CaBeB_2O_5$.
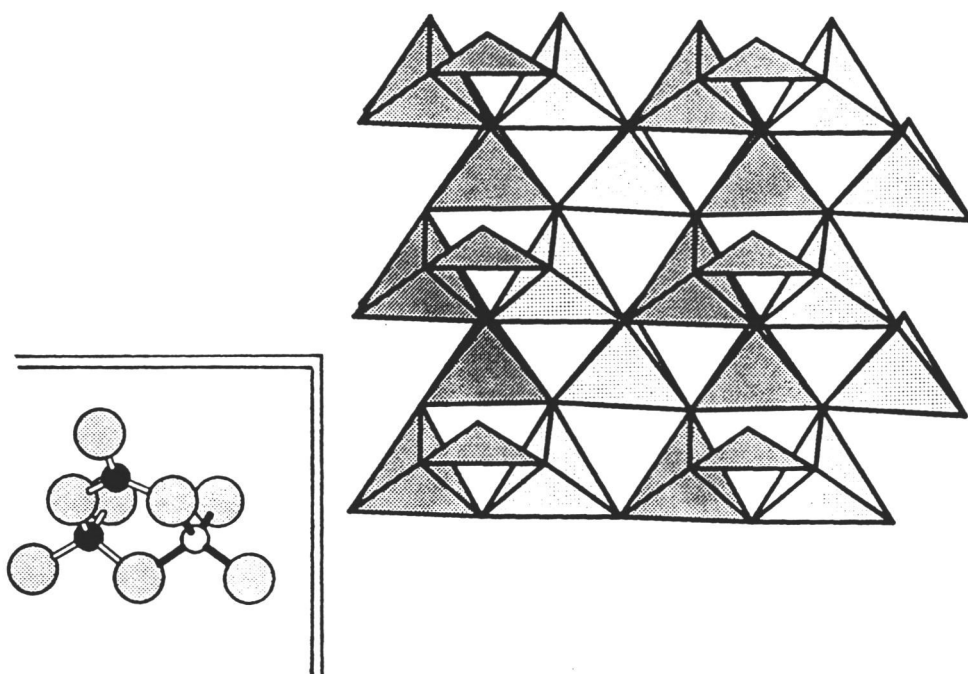
Figure 7.3. A polyhedral sketch of the two-dimensional connectivity of the BeO_4 and BO_4 tetrahedra and BO_3 triangles. Inset - BeB_2O_8 ring.

this connection, the fundamental six-membered ring BeB_2O_8 (*cf.* inset Figure 7.3) is readily identified. The two-dimensional beryllium borate matrix results from fusing these rings through the O atoms of the tetrahedral B and Be sites. The corresponding homoatomic ring B_3O_8 ($1\Delta + 2T$) [Δ= triangular coordination, T= tetrahedral coordination of B1] is rather uncommon in borate systems, but it has been observed in the materials BaB_4O_7 (13), $LaMgB_5O_{10}$ (14), and $Ba_2LiB_5O_{10}$ (15), and the heteroatomic ring BZn_2O_8 ($1\Delta + 2T$) has been identified in the compound $BaZn_2(BO_3)_2$ (16). In each of these phases, however, said rings are interconnected by other types of rings or borate groups. Insofar as we know, the structure of the title compound is the first example of an extended system formed from the exclusive condensation of the $1\Delta + 2T$ ring.

Selected interatomic distances and angles are listed in Table 7.2. The average Ca-O distance is 2.6(2) Å which can be compared to Ca-O distances of 2.5(1) Å for 6-coordinate Ca in $CaCO_3$ (17), 2.5(2) Å for 8-coordinate Ca in $Ca_3(BO_3)_2$ (18), 2.5(2) Å for 9-coordinate Ca in CaB_4O_7 (19), and 2.56 Å calculated from Shannon radii (20).

The average Be-O length of 1.59(1) Å compares to 1.63(4) Å in $SrBe_2(BO_3)_2$, 1.63(4) Å in $BaBe_2(BO_3)_2$, and 1.65 Å calculated from crystal radii. The range of O-Be-O angles from 105.9(3) to 116.0(4)° demonstrate the deviations from tetrahedral values.

Atom B1 is coordinated to three O atoms - O2, O4, and O5 - at distances of 1.395(6), 1.374(6), and 1.352(7) Å, respectively. These lengths are typical when

compared to average B-O bond lengths for BO_3 triangles in $Sr_2Cu(BO_3)_2$ (21), 1.38(2) Å; $Sr_5(BO_3)Cl$ (22), 1.37(3) Å; and $Sr_3Sc(BO_3)_3$ (23), 1.38(1) Å. The triangles reside in layers orthogonal to (001), Figure 6.2, sharing edges with the CaO_9 polyhedra and vertices with the CaO_9, BeO_4, and $B2O_4$ polyhedra. Atom B2 is 4-coordinate to atoms O1 x2, O2, and O3 with an average length of 1.505(8) Å that compares to 1.49(4) Å for CaB_4O_7 (24) and 1.49 Å calculated from crystal radii and a 4-coordinate B atom.

The O atoms occupy 3-, 4-, and 5-coordinate sites where O1 is 3-coordinate; O2, O3, and O4 are 4-coordinate; and O(5) is 5-coordinate. The connectivity may be discerned by considering Table 7.2 and the various cations bound to each O atom.

Table 7.2. Selected interatomic distances (Å) and angles (°) for CaBeB$_2$O$_5$.

Ca -O2	2.601(3)	O2-Ca-O2	96.1(1)
-O2	2.446(3)	O2-Ca-O3	56.3(1)
-O3	2.529(3)	O2-Ca-O4	64.0(1)
-O4	2.621(3)	O2-Ca-O5	70.5(1)
-O4	2.385(3)	O3-Ca-O4	59.1(1)
-O5	2.809(4)	O3-Ca-O5	106.8(1)
-O5	2.651(4)	O4-Ca-O4	97.1(1)
-O5	2.301(3)	O5-Ca-O5	85.8(1)
-O5	2.928(4)	O5-Ca-O5	91.0(1)
		O5-Ca-O5	72.6(1)
Be -O1	1.600(6)	O1-Be-O3	113.3(4)
-O3	1.586(6)	O1-Be-O3	105.9(3)
-O3	1.590(6)	O1-Be-O4	106.6(3)
-O4	1.576(6)	O3-Be-O3	108.2(3)
		O3-Be-O4	116.0(4)
		O3-Be-O4	107.0(3)
B1 -O2	1.395(6)	O2-B1-O4	120.3(4)
-O4	1.374(6)	O2-B1-O5	118.6(4)
-O5	1.352(6)	O4-B1-O5	121.0(4)
B2 -O1	1.502(6)	O1-B2-O1	106.6(3)
-O1	1.511(6)	O1-B2-O2	113.6(4)
-O2	1.511(6)	O1-B2-O2	108.1(3)
-O3	1.494(6)	O1-B2-O3	101.1(1)
		O1-B2-O3	113.4(4)
		O2-B2-O3	107.4(3)

Acknowledgments

References

1. Y. Takéuchi, *Acta Cryst.* 5, 574 (1952).

2. U. L. Schäfer, *Neues Jahrb. Mineral., Monatsh.*, 75 (1968).

3. H. Bartl and W. Schuckmann, *Neues Jahrb. Mineral., Monatsh.*, 253 (1966).

4. O. V. Yakubovich, N. A. Yamnova, B. M. Shehedrin, M. A. Simonov, and N. V. Belov, *Dokl. Akad. Nauk.* SSSR **228**, 842 (1975).

5. K. I. Schaffers and D. A. Keszler, *J. Solid State Chem.* **85**, 270 (1990).

6. K. I. Schaffers and D. A. Keszler, *Chem. Mat.* (1992) to be published.

7. I. A. Bajdina, V. V. Bakakin, N. V. Podberizskaja, B. I. Alekseev, L. R. Baconova, and V. S. Pavlijucenko, *Z. Strukt. Khim.* **19**, 125 (1978).

8. L. P. Solov'eva, and V. V. Bakakin, *Kristallografija* **15**, 922 (1970).

9. Molecular Structure Corporation (1989). TEXSAN Structure Analysis Package. MSC (3200A Research Forest Drive, The Woodlands, TX 77381).

10. G. M. Sheldrick, in "Crystallographic Computing 3" (G. M. Sheldrick, C. Krüger, and R. Godard, Eds.), Oxford Univ. Press, Oxford, 175 (1985).

11. N. Walker, and D. Stuart, *Acta Cryst.* A**39**, 158 (1983).

12. *International Tables for X-ray Crystallography* (1974). Vol. IV. Birmingham: Kynoch Press. (Present distributor: Kluwer Academic Publishers, Dordrecht).

13. S. Block, and A. Perloff, *Acta Cryst.* **20**, 274 (1965).

14. B. Saubat, M. Vlasse, and C. Fouassier, *J. Solid State Chem.* **34**, 271 (1980).

15. R. W. Smith and D. A. Keszler, *Mater. Res. Bull.* **24**, 725 (1989).

16. R. W. Smith and D. A. Keszler, *J. Solid State Chem.* (1992) to be published.

17. J. P. R. De Villiers, *The American Mineralogist.* **56**, 758 (1971).

18. A. Vegas, F. H. Cano, and S. Garcia'-Blanco, *Acta Cryst. B* **31**, 1416 (1975).

19. N. V. Zayakina and A. A. Brovkin, *Sov. Phys. Crystallogr.* **22**(2), 156 (1977).

20. R. D. Shannon, *Acta Cryst. A***32**, 751 (1976).

21. R. W. Smith and D. A. Keszler, *J. Solid State Chem.* **81**, 305 (1989).

22. T. Alekel III and D. A. Keszler, *Acta Cryst.* (1992) in press.

23. P. D. Thompson and D. A. Keszler, *Chem. Mat.* (1992) to be published.

CHAPTER 8

TETRAHEDRAL TRIANGULAR 3-D FRAMEWORK AND

LUMINESCENCE IN THE BORATE $BaBe_2(BO_3)_2$

Kathleen I. Schaffers, Thomas A. Reynolds, and Douglas A. Keszler[*]

Abstract

The new compound $BaBe_2(BO_3)_2$ is readily prepared by solid-state methods. It crystallizes in the orthorhombic space group Fddd with four formula units in a cell of dimensions a = 11.725(2), b = 13.0043(6), c = 6.2859(8) Å and V = 958.4(2) Å^3. Residuals from least-squares refinement with 1652 unique reflections are R = 0.024 and R_w = 0.049. The structure is composed of two interpenetrating polyhedral frameworks. The beryllium-borate matrix comprising dimers of edge-sharing Be-centered tetrahedra linked via regular, planar triangular BO_3 groups is penetrated by a second framework constructed from Ba-centered dodecahedra sharing multiple edges. The optical characteristics of $BaBe_2(BO_3)_2$ doped with the ions Eu^{2+} and Eu^{3+} are also reported.

Introduction

Few oxides containing beryllium and boron together have been reported. The hydrated beryllium borates $Be_2BO_3 \cdot OH$ (1) and $Be_2BO_3OH \cdot H_2O$, (2) the anhydrous borate fluorides Be_2BO_3F (3) and KBe_2BO_3F (4), and the alkaline-earth beryllium borate $SrBe_2(BO_3)_2$ (5) have been the only examples described. To further develop the chemistry of these materials, we have examined phase equilibria in the systems $MO\text{-}BeO\text{-}B_2O_3$ where M= Ca, Sr, and Ba. In a recent article we described the structure of the new compound $SrBe_2(BO_3)_2$ (5). It consists of layers of interconnected tetrahedra and triangles selectively occupied by Be and B atoms, respectively, that are bridged by Sr atoms. Investigation of the Ba system has revealed the existence of a new compound having the same stoichiometry, $BaBe_2(BO_3)_2$, but a distinctive three-dimensional structure. We describe here the structure of this material and its luminescence properties when doped with the ions Eu^{2+} and Eu^{3+}.

Experimental

Crystals of $BaBe_2(BO_3)_2$ were grown in a Pt crucible by using $LiBO_2$ as a flux in the ratio 2 $BaBe_2(BO_3)_2$: 1 $LiBO_2$ by mass. The sample was melted at 1303 K and slowly cooled at a rate of 9 K/h to 1098 K and 60 K/h to room temperature. The resulting crystals were physically separated from the crucible then washed with dilute $HNO_3(aq)$ to remove the final traces of flux. A colorless crystal of approximate dimensions 0.18(1) x 0.2(1) x 0.32(1) mm was selected and mounted on a glass fiber with epoxy for structure analysis. X-ray data were collected with a Rigaku AFC6R single crystal diffractometer equipped with MoKα (λ=0.71069 Å) radiation. The Laue symmetry was established as mmm on the diffractometer. Three reflections chosen as standards and measured after each block of 200 data exhibited an overall average intensity decay of 1.1%.

The structure was solved and refined with computer programs from the TEXSAN crystallographic software package (6). After refinement with isotropic thermal parameters on all atoms, the data were corrected for absorption with the program DIFABS (7). The final refinement converged to R = 0.024 and R_w = 0.049 with anisotropic thermal coefficients on each atom and 1692 data having F_o^2 $\geq 3\sigma(F_o^2)$ included in the procedure. The final difference electron density map exhibits a maximum peak corresponding to 0.49% of the height of a Ba atom. Crystal data and atomic parameters are given in Tables 8.1 and 8.2, respectively.

A powder sample was prepared by heating in air the reagents BaB_2O_4 and

Table 8.1. Crystallographic Data for $BaBe_2(BO_3)_2$.

Formula	$BaBe_2(BO_3)_2$
FW, amu	272.97
Crystal System	Orthorhombic
Space group	Fddd (#70)
a, Å	11.725(2)
b, Å	13.004(1)
c, Å	6.286(1)
Vol., Å^3	958.4(2)
Z	8
D_{calc}, g cm^{-3}	1.891
F(000)	488
Radiation	Mo Kα ($\lambda = 0.71069$)
	graphite monochromated
Data Collected	+h, +k, +l
$(\sin \theta/\lambda)_{max}$, Å	1.219
No. Observations ($F_o^2 \geq 3\sigma(F_o^2)$)	1692
R	0.024
R_w	0.049
Maximum Shift in Final Cycle	0.00

Table 8.2. Positional Parameters and Thermal Displacement
Coefficients for $BaBe_2(BO_3)_2$.

	x	y	z	$B_{eq}(Å^2)$
Ba	5/8	1/8	1/8	0.704(4)
Be	3/8	0.2821(3)	-1/8	0.67(7)
B	0.3397(2)	1/8	1/8	0.58(4)
O(1)	0.2227(1)	1/8	1/8	0.89(4)
O(2)	0.3980(1)	0.21422(8)	0.026(2)	0.72(2)

$$B_{eq} = (\frac{8\pi^2}{3})\sum_i \sum_j U_{ij} a_i^* a_j^* a_i \cdot a_j$$

BeF_2 (CERAC, 99.5%) in a stoichiometric ratio. The reagent BaB_2O_4 was prepared from a 1:1 mol ratio of $Ba(NO_3)_2$ (AESAR, reagent grade): B_2O_3 (ALFA, 99%) by heating at 923 K for 1 h and 1023 K for 12 h. The borate-fluoride mixture was ground under hexane and heated in an alumina crucible at 923 K for 8 h to hydrolyze the BeF_2 to BeO, followed by heating at 1023 K for 24 h and 1073 K for 24 h with intermittent grindings. The diffraction pattern obtained with a Philips automated powder diffractometer agrees well with a pattern calculated with the computer program LAZY-PULVERIX (8) from the results of the structure determination. Unit cell parameters were also refined from the powder data by selecting fifteen peaks in the range $24 \leq 2\theta \leq 60°$; peak positions were corrected with NBS Si standard 640b. Least-squares refinement of the cell parameters with the computer program POLSQ afforded the values a = 11.73(2), b = 13.00(2), and c = 6.292(8) Å. These values compare well to the parameters obtained from the single-crystal data, indicating that the crystal chosen for data collection is representative of the bulk material.

Powder samples of $BaBe_2(BO_3)_2$ doped nominally with 2 mol% Eu (Eu_2O_3, AESAR, 99.99%) were prepared according to the method previously described except the final heating was done in a $95\%N_2:5\%H_2$ reducing atmosphere to produce the Eu^{2+}-doped sample. Charge compensation has ostensibly been maintained in the Eu^{3+}-doped sample by employing 2 mol% substitution by K atoms with the reagent KNO_3 (AESAR, 99.9%). Steady-state room-temperature luminescence and excitation spectra of these samples were obtained on a

computer-controlled right-angle spectrometer. Excitation provided by an Oriel 300 W Xe lamp was passed through a 50 cm water filter and focused onto the slits of a Cary model-15 prism monochromator. Selected excitation was focused onto the sample mounted on a copper sample holder within a quartz emission dewar. Luminescence was collected at a near-right angle to excitation, dispersed through an Oriel 22500 1/8 m monochromator, and detected with a Hamamatsu R636 photomultiplier tube. The signal was collected and amplified with a Keithley model 602 picoammeter then converted to a digital signal for computer acquisition. Spectrometer control and data acquisition were achieved with programs written in this laboratory.

Results and Discussion

A labeled drawing of the unit cell is shown in Figure 8.1. A stereoview showing the 3-dimensional beryllium-borate framework with Ba atoms in the cavities is given in Figure 8.2. The unique connectivity of BeO_4 tetrahedra and BO_3 triangles that affords caverns occupied by edge-shared BaO_8 dodecahedra is displayed. Selected interatomic distances and angles for $BaBe_2(BO_3)_2$ are given in Table 8.3.

The distorted triangulated dodecahedral site having D_2 symmetry is shown in Figure 8.3. It shares O vertices with the BeO_4 tetrahedra and O···O edges with the BO_3 triangles and adjacent Ba-centered dodecahedra. Interatomic distances for the Ba-O(2) interactions are of two lengths, four at 2.915(1) Å and four at 2.797(1) Å. These distances may be compared with Ba-O distances ranging from 2.644(2) to 3.020(2) Å for a Ba atom in a distorted eight-coordinate site in the compound $Ba_2LiB_5O_{10}$ (9) and a value of 2.80 Å calculated from Shannon and Prewitt crystal radii (10). Angles for O(2)-Ba-O(2) range from 48.20(4)° to 133.09(4)°. Each of the Ba-centered dodecahedra shares edges with four adjacent dodecahedra to form a 3-dimensional framework of polyhedra that contains diamond-shaped channels extending along the [100] direction. These polyhedra also form 6-membered rings as shown in Figure 8.4 with a Ba-O(2)-Ba bond angle of 109.00(4)°. The rings are stacked end-to-end in the yz plane by sharing edges
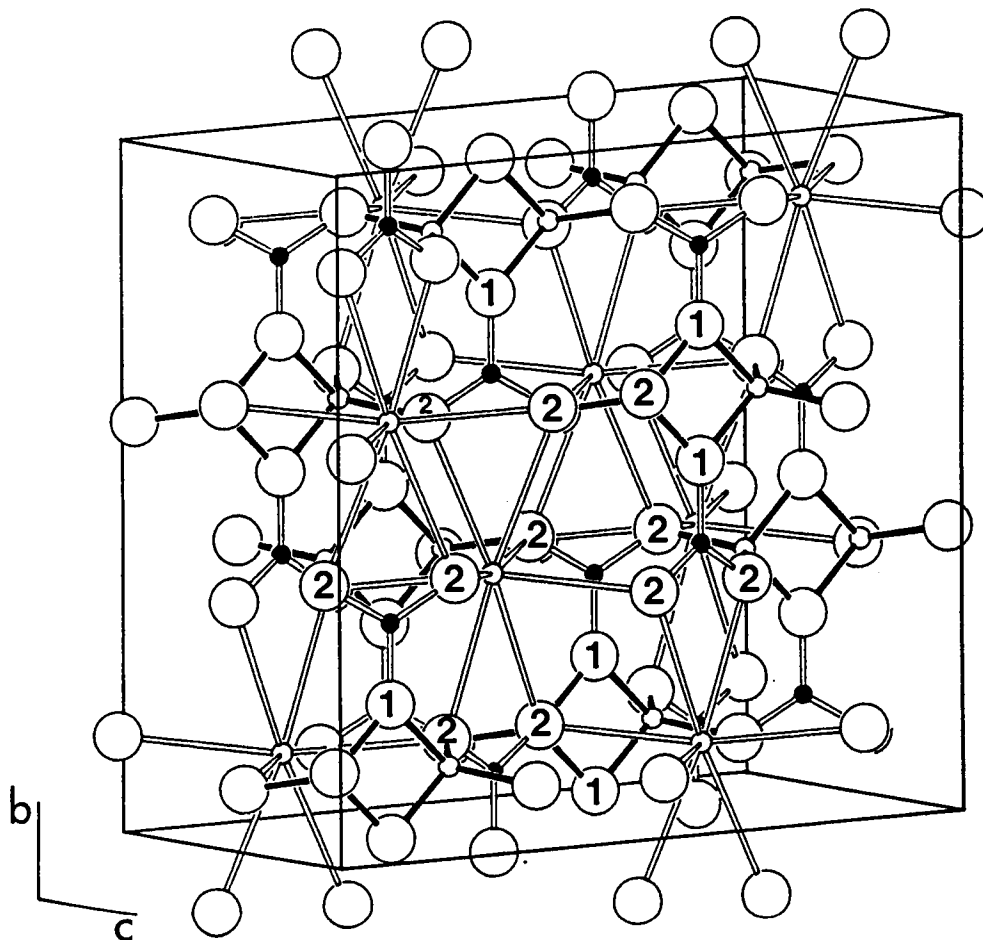
Figure 8.1. Drawing of the unit cell of $BaBe_2(BO_3)_2$ where the small open circles with open bonds are Ba atoms, the small open circles with shaded bonds are Be atoms, the small shaded circles with open bonds are B atoms, and the large open circles are O atoms.
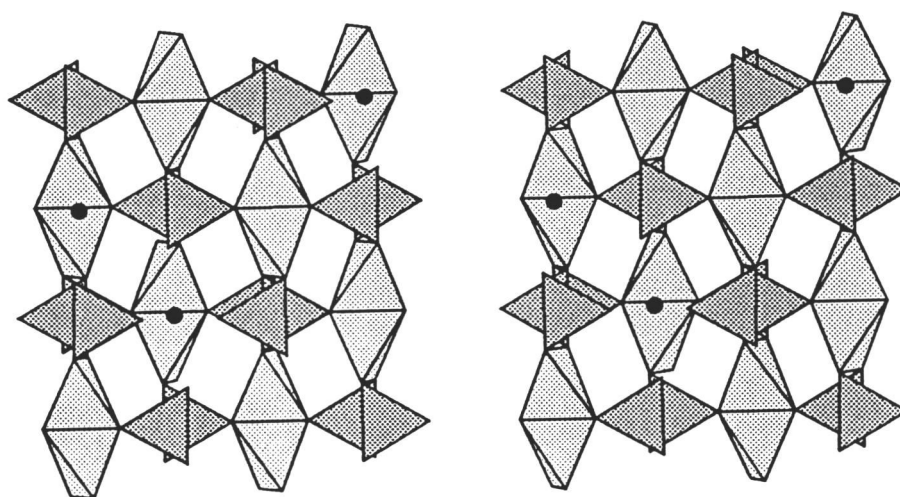
Figure 8.2. Stereoview of the $BaBe_2(BO_3)_2$ framework where the small filled circles are Ba atoms, the lightly shaded polyhedra are BeO_4 tetrahedra, and the darker shaded polyhedra are BO_3 triangles.
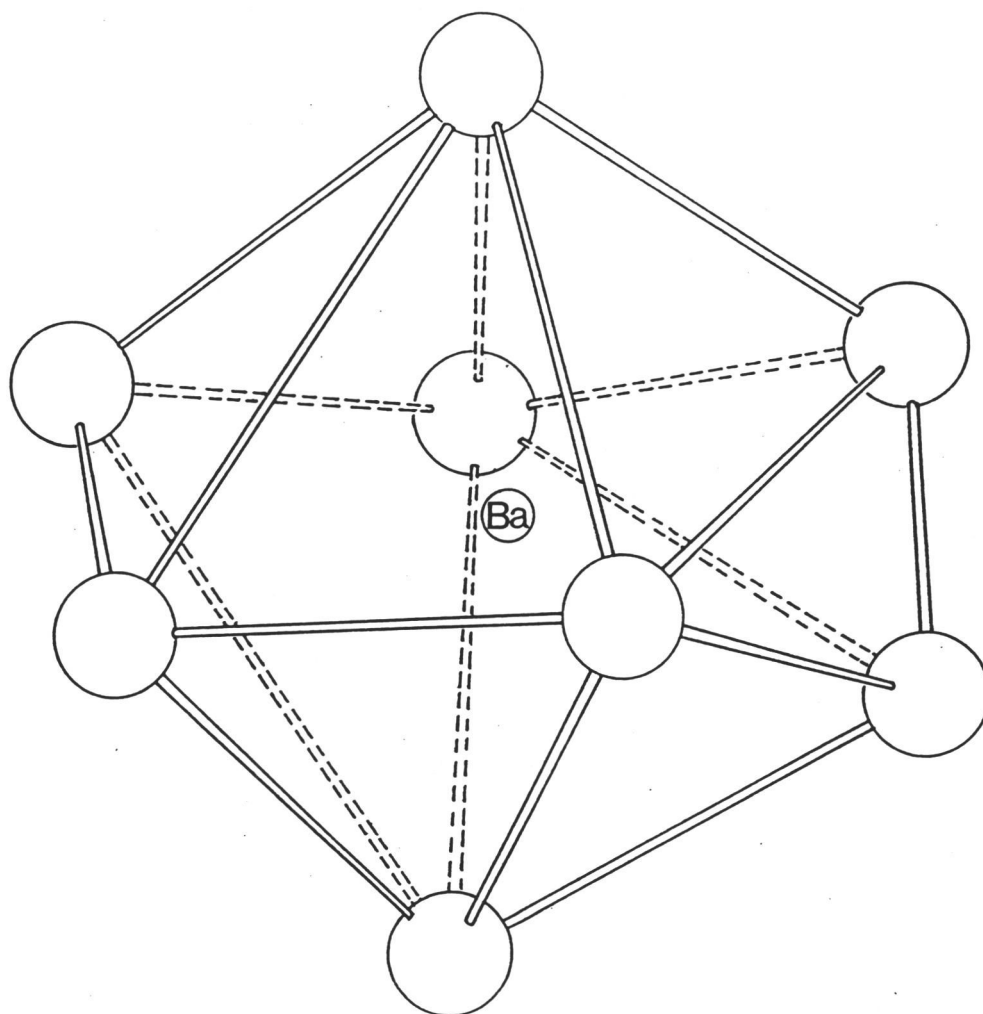
Figure 8.3. The distorted triangulated dodecahedral site centered by Ba.
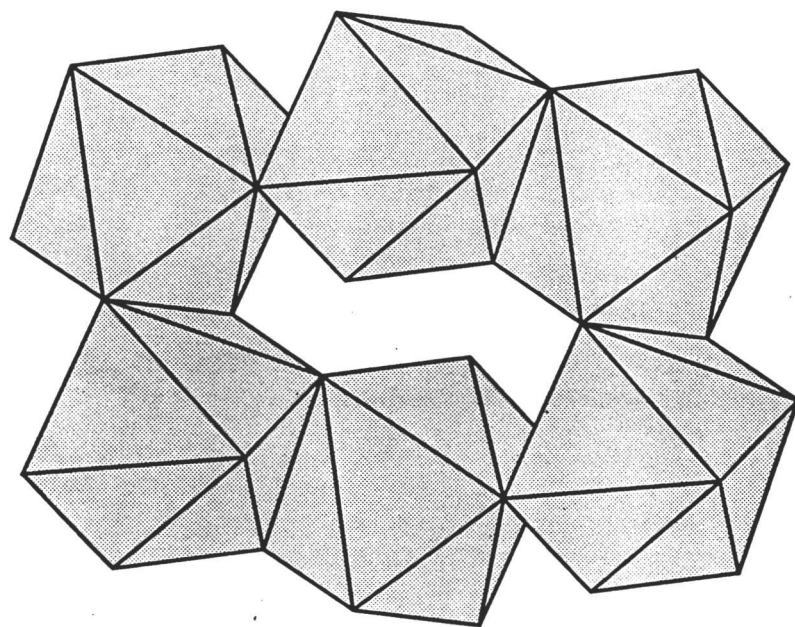
Figure 8.4. Sketch of the 6-membered ring formed by edge-sharing Ba-centered dodecahedra.

with two BaO_8 dodecahedra in the z-direction. These rings are also connected by edge-sharing of dodecahedra in adjacent rings.

The beryllium-borate framework is composed of edge-sharing Be-centered tetrahedral units that are interconnected by BO_3 triangles. The B atom occupies a regular planar, triangular site with the average angle O-B-O = 120.0(2)$^\circ$; it is bonded to one O(1) atom and two O(2) atoms at distances of 1.372(3) Å and 1.373(2) Å, respectively. Similar B-O distances are found in the compounds $Sr_3Sc(BO_3)_3$ (11) and $ScBO_3$ (12) having average distances of 1.38(1) Å and 1.3752(5) Å, respectively. The BO_3 triangles share edges with the Ba-centered dodecahedra and vertices with the BeO_4 tetrahedra.

Each Be atom resides in a distorted tetrahedral environment with Be-O distances of 1.665(3) Å and 1.599(2) Å. These distances are comparable to the average distance 1.63(4) Å observed in $SrBe_2(BO_3)_2$ (5) and the value 1.61 Å computed for a 4-coordinate Be atom by using crystal radii. (10) The Be-centered tetrahedra share vertices with the BO_3 and BaO_8 polyhedra and edges with adjacent BeO_4 tetrahedra. O-Be-O bond angles are listed in Table 8.3.

The presence of two edge-sharing BeO_4 tetrahedra in a borate matrix has been reported for the mineral epididymite, $Na_2Be_2Si_6O_{15} \cdot H_2O$ (13), β-BeO (14), and $SrBe_2(BO_3)_2$. The compound contains a nearly square Be-O-Be-O four-membered ring with Be atoms related by a center of symmetry across the shared edge. In $BaBe_2(BO_3)_2$, the Be atoms are also related by a center of symmetry across the O(1)$\cdots$O(1) shared edge of length 2.291(3) Å. The Be$\cdots$Be atom separation

Table 8.3. Selected Bond Distances (Å) and Angles (°) for $BaBe_2(BO_3)_2$.

Ba -O(2) x4	2.915(1)	O(2)-Ba-O(2)	48.20(4)
Ba -O(2) x4	2.797(1)		71.00(4)
			74.37(2)
			83.25(4)
			97.83(5)
			98.58(3)
			116.47(3)
		Ba-O(2)-Ba	109.00(4)
Be - Be	2.416(7)	Be-O(1)-Be	93.0(2)
Be -O(1) x2	1.665(3)	O(1)-Be-O(1)	87.0(2)
-O(2) x2	1.599(2)	O(1)-Be-O(2)	106.53(5)
			121.14(6)
		O(2)-Be-O(2)	112.9(2)
B -O(1)	1.372(3)	O(1)-B-O(2)	119.9(1)
-O(2) x2	1.373(2)	O(2)-B-O(2)	120.2(2)

is 2.416(7) Å which compares with a distance of 2.35(1) Å for the Sr analog. Bond angles of 93.0(2)° for Be-O(1)-Be and 87.0(2)° for O(1)-Be-O(1) illustrate a significant deviation from a square configuration for the four-membered ring. Also, the two tetrahedra are twisted relative to one another by 12.6°, Figure 8.5.

The coordination geometries about each of the two O atoms are typical for oxides (15,16). Atom O(1) occupies a distorted 3-coordinate site having bonds to 1 B and 2 Be atoms with Be-O(1)-Be and Be-O(1)-B angles of 93.0(2)° and 133.48(9)°, respectively. The second O atom is bound by 1 B, 1 Be, and 2 Ba atoms in a highly distorted tetrahedral environment.

The optical characteristics of Eu^{2+}- and Eu^{3+}-doped $BaBe_2(BO_3)_2$ were measured at room temperature. When illuminated with a UV lamp, the Eu^{3+}-doped powder exhibits an unusual luminescence that appears pink to the eye; typically Eu^{3+}-doped compounds luminesce to give red or orange-red colors. To explain this discrepancy, a room temperature emission spectrum was obtained, Figure 8.6. This spectrum is similar to the emission spectrum of $BaGd_{0.70}Eu_{0.30}B_9O_{16}$ (17) and all peak assignments were made by comparison. The relative intensities of the magnetic-dipole transitions $^5D_0 \rightarrow {^7F_1}$ and the electric-dipole transitions $^5D_0 \rightarrow {^7F_2}$ are consistent with the D_2 site symmetry and the approximate centrosymmetric distribution of ions about the luminescent center. The spectrum indicates that the color of the emitted light should appear to be orange-red. To realize a pink color, a white or blue emission must be included.
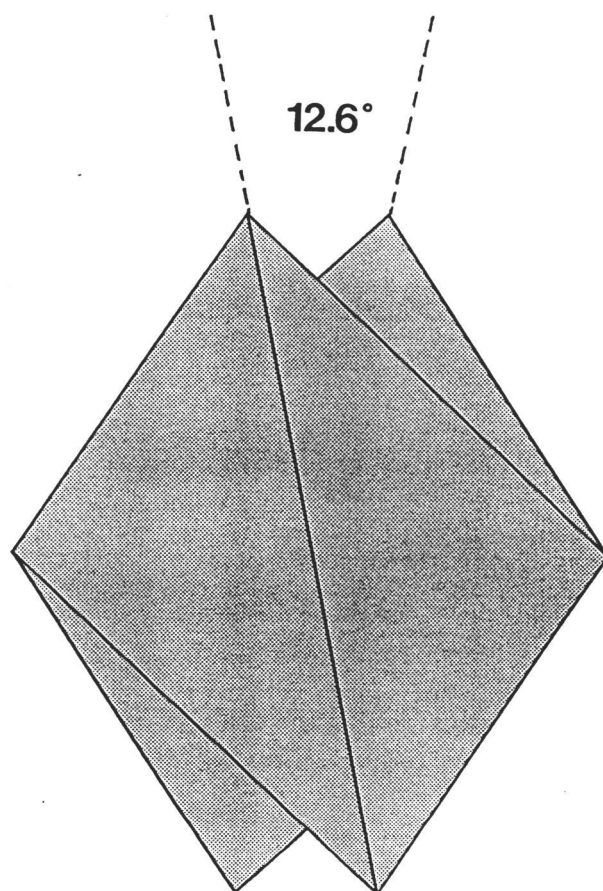
Figure 8.5. Sketch depicting the twist angle of the edge sharing Be-centered tetrahedra.
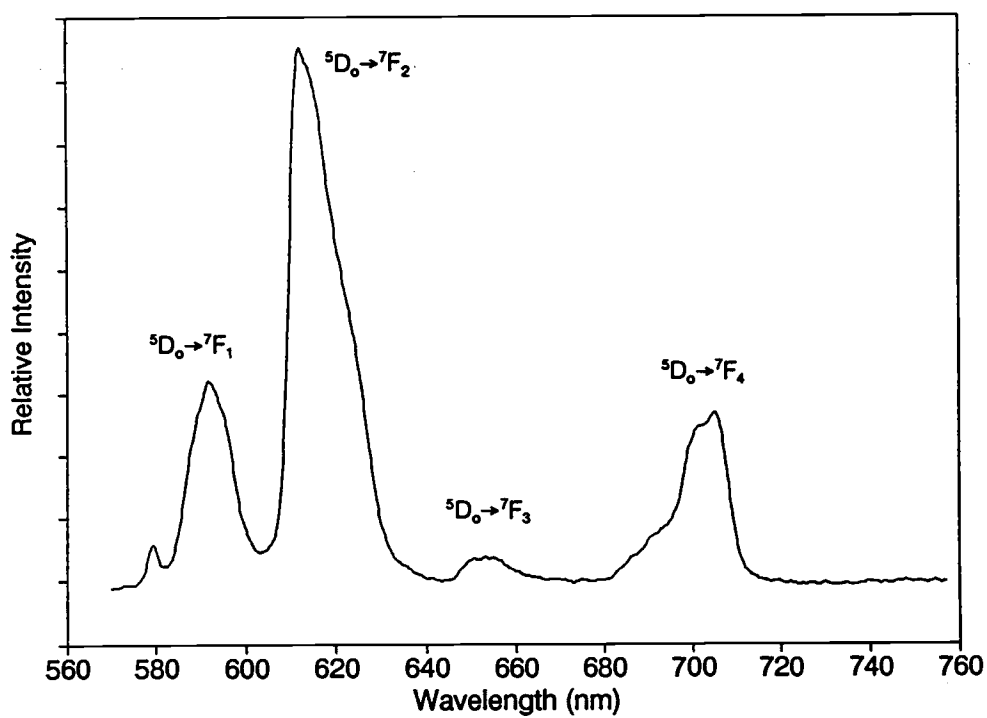
Figure 8.6. Room temperature emission spectrum of Eu^{3+}-doped $BaBe_2(BO_3)_2$

excitation wavelength of 394.2 nm.

We hypothesize this component is present in the form of a Eu^{2+} - emission, as described below.

An excitation and an emission spectrum, Figure 8.7, of the Eu^{2+}-doped $BaBe_2(BO_3)_2$ powder exhibited broad peaks with maxima at 367.0 nm and 391.0 nm, respectively. The wavelength of maximum emission can be compared to the Eu^{2+}-doped compounds $BaGdB_9O_{16}$ (17), 460 nm; SrB_4O_7 (18), 368 nm; BaB_8O_{13} (19), 400 nm; $BaMg_2Al_{16}O_{27}$ (18), 450 nm; SrB_6O_{10} (20), 390 nm; and $BaMgAl_{10}O_{17}$ (21), 450 nm. Several conclusions can be drawn about the nature of the Eu^{2+} site by examining the excitation and emission spectra (22). The broad excitation band indicates the lowest excited state to be from the $4f^75d$ configuration rather than $4f^7$. The $4f^7$ excited state would readily be evident by the presence of a narrow excitation band. The breadth of the excitation band is dictated by the crystal-field splitting of the d levels. Under D_2 symmetry these levels will transform as $a, b_1, b_2,$ and b_3. At sufficiently low temperatures, the splittings among these levels may be resolved in an excitation spectrum.

The 24-nm Stokes shift in Eu^{2+}-$BaBe_2(BO_3)_2$ is extremely small when compared with shifts for other barium borates of approximately 140 nm for $Eu^{2+}:BaB_8O_{13}$ (19) and 110 nm for $Eu^{2+}:BaGdB_9O_{16}$ (17). This small stokes shift is expected because of the rigidity of the beryllium-borate framework which prevents a large relaxation of the Eu^{2+} ion in the excited state.
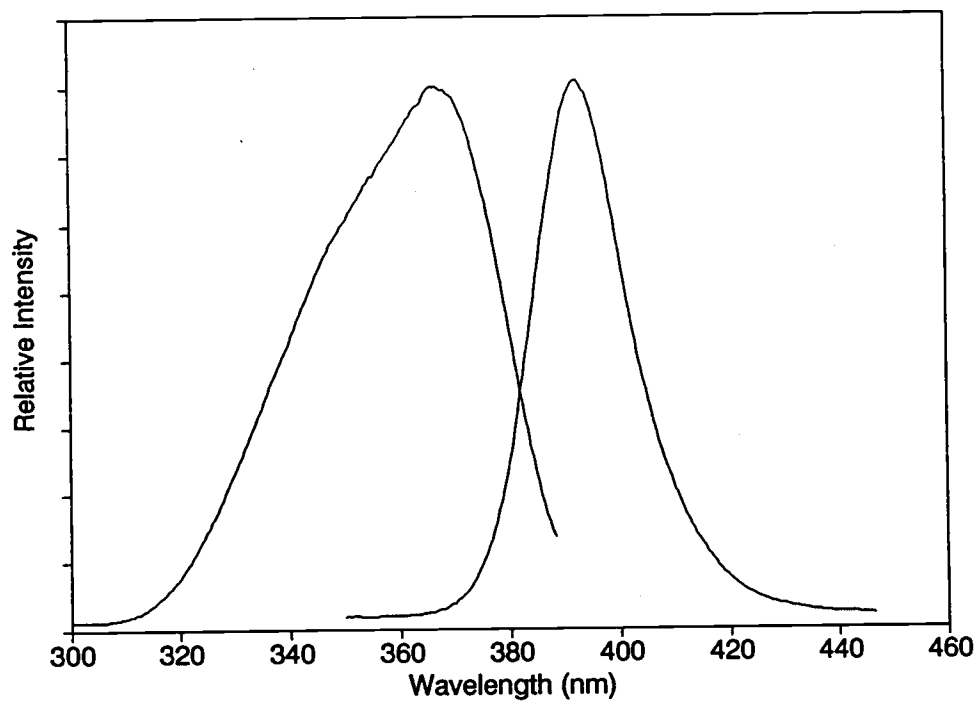
Figure 8.7. Excitation and luminescence spectra of Eu^{2+}-doped $BaBe_2(BO_3)_2$ taken at room temperature.

Acknowledgment

.

References

1. W. H. Zachariasen, H. A. Plettinger, and M.Marezio, *Acta Crystallogr.* **16**, 1144 (1963).

2. M. Schlatti, *Tschermaks miner. petrogr. Mitt.* **12**, 463 (1968).

3. I. A. Bajdina, V. V. Bakakin, N. V. Podberizskaja, B. I. Alekseev, L. R. Baconova, and V. S. Pavlijucenko, *Z. Strukt. Khim.* **19**, 125 (1978).

4. L. P. Solov'eva and V. V. Bakakin, *Kristallografija* **15**, 922 (1970).

5. K. I. Schaffers and D. A. Keszler, *J. Solid State Chem.* **85**, 270 (1990).

6. Molecular Structure Corporation, *TEXSAN*, Structure Analysis Package, MSC (3200A Research Forest Drive, The Woodlands, TX 77381).

7. N. Walker and D. Stuart, *Acta Crystallogr.* **A39**, 158 (1983).

8. K. Yvon, W. Jeitschko, and E. Parthe, *J. Appl. Cryst.* **10**, 73 (1977).

9. R. W. Smith and D. A. Keszler, *Mat. Res. Bull.* **24**, 725 (1989).

10. R. D. Shannon and C. T. Prewitt, *Acta Crystallogr.* **B25**, 925 (1969).

11. P. D. Thompson and D. A. Keszler, *Chem. Mater.* **1**, 292 (1989).

12. H. Sun and D. A. Keszler, *Acta Crystallogr.* **C44**, 1505 (1988).

13. J. H. Fang, P. D. Robinson, and Y. Ohya, *Amer. Miner.* **57**, 1345 (1972).

14. D. K. Smith and C. F. Cline, *Acta Crystallogr.* **18**, 393 (1965).

15. P. D. Thompson and D. A. Keszler, *Solid State Ionics* **32/33**, 521 (1989).

16. R. W. Smith, J. L Luce, and D. A. Keszler, in preparation.

17. F. Wen-Tian, C. Fouassier, and P. Hagenmuller, *Mat. Res. Bull.* **22**, 899 (1987).

18. T. F. Soules and M. V. Hoffman, *Kirk-Othmer: Encyclopedia of Chemical Technology*; John Wiley & Sons, Inc. **14**, 527 (1981).

19. G. Blasse, A. Bril, and J. de Vries, *J. Electrochem. Soc.: Solid State Science* **115(9)**, 977 (1968).

20. M. Leskelä, T. Keskentalo, and G. Blasse, *J. Solid State Chem.* **59**, 272 (1985).

21. A. L. N.Stevels, *J. Luminescence* **12/13**, 97 (1976).

22. M. J. Garcia, W. A. Sibley, C. A. Hunt, and J. M. Spaeth, *J. Luminescence* **42**, 35 (1988).

CHAPTER 9

STRUCTURE OF LiSrAlF$_6$

Kathleen I. Schaffers and Douglas A. Keszler

Abstract

Lithium Strontium Aluminum Fluoride, M_r = 235.53, trigonal, $P\bar{3}1c$, a = 5.071(6), c = 10.189(1) Å, V = 262.93(5) Å^3, Z = 2, D_x = 3.45 g cm-3, Mo Kα, λ = 0.71069 Å, μ = 117.53 cm^{-1}, F(000) = 216, T = 296 K, R = 0.024 for 163 observations with $F_o^2 \geq 3\sigma(F_o^2)$. Each of the cations occupies a distorted octahedral site. The symmetry of the Al site is reduced from O_h to D_3 in part by rotation of the trigonal fluorine faces, one relative to the other, by 7.2°.

Introduction

The compound $LiSrAlF_6$ has been reported to function as a tunable, room temperature laser material when doped with the ion Cr^{3+} (1). Its slope efficiency, 36%, and optical properties differ markedly from the characteristics of the highly efficient and isostructural laser material $Cr^{3+}:LiCaAlF_6$ (2). In this paper we describe structural features that influence these properties.

Experimental

LiSrAlF$_6$ was prepared by grinding a mixture of LiF (99.3%, AESAR), SrF$_2$ (reagent grade), and AlF$_3$ (99.5%, ALFA) containing an excess of 10 mole percent LiF and AlF$_3$ to compensate for volatilization losses during crystal growth. The sample was placed in a Pt tube and hydrofluorinated for 3 hours at 873 K to reduce the oxygen content. Crystals were grown in a horizontal zone-melting apparatus by melting a zone of the sample at 1053 K under an Ar atmosphere and translating the induction coil at a rate of 2.67 mm hr^{-1}. A colorless, rectangular crystal of dimensions 0.12 x 0.15 x 0.08 mm was physically separated from the sample and mounted on a glass fiber with epoxy for data collection with a Rigaku AFC6R diffractometer equipped with Mo Kα radiation. Lattice parameters were determined by automatic centering and least-squares analysis of 15 reflections in the range $30 \leq 2\theta \leq 50°$. Intensity data were collected by using the ω-2θ scan technique; intensities of three standard reflections measured after each block of 200 data exhibited an average fluctuation of 1.7%. A total of 1019 data with F$_o^2$ $\geq 3\sigma$(F$_o^2$) were obtained from 1586 reflections measured to $(\sin\theta_{max})/\lambda$ = 1.32 Å^{-1} in the range $-7 \leq h \leq 7$, $0 \leq k \leq 7$, and $-16 \leq l \leq 16$.

All calculations were performed on a microVAX II computer with programs from the TEXSAN crystallographic software package (3). The Sr, Al, and Li atoms were placed by comparison to the isostructural compound LiCaAlF$_6$ (4). The position of the F atom was determined by examining a difference electron density map. Following refinement of the structure with isotropic thermal

parameters, the data were corrected for absorption (transmission coefficients = 0.889 - 1.141) with the program DIFABS (5) and subsequently averaged (R_{int} = 0.063). Final least-squares refinement on F with 237 unique reflections having F_o^2 $\geq 3\sigma(F_o^2)$ and 17 variables affords the final residuals R = 0.024 and R_w = 0.024 where the function $\Sigma w(|F_o|-|F_c|)^2$ is minimized with weights derived from counting statistics ($w=1/\sigma^2(F)$). The isotropic extinction coefficient = 5.34 x 10^{-7} (6), S = 1.21, and Δ/σ = 0.01. Analysis of the final difference electron density map reveals a maximum peak = 0.62 e $Å^{-3}$ that corresponds to 0.31% of a Sr atom. Final atomic parameters are listed in Table 9.1; other data have been deposited.

Table 9.1. Final Atomic Coordinates for LiSrAlF$_6$

	x	y	z	B$_{eq}$[a]
Li	1/3	2/3	1/4	1.5(3)
Sr	0	0	0	0.84(1)
Al	2/3	1/3	1/4	0.73(4)
F	0.3879(4)	0.0328(4)	0.1485(1)	1.39(5)

$$^aB_{eq} = (\frac{8\pi^2}{3})\sum_i \sum_j U_{ij}a_i^* a_j^* a_i \cdot a_j$$

Results and Discussion

A sketch of the structure is shown in Figure 9.1. The compound is isostructural to the material $LiCaAlF_6$; each crystallizes as an ordered derivative of the structure type Li_2ZrF_6 (7). As a consequence of a larger crystal radius, the volume of the unit cell of the Sr analog is 22.42 $Å^3$ greater than that of the Ca analog. Other important differences are discussed below.

Selected interatomic distances and angles are listed in Table 9.2. The Sr atom occupies the center of a trigonally elongated octahedral environment as evidenced by consideration of the F-Sr-F angle, 94.93(5)°, involving F atoms from adjacent irregular close packed planes. The Sr-F distance, 2.421(1) Å, compares to the length, 2.46 Å, computed from crystal radii for a Sr atom bound to six, three-coordinate F atoms (8).

The Li atom occupies a highly distorted octahedral environment (cf. Table 9.2). The Li-F distance, 2.020(2) Å, compares to similar interactions in the compounds $LiCaAlF_6$, 2.009(3) Å; $LiSbF_6$, 2.032(6) Å (9); and Li_2ZrF_6, 2.025(1) Å.

The AlF_6 unit exhibits D_3 symmetry with an Al-F distance of 1.799(1) Å. This distance is similar to the six-coordinate Al environments in the compounds $LiCaAlF_6$, 1.800(3) Å; $SrAlF_5$, 1.79 and 1.81 Å (10); and $Na_3Al_2Li_3F_{12}$, 1.807(3) Å (11). The heights of the AlF_6 groups along the trigonal axis in $LiSrAlF_6$ and $LiCaAlF_6$ are statistically equivalent. The largest distortions from O_h symmetry arise from the relative rotations of the two trigonal F faces. As viewed along the
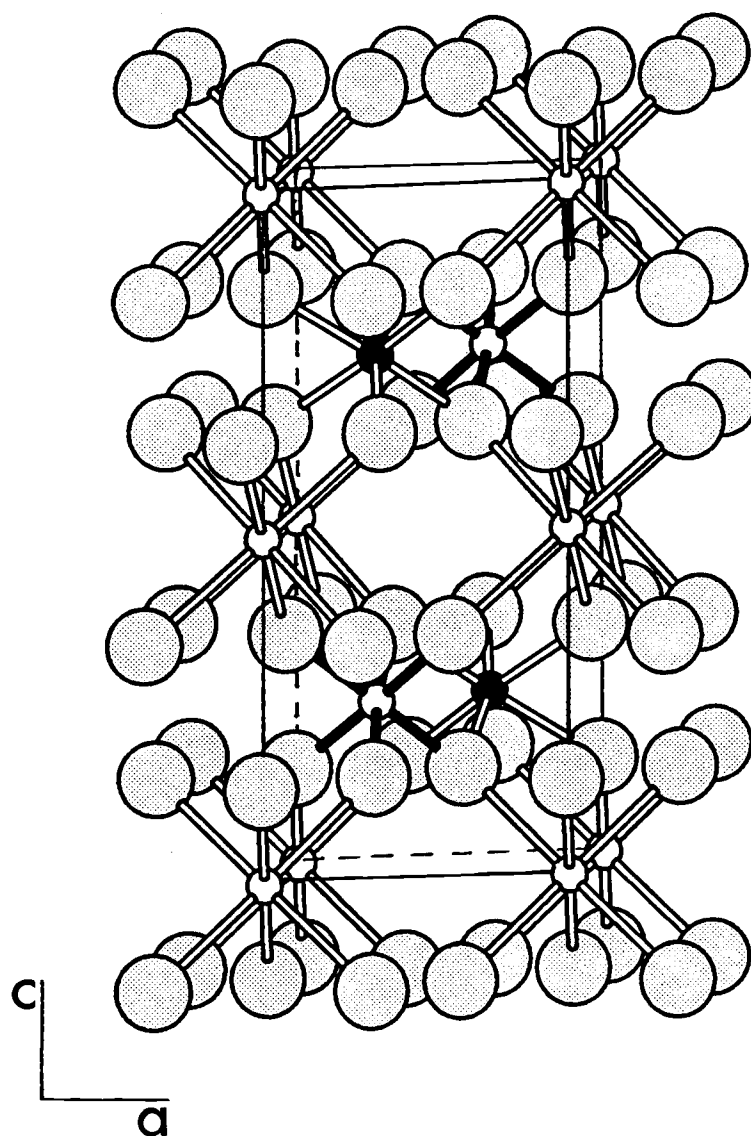
Figure 9.1. Sketch of the unit cell of LiSrAlF$_6$ as viewed approximately along the a axis. The small open circles with unshaded bonds represent Sr atoms, the open circles with shaded bonds represent Al atoms, the small filled circles with unshaded bonds represent Li atoms, and the largest shaded circles represent F atoms.

Table 9.2. Selected bond distances (Å) and bond angles (°) for

LiSrAlF$_6$.

Sr - F	2.424(2)	F - Sr- F	94.93(5)
Al - F	1.799(1)	F - Al - F	94.2(1)
			85.6(1)
			90.24(6)
Li - F	2.020(2)	F - Li - F	94.72(9)
			74.49(8)
			96.12(5)
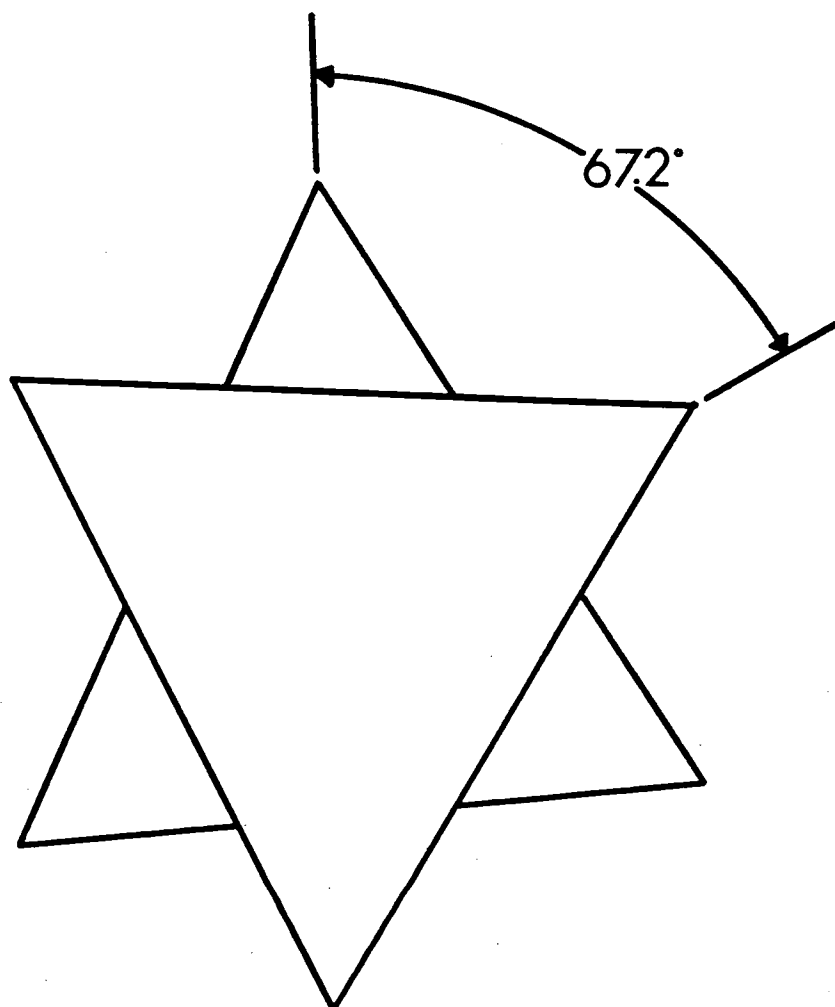
Figure 9.2. Drawing of AlF_6 group exhibiting relative orientation of trigonal F faces.

c axis (Figure 9.2), the angle of rotation between the two faces in $LiSrAlF_6$ is $67.2°$ which compares with the angle of $63.4°$ observed in the derivative $LiCaAlF_6$. These rotations and resulting angular distortions (cf. Table 9.2) are consistent with the emission lifetimes for Cr^{3+} ions doped onto these sites. The lifetime for $Cr^{3+}:LiSrAlF_6$ is 67 μs while that for Cr^{3+}: $LiCaAlF_6$ is 205 μs (12). The larger static distortion of the AlF_6 unit from O_h symmetry in the compound $LiSrAlF_6$ contributes to a greater relaxation of the Laporte selection rule; hence, a shorter lifetime is observed.

The nature of the distortion at the Al site is best appreciated by examination of the projection shown in Figure 9.3. From comparison of the positions of the F atoms in the structure of $LiSrAlF_6$ with those in an ideal close-packed layer, it is seen that the F hollows occupied by Sr atoms are expanded relative to the ideal packing and are displaced toward the Al atoms. This displacement likely arises from the larger electrostatic interaction of the ions Al^{3+} and F^- in comparison with the interactions between Sr^{2+} and F^- and Li^+ and F^-; each F^- anion is 3-coordinate, binding to Sr^{2+}, Li^+, and Al^{3+}. From inspection of Figure 9.3, it is seen that the displacements will occur in an opposite sense relative to the trigonal axis for adjacent F layers, affording the observed distortions of the AlF_6 units. Because the potential well for the Sr-F interaction is likely wider and softer than that of the Ca-F interaction it is not surprising to observe a larger displacement toward the Al^{3+} ion and a more distorted AlF_6 group in the Sr derivative.
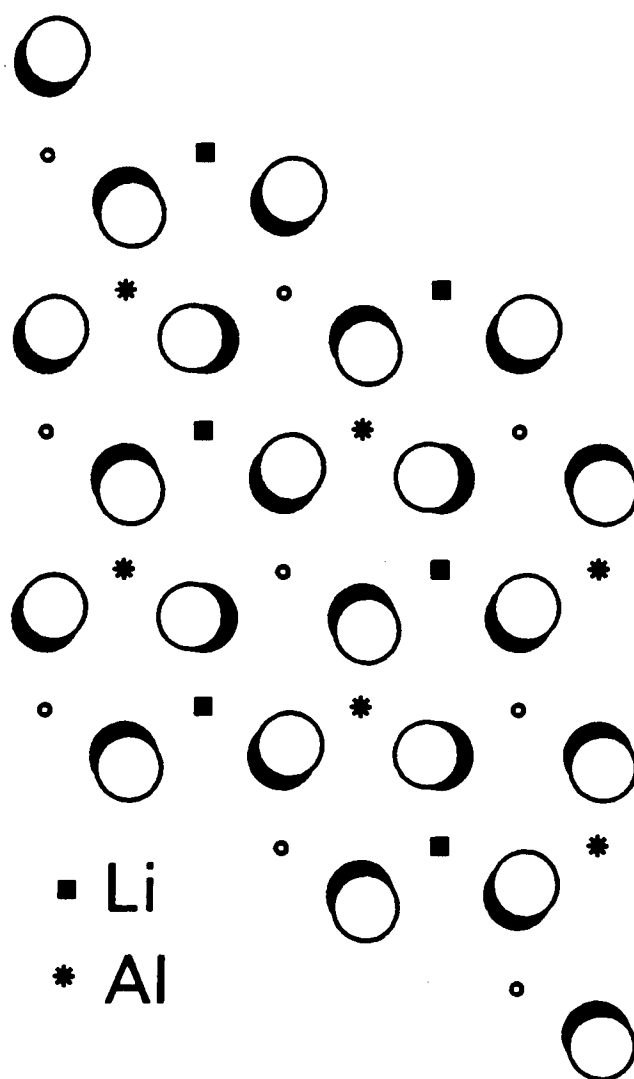
Figure 9.3. Comparison of idealized F closest packing with F packing in the structure of LiSrAlF$_6$ by projection onto (001). The large and small circles represent F and Sr atoms, respectively. The large shaded circles represent the positions of F atoms in an ideal close-packed layer.

Acknowledgments

References

1. S. A. Payne, L. L. Chase, L. K. Smith, W. L. Kway, and H. W. Newkirk, *J. Appl. Phys.* **66**, 1051 (1989).

2. S. A. Payne, L. L. Chase, H. W. Newkirk, L. K. Smith, and W. F. Krupke, *IEEE J. Quantum Electronics* **24**(11), 2243 (1988).

3. Molecular Structure Corporation, TEXSAN, MSC (3200A Research Forest Drive, The Woodlands, TX 77381, USA).

4. V. W. Viebahn, *Z. Anorg. Allg. Chem.* **386**, 335 (1971).

5. N. Walker and D. Stuart, *Acta Cryst. A* **39**, 158 (1983).

6. W. H. Zachariasen, *Acta Cryst. A* **24**, 214 (1968).

7. G. Brunton, *Acta Cryst. B* **29**, 2294 (1973).

8. R. D. Shannon and C. T. Prewitt, *Acta Cryst. B* **25**, 925 (1969).

9. J. H. Burns, *Acta Cryst.* **15**, 1098 (1962).

10. P. R. Von der Mühll, S. Andersson, and J. Galy, *Acta Cryst. B* **27**, 2345 (1971).

11. S. Geller, *Amer. Min.* **56**, 18 (1971).

12. S. A. Payne, L. L. Chase, and G. D. Wilke,(1989). *J. Luminescence* **44**, 167 (1989).

CHAPTER 10

STACK CRYSTAL CHEMISTRY

Kathleen I. Schaffers, Paul D. Thompson, Theodore Alekel III,

James R. Cox, and Douglas A. Keszler[*]

Abstract

The crystal chemistry of the STACK family of orthoborates having the formula $A_6MM'(BO_3)_6$ where A = Sr, Ba, Pb, or Ln (Ln = lanthanide), and M, M' = +2, +3, or +4 metal cation is described. Over 135 individual members of the family have been synthesized; they crystallize in the trigonal space group $R\overline{3}$ with unit cell volumes ranging from 1143.8(1) to 1365.6(3) $Å^3$. In this report, the metal site preferences, disorder, and solid solubility of these phases are discussed. Interrelationships between this structure and the layered structure type of $Ba_3Sc(BO_3)_3$ are also detailed.

Introduction

Among the myriad of known solid-state inorganic structure types, there exist common examples such as rock salt, garnet, spinel, zinc blende, elpasolite, and perovskite where a common arrangement is retained with a great variety of atomic constituents. For example, the compounds NaCl, MgO, MgS, CaO, CaS, TiO, and ScN all adopt the rock salt structure, and the oxides $Ca_3Al_2Si_3O_{12}$, $Y_3Al_5O_{12}$, $Gd_3Ga_5O_{12}$, and $Ca_3Te_2Zn_3O_{12}$ all crystallize in the garnet structure. We derive a sense of order from classifying materials in this way, but the efficacy of doing so certainly derives from the capacity to control physical properties by freely substituting selected atoms at specific sites while maintaining structural integrity. In fact, many of our modern technological advances can be traced to this ability.

In a recent contribution we reported the existence of an entirely new family of compounds whose members now comprise one of the larger structural classes of material reported to date (1). This family, which we designate STACK, is derived from the structure of the compound $Sr_3Sc(BO_3)_3$ (2,3) by substitution of a variety of atoms at the Sr and Sc sites. The general formula is $A_6MM'(BO_3)_6$ where A = Sr, Ba, Pb, or selected lanthanides; M = Ca, Sr, Y, Sc, In, Bi, or selected lanthanides; and M' = Mg, Al, Cr, Mn, Fe, Co, Rh, Zn, Sc, In, Zr, Hf, Sn, or selected lanthanides.

In developing the physical properties of these new materials, it will be necessary to grasp the structural consequences and patterns encountered with the

various chemical substitutions. In this report, we discuss the crystal chemistry of this family and establish interrelationships with the layered structure type of the compound $Ba_3Sc(BO_3)_3$, which we described in the preceding report of this series.

Experimental Section

Synthesis

Powders of the Sr compounds were synthesized by using standard high-temperature solid-state methods. Stoichiometric quantities of the starting reagents (nitrates, carbonates, or oxides, typically ≥99.9%) were mixed with a 5 mol% excess of B_2O_3, ground under hexane, and heated at 923 K for 1 h to decompose the reagents and initiate the reactions. The samples were reground and heated for 6 h at 1028 K, for 12 h at 1123 K, and for 24 h in the range 1173 - 1673 K, depending on the sintering characteristics of the sample. Analysis of powder X-ray diffraction patterns obtained with a Philips automated diffractometer confirmed the formation of the desired product. Further synthesis studies on the derivatives $Sr_3Sc(BO_3)_3$ and $Sr_6YAl(BO_3)_6$ revealed that they could be synthesized by using a flash-synthesis method. The reagents were ground under hexane and heated in a Pt crucible directly at 923 K for 20 min and 1023 K for 15 min to initiate the reaction. The powder was then ground and heated promptly at 1273 K for 3 h. It is likely that most of the Sr derivatives can be prepared by this method.

In general, a different set of conditions is necessary for synthesis of crystalline Ba derivatives. The flash-synthesis method can only be used for a few compounds, and lower heating temperatures (1123 K - 1223 K) are generally required to avoid melting the sample. Also, smaller incremental increases in temperature, 25 - 75 K after each grinding, and longer heating times are typically needed to produce homogeneous samples. Each heating period lasted 12 - 24 h but could be as long

as several days. For example, the compound $Ba_6ErFe(BO_3)_6$ was prepared by grinding together stoichiometric ratios of the starting materials with 5 mol% excess B_2O_3 and heating at 898 K for 1 h, 1008 K for 19 h, 1073 K for 24 h, 1123 K for 21 h, and 1148 K for 14. The compound $Ba_6GdSc(BO_3)_6$, however, is readily prepared by flash heating.

Powder data for the materials were collected on an automated Philips diffractometer; peak positions were corrected by using NIST Si Standard 640b. Unit cell parameters were refined by least-squares analysis with eleven peaks in the range $26 \leq 2\theta \leq 58°$. The hkl assignments of each reflection were determined by comparison to powder X-ray patterns of the parent material $Sr_3Sc(BO_3)_3$ (2) and other selected derivatives.

To establish experimental variation in unit cell parameters, six pairs of samples were compared to determine the variance of their cell parameters **a** and **c** and unit cell volumes **V**. The maximum differences found (Δa, Δc and ΔV) were used as an estimate of maximum deviation from an average value. Reported values were found to be within +/- 0.1% for **a**, +/- 0.2% for **c**, and +/- 0.5% for **V**. Actual statistical deviations from the refinements with X-ray data are included in parentheses in Table 10.3. In each case inclusion of a larger cation should result in a larger unit cell but this may not show up if the enlargement is less than the experimental errors associated with the compound synthesis and cell parameter determination. Reported e.s.d.'s in the cell parameter tables have their origin in the POLSQ program and reflect the uncertainty with which the least squares fit

has settled on a specific value. Actual variations in unit cell parameters up to 0.019 Å are an order of magnitude larger than e.s.d.'s indicated by POLSQ. Sources of experimental error include the precision in weighing the starting reagents which can skew the stoichiometry of the product. Also, in a few cases, poor sample crystallinity affords broad and asymmetric diffraction peaks that lead to uncertainties in selecting peak positions.

Crystal Growth

Single crystals of $Sr_6Y_{1.07}Al_{0.93}(BO_3)_6$, $Sr_6Ho_{0.964}Sc_{1.036}(BO_3)_6$, $Sr_6Er_{1.40}Sc_{0.60}(BO_3)_6$, $Sr_6La_{0.84}Sc_{1.16}(BO_3)_6$, and $Ba_6Gd_{1.28}Sc_{0.72}(BO_3)_6$ were grown by slowly cooling melts. Crystals of $Sr_6Y_{1.07}Al_{0.93}(BO_3)_6$ were seized from a melt with the following mol% composition: 61.5 SrO, 5.1 Y_2O_3, 7.9 Al_2O_3, 20.5 B_2O_3, and 5.1 Li_2O. The melt was cooled from 1273 K to 1073 K at 10 K/h and then to room temperature at 100 K/h. A crystal was removed from the matrix by dissolution of the flux in dilute $HNO_3(aq)$. Crystals of $Sr_6HoSc(BO_3)_6$ were grown by melting a stoichiometric sample in a Pt crucible at 1773 K followed by cooling at 4 K/h to 1273 K and 40 K/h to room temperature. A crystal of $Sr_6Er_{1.40}Sc_{0.60}(BO_3)_6$ was isolated from a melt corresponding to the stoichiometric proportions of $Sr_6ErSc(BO_3)_6$. The heating and cooling programs were the same as those applied to the Ho crystals. Crystals of $Sr_6La_{0.84}Sc_{1.16}(BO_3)_6$ were obtained from a melt of 70 mol% $Sr_6LaSc(BO_3)_6$: 30 mol% CaF_2 that was cooled from 1648 to 1348 K at 15 K/h followed by cooling to room temperature at 130 K/h. Single crystals of $Ba_6Gd_{1.28}Sc_{0.72}(BO_3)_6$ were grown by melting the stoichiometric

material $Ba_6GdSc(BO_3)_6$ in a Pt crucible at 1573 K and then cooling to 1373 K at 5 K/h and at 40 K/h to room temperature.

Single-crystal Work

Relevant crystal data for each of the structures are presented in Table 10.1.

$Sr_6Y_{1.07}Al_{0.93}(BO_3)_6$

A 0.2 x 0.2 x 0.2 mm crystal was selected for analysis. The data were collected on a Rigaku AFC6 rotating anode diffractometer equipped with a graphite monochromator set for Mo $K\alpha$ radiation. 2381 reflections were measured by using ω-2θ scans in covering the range of indices $0 \leq h \leq 17$, $-17 \leq k \leq 17$, and $-12 \leq l \leq 12$ to $2\theta_{max} = 60°$. From these data, 764 unique reflections with $F_o^2 \geq 3\sigma(F_o^2)$ were available for structure determination and refinement. Three standard reflections measured after each block of 200 data exhibited excursions of less than 2.5%. A Digital μVAX-II computer, together with programs from the TEXSAN crystallographic software package (4), were used to solve the structure. The heavy atoms Sr and Y were located by using the direct methods program SHELXS (5), and the positions of the other atoms were determined from analysis of difference electron density maps. After several cycles of the least-squares refinement, the isotropic displacement coefficient at the Al site had refined to a negative value, indicating the presence of additional electron density. The multiplicity of the site was subsequently refined to a value greater than unity. It was then modeled with two disordered atoms (Y and Al) where the population was fixed at unity and the x, y, z, and B parameters of the Y atom were constrained to those of the Al atom. Refinement of the multiplicity indicated that 7.3% of the Al sites were occupied

Table 10.1. Crystal data for $Sr_6YAl(BO_3)_6$, $Sr_6ErSc(BO_3)_6$, $Sr_6HoSc(BO_3)_6$, $LaSr_6Sc(BO_3)_6$, and $Ba_6GdSc(BO_3)_6$.

	$Sr_6YAl(BO_3)_6$	$Sr_6ErSc(BO_3)_6$	$Sr_6HoSc(BO_3)_6$	$LaSr_6Sc(BO_3)_6$	$Ba_6GdSc(BO_3)_6$
Formula Weight, amu	994.46	1090.79	1088.45	1102.51	1379.04
Crystal System			-----Rhombohedral-----		
Space Group			-----$R\overline{3}$-----		
a, Å	12.162(3)	12.322(1)	12.285(3)	12.388(1)	12.960(1)
c, Å	9.103(4)	9.293(2)	9.268(2)	9.294(2)	9.538(2)
V, Å³	1166.1(8)	1221.8(3)	1211.2(5)	1235.2(2)	1387.2(3)
Z	3	3	3	3	3
D_{calc} g cm^{-3}	4.248	4.447	4.476	4.446	4.952
F(000)	1362	1473	1470	1500	1785
Diffractometer			-----Rigaku AFC6R-----		
Radiation			-----Mo Kα (λ=0.71069 Å)-----		
Data Collected			-----+h, ±k, ±l-----		
No. Observations ($F_o^2 \geq 3\sigma(F_o^2)$)	568	835	693	920	1191
R	0.040	0.034	0.025	0.048	0.055
R_w	0.042	0.045	0.039	0.068	0.063

by Y atoms to give the more exact formula $Sr_6Y(Al_{0.927}Y_{.073})(BO_3)_6$. The data were corrected for absorption with the program DIFABS (6) and subsequently averaged (R_{int} = 0.108). Anisotropic displacement coefficients were applied to the Sr, Y, B, and O sites in refinement to the final residuals R = 0.040 and Rw = 0.042. The largest peak in the final difference electron density map corresponds to 0.96% of an Y atom.

$Sr_6Ho_{0.964}Sc_{1.036}(BO_3)_6$

A single crystal of approximate dimensions 0.15 x 0.17 x 0.20 mm was selected for structure analysis on the same diffractometer. From 2456 reflections measured to $2\theta_{max}$ = 60° over the range of indices $0 \le h \le 17$, $-17 \le k \le 17$, and $-13 \le l \le 13$, 693 unique reflections with $F_o^2 \ge 3\sigma(F_o^2)$ were obtained. Three standards measured after every 200 reflections deviated on average by less than 1.5%. Each of the atoms was positioned by comparison to the isostructural compound $Sr_3Sc(BO_3)_3$ (2). After several cycles of least-squares refinement, examination of the isotropic displacement coefficients indicated a disorder over the Ho1 and Sc1 sites. They were then modeled with two atoms at each position with the occupancy constrained to unity. The x, y, z, parameters were fixed, and the B values of atoms Sc2 and Ho2 were constrained to those of atoms Ho1 and Sc1, respectively. The data were corrected for absorption with the program DIFABS and subsequently averaged (R_{int} = 0.045). Least-squares refinement with anisotropic displacement coefficients on the Sr, B, and O atoms and an extinction parameter = 0.19(3) x 10^{-6} afforded the final residuals R = 0.027 and Rw = 0.041.

The largest peak in the final difference electron density map corresponds to 0.27% of a Ho atom. A descriptive formula representing the final result is $Sr_6(Ho_{0.892(5)}Sc_{0.108})(Sc_{0.928(4)}Ho_{0.072})(BO_3)_6$.

$Sr_6Er_{1.40}Sc_{0.60}(BO_3)_6$

A crystal of approximate dimensions 0.20 x 0.20 x 0.25 mm was mounted on the Rigaku diffractometer for structure analysis. Cell constants were obtained from least-squares refinement of the setting angles of 15 reflections in the range $36 < 2\theta < 42°$. From 2135 reflections of the type h, $\pm$k, $\pm$l measured to $2\theta_{max} = 65°$, 979 unique reflections were obtained. The positions of the heavy atoms Sr, Er, and Sc were taken from the solution of the Ho analog. The positions of the B and O atoms were subsequently determined from analyses of difference electron density maps. The occupancies of the M and M' sites were determined in a manner similar to the Ho derivative. The data were corrected for absorption and averaged ($R_{int} = 0.067$). The Er and Sc atoms were subsequently refined with isotropic displacement coefficients while the remaining atoms were refined with anisotropic coefficients. Final refinement on F_o with data having $F_o^2 \geq 3\sigma(F_o^2)$ and a secondary extinction coefficient = 0.25(2) x 10^{-6} afforded the final residuals R = 0.034 and Rw = 0.045. The largest peak in the final difference electron density map corresponds to 1.8% of a Sr atom. The formula that indicates the occupancies of the M and M' sites is $Sr_6(Er_{0.915(5)}Sc_{0.085})(Er_{0.488(5)}Sc_{0.512})(BO_3)_6$.

$Sr_6La_{0.84}Sc_{1.16}(BO_3)_6$

A crystal of approximate size 0.2 x 0.2 x 0.3 mm was mounted for structure analysis. Cell constants were obtained from least-squares refinement with the setting angles of 17 centered reflections in the range $30.5 \leq 2\theta \leq 36°$. Three standard reflections measured throughout the data collection exhibited no significant variations. From 3741 reflections measured over the range of indices $-19 \leq h \leq 19$, $0 \leq k \leq 19$, and $-15 \leq l \leq 15$ to $2\theta_{max} = 70°$, 1205 unique reflections were obtained. The atoms on special positions were placed by analogy to the previous structures, and the remaining atoms were found by interpretation of difference electron density maps. Approximate site occupancies were determined by refining multiplicities with Sr atoms in the general-position sites and the special position 0, 0, ½. These occupancies were subsequently modeled with partial substitution of La on the general position and Sc on the special position. The refinement was then constrained to give a total unit occupancy for the special position and an appropriate La concentration on the general position to maintain charge neutrality. Following refinement of the model with isotropic displacement factors, the data were corrected for absorption and merged ($R_{int} = 0.073$). Final refinement with anisotropic displacement coefficients on the Sc1, B, and O atoms and an extinction correction $= 0.8(1) \times 10^{-6}$ afforded the residuals R = 0.048 and Rw = 0.068. The largest peak in the final difference electron density map corresponds to 4% of a Sc atom. The final results afford the descriptive formula $(Sr_{5.16}La_{0.84})(Sr_{0.84(2)}Sc_{0.16})Sc(BO_3)_6$.

$Ba_6Gd_{1.28}Sc_{0.72}(BO_3)_6$

A single crystal of approximate dimensions 0.1 x 0.1 x 0.15 mm was selected for structure determination. A total of 1176 unique reflections having $F_o^2 \geq 3\sigma(F_o^2)$ were obtained by using the ω-2θ scan technique to collect 4197 reflections in the range $2 \leq 2\theta \leq 80°$. Three standards measured throughout the data collection exhibited an average deviation of 0.23%. The position of the Ba atom was determined from the results of the direct methods program SHELXS, and the Gd and Sc atoms were located by analogy to the structure described above. The remaining atoms were located from examination of difference electron density maps. The magnitude of the temperature factors after least squares refinement indicated disorder at the Gd and Sc sites. Refinement of the multiplicities gave 13% Sc on the Gd site and 41% Gd on the Sc site so that the formula is $Ba_6(Gd_{0.869(3)}, Sc_{0.131})(Sc_{0.589}, Gd_{0.411(4)})(BO_3)_6$. The data were corrected for absorption with the program DIFABS and averaged ($R_{int} = 0.080$). The Ba, B, and O atoms were refined with anisotropic displacement coefficients, and the remaining atoms were refined isotropically. The converged refinement affords the final residuals R = 0.055 and R_w = 0.063. The largest peak in the difference electron density map corresponds to 3.5% of a Gd atom.

Positional parameters and equivalent isotropic displacement coefficients for each of the structures are summarized in Tables 10.2a and 10.2b.

Table 10.2a. Positional parameters for $Sr_6YAl(BO_3)_6$, $Sr_6ErSc(BO_3)_6$, and $Sr_6HoSc(BO_3)_6$.

		$Sr_6YAl(BO_3)_6$[a]	$Sr_6ErSc(BO_3)_6$[b]	$Sr_6HoSc(BO_3)_6$[c]
A	x	0.57169(4)	0.57542(5)	0.57425(5)
	y	0.04230(4)	0.04144(5)	0.04197(5)
	z	0.69465(6)	0.68987(6)	0.69082(5)
	B_{eq}	0.70(2)	0.60(2)	0.55(2)
M	x	0	0	0
	y	0	0	0
	z	0	0	0
	B_{eq}	0.50(2)	0.35(2)	0.31(2)
M'	x	0	0	0
	y	0	0	0
	z	½	½	½
	B_{eq}	0.38(5)	0.46(2)	0.20(5)
B	x	0.1906(5)	0.1982(6)	0.1974(5)
	y	0.1354(5)	0.1427(5)	0.1407(5)
	z	0.7569(8)	0.7614(7)	0.7597(6)
	B_{eq}	0.7(2)	0.6(2)	0.5(2)
O1	x	0.1717(3)	0.1686(4)	0.1683(4)
	y	0.6327(3)	0.6254(4)	0.6276(4)
	z	0.8175(5)	0.8149(5)	0.8154(4)
	B_{eq}	1.1(1)	0.9(1)	0.8(1)
O2	x	0.6234(3)	0.6150(4)	0.6170(4)
	y	0.1802(3)	0.1643(4)	0.1687(4)
	z	0.9443(4)	0.9501(5)	0.9483(4)
	B_{eq}	0.9(1)	1.0(1)	0.8(1)
O3	x	0.5954(3)	0.5937(4)	0.5949(4)
	y	-0.0762(3)	-0.0712(4)	-0.0731(4)
	z	0.4724(5)	0.4763(5)	0.4756(4)
	B_{eq}	1.0(1)	1.1(1)	0.9(1)

[a] A= Sr; M=Y; M'= Al(0.93), Y(0.07)
[b] A= Sr; M=Er(0.915), Sc(0.085); M'=Er(0.488), Sc(0.512)
[c] A= Sr; M= Ho(0.892), Sc(0.108); M'= Sc(0.928), Ho(0.072)

Table 10.2b. Positional parameters for $LaSr_6Sc(BO_3)_6$ and $Ba_6GdSc(BO_3)_6$.

		$LaSr_6Sc(BO_3)_6$[d]	$Ba_6GdSc(BO_3)_6$[e]
A	x	0.57741(5)	0.57506(3)
	y	0.04338(5)	0.04058(3)
	z	0.69168(6)	0.69372(4)
	B_{eq}	0.87(2)	1.21(2)
M	x	0	0
	y	0	0
	z	0	0
	B_{eq}	0.76(3)	1.05(2)
M'	x	0	0
	y	0	0
	z	½	½
	B_{eq}	0.89(6)	2.80(8)
B	x	0.2014(7)	0.1936(8)
	y	0.1433(7)	0.1378(7)
	z	0.7572(8)	0.7558(9)
	B_{eq}	0.9(2)	1.6(2)
O1	x	0.1555(4)	0.1691(6)
	y	0.6228(5)	0.6257(6)
	z	0.8255(6)	0.8217(8)
	B_{eq}	1.2(1)	2.6(2)
O2	x	0.6217(5)	0.6207(5)
	y	0.1669(5)	0.1734(5)
	z	0.9465(5)	0.9509(6)
	B_{eq}	1.6(2)	1.9(2)
O3	x	0.5911(5)	0.5879(5)
	y	-0.0720(5)	-0.0825(5)
	z	0.4766(6)	0.4726(7)
	B_{eq}	1.6(2)	2.1(2)

[d] A= Sr(5.16), La(0.84); M= Sr(.84), Sc(0.16); M'= Sc
[e] A= Ba; M= Gd(0.92), Sc(0.08); M'= Sc(0.66), Gd(0.34)

Results and Discussion

STACK Structure

A listing of the STACK compounds that we have prepared along with their unit-cell parameters is given in Table 10.3. The unit-cell volumes range from 1143.8(1) Å^3 for the compound $Sr_6ScAl(BO_3)_6$ to 1414.0(2) Å^3 for the derivative $Ba_6SrZr(BO_3)_6$. The precision attained in the refinement of the parameters is an indication of the high crystallinity of most of the samples. They are, in fact, hard, dense, and stable ceramic materials, much like the members of other oxide families such as spinel and perovskite. Melting points of the more stable derivatives extend to approximately 1673 K.

The nominal formula $A_6MM'(BO_3)_6$ results from structural considerations of the parent compound $Sr_3Sc(BO_3)_3 \equiv Sr_6ScSc'(BO_3)_6$. As reported in the first paper of this series, the structure is a high symmetry trigonal type forming in a rhombohedral cell. It contains two types of Sc-centered O octahedra that alternately stack between planar triangular BO_3 groups to form chains (Figure 10.1) that extend along the trigonal axis. The 3-dimensional structure (Figure 10.2) results from linkage of these chains through the 9-coordinate Sr atoms. It is the specific linkages between the Sc- and Sr-centered sites that afford the inequivalence of the octahedra. One octahedron is larger, trigonally elongated, and shares only vertices with the 9-fold site, while the other is trigonally compressed and shares its triangular faces with the 9-fold site. In the formula $A_6MM'(BO_3)_6$, A then represents an atom on the 9-coordinate site, M is an atom

Table 10.3. Cell parameters for the family $A_6MM'(BO_3)_6$ (STACK).

Compound	a (Å)	c (Å)	V (Å³)
$Sr_6ScAl(BO_3)_6$	12.082(1)	9.047(1)	1143.8(1)
$Sr_6ScCr(BO_3)_6$	12.104(1)	9.095(2)	1154.0(2)
$Sr_6LuAl(BO_3)_6$	12.141(1)	9.071(2)	1158.1(2)
$Sr_6YbAl(BO_3)_6$	12.147(1)	9.077(1)	1159.9(2)
$Sr_6InCr(BO_3)_6$	12.136(2)	9.116(3)	1162.7(4)
$Sr_6TmAl(BO_3)_6$	12.160(1)	9.092(1)	1164.2(1)
$Sr_6InMn(BO_3)_6$	12.138(2)	9.136(2)	1165.8(3)
$Sr_6ErAl(BO_3)_6$	12.171(1)	9.097(2)	1166.9(3)
$Sr_6ScGa(BO_3)_6$	12.143(1)	9.146(1)	1167.8(2)
$Sr_6HoAl(BO_3)_6$	12.182(1)	9.095(2)	1169.0(2)
$Sr_6YbGa(BO_3)_6$	12.174(1)	9.120(2)	1170.4(2)
$Sr_6ScSc(BO_3)_6$	12.135(1)	9.184(1)	1171.3(3)
$Sr_6YAl(BO_3)_6$	12.190(2)	9.109(5)	1172.3(5)
$Sr_6LuGa(BO_3)_6$	12.187(2)	9.130(3)	1174.5(4)
$Sr_6ErGa(BO_3)_6$	12.190(1)	9.128(1)	1174.6(2)
$SmSr_5YNi(BO_3)_6$	12.175(2)	9.159(3)	1175.9(3)
$Sr_6DyAl(BO_3)_6$	12.218(1)	9.111(1)	1177.9(1)
$Sr_6TbAl(BO_3)_6$	12.218(1)	9.115(1)	1178.3(1)
$Pb_2Sr_4ScSc(BO_3)_6$	12.171(1)	9.186(1)	1178.4(2)
$PrSr_5YNi(BO_3)_6$	12.182(2)	9.170(2)	1178.4(3)
$NdSr_5YMg(BO_3)_6$	12.185(1)	9.180(2)	1180.4(2)
$Sr_6GdAl(BO_3)_6$	12.230(1)	9.114(2)	1180.6(3)
$Sr_6YCr(BO_3)_6$	12.213(1)	9.146(1)	1181.5(2)
$Sr_6InSc(BO_3)_6$	12.184(2)	9.190(2)	1181.5(3)
$Sr_6YRh(BO_3)_6$	12.228(2)	9.126(2)	1181.7(3)
$Sr_6HoGa(BO_3)_6$	12.220(1)	9.150(1)	1183.3(2)
$NdSr_5YNi(BO_3)_6$	12.208(2)	9.169(2)	1183.4(3)
$LaSr_5ErNi(BO_3)_6$	12.199(1)	9.184(1)	1183.6(2)
$SmSr_5YZn(BO_3)_6$	12.205(1)	9.177(2)	1183.9(3)
$LaSr_5YNi(BO_3)_6$	12.202(1)	9.187(1)	1184.6(1)

Table 10.1. continued.

SmSr$_5$YMg(BO$_3$)$_6$	12.213(1)	9.171(2)	1184.6(3)
Sr$_6$YGa(BO$_3$)$_6$	12.223(2)	9.159(2)	1185.0(3)
LaSr$_5$HoNi(BO$_3$)$_6$	12.209(1)	9.185(1)	1185.7(1)
NdSr$_5$HoCo(BO$_3$)$_6$	12.218(1)	9.179(1)	1186.7(1)
Sr$_6$EuAl(BO$_3$)$_6$	12.254(1)	9.126(2)	1186.7(2)
Sr$_6$SmAl(BO$_3$)$_6$	12.258(1)	9.126(1)	1187.5(2)
Sr$_6$HoFe(BO$_3$)$_6$	12.223(1)	9.188(1)	1188.8(2)
PrSr$_5$YZn(BO$_3$)$_6$	12.217(2)	9.197(3)	1188.8(4)
PrSr$_5$YMg(BO$_3$)$_6$	12.227(1)	9.188(2)	1189.5(2)
LaSr$_5$CaAl(BO$_3$)$_6$	12.258(2)	9.141(2)	1189.5(3)
Sr$_6$YFe(BO$_3$)$_6$	12.235(2)	9.192(2)	1191.7(3)
LaSr$_5$YCo(BO$_3$)$_6$	12.236(1)	9.199(1)	1192.8(2)
Sr$_6$LuSc(BO$_3$)$_6$	12.225(7)	9.217(1)	1192.9(2)
NdSr$_5$ErCo(BO$_3$)$_6$	12.251(1)	9.180(2)	1193.1(2)
Sr$_6$EuGa(BO$_3$)$_6$	12.261(1)	9.166(1)	1193.3(1)
LaSr$_5$YZn(BO$_3$)$_6$	12.235(1)	9.206(1)	1193.5(1)
Sr$_6$BiAl(BO$_3$)$_6$	12.279(1)	9.142(2)	1193.7(2)
LaSr$_5$HoCo(BO$_3$)$_6$	12.241(1)	9.204(1)	1194.3(2)
LaSr$_5$TbNi(BO$_3$)$_6$	12.243(1)	9.202(1)	1194.5(2)
LaSr$_5$YMg(BO$_3$)$_6$	12.237(2)	9.215(3)	1194.9(4)
Sr$_6$DyGa(BO$_3$)$_6$	12.274(2)	9.158(2)	1194.9(4)
LaSr$_5$HoMg(BO$_3$)$_6$	12.250(1)	9.200(2)	1195.6(3)
NdSr$_5$YZn(BO$_3$)$_6$	12.257(2)	9.199(3)	1196.8(3)
NdSr$_5$ScMg(BO$_3$)$_6$	12.257(2)	9.210(3)	1198.2(4)
LaSr$_5$EuNi(BO$_3$)$_6$	12.254(1)	9.214(1)	1198.3(1)
PrSr$_5$ScMg(BO$_3$)$_6$	12.251(1)	9.222(1)	1198.7(2)
Sr$_6$InIn(BO$_3$)$_6$	12.249(2)	9.228(3)	1199.0(5)
NdSr$_5$TbCo(BO$_3$)$_6$	12.269(1)	9.199(2)	1199.2(2)
NdSr$_5$ScCo(BO$_3$)$_6$	12.257(1)	9.220(2)	1199.6(2)
LaSr$_5$HoZn(BO$_3$)$_6$	12.265(2)	9.209(3)	1199.6(5)
NdSr$_5$ErZn(BO$_3$)$_6$	12.272(1)	9.198(1)	1199.7(2)
Sr$_6$YbSc(BO$_3$)$_6$	12.242(3)	9.246(4)	1200.0(6)
Nd$_2$Sr$_4$SrMg(BO$_3$)$_6$	12.268(1)	9.212(1)	1200.5(2)
Sr$_6$SmGa(BO$_3$)$_6$	12.297(1)	9.170(2)	1200.9(2)
La$_2$Sr$_4$CaZn(BO$_3$)$_6$	12.259(1)	9.233(1)	1201.7(1)

Table 10.1. continued.

NdSr$_5$EuZn(BO$_3$)$_6$	12.273(1)	9.212(1)	1201.7(2)
Sr$_6$GdFe(BO$_3$)$_6$	12.274(1)	9.212(3)	1201.9(3)
Sr$_6$ErSc(BO$_3$)$_6$	12.258(1)	9.236(1)	1202.0(2)
LaSr$_5$TbMg(BO$_3$)$_6$	12.273(1)	9.216(2)	1202.1(2)
LaSr$_5$TbZn(BO$_3$)$_6$	12.273(1)	9.221(2)	1203.0(3)
LaSr$_5$ScMg(BO$_3$)$_6$	12.273(1)	9.229(1)	1203.9(1)
Pr$_2$Sr$_4$SrMg(BO$_3$)$_6$	12.279(1)	9.223(2)	1204.4(2)
Sr$_6$TbGa(BO$_3$)$_6$	12.324(1)	9.167(2)	1205.8(3)
Sr$_6$PrGa(BO$_3$)$_6$	12.315(1)	9.190(1)	1207.0(2)
Sr$_6$TmSc(BO$_3$)$_6$	12.271(2)	9.256(3)	1207.0(4)
Sr$_6$GdGa(BO$_3$)$_6$	12.333(1)	9.165(2)	1207.2(2)
NdSr$_5$ScZn(BO$_3$)$_6$	12.289(1)	9.245(1)	1209.0(1)
Sr$_6$YMn(BO$_3$)$_6$	12.320(2)	9.198(3)	1209.0(4)
Sr$_6$BiFe(BO$_3$)$_6$	12.310(2)	9.215(2)	1209.4(3)
Sr$_6$NdGa(BO$_3$)$_6$	12.330(1)	9.189(1)	1209.9(2)
LaSr$_5$ScCo(BO$_3$)$_6$	12.290(1)	9.251(2)	1210.1(2)
Sr$_6$DySc(BO$_3$)$_6$	12.288(1)	9.257(1)	1210.6(1)
LaSr$_5$ScNi(BO$_3$)$_6$	12.295(1)	9.250(1)	1210.9(1)
Sr$_5$BaHoFe(BO$_3$)$_6$	12.316(2)	9.219(2)	1211.0(3)
Sr$_6$YSc(BO$_3$)$_6$	12.284(1)	9.268(2)	1211.2(4)
Sr$_6$HoSc(BO$_3$)$_6$	12.285(3)	9.268(2)	1211.2(5)
Sr$_6$GdMn(BO$_3$)$_6$	12.330(4)	9.206(4)	1212.0(7)
LaSr$_5$MgAl(BO$_3$)$_6$	12.314(1)	9.232(1)	1212.3(2)
Sr$_6$TbIn(BO$_3$)$_6$	12.329(1)	9.219(1)	1213.5(3)
PrSr$_5$ScZn(BO$_3$)$_6$	12.307(1)	9.252(1)	1213.6(1)
Sr$_6$LaGa(BO$_3$)$_6$	12.339(1)	9.209(1)	1214.3(1)
Sr$_6$TbSc(BO$_3$)$_6$	12.306(2)	9.263(3)	1214.9(4)
La$_2$Sr$_4$SrZn(BO$_3$)$_6$	12.319(2)	9.264(2)	1217.4(3)
La$_2$Sr$_4$SrMg(BO$_3$)$_6$	12.318(1)	9.254(2)	1216.1(2)
Sr$_6$EuSc(BO$_3$)$_6$	12.327(1)	9.262(1)	1219.0(2)
LaSr$_5$ScZn(BO$_3$)$_6$	12.327(1)	9.266(2)	1219.3(2)
Sr$_6$EuIn(BO$_3$)$_6$	12.361(1)	9.234(1)	1221.9(2)
Sr$_6$CaSn(BO$_3$)$_6$	12.381(1)	9.206(1)	1222.0(1)
Sr$_6$SmSc(BO$_3$)$_6$	12.350(1)	9.276(2)	1225.2(2)
La$_2$Sr$_4$CdCd(BO$_3$)$_6$	12.364(1)	9.273(2)	1227.6(2)

Table 10.1. continued.

LaSr$_5$CaSc(BO$_3$)$_6$	12.378(1)	9.273(2)	1230.4(3)
Sr$_6$NdSc(BO$_3$)$_6$	12.373(1)	9.286(1)	1231.0(2)
Sr$_6$GdSc(BO$_3$)$_6$	12.395(3)	9.262(4)	1232.3(6)
Sr$_6$PrSc(BO$_3$)$_6$	12.384(1)	9.293(1)	1234.2(1)
Sr$_6$CdSn(BO$_3$)$_6$	12.434(2)	9.236(2)	1236.5(3)
LaSr$_5$SrSc(BO$_3$)$_6$	12.398(1)	9.302(1)	1238.1(2)
Sr$_6$LuLu(BO$_3$)$_6$	12.433(1)	9.262(2)	1239.9(3)
Sr$_6$SrSn(BO$_3$)$_6$	12.464(1)	9.241(1)	1243.2(1)
Sr$_6$ErEr(BO$_3$)$_6$	12.478(1)	9.240(1)	1246.0(2)
LaSr$_5$SrCd(BO$_3$)$_6$	12.425(1)	9.324(1)	1246.5(1)
Sr$_6$CdHf(BO$_3$)$_6$	12.412(1)	9.346(2)	1246.8(3)
Sr$_6$YY(BO$_3$)$_6$	12.503(2)	9.248(2)	1252.1(4)
Sr$_6$DyDy(BO$_3$)$_6$	12.487(3)	9.234(3)	1246.9(4)
Sr$_6$HoHo(BO$_3$)$_6$	12.509(1)	9.254(1)	1254.0(2)
Sr$_6$TbTb(BO$_3$)$_6$	12.521(1)	9.247(1)	1255.4(2)
Sr$_6$GdGd(BO$_3$)$_6$	12.534(2)	9.251(3)	1258.7(4)
Sr$_6$CaZr(BO$_3$)$_6$	12.453(1)	9.367(1)	1258.0(2)
Sr$_6$CaHf(BO$_3$)$_6$	12.460(2)	9.358(3)	1258.3(4)
Sr$_6$CdZr(BO$_3$)$_6$	12.469(2)	9.371(2)	1261.7(4)
Sr$_6$SrHf(BO$_3$)$_6$	12.493(1)	9.373(1)	1266.9(1)
Sr$_6$SrZr(BO$_3$)$_6$	12.512(1)	9.392(1)	1273.5(1)
LaSr$_5$SrY(BO$_3$)$_6$	12.578(3)	9.317(3)	1276.5(5)
Sr$_3$Ba$_3$HoFe(BO$_3$)$_6$	12.663(3)	9.301(3)	1291.6(5)
Ba$_6$InIn(BO$_3$)$_6$	12.769(1)	9.737(1)	1323.4(2)
Ba$_6$YFe(BO$_3$)$_6$	12.797(1)	9.372(2)	1329.1(2)
Ba$_6$ErFe(BO$_3$)$_6$	12.796(0)	9.364(0)	1327.9(1)
Ba$_6$HoFe(BO$_3$)$_6$	12.796(2)	9.383(4)	1330.4(6)
Ba$_6$LuIn(BO$_3$)$_6$	12.809(2)	9.395(2)	1334.8(3)
Ba$_6$DyFe(BO$_3$)$_6$	12.815(1)	9.387(2)	1335.1(3)
Ba$_6$TbFe(BO$_3$)$_6$	12.818(1)	9.398(1)	1337.2(1)
Ba$_6$YbIn(BO$_3$)$_6$	12.818(1)	9.414(1)	1339.6(1)
Ba$_6$GdFe(BO$_3$)$_6$	12.830(1)	9.408(1)	1341.1(1)
Ba$_6$TmIn(BO$_3$)$_6$	12.821(1)	9.421(3)	1341.2(5)

Table 10.1. continued.

Ba$_6$EuFe(BO$_3$)$_6$	12.835(1)	9.415(1)	1343.2(2)
Ba$_6$SmFe(BO$_3$)$_6$	12.835(1)	9.416(2)	1343.4(2)
Ba$_6$ErIn(BO$_3$)$_6$	12.842(1)	9.427(1)	1346.5(2)
Ba$_6$DySc(BO$_3$)$_6$	12.832(1)	9.446(1)	1347.0(2)
Ba$_6$HoIn(BO$_3$)$_6$	12.853(1)	9.424(2)	1348.4(3)
Ba$_6$YIn(BO$_3$)$_6$	12.849(1)	9.433(2)	1348.7(2)
Ba$_6$DyIn(BO$_3$)$_6$	12.852(2)	9.451(2)	1352.1(4)
Ba$_6$TbIn(BO$_3$)$_6$	12.851(1)	9.456(2)	1352.6(3)
Ba$_6$TbSc(BO$_3$)$_6$	12.849(1)	9.462(1)	1352.8(2)
Ba$_6$GdIn(BO$_3$)$_6$	12.865(2)	9.459(3)	1355.9(4)
Ba$_6$SmIn(BO$_3$)$_6$	12.878(2)	9.462(3)	1359.1(4)
Ba$_6$EuIn(BO$_3$)$_6$	12.886(1)	9.475(1)	1362.5(1)
Ba$_6$GdSc(BO$_3$)$_6$	12.880(1)	9.485(2)	1362.7(3)
Ba$_6$SmSc(BO$_3$)$_6$	12.887(1)	9.491(1)	1365.0(2)
Ba$_6$EuSc(BO$_3$)$_6$	12.888(1)	9.493(2)	1365.6(3)
Ba$_6$NdIn(BO$_3$)$_6$	12.903(1)	9.491(2)	1368.4(3)
Ba$_6$PrIn(BO$_3$)$_6$	12.918(1)	9.504(1)	1373.5(2)
Ba$_6$NdSc(BO$_3$)$_6$	12.950(1)	9.530(1)	1384.2(1)
Ba$_6$PrSc(BO$_3$)$_6$	12.946(1)	9.540(3)	1384.8(3)
Ba$_6$LaIn(BO$_3$)$_6$	12.965(1)	9.548(1)	1389.8(2)
Ba$_6$LaSc(BO$_3$)$_6$	12.981(1)	9.557(1)	1394.7(2)
Ba$_6$SrZr(BO$_3$)$_6$	13.035(1)	9.609(2)	1414.0(2)
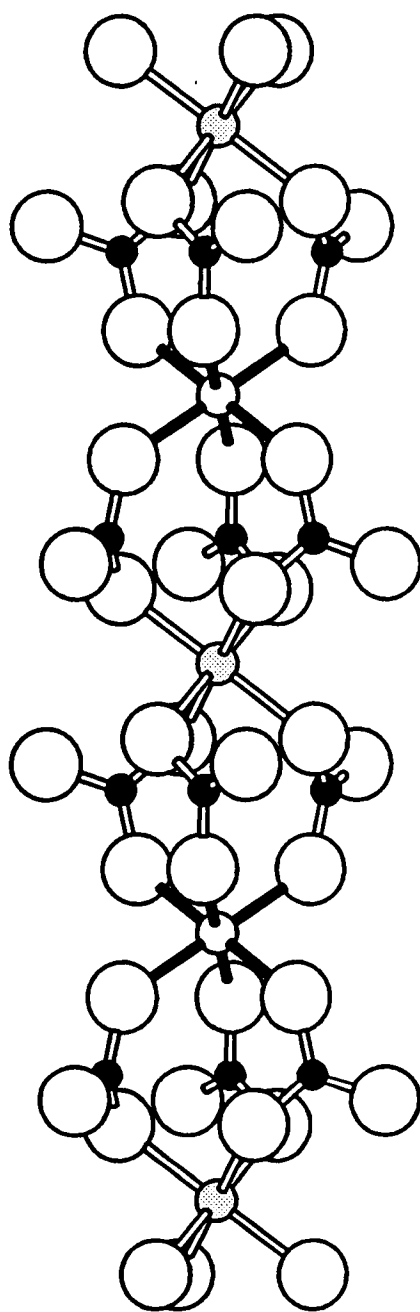
Figure 10.1. Chain of alternately stacked metal-centered octahedra linked by BO_3 groups.
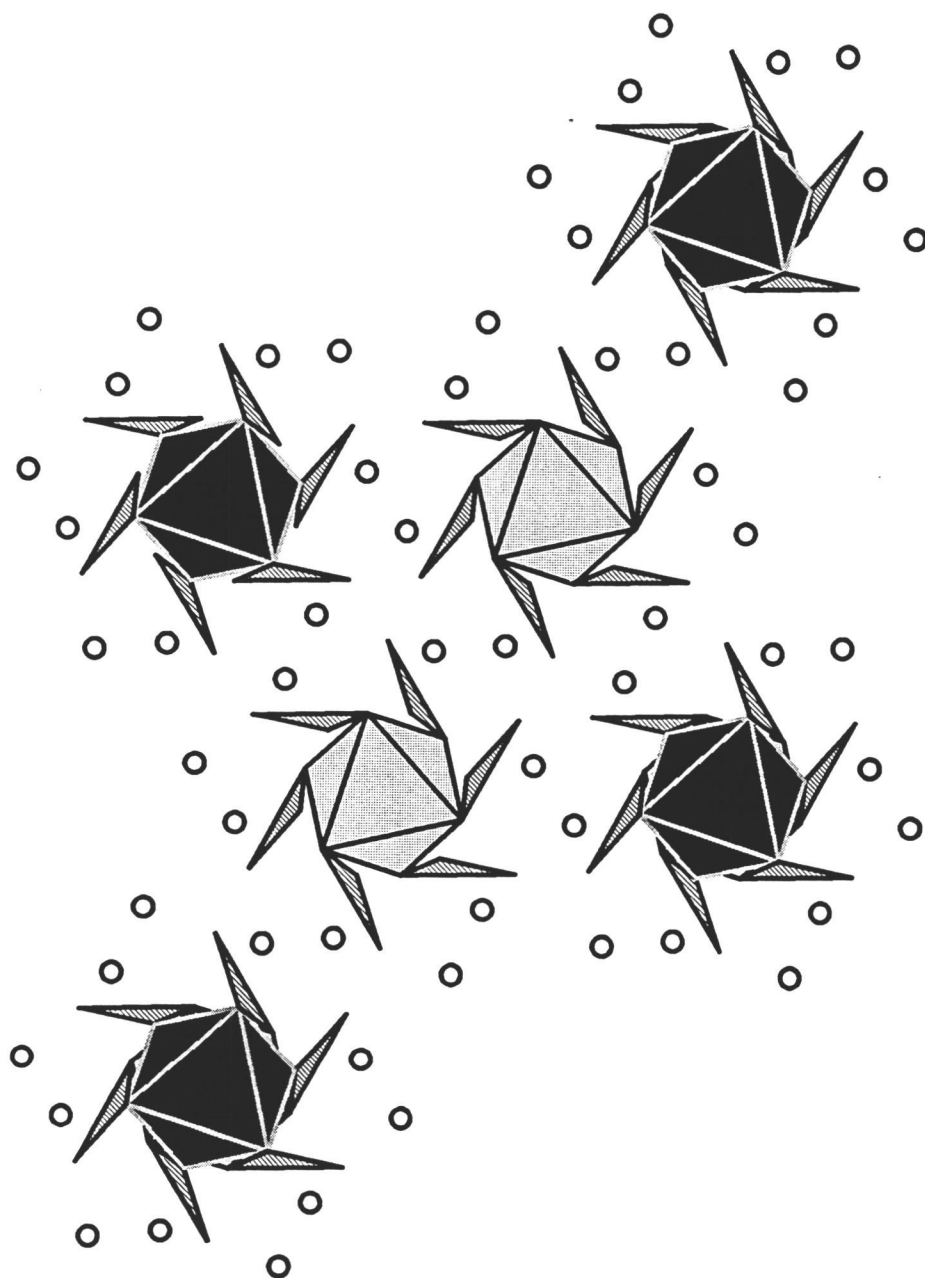
Figure 10.2. Sketch of the 3-dimensional structure of STACK viewed along the trigonal axis; the one-dimensional chains (Figure 10.1) are linked by Sr atoms.

on the larger octahedral site, and M′ is an atom on the smaller octahedral site. For example, the formula $Sr_6YSc(BO_3)_6$ contains A = Sr, M = Y, and M′ = Sc.

We describe below in more detail the microscopic characteristics of these materials. In particular, we examine the distribution of cations among the A, M, and M′ sites, establish regions of stability within various subclasses, and illustrate the types of chemical substitutions that will allow incorporation of ~ 50% of the elements from the periodic table into this structure type. The crystal-chemical results are certainly not exhaustive at the present time, but we can proceed in identifying important properties and trends in the family.

One subclass of the family contains the elements A = Sr and M and M′ atoms of the same type (M = M′ = Sc, In, Lu, Er, Y, Dy, Ho, Tb, and Gd). The derivative $Sr_3Sc(BO_3)_3$ ($r(Sc^{3+})$ = 0.885 Å) (7) contains the smallest M and M′ atoms while the derivative $Sr_3Gd(BO_3)_3$ ($r(Gd^{3+})$ = 1.078 Å) contains the largest. By interpolation, the structure should exist for all +3 cations of intermediate size. Hypothetical compounds such as "$Sr_3Al(BO_3)_3$" and "$Sr_3Cr(BO_3)_3$" do not exist because the +3 ions ($r(Al^{3+})$ = 0.675 Å and $r(Cr^{3+})$ = 0.755 Å) are too small to support the large M site. We note that no attempts have been made to employ reducing conditions for the production of Ti^{3+} (r = 0.810 Å) derivatives. In a similar manner, the derivative $Sr_3Eu(BO_3)_3$ does not exist because the Eu^{3+} ion is likely too large to fully occupy the small M′ site.

A larger subclass contains A = Sr and two different ions M ≠ M′ having formal charges of +3; examples include $Sr_6ScAl(BO_3)_6$, $Sr_6YFe(BO_3)_6$, and $Sr_6TbIn(BO_3)_6$. Compounds form with M and M′ cations ranging from the small

Al^{3+} ion to the large lanthanide La^{3+} (r = 1.172 Å). To establish the approximate limits of the structure field within this subclass, we will first examine the distribution of cations over the A, M, and M′ sites. The compounds $Sr_6LnSc(BO_3)_6$ (Ln = lanthanide or Y) are convenient for this purpose because the atom M may be any of those falling in the size range between Al^{3+} and La^{3+}.

To probe the characteristics of Al substitution in these Sc analogs, we examined the solid solution series $Sr_6Sc_{2-x}Al_x(BO_3)_6$ over the range 0 < x ≤ 2; results from powder X-ray diffraction measurements are summarized in Figure 10.3. As seen from the steady decrease in unit-cell volume for x = 0 to ~1, a complete solid solubility exists in this range. For x > 1, the volume remains constant and additional phases are observed in the powder patterns. We infer from this result that the Al atom has a preference for the smaller M′ site. This supposition is consistent with the nonexistence of the phase "$Sr_3Al(BO_3)_3$".

The results of a solid solubility study in the series $Sr_6Y_{2-x}Al_x(BO_3)_6$ are also summarized in Figure 10.3. The behavior here differs markedly from the Sc series. Because of the size disparity of the Y and Al atoms, solubility exists only in the range 0 < x < ~0.2. In the range 0.2 < x < 1 simple equilibrium mixtures of the two end members, x = ~0.2 and x = 1, were found to exist. Again, these results are consistent with preference of Al atoms for the smaller M′ site and the single-crystal structure analysis of the compound $Sr_6Y_{1.07}Al_{0.93}(BO_3)_6$. Here, the refinement clearly verifies the preference of the Al atom for the M′ site (Table 10.2). We have attempted to reproduce the stoichiometry observed from the single-crystal study; the unit-cell volumes of all the nonstoichiometric samples of
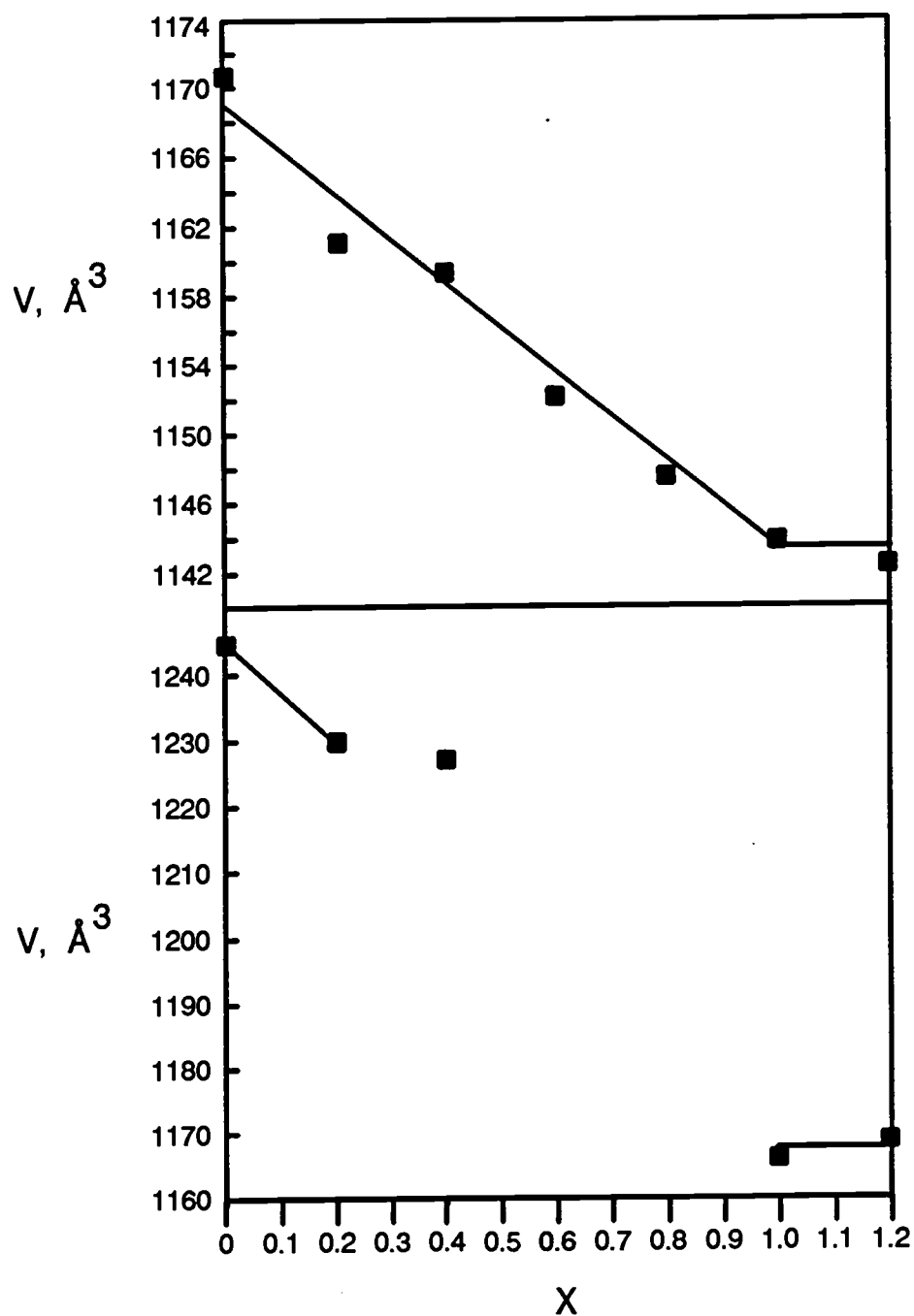
Figure 10.3. Cell volumes for the series $Sr_6Sc_{2-x}Al_x(BO_3)_6$ (top) and

$Sr_6Y_{2-x}Al_x(BO_3)_6$ (bottom) for $0 \leq x \leq 1.2$.

$Sr_6Y_{1+x}Al_{1-x}(BO_3)_6$ with x $\approx$ 0.1 exhibited statistically equivalent unit-cell parameters. This discrepancy between the powder and single-crystal data may be a result of the presence of the flux in the melt growth of the single crystal.

An example of substituting a larger atom for Sc is given by the solid solution series $Sr_6Ho_xSc_{2-x}(BO_3)_6$ (0 < x < 2). As seen in Figure 10.4, powder X-ray diffraction results reveal a steadily increasing cell volume with increasing content of the larger Ho atom and a complete solid solution over the entire range of x. The materials crystallize in a rhombohedral cell characterized by two parameters a and c. The c axis is coincident with the trigonal rotation element and the extension of the chains depicted in Figure 10.1; the a axis is orthogonal to c. The change in the c parameter with variation in x exhibits a peculiar behavior. The parameter increases with Ho content up to x $\approx$ 1, but beyond this value the parameter *decreases* even though the *larger* Ho atom is being substituted into the structure. Of course, the volume still increases in this regime because of the more steeply increasing a parameter. Our interpretation of these results is that in the region 0 < x $\leq$ 1 the Ho atoms exhibits a preference for the larger octahedral M site. Beyond x $\approx$ 1 the Ho atom begins to occupy the smaller octahedral M' site. The c parameter decreases because of a compression of the M' site along the trigonal axis. This compression is coupled with a more significant expansion in directions orthogonal to the c axis. This expansion is seen in the larger slope of the line representing the change in the a parameter for x > 1.
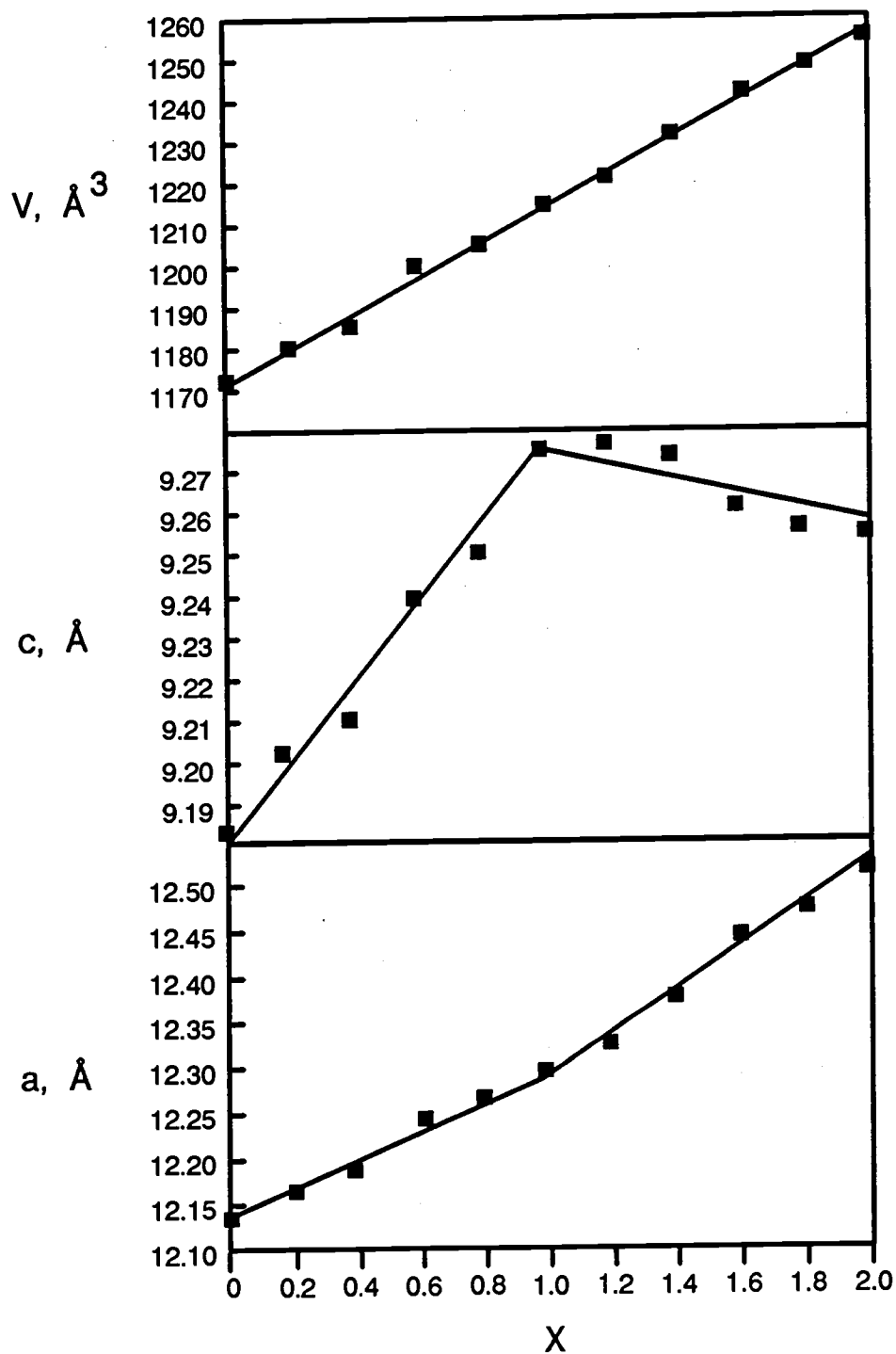
Figure 10.4. Cell parameters for the series $Sr_6Sc_{2-x}Ho_x(BO_3)_6$ for $0 \leq x \leq 2.0$.

This interpretation is supported by results of single-crystal structural studies of the compounds $Sr_6Ho_{0.964}Sc_{1.036}(BO_3)_6$ and $Sr_6Er_{1.4}Sc_{0.6}(BO_3)_6$. In the Ho compound, the Ho:Sc ratio is approximately 1:1, and the larger Ho atom was found to prefer occupancy of the larger M site; the occupancy of the M site is 89% Ho and 11% Sc atoms while the occupancy of the M' site is 93% Sc and 7% Ho atoms. In the Er derivative, the larger Er atoms again exhibit a preference for the larger site with occupancies of 91% Er and 9% Sc atoms on the M site and 49% Er and 51% Sc atoms on the smaller M' site. In this derivative the M' - O distance, 2.144(4) Å, is larger than the corresponding Sc2-O distance, 2.077(2) Å, in the compound $Sr_3Sc(BO_3)_3$. Also, the O2-M'-O2 angle, 83.3(2)°, represents a larger trigonal compression in comparison with the angle O2-Sc2-O2, 85.20(7)°, in the simple Sc derivative, a result that is consistent with the contraction of the c axis for $x > 1$ (Figure 10.4).

The results of substituting larger lanthanides into the structure are partially revealed by the solid-solution series $Sr_6Sc_{2-x}La_x(BO_3)_6$. Because of the absence of the phase "$Sr_3La(BO_3)_3$", incomplete solid solubility exists in this series and $x_{max} \approx$ 0.8. This result, determined from powder X-ray measurements (Figure 10.5), is consistent with the stoichiometry found in a single-crystal study on the compound $Sr_6La_{0.84}Sc_{1.16}(BO_3)_6$. We also found that the La atom occupies the 9-coordinate A site. As x increases in this series, the Sr atoms likely slip off the A site and substitute for the Sc atoms on the M site, being replaced in the process by La atoms on the A site.
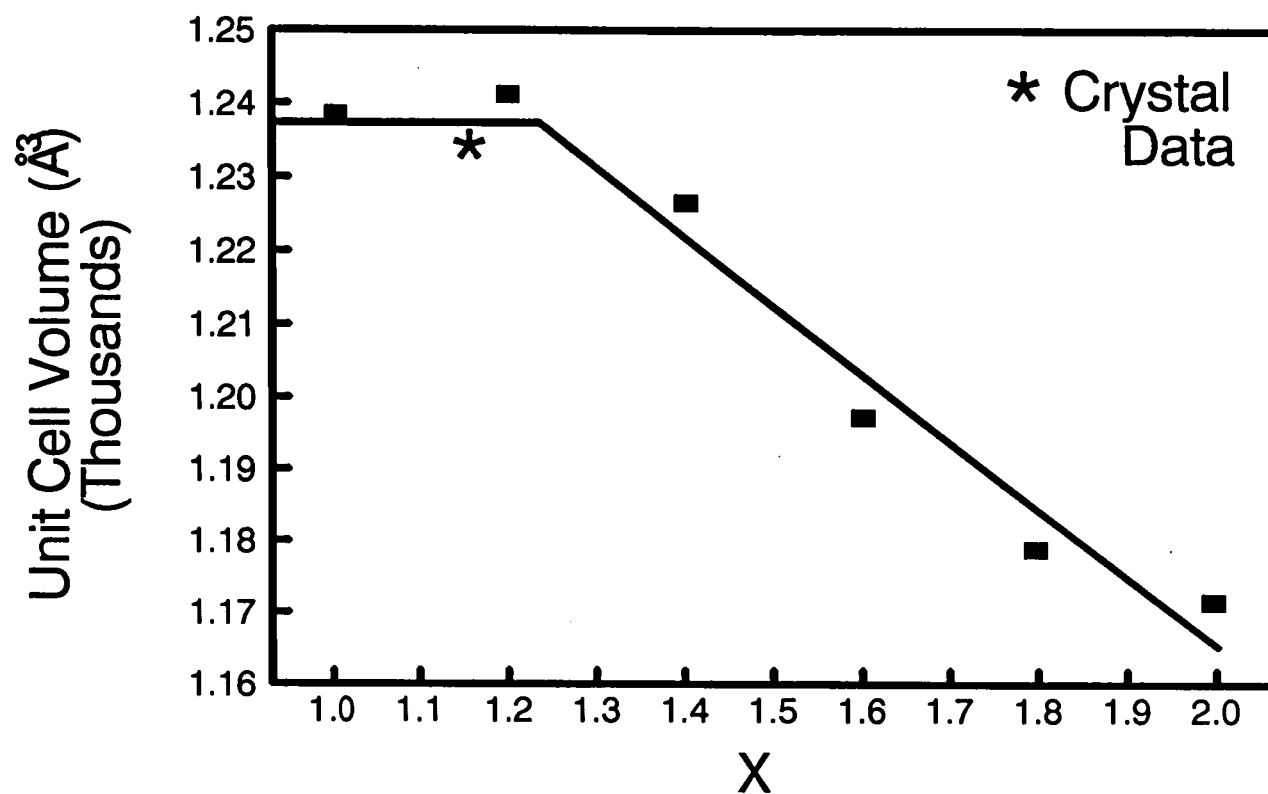
Figure 10.5. Unit cell volumes ($Å^3$) for the solid solution series $Sr_6Sc_{2-x}La_x(BO_3)_6$.

For the nominal stoichiometries $Sr_6LnGa(BO_3)_6$ containing the smaller Ga atom (r = 0.76 Å), STACK derivatives have also been found to exist for the complete lanthanide series. For the Al compounds $Sr_6LnAl(BO_3)_6$ ($r(Al^{3+})$ = 0.675 Å), however, the structure is formed only with those lanthanides up to the size of Sm.

Because the larger lanthanides exhibit a preference for the large A site, a means is provided for the introduction of smaller dipositive cations. Examples of these materials include the nominal formulations $LaSr_5ScZn(BO_3)_6$ (A= La and Sr, M= Sc, and M'= Zn) and $LaSr_5HoCo(BO_3)_6$ (A= La and Sr, M= Ho, and M'= Co). From consideration of all the previous results, we anticipate that the small Zn^{2+} (r = 0.88 Å) and Co^{2+} (r = 0.79 Å) ions occupy the M' sites. By charge compensating in this way, it is likely that any dipositive transition-metal ion that will occupy an octahedral site can be stoichiometrically incorporated into the structure. By substituting two large lanthanides onto the A site it is possible to place dipositive ions on both the M and M' sites as exemplified by the derivatives $(La_2Sr_4)CaZn(BO_3)_6$ and $(La_2Sr_4)CdCd(BO_3)_6 \equiv LaSr_2Cd(BO_3)_3$. Results on these derivatives are similar to those found for the simpler compounds $A_6MM'(BO_3)_6$ where A = Sr and M and M' are +3 cations. The compound "$(La_2Sr_4)MgMg(BO_3)_6$" does not exist. The Mg^{2+} ion (r = 0.86 Å) is slightly smaller than the Sc^{3+} ion so the absence of this compound is consistent with the result that an ion at least as large as Sc^{3+} must be present at the M site for stabilization and existence of the phase. The presence of $La_2Sr_4CdCd(BO_3)_6$ and nonexistence of "$La_2Sr_4CaCa(BO_3)_6$" is consistent with the series $Sr_6LnLn(BO_3)_6$

where the largest lanthanide incorporated is Gd. The crystal radius of Cd^{2+} (r = 1.09 Å) is intermediate to those of the ion Gd^{3+} and Eu^{3+}, while the radius of Ca^{2+} (r = 1.14 Å) is much larger.

A small class of compounds with M = cation of formal charge +2 and M' = cation of formal charge +4 has also been prepared. In this family M = Ca, Sr, or Cd and M' = Zr, Hf, or Sn. Attempts to prepare derivatives containing Ti^{4+} and Th^{4+} did not afford the STACK structure. The sizes of ions Zr^{4+} (r = 0.86 Å), Hf^{4+} (r = 0.85 Å), and Sn^{4+} (r = 0.83 Å) indicate they are likely to occupy the M' site. The distribution of X-ray intensities in the powder patterns verifies this supposition. Existence of the compound $Sr_7Zr(BO_3)_6 \equiv Sr_6SrZr(BO_3)_6$ clearly demonstrates that the Sr atom will occupy the M site. Because we have found very limited solubilities of Ca on the A site (vide infra) we anticipate that the Ca atom will reside on the larger M site in this subclass.

Before considering the characteristics of the Ba analogs, it is useful to analyze the results of the single-crystal studies in more detail. Interatomic distances for each of the structure refinements is listed in Table 10.4. For the Sr derivatives, the average A-O and B-O distances are statistically equivalent. The M-O1 and M'-O2 distances associated with the disordered M and M' sites agree favorably with averages of crystal radii that were determined by weighting the radii according to the site occupancies. For example, the distance 2.477(5) Å for the M-O1 interaction compares to the length 2.49 Å computed for a 6-coordinate site comprised of 0.84 La and 0.16 Sc atoms bound by 4-coordinate O atoms. For

Table 10.4. Interatomic distances (Å) for $Sr_6YAl(BO_3)_6$, $Sr_6ErSc(BO_3)_6$, $Sr_6HoSc(BO_3)_6$, $LaSr_6Sc(BO_3)_6$, and $Ba_6GdSc(BO_3)_6$.

	$Sr_6YAl(BO_3)_6$	$Sr_6ErSc(BO_3)_6$	$Sr_6HoSc(BO_3)_6$	$LaSr_6Sc(BO_3)_6$	$Ba_6GdSc(BO_3)_6$
A -O1	2.523(8)	2.530(4)	2.520(4)	2.473(5)	2.657(7)
-O1	2.643(8)	2.707(5)	2.683(4)	2.589(5)	2.799(7)
-O2	2.632(8)	2.768(4)	2.728(4)	2.709(6)	2.872(6)
-O2	2.810(8)	2.798(4)	2.799(4)	2.858(6)	2.975(6)
-O2	2.706(8)	2.763(5)	2.752(4)	2.723(6)	2.883(6)
-O3	2.886(9)	3.033(5)	2.983(5)	3.069(6)	3.110(6)
-O3	2.578(8)	2.495(5)	2.529(4)	2.512(5)	2.700(6)
-O3	2.561(8)	2.569(4)	2.569(5)	2.589(6)	2.746(6)
-O3	2.727(9)	2.761(5)	2.763(4)	2.769(6)	2.902(6)
A -O (avg.)	2.67(12)	2.71(16)	2.70(15)	2.70(18)	2.85(14)
M -O1	2.250(8)	2.291(4)	2.295(4)	2.477(5)	2.423(7)
M'-O2	1.931(8)	2.144(4)	2.090(4)	2.125(5)	2.162(5)
B -O1	1.37(1)	1.386(7)	1.393(7)	1.361(9)	1.40(1)
-O2	1.41(1)	1.386(7)	1.390(7)	1.390(9)	1.374(9)
-O3	1.37(1)	1.352(8)	1.353(7)	1.359(9)	1.36(1)
B -O (avg.)	1.38(2)	1.37(2)	1.38(2)	1.37(2)	1.38(2)

each derivative, the average A-O distances increase in the order A-O2 > A-O3 > A-O1. The short A-O1 distances are consistent with the 4-coordination of atom O1 and the 5-coordination of atoms O2 and O3. The lengthened A-O2 interaction is associated with the shared triangular face of the M'-centered octahedron. There is a trend of increasing A-O2 distances with increasing sizes of the M' atoms. In the Y-Al compound the M'-O2 distance is 1.931(8) Å and the average A-O2 distance 2.72 Å. In the Er-Sc analog the M'-O2 distance is 2.144(4) Å and the average A-O2 distance is 2.78 Å. Evidence for La atoms on the A site in the La-Sc derivative is seen from the shortened A-O1 distances ($r(La^{3+})$=1.36 Å and $r(Sr^{2+})$=1.45 Å) and a general lengthening of the A-O3 distances.

Interatomic angles are listed in Table 10.5. A rather notable consistency is observed in these data, as angular values deviate by no more than 3° among the various structures. The La derivative affords a curious result in affording the most regular M site with the O1-M-O1 angle of 91.9(2)° most closely approaching orthogonality, while at the same time producing the most trigonally compressed M' site with O2-M'-O2 = 82.4(2)°. Adjacent MO_6 and $M'O_6$ octahedra are rotated by approximately 30°, one relative to the other, along the C_3, c axis. The largest deviation, 2.7°, from this angle is observed in the Y-Al derivative.

The structure fields of the Ba derivatives are much more restricted than those of the Sr analogs. The compound $Ba_3In(BO_3)_3$ is the only Ba derivative containing M = M'. We have prepared several examples with M and M' being different cations of formal charge +3. No Al or Ga derivatives, however, could be

Table 10.5. Interatomic angles (°) for $Sr_6YAl(BO_3)_6$, $Sr_6ErSc(BO_3)_6$, $Sr_6HoSc(BO_3)_6$, $LaSr_6Sc(BO_3)_6$, and $Ba_6GdSc(BO_3)_6$.

	$Sr_6YAl(BO_3)_6$	$Sr_6ErSc(BO_3)_6$	$Sr_6HoSc(BO_3)_6$	$LaSr_6Sc(BO_3)_6$	$Ba_6GdSc(BO_3)_6$
O1- A -O1	155.5(3)	158.6(2)	157.4(1)	158.7(2)	159.7(2)
O1- A -O2	96.6(2)	90.7(1)	91.9(1)	88.7(2)	93.5(2)
	75.3(2)	77.3(1)	77.2(1)	80.4(2)	74.6(2)
	105.7(2)	109.4(1)	108.9(1)	109.2(2)	105.3(2)
O1- A -O3	51.9(2)	50.0(1)	50.7(1)	49.4(1)	48.2(2)
	85.2(3)	87.9(1)	87.1(1)	89.7(2)	86.0(2)
	72.6(3)	72.5(1)	72.4(1)	74.9(1)	73.9(2)
	70.4(2)	70.7(1)	70.4(1)	70.4(2)	71.9(2)
O2- A -O2	63.3(3)	62.1(6)	61.2(1)	62.1(2)	66.4(2)
	58.2(3)	61.7(2)	60.3(1)	60.2(2)	59.5(2)
O2- A -O3	75.1(2)	70.6(1)	71.4(1)	78.6(2)	77.7(2)
	78.0(2)	78.0(1)	78.1(1)	78.2(2)	80.3(2)
	74.4(2)	70.7(1)	71.8(1)	73.0(2)	73.6(2)
O3- A - O3	83.26(9)	85.0(2)	85.3(1)	83.8(2)	84.43(6)
	86.9(3)	86.2(1)	86.0(1)	86.0(1)	87.1(2)
O1- M -O1	93.1(3)	92.5(2)	92.3(1)	91.9(2)	93.4(2)
O2- M'-O2	84.5(3)	83.3(2)	83.7(2)	82.4(2)	84.5(2)
O1- B -O2	119(1)	117.3(5)	117.8(5)	118.1(6)	117.9(7)
O1- B -O3	121(1)	122.2(5)	121.2(5)	122.0(5)	120.2(7)
O2- B -O3	120(1)	120.5(5)	121.0(5)	119.9(6)	121.9(7)

crystallized. In the series $Ba_6LnIn(BO_3)_6$, incorporation of each lanthanide afforded the STACK structure. In the series $Ba_6LnFe(BO_3)_6$ only those compounds containing Ln = Sm, Eu, Gd, Tb, Dy, Ho, Y, and Er were found to form the structure, while in the series $Ba_6LnSc(BO_3)_6$ only those compounds containing Ln = La, Pr, Nd, Sm, Eu, Gd, Tb, and Dy could be formed. In the Fe and Sc series a sufficient size differential between these atoms and the Ln atoms must be present for the STACK structure to form. For the Fe series the minimum differential occurs at M = Er while for the Sc series it occurs at M = Dy. These limits are dictated by the formation of the layered-type phases $Ba_3Ln(BO_3)_3$ that were discussed in the previous report of this series. For the Fe compounds, the phases $Ba_3LnFe(BO_3)_3$ form when the radius of the Ln atoms is smaller than that of Er. For the Sc compounds, solid solutions $Ba_3(Ln,Sc)(BO_3)_3$ form in the layered structure type when Ln is smaller than Dy. The structures of STACK and the layered-type Ba phases are rather complex and the energetic difference between them can be quite small. An example of this behavior is given by the solid-solution series $Ba_6Dy_{2-x}Sc_x(BO_3)_6$. This series represents equilibria between the two end members $Ba_3Dy(BO_3)_3$ and $Ba_3Sc(BO_3)_3$ which both adopt the layered-type structure. As seen in Figure 10.6, an extensive solid solution exists in this series with retention of the layered structure except, at the stoichiometry $Ba_6DySc(BO_3)_6$ where a considerable expansion of the unit cell is observed with formation of the STACK structure.
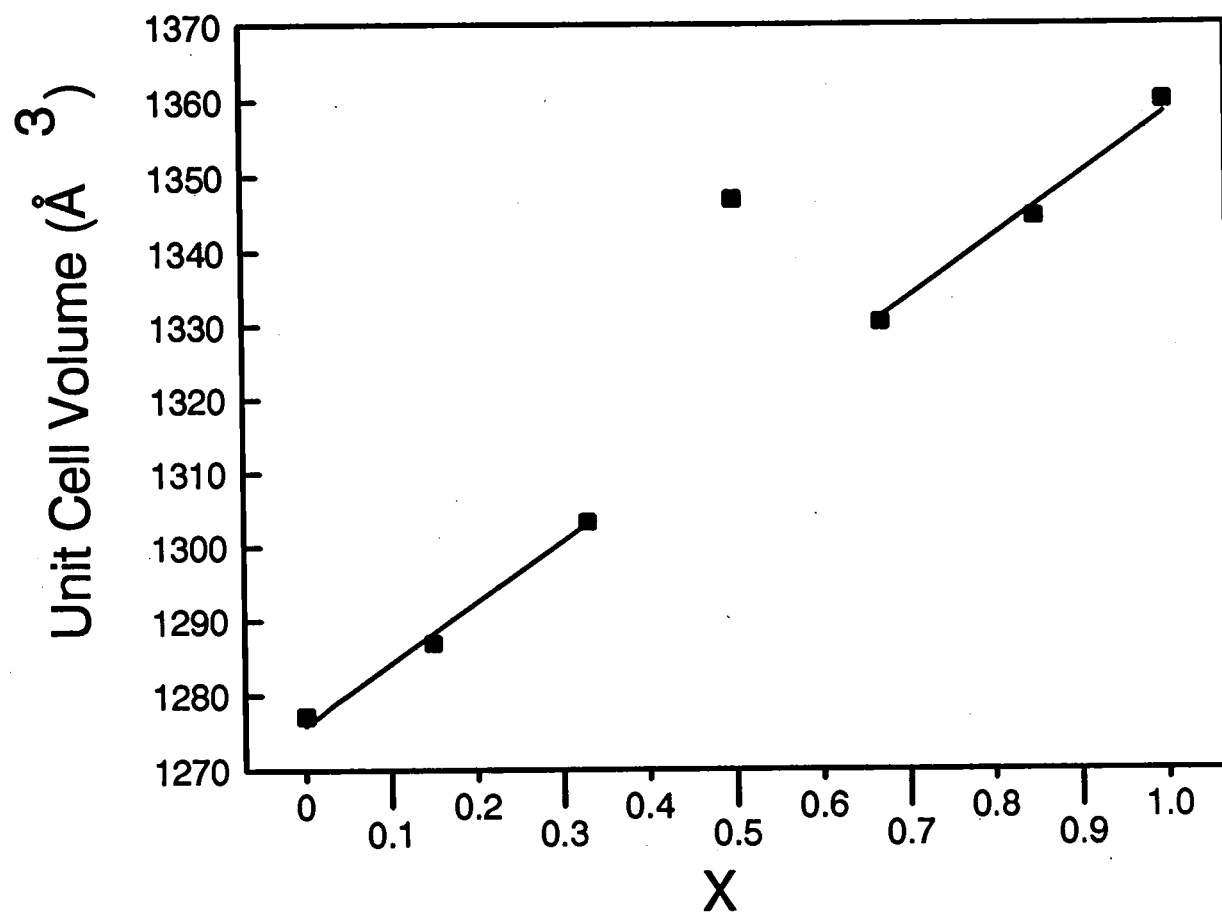
Figure 10.6. Cell parameters for the series $Ba_6Dy_{2-x}Sc_x(BO_3)_6$.

We also probed the relationship between the STACK and layered-type structures by examining the solid-solution series $Ba_{3-x}Sr_xSc(BO_3)_3$. In this series, the compound $Ba_3Sc(BO_3)_3$ forms the layered structure and $Sr_3Sc(BO_3)_3$ is a STACK derivative. As seen in Figure 10.7, a steady decrease in unit-cell volume in the range $0 < x < 2.25$ indicates a range of solubility of Sr atoms in the Ba layered structure. The zero slope in the range $2.25 < x < 2.6$ defines a region of immiscibility, i.e., the layered-type and STACK structures are present in equilibrium mixtures. In the range $2.6 < x < 3$, only the STACK structure is observed with a steadily decreasing unit-cell volume with increasing x. This region represents the solid solubility of Ba^{2+} in the STACK derivative. These results were extended with examination of the series $Sr_{3-x}Ca_xSc(BO_3)_3$. As seen from Figure 10.7, only small amounts of Ca may be incorporated ($x_{max} = 1.5$) into the structure in this way. The Ca atom is too small to occupy the large 9-coordinate A site where, for this derivative, the size of this site is largely determined by the integrity of the one-dimensional Sc borate chains. This result contrasts to the isostructural compounds $Ca_3(BO_3)_2$ and $Sr_3(BO_3)_2$ where the BO_3 groups are free to move in response to the size demands of the alkaline-earth atoms, maintaining in each case a 9-coordinate site in each structure.

We also synthesized compounds with M = +2 cation and M' = +4 cation. Highly crystalline samples were only realized with M = Sr.
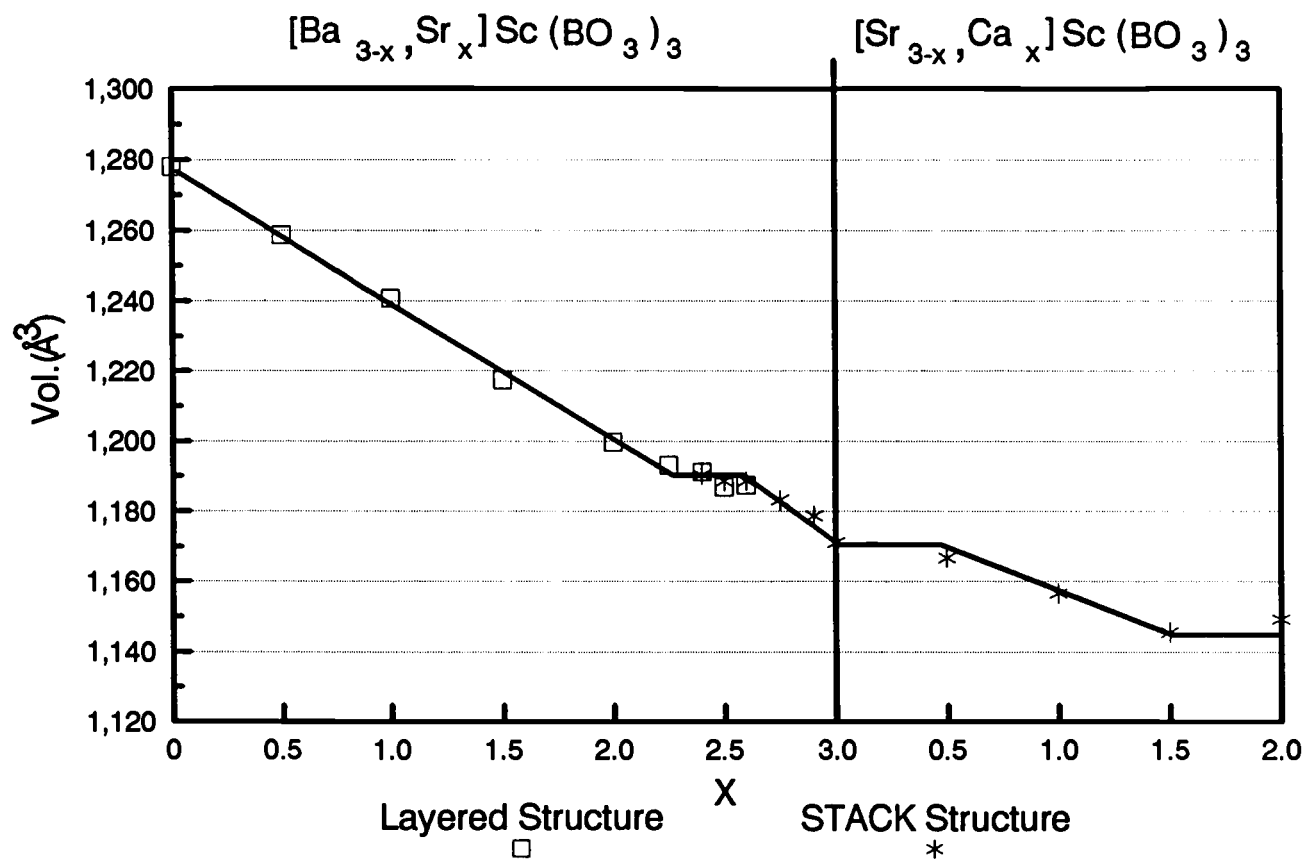
Figure 10.7. Unit cell volumes for the solid solution series $Ba_{3-x}Sr_xSc(BO_3)_3$ and $Sr_{3-x}Ca_xSc(BO_3)_3$.

Summary

The borates of composition $A_6MM'(BO_3)_6$ represent a broad new class of oxide. By utilizing appropriate charge-compensation techniques, nearly all +2, +3, or +4 ions of the elements in the periodic table can be incorporated into the structure. Analysis of the metrical details from single-crystal studies indicates little variation in nearest-neighbor interatomic angles. This feature, coupled with the centrosymmetric S_6 symmetry of the M and M' sites, indicates that physical properties will be primarily controlled by interatomic distances, the electronic nature of the A, M, and M' atoms, and stoichiometry.

Acknowledgments

References

1. K. I. Schaffers, T. Alekel III, P. D. Thompson, J. R. Cox, and D. A. Keszler, *J. Am. Chem. Soc.* **112**, 7068 (1990).

2. P. D. Thompson and D. A. Keszler, *Chem. Mat.* **1**, 292 (1989).

3. P. D. Thompson and D. A. Keszler, *Chem. Mat.* (1992), submitted.

4. Molecular Structure Corporation, *TEXSAN*, Structure Analysis Package, MSC (3200A Research Forest Drive, The Woodlands, TX 77381).

5. G. M. Sheldrick in "Crystallographic Computing 3" (G. M. Sheldrick, C. Krüger, and R. Goddard, Eds.) pp. 175-189, Oxford Univ. Press, Oxford, (1985).

6. N. Walker and D. Stuart, *Acta Cryst.* **A24**, 214 (1968).

7. R. D. Shannon, *Acta Cryst.* **A32**, 751 (1976).

CHAPTER 11

STRONTIUM SCANDIUM BORATE, STRONTIUM YTTRIUM ALUMINUM BORATE, AND LANTHANUM STRONTIUM MAGNESIUM BORATE

Kathleen I. Schaffers and Douglas A. Keszler

Borates have been extensively used for some time in the glass, ceramic, and porcelain industries to produce materials with small coefficients of thermal expansion. More recently, they have proven to be useful as optical materials and heterogeneous catalysts. The compounds BaB_2O_4 (1) and LiB_3O_5 are exceptional materials for frequency conversion of laser light at high powers to short wavelengths, and the compound $Cr^{3+}:ScBO_3$ (2) functions as a broadly tunable solid-state laser material. The compound $Cu_{2-x}Zn_xAl_6B_4O_{17}$ is one example of a borate that serves as a heterogeneous catalyst for the production of methanol.

We recently reported the existence of the largest structural family of borates discovered to date (3). The family has the nominal composition $A_6MM'(BO_3)_6$ where A = Sr, Ba, or large lanthanide and the elements M and M' are any of those cations having a +2, +3, or +4 formal oxidation state and a preference for octahedral coordination. The structure of the materials contains chains (Figure 11.1) that are comprised of octahedra occupied by atoms M or M' separated by triangular planar BO_3 groups. The distorted octahedron occupied by atom M' is smaller than that occupied by atom M. The sizes of the octahedra are primarily dictated by the interactions of the chain with the A atoms that link the chains into the three-dimensional structure.

We have prepared 135 compounds that crystallize in this structural type; the large number of derivatives results from the variety of elements that will occupy the A, M, and M' sites. We describe here the preparation of three types of derivatives. The compound $Sr_3Sc(BO_3)_3$ contains A = Sr and M = M' = Sc,
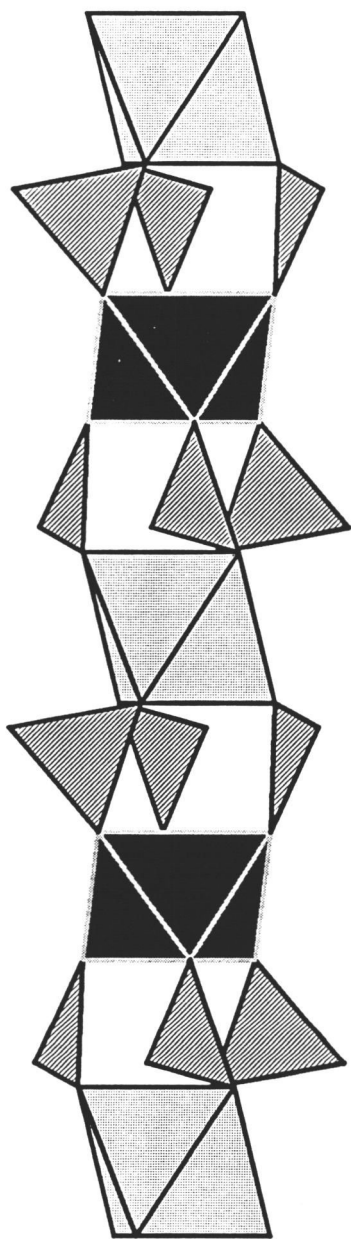
Figure 11.1. Drawing of a single chain in the structure of the family of borates $A_6MM'(BO_3)_6$.

a formally +3 cation. The compound $Sr_6YAl(BO_3)_6$ contains M = Y and M' = Al, two cations of formal charge +3 but of disparate sizes. The compound $La_2Sr_5Mg(BO_3)_6$ contains M = Sr and M' = Mg, cations of formal charge +2, and the larger La atom distributed on the A site.

Procedure

Standard high-temperature techniques are efficient means for the synthesis of the materials. These techniques have proven to be superior to heating precipitates from aqueous solutions formed with an assortment of reagents at various pH levels. To prepare the compounds, stoichiometric quantities of the reagents[1] are mixed and ground with a 3 mol% excess of B_2O_3. The use of the reagent B_2O_3 is preferred to boric acid, H_3BO_3, as the acid tends to froth on dehydration, subsequently wetting the walls of the crucible. The reagent B_2O_3, however, is difficult to retain in an anhydrous state (4). We dry B_2O_3 by heating it at 393 K for 3 days followed by melting in a Pt crucible at 1073 K for 3.5 h. A 3 mol% excess of the reagent is used in each synthesis to compensate for residual H_2O and minor volatilization losses during heating. Prior to use, $Sr(NO_3)_2$ is heated in a Pt crucible at 573 K for 3 days, and Sc_2O_3 is heated at 1173 K for 5 h in a Au crucible under flowing O_2.

The compounds are readily prepared by flash heating in a Pt crucible ground quantities of the starting materials; the furnace is set to the desired temperature followed by introduction of the samples. The initial heating is

---

[1]The reagents used in the syntheses are $Sr(NO_3)_2$ (reagent grade or Puratronic, Johnson-Matthey), Sc_2O_3 (99.0%, Boulder Scientific), Y_2O_3 (99.99%, Rare Earth Products), Al_2O_3 (99.99%, CERAC), $La(NO_3)_3 \cdot 6H_2O$ (99.9%, AESAR), $Mg(NO_3)_2 \cdot 2H_2O$ (Puratronic, Johnson-Matthey), and B_2O_3 (99.99%, ALFA).

performed at 923 K for 30 min and the second at 1023 K for 20 min. As oxides of nitrogen are released in these initial heatings, the furnace is placed in a fume hood. The sample is then reground and flash heated at 1303 K for 3 h. The crystallinity of the sample $Sr_6YAl(BO_3)_6$ is improved by annealing at 1373 K for 24 h.

Another method may be employed to reduce the particle sizes of the starting materials, thereby increasing their reactivity. Stoichiometric quantities of the reagents are first heated at 923 K for 1 h to decompose the nitrates. The resulting mixture, corresponding to 1 mmol of product, and 1.5 mL of 20% $NH_4OH(aq)$ (Baker, ultrapure, ULTREX) are placed in a 23 mL teflon container and heated in a Parr 4745 digestion bomb at 393 K for 16 h. The lid of the teflon container is removed after cooling, and the liquid is evaporated at 393 K. The sample is then flash heated as detailed above or according to the following schedule: 923 K, 1h; 998, 4h; 1098 K, 12 h; 1198 K, 12 h; and 1273 K, 24 h.

Properties

X-ray powder diffraction data for the compounds $Sr_3Sc(BO_3)_3$ and $Sr_6YAl(BO_3)_6$ are given in Table 11.1. Rhombohedral unit cell parameters for each of the compounds prepared by the two different synthetic methods are listed in Table 11.2. Cell parameters were determined by least-squares analysis of 10 reflections collected by using an automated Philips powder diffractometer and corrected with NBS Si standard 640b.

Differential thermal analysis of $Sr_3Sc(BO_3)_3$ prepared by the flash heating method indicates a melting point of $1233.9(4)°C$. The melting point of Au was used as a standard to correct the data. The derivatives $Sr_3Sc(BO_3)_3$ and $Sr_6YAl(BO_3)_6$ are particularly interesting as possible new laser materials when doped with the ion Cr^{3+}. Fluorescence spectra from samples of $Sr_3Sc_{0.98}Cr_{0.02}(BO_3)_3$ and $Sr_6YAl_{0.98}Cr_{0.02}(BO_3)_6$ prepared by flash heating exhibit maxima in their broad emission bands at 745nm.

Table 11.1 (a). $Sr_3Sc(BO_3)_3$ Diffraction Data[*]

2θ (°)	hkl	I/I_{100}
19.43	021	8
21.10	012	6
24.37	211	30
25.72	202	18
29.19/29.37/29.71	003/220/21$\bar{2}$	100
32.17	31$\bar{1}$	36
32.76	11$\bar{3}$	14
35.47	401	11
36.46	312	29
38.52	23$\bar{1}$	33
39.19	140	28
41.89/42.27	223/32$\bar{2}$	28
45.62	214	27
49.20/49.60	15$\bar{1}$/413	48
50.56	31$\bar{4}$	19
52.32/52.81	152/205	32
53.90/54.42	431/520	32
56.85	43$\bar{2}$	12

[*] $\lambda = 1.54184$ Å

Table 11.1 (b). $Sr_6YAl(BO_3)_6$ Diffraction Data[*]

2θ (°)	hkl	I/I_{100}
21.23	012	7
24.34	211	39
25.84	202	13
29.32/29.75	003/21$\bar{2}$	100
32.08	31$\bar{1}$	34
32.95	11$\bar{3}$	11
35.38	401	5
36.44	312	26
38.37	23$\bar{1}$	22
39.08	140	24
42.01	223	34
45.89	214	23
49.03/49.67	15$\bar{1}$/413	53
50.81	31$\bar{4}$	20
52.24	152	17
53.20/53.75/54.25	205/431/520	33
56.73	43$\bar{2}$	12

[*]$\lambda = 1.54184$ Å

Table 11.2. Unit Cell Data

	a (Å)	c (Å)	V (Å^3)
I. Flash synthesis			
$Sr_3Sc(BO_3)_3$	12.151(1)	9.178(1)	1173.6(1)
$Sr_6YAl(BO_3)_6$	12.194(1)	9.102(1)	1172.1(2)
$La_2Sr_5Mg(BO_3)_6$	12.318(1)	9.263(1)	1217.1(2)
II. NH$_4$OH synthesis			
$Sr_3Sc(BO_3)_3$	12.144(1)	9.184(1)	1173.0(1)
$Sr_6YAl(BO_3)_6$	12.179(1)	9.096(1)	1168.4(1)
$La_2Sr_5Mg(BO_3)_6$	12.319(1)	9.258(1)	1216.8(2)

References

1. D. Eimerl, L. Davis, S. Velsko, E. K. Graham, and A. Zalkin, *J. Appl. Phys.* **62**, 1968 (1987).

2. S. T. Lai, B. H. T. Chai, M. Long, and R. C. Morris, *IEEE J. Quant. Electron.* **QE-22**, 1931 (1986).

3. K. I. Schaffers, T. Alekel III, P. D. Thompson, J. R. Cox, and D. A. Keszler, *J. Am. Chem. Soc.* **112**, 7068 (1990).

4. J. D. MacKenzie, *J. Phys. Chem.* **63**, 1875 (1959).

CHAPTER 12

STRUCTURE AND OPTICAL FEATURES OF $Sr_3In(BO_3)_3$

Kathleen I. Schaffers and Douglas A. Keszler

Abstract

The structure of the compound $Sr_3In(BO_3)_3$ has been characterized by single-crystal X-ray diffraction. It crystallizes in the rhombohedral space group $R\bar{3}$(h) in a cell of dimensions $a= 12.182$ Å, $c= 9.186(2)$ Å, and $V= 1180.5(4)$ Å^3 with $Z=6$. Least squares refinement affords the final residuals $R=0.041$ and $R_w=0.051$. The structure consists of distorted In-centered octahedra bridged by BO_3 groups to form chains that extend along the c axis. The chains are connected by Sr atoms occupying an irregular nine-coordinate site. Results from Cr^{3+} and Eu^{3+} doping studies are also reported.

Introduction

Recently, we reported the existence of a new structural class of solid-state oxide (1). The class is represented by the formula $A_6MM'(BO_3)_6$ where A= Sr or Ba; M= Sc, Y, In, Bi, Ca, Cd, or a lanthanide; M'= Sc, Y, In, Mg, Al, Ga, Co, Ni, Zr, Cr, Mn, Hf, Rh, Fe, or a small lanthanide. The structure is characterized by the presence of chains formed by M- and M'-centered octahedra connected by BO_3 groups that propagate down the c axis of the trigonal cell. We have prepared several compounds with M=M', but in the Ba series only one derivative of this type has been found to exist - $Ba_3In(BO_3)_3$. As part of a comparative study between this unique compound and its Sr analog, I describe in this chapter the structural features and luminescence results from Cr^{3+} and Eu^{3+} doping studies of the material $Sr_3In(BO_3)_3$.

Experimental

A powder sample of the title compound was prepared by grinding together a stoichiometric ratio of $Sr(NO_3)_2$ (AESAR, 99.99%), In_2O_3 (AESAR, 99.99%), and B_2O_3 (ALFA, 99.99%) and heating in an alumina crucible at 923 K for 0.25 h, 1023 K for 0.25 h, and 1323 K for 12 h with intermittent grindings. The powder yielded an X-ray diffraction pattern that compares well to a pattern calculated with the computer program LAZY-PULVERIX (2) and the data from the single-crystal refinement that are presented below. Crystals of $Sr_3In(BO_3)_3$ were grown in a Pt crucible from a melt containing 25 mol% SrB_2O_4 as a flux. The sample was melted at 1548 K, slowly cooled to 1248 K at 6 K/h, then rapidly cooled to room temperature.

A clear, colorless crystal of approximate dimensions 0.10 x 0.07 x 0.30 mm was physically separated from the melt and mounted on a glass fiber with epoxy for structure determination. X-ray data were collected with a Rigaku AFC6R diffractometer equipped with Mo $K\alpha$ radiation. Unit cell parameters were obtained by automatic centering and least squares refinement with 16 peaks in the range $30 < 2\theta < 42°$. Intensity data covering the range of indices $0 \leq h \leq 18$, $-18 \leq k \leq 18$, and $-13 \leq l \leq 13$ were collected by using ω-2θ scans and a scan speed of $16°$/min. in ω. Three standard reflections measured after every block of 200 reflections exhibited no significant fluctuations. From 2987 data collected in the range $2 \leq 2\theta \leq 65°$, 758 unique observations were found to have $F_o^2 > 3\sigma(F_o^2)$. The systematic absences $-h + k + l \neq 3n$ are consistent with the Laue group $\bar{3}$.

The structure was determined by using computer programs from the TEXSAN crystallographic software package (3). The Sr atom was located by using the direct methods program MITHRIL (4), and the positions of the In atoms were determined by comparison with the isostructural compound $Sr_3Sc(BO_3)_3$ (5). The positions of the remaining atoms were determined by examining subsequent difference electron density maps. Following refinement with isotropic thermal parameters, the data were corrected for absorption with the program DIFABS (6) and averaged ($R_{int} = 0.089$). Final least squares refinement on F_o with those data having $F_o^2 > 3\sigma(F_o^2)$ and anisotropic thermal displacement coefficients on each atom resulted in the residuals R=0.041 and R_w=0.051. Analysis of the final difference electron density map revealed no peak greater than 0.5% of a Sr atom. Crystal data and final atomic parameters are listed in Tables 12.1 and 12.2, respectively.

Powder samples of $Sr_3In(BO_3)_3$ doped nominally with 2 and 50 mol% Cr^{3+} (Cr_2O_3, AESAR, 99.99%) were prepared according to the methods previously described. Steady-state room-temperature luminescence spectra of these samples were obtained on a computer-controlled right-angle spectrometer. Excitation provided by an Oriel 300 W Xe lamp was passed through a 50 cm water filter and focused onto the slits of a Cary model-15 prism monochromator. Selected excitation was focused onto the sample mounted on a copper sample holder within a quartz emission dewar. Luminescence was collected at a near-right angle to excitation, dispersed through an Oriel 22500 1/8 m monochromator, and detected

with a Hamamatsu R636 photomultiplier tube. The signal was collected and amplified with a Keithley model 602 picoammeter then converted to a digital signal for computer acquisition. Spectrometer control and data acquisition were achieved with programs written in this laboratory.

Table 12.1. Crystal Data for $Sr_3In(BO_3)_3$.

Formula Weight, amu	554.10
Crystal System	Rhombohedral
Space Group	$R\bar{3}$(h) (#148)
a, Å	12.182(2)
c, Å	9.186(2)
V, Å^3	1180.5(4)
Z	6
D_{calc}, g cm^{-3}	4.676
F(000)	1500
Diffractometer	Rigaku AFC6
Radiation	Mo Kα (λ=0.71069) graphite-monochromated
Data Collection	$0 \leq h \leq 18$, $-18 \leq k \leq 18$ $-13 \leq l \leq 13$
No. of Unique Observations ($F_o^2 > 3\sigma(F_o^2)$)	758
R	0.041
R_w	0.051
Maximum Shift in Final Cycle	0.02

Table 12.2. Positional parameters and B_{eq} for $Sr_3In(BO_3)_3$.

	x	y	z	B_{eq}[a]
Sr	-0.13523(5)	-0.37287(5)	0.47366(6)	0.22(2)
In1	0	0	½	0.11(2)
In2	0	0	0	0.04(2)
B	-0.3895(6)	-0.5291(7)	0.5972(7)	0.3(2)
O1	0.1230(4)	-0.0325(4)	0.6454(5)	0.4(1)
O2	-0.1632(4)	-0.6146(4)	0.4497(5)	0.3(1)
O3	0.0043(5)	-0.2584(4)	0.6836(5)	0.4(1)

[a]$B_{eq} = (8\pi^2/3)\Sigma_i\Sigma_j U_{ij} a_i^* a_j^* \mathbf{a}_i \cdot \mathbf{a}_j$

Results and Discussion

A sketch of the structure of $Sr_3In(BO_3)_3$ is shown in Figure 12.1. It is isostructural to the previously reported compound $Sr_3Sc(BO_3)_3$ (5), and is characterized by chains of octahedra that propagate down the c axis, Figure 12.2. Each of the chains is composed of alternating octahedra of different size isolated by BO_3 groups, Figure 12.3. Selected bond distances and angles are listed in Table 12.3.

The Sr atom occupies an irregular nine-coordinate site bridging the octahedral chains, Figure 12.1. The Sr-O bond distances range from 2.487(5)-2.856(5) Å and compare to the distances 2.500(2)-2.857(2) Å for $Sr_3Sc(BO_3)_3$ (5) and 2.539(7)-2.93(2) Å for $SrNaBO_3$ (7).

The B atoms reside in a planar triangular site having slight deviations from trigonal symmetry as evidenced by O-B-O angles of 118.8(6), 119.7(6), and 121.4(5)°. B-O bond distances of 1.398(8), 1.381(8), and 1.366(8) Å are typical when compared with an average length of 1.38(2) Å for $SrNaBO_3$ (7), 1.37(1) Å for $SrBe_2(BO_3)_2$ (8), and a length of 1.40 Å calculated using crystal radii (9).

The O atoms occupy irregular 4- and 5-coordinate sites. Atoms O1 and O2 are 4- and 5-coordinate, respectively, with bonds to Sr, In, and B. Atom O3 has five bonds to Sr and B forming an irregular square pyramid.

Two crystallographically independent In atoms are present in the structure. Each occupies an octahedron that is either trigonally elongated or compressed
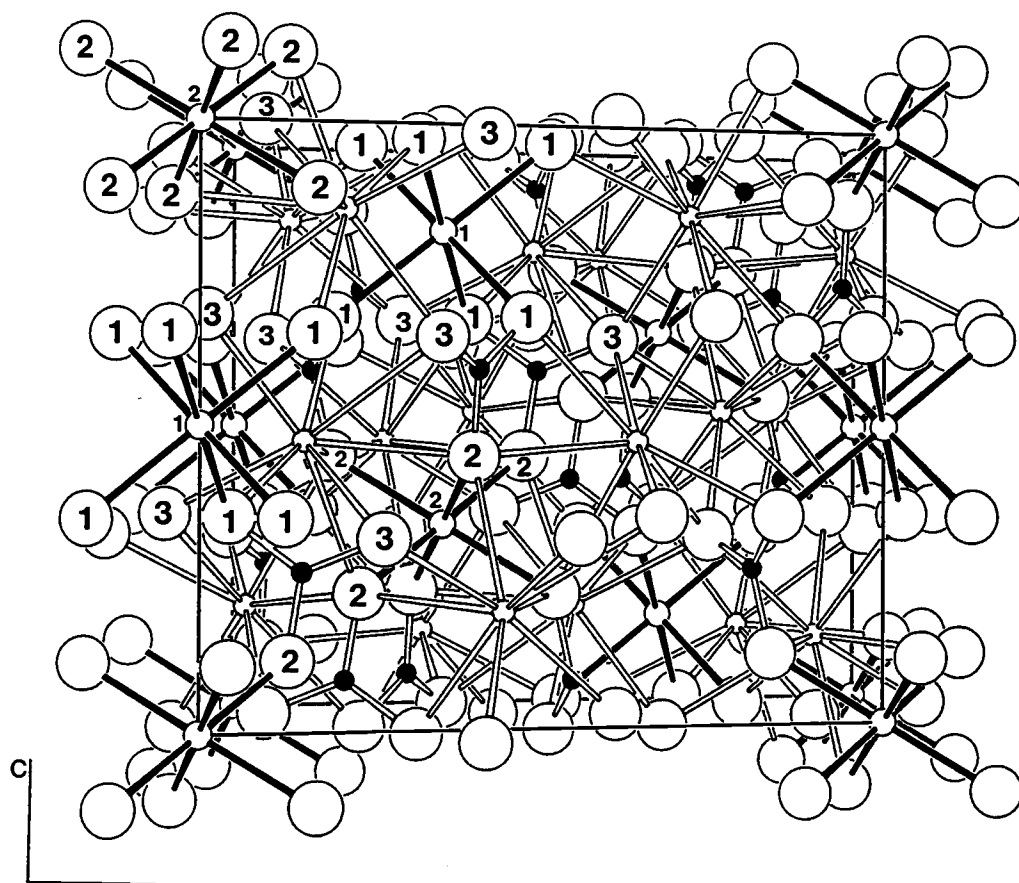
Figure 12.1. Sketch of the unit cell of $Sr_3In(BO_3)_3$ as viewed orthogonal to the c axis. The large open circles represent O atoms, the small open circles with open bonds represent Sr atoms, the open circles with filled bonds represent In atoms, and the filled circles with open bonds represent B atoms.
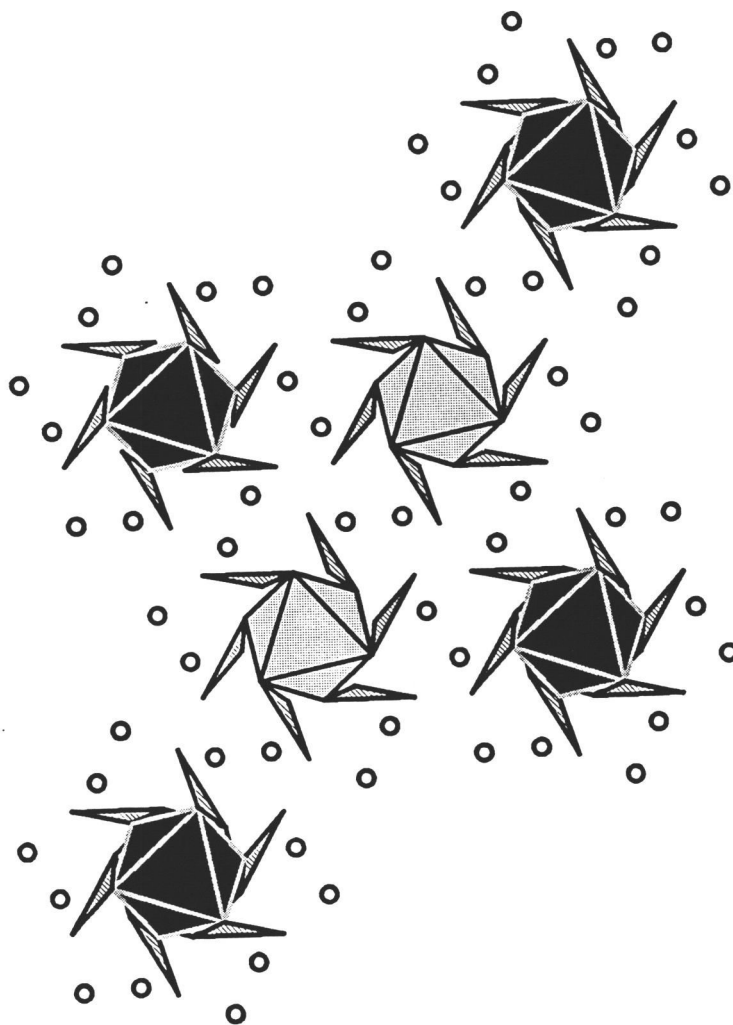
Figure 12.2. View of $Sr_3In(BO_3)_3$ along the c axis.
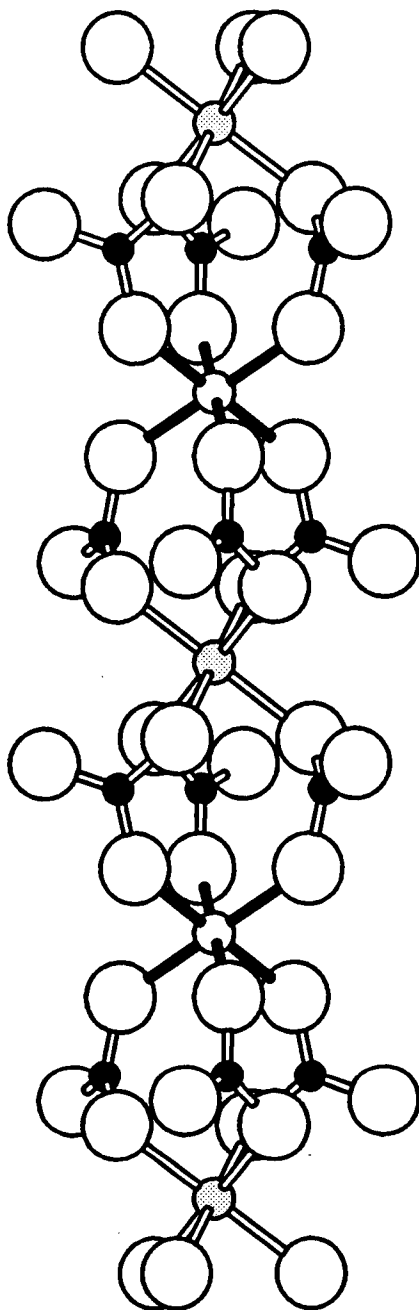
Figure 12.3. Sketch of a chain of In octahedra as viewed orthogonal to the c axis.

Table 12.3. Selected Bond Distances (Å) and Angles (°) for $Sr_3In(BO_3)_3$.

In1-O1	2.186(4)	O1-In1-O1	93.4(2)
In2-O2	2.127(4)	O2-In2-O2	83.0(2)
Sr-O1	2.542(5)	O1-Sr-O2	93.3(1)
	2.719(5)	O1-Sr-O2	109.1(1)
Sr-O2	2.798(5)	O1-Sr-O3	84.7(1)
	2.704(5)	O1-Sr-O3	73.0(1)
	2.720(4)	O1-Sr-O3	69.3(1)
Sr-O3	2.487(5)	O1-Sr-O3	52.6(1)
	2.856(5)	O2-Sr-O2	61.6(2)
	2.796(5)	O2-Sr-O3	74.8(1)
	2.585(5)	O2-Sr-O3	51.0(1)
		O3-Sr-O3	113.22(3)
		O3-Sr-O3	86.6(2)
B-O1	1.398(8)	O1-B-O2	121.4(5)
B-O2	1.381(8)	O1-B-O3	118.8(6)
B-O3	1.366(8)	O2-B-O3	119.7(6)

along the c axis. The elongated octahedron has In1-O1 interatomic distances of 2.186(4) Å and an O1-In1-O1 angle of 93.4(2)° while the compressed octahedron has an In2-O2 interatomic distance of 2.127(4) Å and an O2-In2-O2 angle of 83.0(2)°. The In-O distances compare to a distance of 2.17 Å (9), calculated from crystal radii for an In atom in an octahedral site, and 2.172 Å for In_2O_3 (10).

The distortions of the octahedral sites derive from the constraints imposed by their interactions with the neighboring Sr atoms. The elongation of the In1 site originates from its interaction with two Sr atoms that share the edge O3···O3. The span Sr-O3-Sr and the hinging about the edge O3···O3 dictate the degree of O1-In1-O1 angle opening, Figure 12.4. In contrast, the compressed site shares a face with the Sr polyhedra so that the O2-In2-O2 angle of 83.0(2)° is constrained by the area of the Sr-O1 face. These interactions afford two chemically and crystallographically distinct octahedral sites that can accommodate metals with varying degrees of order depending on their relative sizes as outlined in Chapter 10.

Luminescence

Room-temperature luminescence studies were done for $Sr_3In(BO_3)_3$:2 mol% Cr^{3+} and $Sr_6InCr(BO_3)_6$ where 50 mol% Cr was substituted onto the distorted octahedral sites to give the stoichiometric $A_6MM'(BO_3)_6$ formula. The spectra contain broad emission bands centered at 740 nm and 750 nm, respectively, as seen in Figures 12.5 and 12.6. These broad features are similar to those seen for Cr^{3+} doped samples of $Sr_2LiScB_4O_{10}$ (11), $Sr_3Sc(BO_3)_3$ (5), and $LiCaAlF_6$ (12). This band derives from a d→d transition that is predominantly $^4T_{2g} \rightarrow {}^4A_{2g}$ in
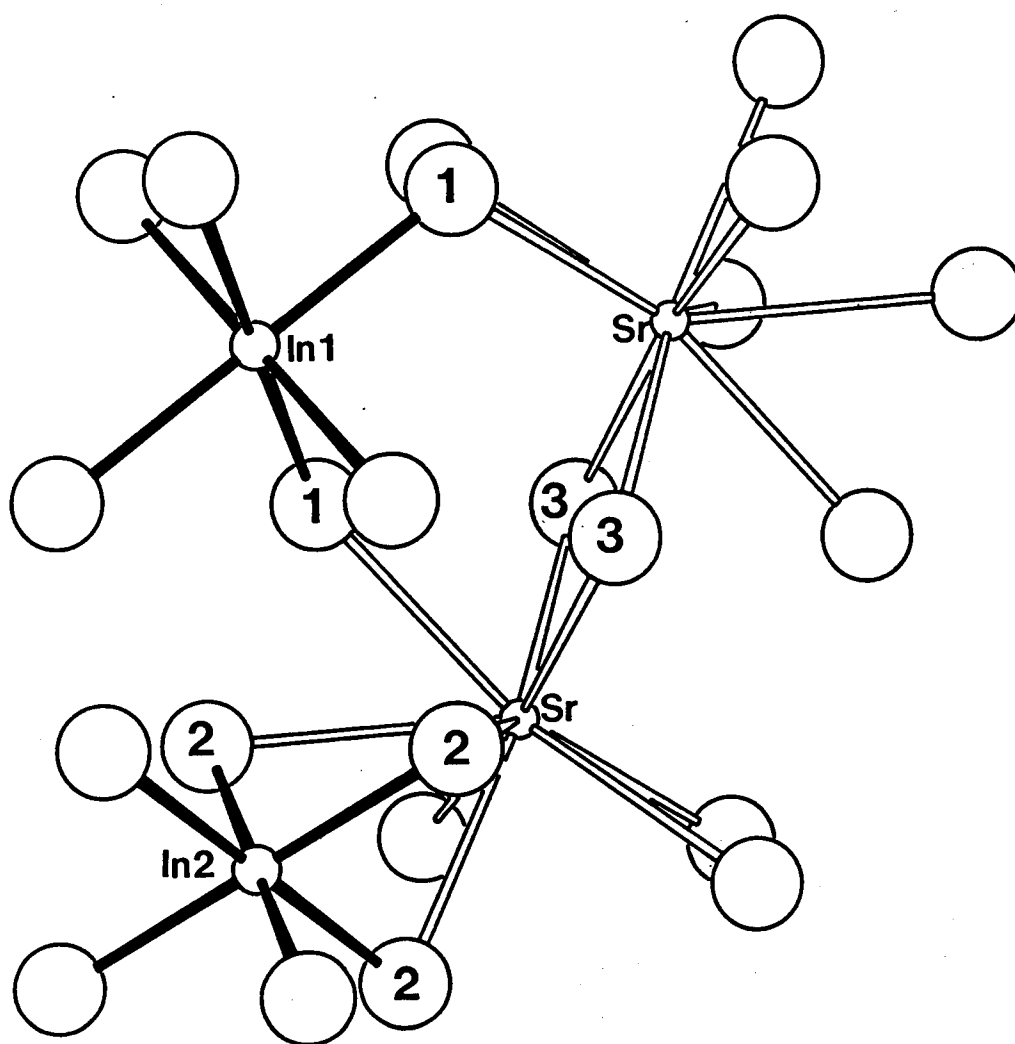
Figure 12.4. View of the In-O-Sr bonding interactions.
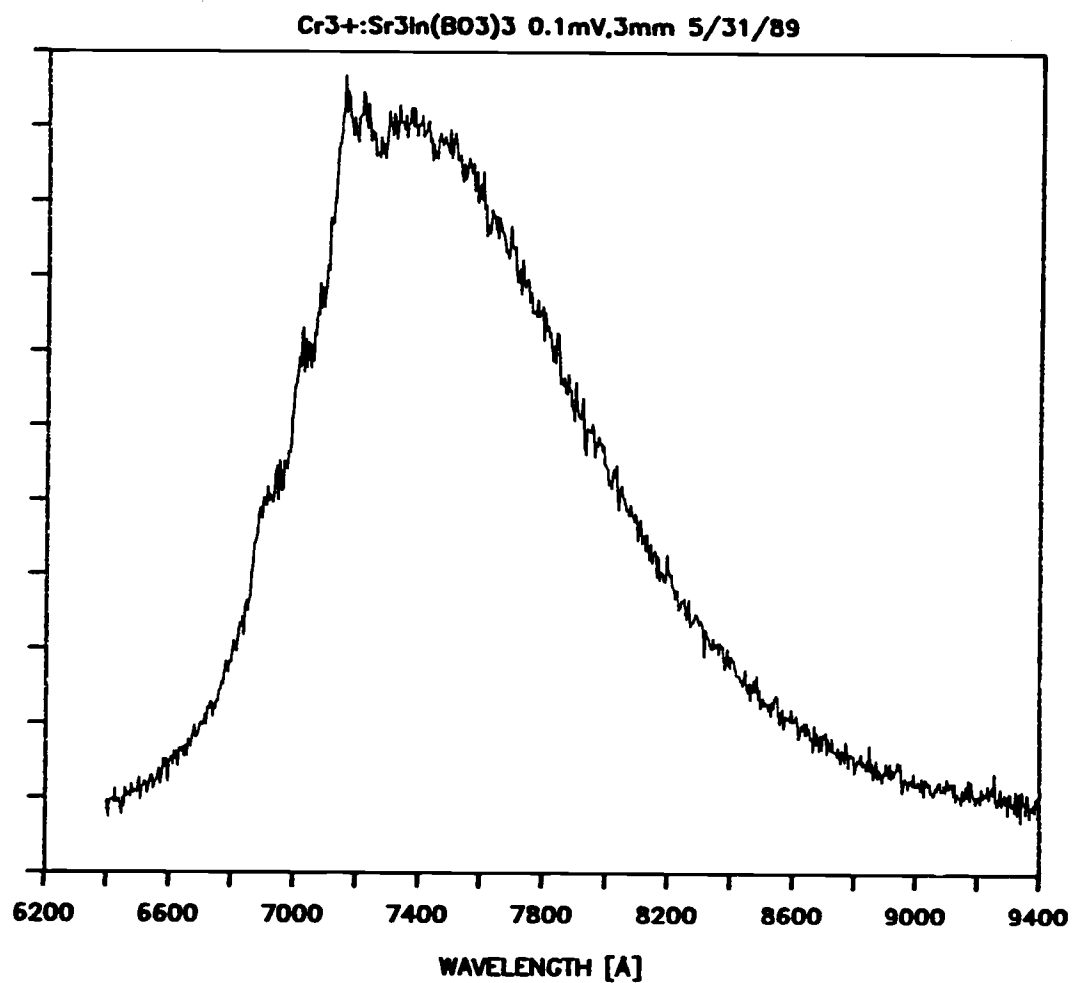
Figure 12.5. Room-temperature emission spectrum of $Sr_3In(BO_3)_3$:2 mol% Cr^{3+}.
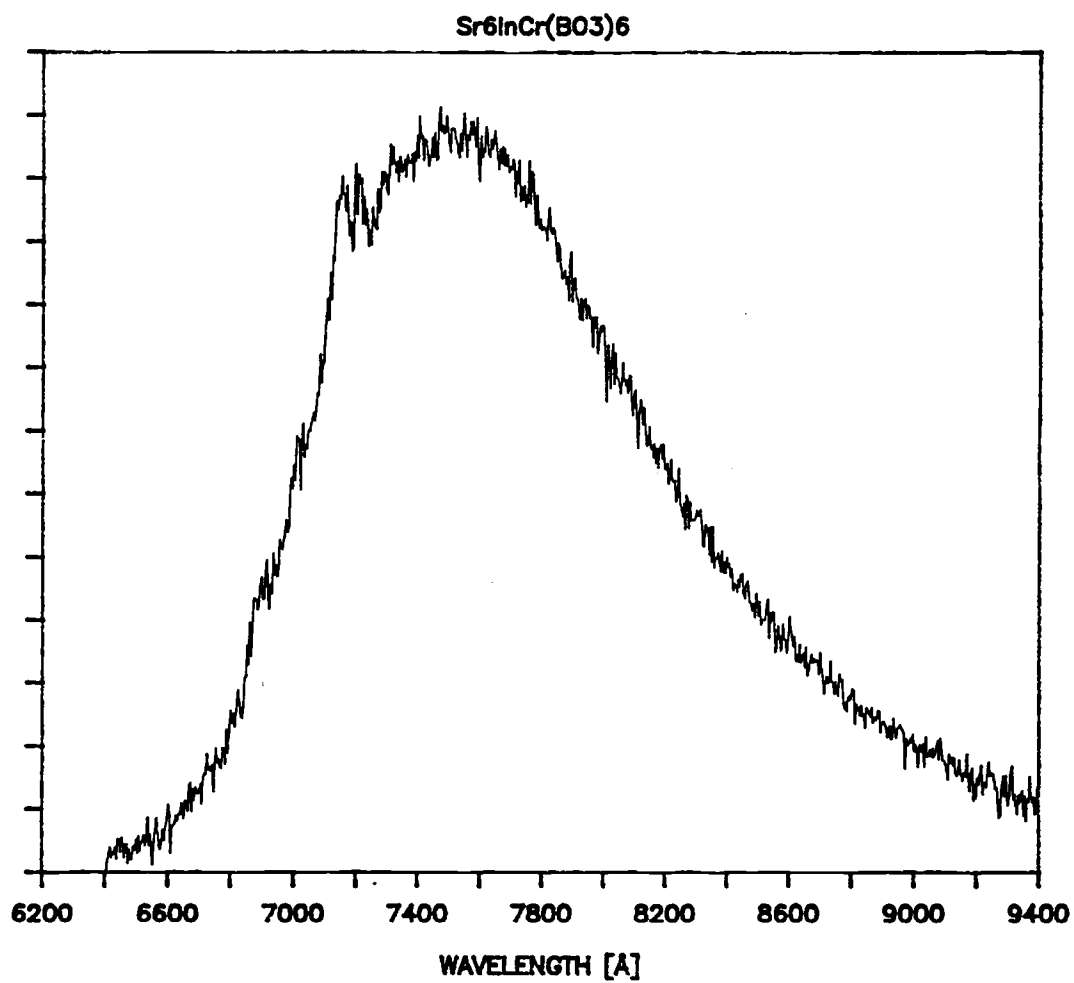
Figure 12.6. Room-temperature emission spectrum of $Sr_6InCr(BO_3)_6$.

character and an essential characteristic for a tunable solid-state laser. Each spectrum also contains sharp features centered at approximately 710 nm that are indicative of $^2E_g \rightarrow ^4A_{2g}$ transition. These broad and sharp bands indicate the proximity of the Cr^{3+} ion emission to the $^4T_{2g}$ - ^2E_g crossover point as seen in the Tanabe-Sugano diagram provided in Figure 12.7.

Blasse and coworkers have concluded that the ion Eu^{3+} is an effective probe for determining if the crystallographic site it occupies is centrosymmetric or non-centrosymmetric (13). If the site is centric, magnetic-dipole transitions are allowed while electric-dipole transitions are forbidden. If the site is acentric, electric- and magnetic-dipole transitions are both allowed but the magnetic-dipole transitions are much weaker and may appear to be absent. By inspecting the peaks in Eu^{3+} emission spectra that represent these transitions, site preference for the ion Eu^{3+} can be determined.

In the compound $Sr_3In(BO_3)_3$, emission peaks representing both magnetic-[$^5D_o \rightarrow ^7F_1$] and electric- [$^5D_o \rightarrow ^7F_2$] dipole transitions are present with approximately equal intensities, Figure 12.8. The assignments of the transitions were made by comparison with the spectra of previously reported Eu^{3+} doped materials (13-14). These results indicate that Eu^{3+} likely populates both the A and M sites. This result is consistent with the crystal-chemical data presented in Chapter 10, where the large lanthanide La^{3+} was found to prefer occupation of the large 9-coordinate site and the smaller lanthanides Ho^{3+} and Er^{3+} occupy the smaller 6-coordinate M and M' sites. For lanthanides of intermediate size, such as the ion Eu^{3+}, a

distribution over the A and M sites is to be expected. The earlier results also indicate that charge compensation is maintained in the doped Eu^{3+} system by placing Sr^{2+} ions in place of In^{3+} ions on the M site.
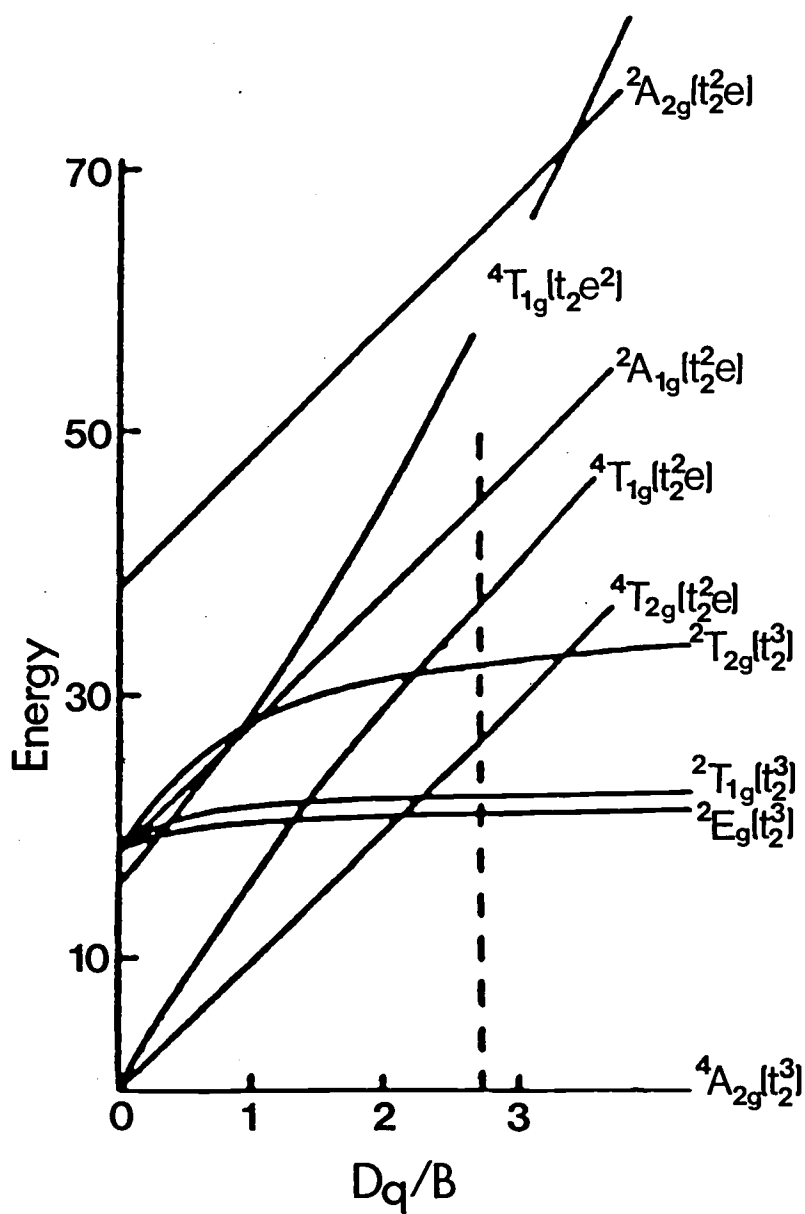
Figure 12.7. Tanabe-Sugano diagram for a d³ transition metal in an octrahedral environment.
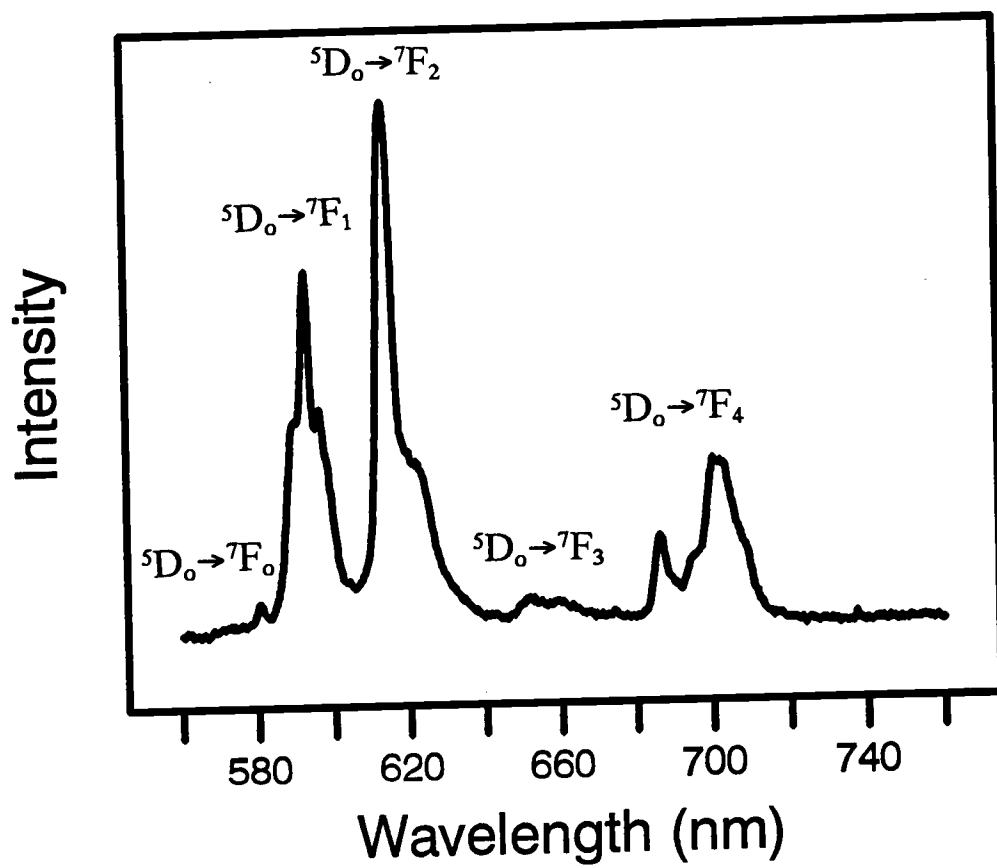
Figure 12.8. Luminescence spectrum of Eu^{3+} doped $Sr_3In(BO_3)_3$.

Acknowledgments

References

1. K. I. Schaffers, T. Alekel III, P. D. Thompson, J. R. Cox, and D. A. Keszler, *J. Am. Chem. Soc.* **112**, 7068 (1990).

2. K. Yvon, W. Jeitschko, and E. Parthe, *J. Appl. Cryst.* **10**, 73 (1977).

3. Molecular Structure Corporation, TEXSAN, Structure Analysis Package, MSC (3200A Research Forest Drive, The Woodlands, Tx 77381, USA).

4. G. J. Gilmore (1983), MITHRIL: A Computer Program for the Automatic Solution of Crystal Structures from X-ray Data. University of Glasgow, Scotland.

5. P. D. Thompson and D. A. Keszler, *Chemistry of Materials* **1**, 292 (1989).

6. N. Walker and D. Stuart, *Acta Crystallogr., Sect. A***39**, 158 (1983).

7. H. Sun and D. A. Keszler, results to be published.

8. K. I. Schaffers and D. A. Keszler, *J. Solid State Chem.* **85**, 270 (1990).

9. R. D. Shannon and C. T. Prewitt, *Acta Crystallogr. B***25**, 925 (1969).

10. M. Marezio, *Acta Crystallogr.* **20**, 723 (1966).

11. P. D. Thompson and D. A. Keszler, *Solid State Ionics*, **32/33**, 521 (1989).

12. L. L. Chase, and S. A. Payne, *IEEE J. Quantum Electron.*, in press.

13. G. Blasse and A. Bril, *Phil. Tech. Rev.*, **31**, 303 (1970).

14. G. Blasse, *J. Solid State Chem.*, **2**, 27 (1970).

CHAPTER 13

CRYSTAL STRUCTURE OF $Sr_2LiInB_4O_{10}$

Kathleen I. Schaffers and Douglas A. Keszler

Abstract

Strontium Lithium Indium Pyroborate, $Sr_2LiInB_4O_{10}$, $M_r = 500.23$, monoclinic, $P2_1/n$, $a = 12.637(1)$, $b = 5.251(1)$, $c = 13.748(1)$ Å, $\beta = 116.94(1)°$, $V = 813.2(4)$ Å^3, $Z = 4$, $D_x = 4.085$ g cm^{-3}, Mo Kα, $\lambda = 0.71069$ Å, $\mu = 154.94$ cm^{-1}, $F(000) = 912$, $T = 298$ K, $R = 0.060$ for 1731 reflections having $F_o^2 \geq 3\sigma(F_o^2)$. The structure is composed of a 3-dimensional SrO_7 polyhedral framework with hexa-coordinate In and penta-coordinate Li atoms in interstitial sites. Pyroborate groups form layers extending in the plane (-101).

Introduction

While searching for a suitable lithium borate flux for crystal growth of the compound $Sr_3In(BO_3)_3$ (1), we discovered an interaction of the In compound with the metaborate $LiBO_2$ to form the new material $Sr_2LiInB_4O_{10}$. Here, we describe the structure of this material which is a derivative of the Sc analog $Sr_2LiScB_4O_{10}$ (2).

Experimental

Crystals of the title compound were grown from a melt containing 40 mol% SrO made by heating $Sr(NO_3)_2$ (AESAR, ACS) in air, 6 mol% In_2O_3 (ALFA, ultrapure), 28 mol% $LiBO_2$ (AESAR, 99.9%), and 26 mol% B_2O_3 (ALFA, 99.98%). The sample was melted in a Pt crucible at 1303 K and slowly cooled at 10 K/h to 1003 K then 88 K/h to 300 K. The resulting crystals were washed in hot distilled water to remove any excess $LiBO_2$. A clear, colorless plate of dimensions 0.15(1) x 0.07(1) x 0.25(1) mm was selected for X-ray structure analysis, and data were collected on a Rigaku AFC6R single-crystal diffractometer equipped with Mo $K\alpha$ radiation. Accurate unit cell parameters were derived by automatic centering and least squares analysis of 20 peaks collected in the range $30 \leq 2\theta \leq 36°$. The ω-2θ scan technique was used to collect 2627 data in the range of indices $0 \leq h \leq 17$, $0 \leq k \leq 7$, and $-19 \leq l \leq 19$. From these measurements, 1731 unique reflections having $F_o^2 \geq 3\sigma(F_o^2)$ were obtained to $\sin \theta/\lambda = 1.36$ Å^{-1}. The intensities of three standard reflections measured after each segment of 200 data exhibited no significant decay during the collection.

The structure was refined by utilizing the *TEXSAN* crystallographic software package (3). All atomic coordinates were determined by comparison to the isostructural compound $Sr_2LiScB_4O_{10}$. Positional parameters and isotropic thermal factors were refined for each atom, followed by correction for absorption (transmission coefficients= 0.74 - 1.44) with the program *DIFABS* (4) and full refinement with anisotropic thermal parameters on each atom. Final least-squares

yminimization on F_o with those 1731 reflections having $F_o{}^2 \geq 3\sigma(F_o{}^2)$ and 163 variables gave the residuals R= 0.060 and wR= 0.067 where the function $\Sigma w(|F_o|-|F_c|)^2$ is minimized with weights derived from counting statistics $[w=1/\sigma^2(F_o)]$. Atomic form factors are from *International Tables for X-ray Crystallography* (5). Final refinement afforded values of S= 2.11, and $\Delta/\sigma= 0.01$. Analysis of the final difference electron density map revealed maximum and minimum peaks corresponding to 1.05% and 0.81% of a Sr atom, respectively. Atomic parameters are given in Table 13.1.

A powder sample was made by grinding a stoichiometric combination of the reagents $Sr(NO_3)_2$ (AESAR, ACS), In_2O_3 (ALFA, ultrapure), $LiNO_3$ (Mallinckrodt, reagent grade), and B_2O_3 (ALFA, 99.98%) and heating in a Pt crucible at 923 K for ½ h. The sample was reground and heated at 1123 K for 16 h to give a single phase as identified by using X-ray powder diffraction.

Table 13.1. Positional parameters and B_{eq} for $Sr_2LiInB_4O_{10}$.

	x	y	z	B_{eq}
Sr1	0.6849(1)	0.3752(2)	0.35420(9)	0.84(3)
Sr2	0.64955(9)	0.4304(2)	0.62330(8)	0.79(3)
In	0.63264(6)	0.4272(2)	0.88365(6)	0.60(2)
Li	0.116(2)	0.110(5)	0.600(1)	1.5(8)
B1	0.913(1)	0.435(3)	0.771(1)	0.7(4)
B2	0.603(1)	0.861(3)	0.209(1)	0.9(4)
B3	0.594(1)	-0.100(3)	0.448(1)	0.8(4)
B4	0.927(1)	0.415(2)	0.551(1)	0.6(4)
O1	0.6469(7)	0.157(2)	0.7712(6)	0.8(3)
O2	0.8902(7)	0.186(2)	0.5047(6)	1.0(3)
O3	0.6830(7)	0.024(2)	0.5326(6)	1.2(3)
O4	0.5528(6)	0.622(2)	0.1914(7)	0.9(3)
O5	0.5710(7)	0.649(2)	0.4420(6)	0.9(3)
O6	0.8548(7)	0.627(2)	0.5091(6)	1.1(3)
O7	0.5203(6)	0.074(2)	0.3658(6)	1.0(3)
O8	0.5370(7)	0.072(2)	0.1463(7)	1.2(3)
O9	0.8619(7)	0.209(2)	0.7261(6)	0.7(3)
O10	0.7114(7)	-0.089(2)	0.2875(7)	1.1(3)

$$B_{eq} - (\frac{8\pi^2}{3})\sum_i \sum_j U_{ij} a_i^* a_j^* a_i \cdot a_j$$

Discussion

The O environment about each cation may be discerned by examination of the labeled sketch of the unit cell provided in Figure 13.1. The compound contains 7-coordinate Sr, 6-coordinate In, 5-coordinate Li, and 3-coordinate B atoms. The integrity of the structure may be viewed as arising from a 3-dimensional SrO_7 polyhedral framework (Figure 13.2). The remaining cations occupy sites associated with oblong tunnels that extend along the b axis. As indicated by the descriptive formula $Sr_2LiIn(B_2O_5)_2$ the compound contains a pyroborate group; the group is essentially flat in the principal atomic plane (-101). Cations of like type also form sheets parallel to this plane so the structure adopts a common trait of borate and carbonate structures where cations are interleaved between layers of planar oxoanions.

Two chemically and crystallographically distinct Sr atoms are present in the structure. The Sr2 atom is 7-coordinate occupying a distorted tetragonal base-trigonal base environment having an average Sr2-O bond length of 2.57(6) Å. This length is equal within uncertainty to the average bond length of 2.58(7) Å for Sr2-O in the compound $Sr_2LiScB_4O_{10}$ and 2.59(6) Å for 7-coordinate Sr in $Sr_2Cu(BO_3)_2$ (6). All of the Sr2O_7 polyhedra share edges with three neighboring Sr2O_7 polyhedra in the plane orthogonal to [-101] to form a two dimensional network as shown in Figure 12.3; shared edges include the following O pairs - one O5$\cdots$O5 and two O1$\cdots$O9. These layers repeat at intervals of half a unit cell. The Sr1 atom is bound to seven O atoms at lengths ranging from 2.468(8) - 2.805(9) Å
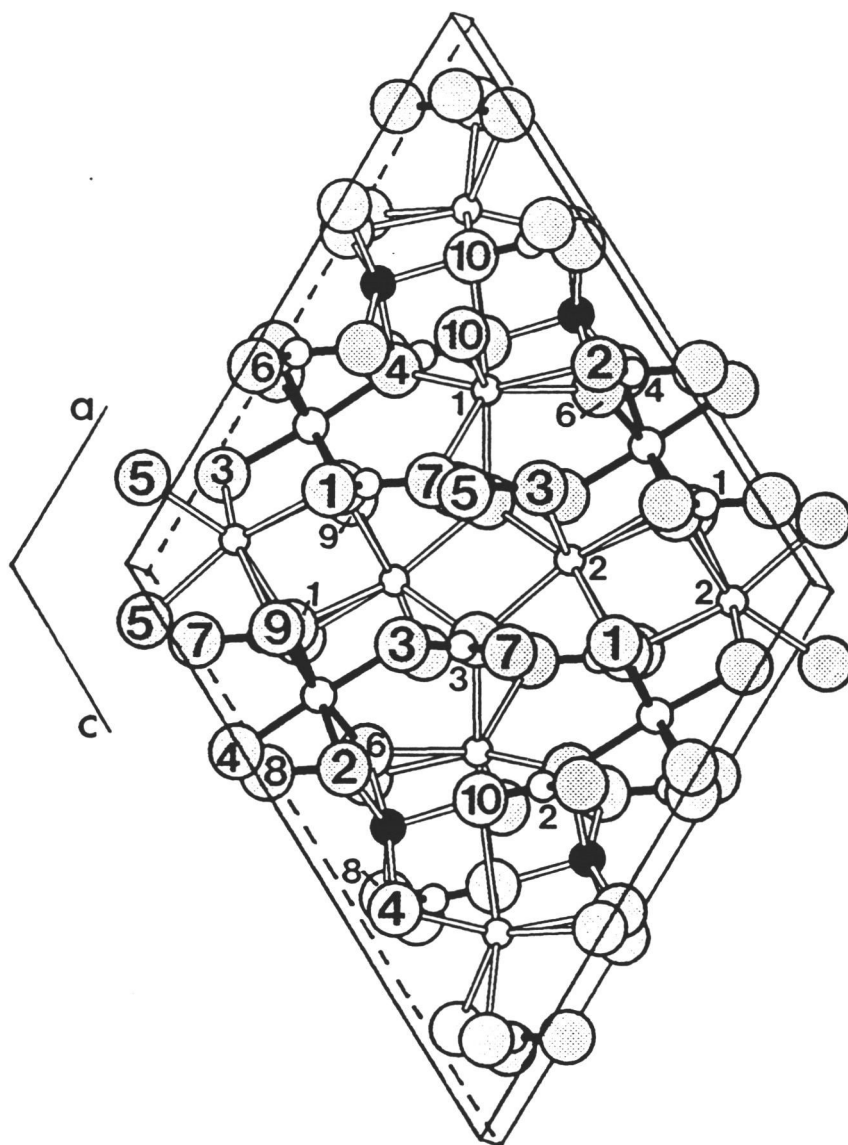
Figure 13.1. Labeled drawing of the unit cell of $Sr_2LiInB_4O_{10}$ as viewed down the b axis where the small open circles with open bonds are Sr, the larger shaded circles with open bonds are Li, the larger open circles with shaded bonds are In, the small open circles with shaded bonds are B, and the largest shaded circles are O atoms.
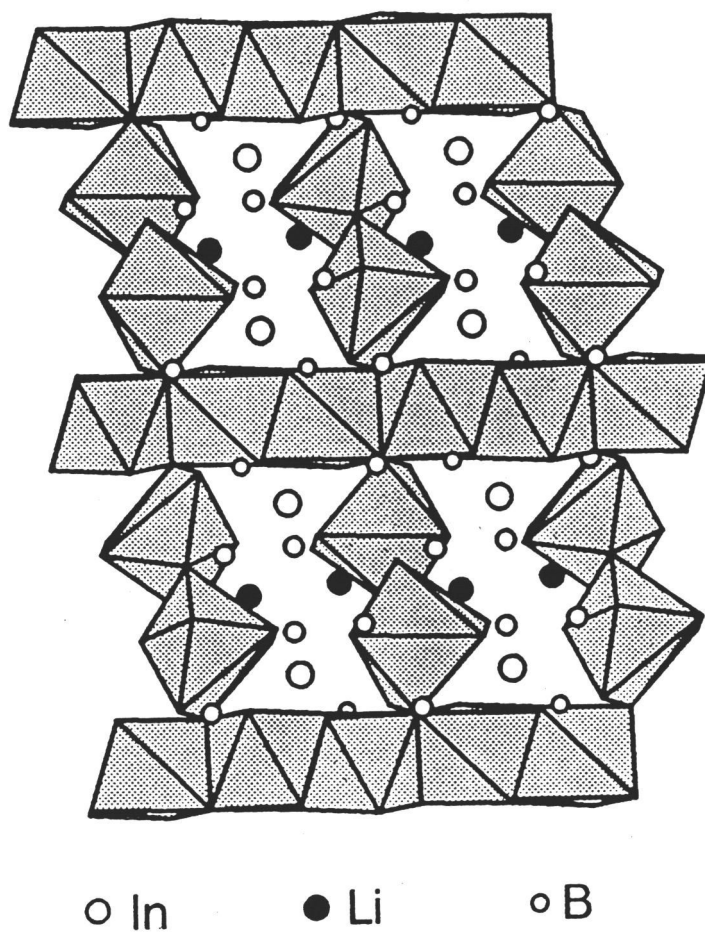
Figure 13.2. Perspective view of the SrO$_7$ polyhedral framework along [010].
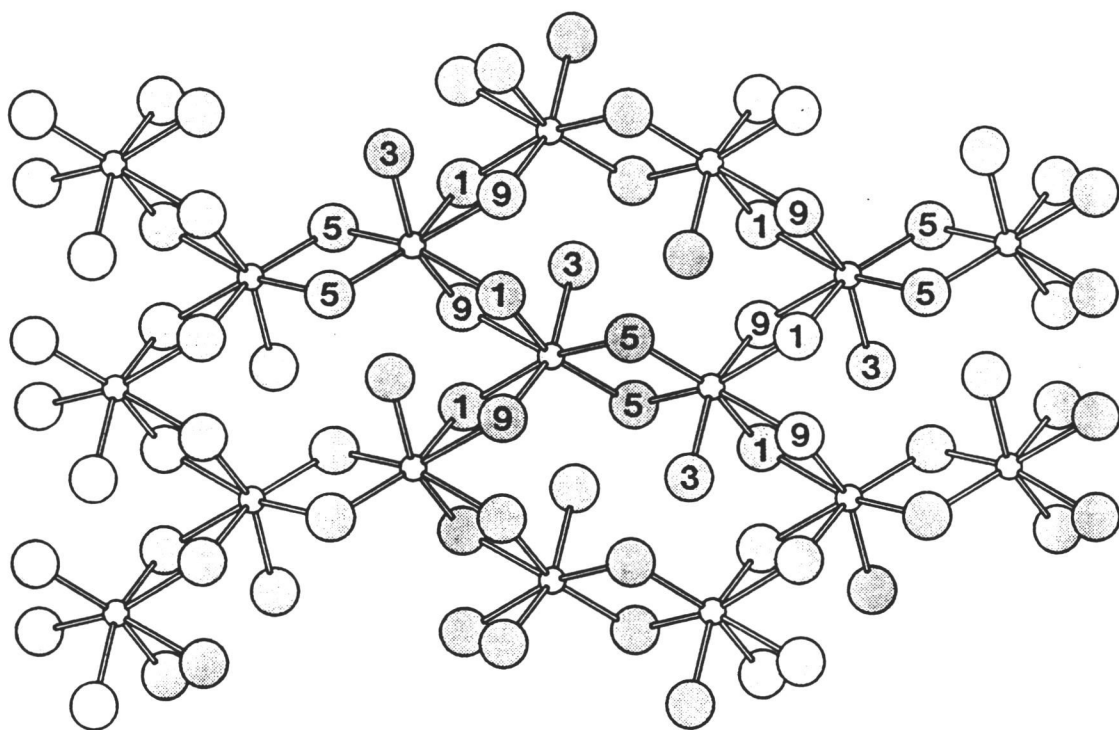
Figure 13.3. Sketch of the two-dimensional Sr2-O network extending in the

plane (-101).

with three additional O atoms, O3, O8, and O10, at the distances 3.078(9), 3.059(8), and 3.023(9) Å, respectively. In the material $Sr_2LiScB_4O_{10}$ the Sr1-O bond lengths range from 2.478(3) - 2.745(4) Å, comparing closely to those observed for the In-derivative. Adjacent Sr1 atoms link through atom O10 creating double chains that propagate in the b direction. The chains of Sr1 environments bridge two layers of $Sr2O_7$ polyhedra through atoms O5 to form the 3-dimensional Sr-O polyhedral framework constructed in Figure 13.2.

The five O atoms about the Li atom form a distorted square pyramid. Li-O distances range from 2.02(2) - 2.19(3) Å and compare to the distance of 2.06 Å calculated from crystal radii (7). A long Li-O2 interaction of 2.58(2) Å would provide a distorted octahedral environment for the Li atom. From a bond-valence calculation (8), this interaction contributes approximately 7% of the univalent charge to the Li atom. Considering this interaction, a link is formed between adjacent LiO_5 polyhedra thereby creating edge-sharing Li_2O_{10} dimers with a Li⋯Li separation of 3.19(4) Å. The corresponding long Li-O2 interaction in the Sc analog is 2.67(1) Å.

The In atoms occupy distorted octahedral environments aligned in discreet rows along the b axis. The octahedra, however, are separated in these rows by B_2O_5 groups so that the In atoms are completely isolated from one another. The average In-O distance of 2.14(3) Å is comparable to lengths of 2.18(5) Å (9) in In_2O_3, 2.127(4) and 2.186(4) Å in $Sr_3In(BO_3)_3$ (1), and 2.17 Å calculated with crystal radii for a 6-coordinate In atom.

Each pyroborate layer is formed from one type of group with sheets of $B1B3O_5$ units and $B2B4O_5$ units alternately stacking along [-101]. B-O lengths range from 1.33(2) - 1.42(1) Å and compare to 1.342(7) - 1.432(7) Å for $Sr_2LiScB_4O_{10}$, 1.33 - 1.38 Å for $Mg_2B_2O_5$ (10), and 1.353(3) - 1.438(3) Å for $Na_4B_2O_5$ (11). The angles across the bridging O atoms, B1-O7-B3, 137(1)°, and B2-O8-B4, 131(1)°, are similar to those in the compound $Sr_2LiScB_4O_{10}$, 133.8(4)° and 129.2(4)°, respectively. Terminal BO_2 groups for each pyroborate anion are twisted from coplanarity by 10.5° for the $B1B3O_5$ unit and 3.1° for $B2B4O_5$ unit which compare to 13.8° and 1.1° for the corresponding anions in the Sc analog. Similar calculations have been performed on pyroborate anions for a variety of compounds (12) and deviations from planarity have been found to range from 0 to 76.8°.

The ten crystallographically distinct O atoms in the structure have coordination numbers of three or four. Corresponding environments may be discerned from examination of Table 13.2.

Table 13.2. Selected Bond Distances (Å) and Angles (°) for Sr₂LiInB₄O₁₀.

Sr1 -O2	2.671(8)	O2-Sr1-O3	61.0(2)
-O4	2.468(8)	O2-Sr1-O5	112.5(2)
-O5	2.678(9)	O2-Sr1-O6	53.3(3)
-O6	2.599(8)	O2-Sr1-O10	72.5(2)
-O7	2.675(8)	O4-Sr1-O5	81.1(3)
-O10	2.679(9)	O4-Sr1-O8	63.3(3)
-O10	2.805(9)	O4-Sr1-O10	50.1(2)
-O3	3.078(9)	O5-Sr1-O6	76.7(3)
-O8	3.059(8)	O5-Sr1-O7	72.6(3)
-O10	3.023(9)	O6-Sr1-O7	128.9(3)
		O7-Sr1-O10	72.7(3)
		O8-Sr1-O10	47.5(2)
		O10-Sr1-O10	69.7(2)
Sr2 -O1	2.502(8)	O1-Sr2-O1	100.6(2)
-O1	2.600(8)	O1-Sr2-O3	89.1(3)
-O3	2.602(9)	O1-Sr2-O3	77.1(3)
-O5	2.505(8)	O1-Sr2-O9	69.5(3)
-O5	2.546(8)	O1-Sr2-O9	53.1(3)
-O9	2.666(8)	O3-Sr2-O5	94.9(3)
-O9	2.593(8)	O3-Sr2-O9	63.5(2)
		O5-Sr2-O5	81.2(3)
		O5-Sr2-O9	113.3(3)
		O9-Sr2-O9	103.3(2)

Table 13.2 (cont.)

In -O1	2.165(8)	O1-In-O2	176.8(3)
-O2	2.165(9)	O1-In-O3	96.7(3)
-O3	2.140(8)	O1-In-O4	90.2(3)
-O4	2.105(7)	O2-In-O3	86.1(3)
-O6	2.114(9)	O2-In-O4	87.1(3)
-O9	2.139(8)	O3-In-O9	80.8(3)
		O6-In-O9	172.9(3)
Li -O2	2.09(3)	O2-Li-O4	76.3(7)
-O4	2.15(2)	O2-Li-O6	92.7(8)
-O6	2.18(2)	O2-Li-O10	100(1)
-O8	2.19(3)	O4-Li-O8	85.4(8)
-O10	2.02(2)	O6-Li-O10	95.9(8)
-O2	2.58(2)	O8-Li-O10	107(1)
		O2-Li-O2	94.5(8)
B1 -O1	1.37(1)	O1-B1-O7	123(1)
-O7	1.39(1)	O1-B1-O9	119(1)
-O9	1.36(2)	O7-B1-O9	117(1)
B2 -O4	1.37(2)	O4-B2-O8	121(1)
-O8	1.42(2)	O4-B2-O10	123(1)
-O10	1.33(2)	O8-B2-O10	116(1)
B3 -O3	1.37(2)	O3-B3-O5	126(1)
-O5	1.34(2)	O3-B3-O7	111(1)
-O7	1.42(1)	O5-B3-O7	123(1)

Table 13.2 (cont.)

B4 -O2	1.34(1)	O2-B4-O4	120.0(9)
-O4	1.39(1)	O2-B4-O8	118(1)
-O8	1.42(1)	O4-B4-O8	122(1)
		B1-O7-B3	137(1)
		B2-O8-B4	131(1)

Acknowledgments

References

1. J. R. Cox, K. I. Schaffers, and D. A. Keszler, *J. Solid State Chem.* (1992) to be published.

2. P. D. Thompson and D. A. Keszler, *Solid State Ionics.* **32/33**, 521 (1989).

3. Molecular Structure Corporation. (1989). *TEXSAN, Structure Analysis Package.* MSC (3200A Research Forest Drive, The Woodlands, TX 77381).

4. N. Walker and D. Stuart, *Acta Cryst. A***39**, 158 (1983).

5. *International Tables for X-ray Crystallography* (1974). Vol IV. Birmingham: Kynoch Press. (Present distributor: Kluwer Academic Publishers, Dordrecht).

6. R. W. Smith and D. A. Keszler, *J. Solid State Chem.* **81**, 305 (1989).

7. R. D. Shannon, *Acta Cryst. A***32**, 751 (1976).

8. I. D. Brown, "The Bond Valence Method: An Empirical Approach to Chemical Structure and Bonding." *Structure and Bonding in Crystals II.* (Editors: M. O'Keeffe & A. Navrotsky). Academic Press, Inc., 1 (1981).

9. M. Marezio, *Acta Cryst.* **20**, 723 (1966).

10. Y. Takéuchi, *Acta Cryst.* **5**, 574 (1952).

11. V. H. König, R. Hoppe, and M. Jansen, *Z. anorg. allg. Chem.* **449**, 91 (1979).

12. P. D. Thompson, J. Huang, R. W. Smith, and D. A. Keszler, *J. Solid State Chem.* **95**, 126 (1991).

Bibliography

Abdullaev, G. K., and K. S. Mamedov, *Sov. Phys. Crystallogr.* **19**, 98 (1974).

Alekel III, T., and D. A. Keszler, *Acta Cryst.* **C48**, in press (1992).

Alekel III, T., and D. A. Keszler, *J. Solid State Chem.* (1992), to be submitted.

Bajdina, I. A., V. V. Bakakin, N. V. Podberizskaja, B. I. Alekseev, L. R. Bacanova, and V. S. Pavlijucenko, *Z. Strukt. Khim.* **19**, 125 (1978).

Ballman, A. A., *Amer. Mineral.* **47**, 1380 (1962).

Bartl, H., and W. Schuckmann, *Neues Jahrb. Mineral., Monatsh.*, 253 (1966).

Baucher, P. A., and M. G. B. Cervelle, *Acta Cryst.* **B32**, 2211 (1976).

Baur, W. H., and E. Tillmanns, *Z. Kristallogr.* **131**, 213 (1970).

Blasse, G., *J. Solid State Chem.*, **2**, 27 (1970).

Blasse, G., A. Bril, and J. de Vries, *J. Electrochem. Soc.: Solid State Science* **115(9)**, 977 (1968).

Blasse, G., and A. Bril, *Phil. Tech. Rev.*, **31**, 303 (1970).

Block, S., and A. Perloff, *Acta Cryst.* **20**, 274 (1965).

Bondareva, O. S., M. A. Simonov, Yu. K. Egorov-Tismenko, and N. V. Belov, *Sov. Phys. Crystallogr.* **23**, 269 (1978).

Bosenberg, W. S., W. S. Pelouch, and C. L. Tang, *Appl. Phys. Lett.* **55**, 1952 (1989).

Brown, I. D., "The Bond Valence Method: An Empirical Approach to Chemical Structure and Bonding." *Structure and Bonding in Crystals II.* (Editors: M. O'Keeffe & A. Navrotsky). Academic Press, Inc., 1 (1981).

Brunton, G., *Acta Cryst. B* **29**, 2294 (1973).

Burns, J. H., *Acta Cryst.* **15**, 1098 (1962).

CRC Handbook of Laser Science and Technology, M. J. Weber, Ed., CRC Press: Boca Raton, 1986, Vol. 3.

Caird, J. A., S. A. Payne, P. R. Staver, A. J. Ramponi, L. L. Chase, and W. F. Krupke, *IEEE J. Quantum Electron.* **24**, 1077 (1988).

Chase, L. L., and S. A. Payne, *IEEE J. Quantum Electron.*, in press.

Chen, C., Y. Wu, A. Jiang, B. Wu, G. You, R. Li, and S. Lin, *J. Opt. Soc. Am. B* **6(4)**, 616 (1989).

Chen, C. T., *Sci Sinica* **22**, 756 (1979).

Chen, C., and G. Liu, *Ann. Rev. Mater. Sci.* **16**, 203 (1986).

Chen, C., B. Wu, A. Jiang, and G. You, *Sci. Sin., Ser B* **28**, 235 (1985).

Chen, C., Y. Wu, and R. Li, *J. Cryst. Growth* **99**, 790 (1990).

Chen, D., M. S. Hopkins, and J. T. Lin, *Technical Digest, Advanced Solid-State Lasers*, 11 (1992).

Cox, J. R., and D. A. Keszler, *Chem. Mat.*, in press (1992).

Cox, J. R., K. I. Schaffers, and D. A. Keszler, *J. Solid State Chem.* (1992) to be published.

Dana, J. D., *Manual of Mineralogy*, (Eds. C. Klein and C. S. Hurlbut, Jr., John Wiley & Sons, 1977).

De Villiers, J. P. R., *The American Mineralogist.* **56**, 758 (1971).

Ebbers, C. A., L. Davis, M. Webb, S. P. Velsko, and D. A. Keszler, *IEEE J. Quant. Electron.*, in press.

Ebbers, C., and S. Velsko, Lawrence Livermore National Laboratories, (Properties of $K_2La(NO_3)_5 \cdot 2H_2O$) to be submitted.

Ebrahimzadeh, M., A. J. Henderson, and M. H. Dunn, *IEEE J. Quant. Electron.* **26(7)**, 1241 (1990).

Eckardt, R. C., H. Masuda, Y. X. Fan, and R. L. Byer, *IEEE J. Quantum Electron.* **26(5)**, 922 (1990).

Eimerl, D., *IEEE J. Quant. Electron.* **QE-23**, 575 (1987).

Eimerl, D., L. Davis, S. Velsko, E. K. Graham, and A. Zalkin, *J. Appl. Phys.* **62**, 1968 (1987).

Eimerl, D., L. Davis, S. Velsko, E. K. Graham, and A. Zalkin, *J. Appl. Phys.* **62(5)**, 1 (1987).

Eimerl, D., S. Velsko, L. Davis, and F. Wang, *Prog. Crystal Growth Charact.*, **20**, 59 (1990).

Fang, J. H., P. D. Robinson, and Y. Ohya, *Amer. Miner.* **57**, 1345 (1972).

Fink, M. J., K. J. Haller, R. West, and J. Michel, *J. Am. Chem. Soc.* **106**, 822 (1984); Also, see M. O'Keeffe and G. V. Gibbs, *J. Phys. Chem.* **89**, 4574 (1985).

Fix, A., T. Schroder, and R. Wallenstein, *Laser Optoelektron.* **23**, 106 (1991).

Flook, R. J., H. C. Freeman, F. Hug, and J. M. Rosalky, *Acta Cryst. B* **29**, 903 (1973).

Fon, Y. X., R. Schlecht, M. W. Qin, D. Luo, A. D. Jiang, and Y. C. Huang, *Technical Digest, Advanced Solid-State Lasers*, 311 (1992).

Franken, P., A. Hill, C. Peters, and G. Weinreich, *Phys. Rev. Lett.* **7**, 118 (1961).

Fröhlich, R., *Z. Kristallogr.* **168**, 109 (1984).

Garcia, M. J., W. A. Sibley, C. A. Hunt, and J. M. Spaeth, *J. Luminescence* **42**, 35 (1988).

Geller, S., *Amer. Min.* **56**, 18 (1971).

Gilmore, G. J., (1983), MITHRIL: A Computer Program for the Automatic Solution of Crystal Structures from X-ray Data. University of Glasgow, Scotland.

Guenther, R. D., *Modern Optics*, (John Wiley & Sons, Inc., 1990).

Harris, L. A., and H. L. Yakel, *Acta Crystallogr.* **22**, 354 (1967).

International Tables for X-ray Crystallography (1974). Vol. IV. Birmingham: Kynoch Press. (Present distributor: Kluwer Academic Publishers, Dordrecht).

Kato, K., *IEEE J. Quant. Electron.* **QE-22**, 1013 (1986).

König, V. H., R. Hoppe, and M. Jansen, *Z. anorg. allg. Chem.* **449**, 91 (1979).

Krogh-Moe, J., *Acta Cryst.* **B30**, 1178 (1974).

Kurtz, S. W., and T. T. Perry, *J. Appl. Phys.* **39**, 3798 (1968).

Lai, S. T., "Highly efficient emerald laser," presented at the Int. Laser Sci. Conf., Oct. 21-24, 1986, Seattle, WA, paper THH2.

Lai, S. T., B. H. T. Chai, M. Long, and R. C. Morris, *IEEE J. Quant. Electron.* **QE-22**, 1931 (1986).

Lalama, S. J., and A. F. Garito, *Phys. Rev. A* **20(3)**, 1179 (1979).

Leligny, H., and J. C. Monier, *Acta Cryst.* **B35**, 569 (1979).

Leskelä, M., T. Keskentalo, and G. Blasse, *J. Solid State Chem.* **59**, 272 (1985).

Lin, W., H. Qingzhen, Z. Zicong, Y. Xiangde, D. Guiqin, and L. Jinhkui, *J. Solid State Chem.*, **89**, 16 (1990).

Luce, J. L., K. I. Schaffers, and D. A. Keszler, *Inorg. Chem.* (1992), in preparation.

MacKenzie, J. D., *J. Phys. Chem.* **63**, 1875 (1959).

Marezio, M., *Acta Crystallogr.* **20**, 723 (1966).

Martinez-Ripoll, M., S. Martinez-Carrera, S. Garcia-Blanco, *Acta Cryst.* **B27**, 672 (1971).

Molecular Structure Corporation, TEXSAN, Structure Analysis Package, MSC (3200A Research Forest Drive, The Woodlands, TX 77381, USA).

Moulton, P. F., *Laser Focus/Electro-Optics*, 56 (August 1987).

Nagai, T., and M. Ihara, *Yogyo-Kyokai-Shi* **80**[11], 432 (1972).

Nardelli, M., L. Cavalca, and G. Fava, *Gazz. Chim. Ital.* **87**, 1232 (1957).

Nebel, A., and R. Beigang, *Technical Digest, Advanced Solid-State Lasers*, 8 (1992).

Paulus, V. H., *Z. Anorg. Allg. Chem.* **369**, 38 (1969).

Payne, S. A., L. L. Chase, L. K. Smith, W. L. Kway, and H. W. Newkirk, *J. Appl. Phys.* **66**, 1051 (1989).

Payne, S. A., L. L. Chase, H. W. Newkirk, L. K. Smith, and W. F. Krupke, *IEEE J. Quantum Electron.* **24**, 2243 (1988).

Payne, S. A., L. L. Chase, L. K. Smith, W. L. Kway, and H. W. Newkirk, *J. Appl. Phys.* **66(3)**, 1051 (1989).

Payne, S. A., L. L. Chase, and G. D. Wilke, *J. Luminescence* **44**, 167 (1989).

Payne, S. A., L. L. Chase, and G. D. Wilke, *Phys. Rev. B* **37**, 998 (1988).

Perloff, A., and S. Block, *Acta Cryst.* **20**, 274 (1966).

Reynolds, T. A., and D. A. Keszler, *Chem. Mat.* (1992), submitted.

Saubat, B., M. Vlasse, and C. Fouassier, *J. Solid State Chem.* **34**, 271 (1980).

Schaffers, K. I., and D. A. Keszler, *Acta Cryst. C* (1992), in press.

Schaffers, K. I., and D. A. Keszler, *Chem. Mat.* (1992) to be published.

Schaffers, K. I., and D. A. Keszler, *J. Solid State Chem.* **85**, 270 (1990).

Schaffers, K. I., T. Alekel III, P. D. Thompson, J. R. Cox, and D. A. Keszler, *J. Am. Chem. Soc.* **112**, 7068 (1990).

Schuckmann, W., *Neues Jb. Miner. Mh.* **80** (1968).

Schäfer, U. L., *Neues Jahrb. Mineral., Monatsh.*, 75 (1968).

Schlatti, M., *Tschermaks miner. petrogr. Mitt.* **12**, 463 (1968).

Shäfer, U. L., and H.-J. Kuzel, *Neues Jb. Miner. Mh.* **4 & 5**, 131 (1967).

Shand, M. L., and S. T. Lai, *IEEE J. Quantum Electron.* **QE-20**, 105 (1984).

Shannon, R. D., *Acta Cryst. A***32**, 751 (1976).

Shannon, R. D., and C. T. Prewitt, *Acta Crystallogr., Sect. B* **25**, 925 (1969).

Sheldrick, G. M., "Crystallographic Computing 3," Eds. G. M. Sheldrick, C. Krüger, and R. Goddard, pp. 175-189, Oxford University Press, Oxford (1985).

Simpson, H. J., Jr. and R. E. Marsh, *Acta Cryst.* **20**, 550 (1966).

Smith, D. K., and C. F. Cline, *Acta Crystallogr.* **18**, 393 (1965).

Smith, R. W., Ph.D. Dissertation, Oregon State University (1989).

Smith, R. W., and D. A. Keszler, *Acta Crystallogr., Sect. C*, in press.

Smith, R. W., and D. A. Keszler, *Chem. Mat.* (1992), to be submitted.

Smith, R. W., and D. A. Keszler, *J. Solid State Chem.* **81**, 305 (1989).

Smith, R. W., and D. A. Keszler, *J. Solid State Chem.* (1992) to be published.

Smith, R. W., and D. A. Keszler, *Mater. Res. Bull.* **24**, 725 (1989).

Smith, R. W., and D. A. Keszler, unpublished results.

Smith, R. W., J. L. Luce, and D. A. Keszler, unpublished results.

Sokolova, E. V., M. A. Simonov, and N. V. Belov, *Kristallogr.* **25**, 1285 (1980).

Solov'eva, L. P., and V. V. Bakakin, *Kristallografija* **15**, 922 (1970).

Solov'eva, L. P., and V. V. Bakakin, *Soviet Physics - Crystallogr.* **15**, 802 (1971).

Soules, T. F., and M. V. Hoffman, *Kirk-Othmer: Encyclopedia of Chemical Technology*; John Wiley & Sons, Inc. **14**, 527 (1981).

Stevels, A. L. N., *J. Luminescence* **12/13**, 97 (1976).

Sun, H., Ph.D. Dissertation, Oregon State University (1989).

Sun, H., and D. A. Keszler, *Acta Crystallogr.* **C44**, 1505 (1988).

Sun, H., and D. A. Keszler, unpublished results.

Takéuchi, Y., *Acta Cryst.* **5**, 574 (1952).

Thompson, P. D., Doctoral thesis (1991).

Thompson, P. D., J. Huang, R. W. Smith, and D. A. Keszler, *J. Solid State Chem.* **95**, 126 (1991).

Thompson, P. D., and D. A. Keszler, *Chem. Mat.* **1**, 292 (1989).

Thompson, P. D., and D. A. Keszler, *Chem. Mat.* (1992), submitted.

Thompson, P. D., and D. A. Keszler, *Solid State Ionics* **32/33**, 521 (1989).

Tiščenko, G. N., *Trudy Inst. Krist. Akad. Nauk* **11**, 93 (1955).

Vegas, A., F. H. Cano, and S. Garcia'-Blanco, *Acta Cryst. B* **31**, 1416 (1975).

Velsko, S., Lawrence Livermore National Laboratory, private communication.

Velsko, S. P., M. Webb, L. Davis, and C. Huang, *IEEE J. Quant. Electron.* **27**(9), 2182 (1991).

Viebahn, V. W., *Z. Anorg. Allg. Chem.* **386**, 335 (1971).

Villa, A. C., L. Coghi, A. Mangio, M. Nardelli, and G. Pelizzi, *J. Cryst. Mol. Struct.* **1**, 291 (1971).

Von der Mühll, P. R., S. Andersson, and J. Galy, *Acta Cryst. B* **27**, 2345 (1971).

Walker, N., and D. Stuart, *Acta Crystallogr., Sect. A* **24**, 214 (1968).

Walling, J. C., O. G. Peterson, H. P. Jenssen, R. C. Morris, and E. W. O'Dell, *IEEE J. Quantum Electron.* **16**, 1302 (1980).

Weber, M. J., *CRC Handbook of Laser Science and Technology*, "Section 1: Nonlinear Optical Materials", Boca Raton, Fla.: CRC Press, 1986.

Wen-Tian, F., C. Fouassier, and P. Hagenmuller, *Mat. Res. Bull.* **22**, 899 (1987).

Wimerl, D., *Ferroelectrics* **72**, 95 (1987).

Yakubovich, O. V., N. A. Yamnova, B. M. Shehedrin, M. A. Simonov, and N. V. Belov, *Dokl. Akad. Nauk. SSSR* **228**, 842 (1975).

Yvon, K., W. Jeitschko, and E. Parthe, *J. Appl. Cryst.* **10**, 73 (1977).

Zachariasen, W. H., *Acta Cryst. A* **24**, 214 (1968).

Zachariasen, W. H., H. A. Plettinger, and M.Marezio, *Acta Crystallogr.* **16**, 1144 (1963).

Zayakina, N. V., and A. A. Brovkin, *Sov. Phys. Crystallogr.* **22**(2), 156 (1977).

Zyss, J., and J. L. Oudar, *Phys. Rev. A* **26**(4), 2028 (1982).

APPENDIX

CURRICULUM VITAE

Kathleen I. Schaffers
Department of Chemistry
Oregon State University
Corvallis, Oregon 97331-4003

Birth Date

July 16, 1966

Education

Oregon State University   B.S. 1984

Professional Societies

Phi Lambda Upsilon
Iota Sigma Pi

Publications

K. I. Schaffers and D. A. Keszler, "The Layered Borate $SrBe_2(BO_3)_2$," *J. Solid State Chem.*, **85**, 270 (1990).

K. I. Schaffers and D. A. Keszler, "Structure of $LiSrAlF_6$," *Acta Crystallogr., Sect. C*, **47**, 18 (1991).

K. I. Schaffers, T. Alekel III, P. D. Thompson, J. R. Cox, and D. A. Keszler, "A New Structural Class of Solid-State Oxide," *J. Am. Chem. Soc.*, **112**, 7068 (1990).

K. I. Schaffers, P. D. Thompson, T. Alekel III, J. R. Cox, J. Huang, and D. A. Keszler, "STACK Crystal Chemistry," *Chemistry of Materials*, in preparation.

K. I. Schaffers and D. A. Keszler, "Strontium Scandium Borate, Strontium Yttrium Aluminum Borate, and Lanthanum Strontium Magnesium Borate," *Inorganic Synthesis*, submitted.

K. I. Schaffers, Thomas A. Reynolds, and D. A. Keszler, "Tetrahedral, Triangular 3-D Framework and Luminescence in the Borate $BaBe_2(BO_3)_2$," *Inorganic Chemistry*, in preparation.

K. I. Schaffers and D. A. Keszler, "The Alkaline Earth Beryllium Borate $CaBeB_2O_5$," *Acta Crystallogr. C*, submitted (1992).

K. I. Schaffers, J. L. Luce, and D. A. Keszler, "The Borate $Li_{28}Be_{10}B_2(BO_3)_{18}$," *Inorg. Chem.*, in preparation.

K. I. Schaffers and D. A. Keszler, "Structure of $Sr_2InLiB_4O_{10}$," *Acta Crystallogr. C*, submitted (1992).

K. I. Schaffers and D. A. Keszler, "Optical Second-Harmonic Generation from Triangular Oxoanions," *Chemistry of Materials*, in preparation.

J. R. Cox, K. I. Schaffers, and D. A. Keszler, "Structural and Optical Features of $Ba_3In(BO_3)_3$ and $Sr_3In(BO_3)_3$," *J. Solid State Chem.*, in preparation.

S. Sarkar, K. I. Schaffers, and D. A. Keszler, "Structure and Properties of $Sr_2Mg(BO_3)_2$," *Acta Crystallogr.*, in preparation.

K. I. Schaffers and D. A. Keszler, "One-dimensional Structure of $CdCl_2C_3H_7NO_2$," *Acta Crystallogr. C*, in press.